Thermal Analysis and Performance Validation for In-Vacuum Operation of Compton HV-MAPS Electron Detector for the MOLLER Experiment

by

Shefali

A Thesis submitted to the Faculty of Graduate Studies of
The University of Manitoba
in partial fulfillment of the requirements of the degree of

MASTER OF SCIENCE

Department of Physics and Astronomy
University of Manitoba
Winnipeg

Copyright © 2025 Shefali

Abstract

The Measurement Of a Lepton-Lepton Electroweak Reaction (MOLLER) experiment aims to explore new dynamics beyond the Standard Model. The experiment is placed in Hall A at the Thomas Jefferson National Accelerator Facility (JLab) in Newport News, Virginia, USA. The measurements are acquired by the scattering of longitudinally polarized electrons off unpolarized electrons in a liquid hydrogen target. MOLLER will utilize High Voltage-Monolithic Active Pixel Sensors (HV-MAPS) in the Hall A's Compton polarimeter to monitor the polarization of the incoming beam from the Continuous Electron Beam Acceleration Facility (CEBAF). The HV-MAPS based electron detector contains a quad-planar geometry and each plane incorporates three HV-MAPS chips attached. Compton polarimeter utilizes this detector assembly placed inside the vacuum to detect the compton scattered electrons. The chips generate heat during operation, and thus require an effective cooling system in vacuum. The temperature measurement of the HV-MAPS is useful to understand the thermal properties of the pixel detector and cooling needs. The present study reviews the efforts towards the cooling strategies, structure modification, and thermal simulations to achieve an in-vacuum operation. Further, the prototyping and successful testing of the electron detector's cooling system (using a test version of HV-MAPS chips with equivalent heat load) in a local laboratory was performed, and computational fluid dynamics studies are compared with the collected data.

Acknowledgements

I am deeply grateful to my supervisor, Dr. Wouter Deconinck, without whose support I could not have reached this far. I sincerely thank him for his steady guidance, patience and encouragement. I truly appreciate the time he devoted to meetings and discussions, as well as the freedom he gave me to explore my own ideas. His in-depth knowledge of both theoretical and experimental physics has continually inspired me to learn more and deepen my understanding of the subject. His ability to explain complex concepts in a strategic and simple way has motivated me to follow his example as a researcher and teacher.

I also value the opportunity to take the prototyping and machining course with him, which strengthened my practical skills.

I would also like to thank my committee members, Dr. Michael Gericke and Dr. Savino Longo, for their time, insightful feedback during annual progress meetings, and their valuable suggestions for my thesis. Their input has significantly improved my work.

My sincere thanks go to my lab colleagues and group members. I am grateful to Nafis Rafat Niloy, PhD student, and Kristofer Isaak, engineer in the MOLLER group, for machining the cold plates, cooling blocks, and modifying CAD models required for my simulations. The many discussions with Kristofer on computational fluid dynamics greatly enriched my understanding, and I truly appreciate his time and ideas. I also thank Jie Pan, Research Associate in the MOLLER group, for designing the PCB and for sharing her knowledge about them. A huge thanks goes to Dr. Mohammad Laheji, who was an integral part of this journey. His supervision during detector assembly preparations and testing, along with his valuable discussions and suggestions, made my research much smoother. I am also thankful to my group members Akshaya Vijay, Elham Gorgannejad, Bardh Quni, and former members Tooba and Omar Hassan, for all the Friday group meetings. These meetings were not only useful for sharing updates and ideas but also enjoyable, as they gave me the chance to learn more about their work.

I would like to thank the office staff of the Department of Physics and Astronomy for their continuous support. I am grateful to Susan Beshta for her guidance with graduate student inquiries, Aymsley Bishop Mahon for promptly processing research orders, and Robyn Beaulieu and Milijana Prstojevic for helping with the administrative work.

Beyond the department, I am deeply thankful to all my friends in Winnipeg, with whom I explored biking trails, hiked a few mountains in Canada, and went on our unforgettable quest for rhododendrons in Vancouver. While I cannot name all of them here, their presence made my stay comfortable, joyful, and full of memorable moments. Particular thanks to Akshaya Vijay and Premarun Barik, who have stood by me through thick and thin. This journey has been easier with their presence. I am also thankful to my friends from afar for their support, no matter the distance.

Finally, I would like to extend appreciation to my family. I softly think of my father, who I know is smiling down on me whenever I look at the sky. I learned the value of curiosity and perseverance from him, which continue to guide me every day. I thank my mother, my backbone through every challenge, whose silent sacrifices have been the foundation of all that I have achieved. Maa, your kindness, care and faith in me have carried me through this journey. I'm grateful to my grandmother, the strongest woman I have ever known, for teaching me to never lose hope. A very special thanks goes to my brother, Sachin, who reminded me of my own resilience and stood by me unconditionally, even from afar- just know that I could not have done this without you.

Contents

Abstract ii

Acknowledgements iii

List of Figures vii

List of Tables xi

1 Introduction 1
- 1.1 Overview of the thesis . . . 2
- 1.2 Fundamental particles and their interactions: The Standard Model . . . 2
- 1.3 Electroweak Unification theory and weak mixing angle . . . 9
- 1.4 The Standard Model vertices . . . 11
- 1.5 Production of elementary particles . . . 13
- 1.6 Detection of Elementary particles . . . 14
- 1.7 Spin, Helicity and Parity of fundamental particles . . . 18
- 1.8 MOLLER Experiment Overview . . . 20
- 1.9 Experimental apparatus for the MOLLER . . . 22

2 The CEBAF Facility and Compton polarimetry 27
- 2.1 The Continuous Electron Beam Accelerator Facility . . . 27
- 2.2 Compton Polarimetry . . . 34
  - 2.2.1 Mechanics of Compton Scattering . . . 34
  - 2.2.2 Cross Section and Asymmetry of Compton Scattering . . . 36
  - 2.2.3 Compton Polarimeter . . . 40
- 2.3 Semiconducting detectors in MOLLER experiment . . . 45
  - 2.3.1 Silicon diodes as Electron Detector HV-MAPS Technology . . . 47
  - 2.3.2 Silicon diodes as Temperature Sensors . . . 50

3 Optimization of HV-MAPS Electron Detector models based on Thermal Simulations 53
- 3.1 Electron detector design in Compton Polarimeter . . . 57
- 3.2 Iterative design of the electron detector driven by cooling simulations . . . 59
  - 3.2.1 Model 1 . . . 60
  - 3.2.2 Model 2 . . . 64
  - 3.2.3 Model 3 . . . 69
  - 3.2.4 Model 4 . . . 72
  - 3.2.5 Model 5 . . . 77
  - 3.2.6 Model 6 . . . 79
- 3.3 Adapting Model 6 for final prototyping . . . 85
- 3.4 Calculation of Energy deposited by Beam Halo on the Electron Detector . . . 87

4 Assembly and Testing of HV-MAPS Electron Detector in a local laboratory 91
4.1 Components required for prototyping and testing 92
4.1.1 PCB 92
4.1.2 Cold plate 94
4.1.3 Cooling block and Top plate 97
4.1.4 Coolant Feed through system 100
4.1.5 Silicon wafer chips 101
4.1.6 Thermal pads 102
4.1.7 Integration of chips over PCB 103
4.2 Dummy HV-MAPS chip assembly with heaters 104
4.2.1 Use of resistors as a heating element 104
4.2.2 Use of Nichrome wire as a heating element 106
4.2.3 Comparison of above two heating elements 107
4.2.4 Preparation and testing of Nichrome wire final heater assemblies 108
4.3 Placement of temperature sensors over the critical points of PCB for final testing 110
4.4 Temperature measurement with 4-plane assembly under ambient conditions . . . 114
4.5 Comparison of final measurements inside the vacuum chamber with simulations 117

5 Summary and Conclusion 123

Appendix A 125

List of Figures

1.1 The Standard Model of Particle Physics [4] . . . 3
1.2 Bag of quarks releasing a jet of mesons upon imparting enough energy [7]. . . . 7
1.3 Most precise measurements of the weak mixing angle shown as red diamonds in error bars vs. energy scale μ. The proposed MOLLER goal is shown as green diamond in the error bar. [18] . . . 10
1.4 Subset of interaction vertices of the Standard Model. [1] . . . 11
1.5 Scattering process [1] . . . 12
1.6 Silicon tracking detector mechanism [1] . . . 16
1.7 The bremsstrahlung process [1] . . . 17
1.8 The pair production process [1] . . . 17
1.9 Spin and momentum vector orientation for left-handed and right-handed particles. [21] . . . 19
1.10 The Feynmann diagras for s-channel and u-channel of the Møller scattering with photon and Z bosons as exchange particles. [24] . . . 21
1.11 The schematic diagram of the key components of the MOLLER experiment. The arrows shown in red are the paths followed by the electrons. Image Link: Schematic Diagram . . . 23
1.12 CAD model of the Experimental Apparatus of the MOLLER experiment at Hall A, Thomas Jefferson National Accelerator Facility (TJNAF). [19] . . . 26

2.1 Continuous Electron Beam Accelerator Facility (CEBAF) at the Thomas Jefferson National Accelerator Facility, Newport News, Virginia, USA [35]. . . . 28
2.2 Schematic diagram of the beam transport line [38]. . . . 29
2.3 Production of polarized electrons from circularly polarized laser light shown via band structure of GaAs [38]. . . . 30
2.4 Superconducting radiofrequency (SRF) cavities [45] . . . 32
2.5 Intended improvements in CEBAF facility for upgrade to 12 GeV beam energy. [47] . . . 33
2.6 Compton scattering [48] . . . 35
2.7 Feynman diagrams for Compton Scattering [48] . . . 36
2.8 Variation of the unpolarised differential cross-section ($\frac{d\sigma}{d\rho}$) as a function of ρ (gernerated using Python). . . . 37
2.9 Helicity configuration of electron and photon. [49] . . . 39
2.10 Plot of theoretical longitudinal asymmetry (A_l) as function of (ρ) (generated using Python). . . . 39
2.11 Hall A Compton polarimeter setup [55] . . . 41
2.12 Transverse motion of electron beam trajectory [55] . . . 43
2.13 Transverse deviation of electron beam trajectory between D2 and D3. [55] . . . 44
2.14 Energy band representation of semiconductors [57] . . . 46
2.15 HV-MAPS design [65] . . . 48

2.16 DT-670 diode Voltage Curve [68] . . . 51
2.17 Lead arrangement of the DT-670 silicon diode [67] . . . 52
2.18 4-Lead arrangement for DT-670 diode [67] . . . 52

3.1 Vertical translator for strip detectors in Hall A [55] . . . 58
3.2 Comparison of new and old version of the detector, Credits for left image: [55] . 59
3.3 Computational Aided Design (CAD) of the Model 1 for the electron detetor(Front View featuring therml pad, chips and PCB) . . . 61
3.4 CAD of the Model 1 for the electron detector (front View featuring cold plate) . 62
3.5 CAD of the Model 1 for the electron detector (angled view) . . . 62
3.6 CAD drawing of Model 1 (units: mm) . . . 63
3.7 Thermal simulation results from Computational Fluid Dynamics (CFD) . . . 64
3.8 CAD of the Model 2 for the electron detetor . . . 65
3.9 CAD drawing of Model 2 (units: mm) . . . 65
3.10 Thermal simulation results from CFD for cold plate as aluminum featuring the heat flow path and the periphery temperature. . . . 66
3.11 CFD thermal simulation results for the aluminum cold plate, showing temperature values along various points in the heat flow path. . . . 67
3.12 Thermal simulation results from CFD results for an aluminum cold plate, illustrating temperature generated at at the periphery and its variation along the depth of the aluminum block. . . . 67
3.13 Thermal simulation results from CFD for Copper cold plate. . . . 68
3.14 CFD's thermal simulation results for the copper cold plate, showing temperature values along various points in the heat flow path. . . . 68
3.15 Thermal simulation results from CFD results for a copper cold plate, illustrating temperature generated at the periphery and its variation along the copper block. 69
3.16 CAD of the Model 3 for the electron detetor . . . 70
3.17 Thermal simulation results from CFD for a metal core PCB featuring the heat flow path and the periphery temperature. . . . 70
3.18 CFD's thermal simulation results for the metal core PCB, showing temperature values along various points in the heat flow path. . . . 71
3.19 Thermal simulation results from CFD results for a metal core PCB, illustrating temperature generated at the periphery and its variation along the copper block. 71
3.20 Flexible thermal copper strap [75] . . . 72
3.21 Flexible thermal copper strap [75] . . . 72
3.22 Front view of the Computational Aided Design (CAD) of the Model 4 for the electron detetor. . . . 73
3.23 Side view of the CAD of the Model 4 for the electron detetor . . . 74
3.24 Angled view of the CAD of the Model 4 for the electron detetor . . . 74
3.25 CAD drawing of Model 4 (units: mm) . . . 75
3.26 CFD results for model 4 . . . 76
3.27 Angled view of CFD results for model 4 . . . 76
3.28 CAD model of Model 5. . . . 78
3.29 CAD model for Model 5 featuring detector planes. . . . 78
3.30 CAD drawing of Model 5 (units: mm) . . . 79
3.31 Front view of the CAD model for Model 6 . . . 80
3.32 Side view of CAD model for Model 6 . . . 81
3.33 Illustration of water flowing through the shaft, depicted in blue, highlights the internal cooling mechanism . . . 82
3.34 CAD drawing of Model 6 (units: mm) . . . 83

3.35 CFD simulation for Model 6 featuring front view showing various potential temperature regions. . . . 84
3.36 Temperature variation for Model 6 along the depth of the cold plates. . . . 85
3.37 Electron beam halo interacting with the detector . . . 89

4.1 Printed Circuit Board with J1 connector and chip placement strategy. . . . 93
4.2 Printed Circuit Board [79], with highlighted path of the electrical traces over it. 93
4.3 CAD drawing of the Printed Circuit Board, Units: mm. . . . 94
4.4 Machined cold plate [73, 80] . . . 95
4.5 CAD drawing of the cold plate. . . . 96
4.6 Design of the cold plate acommodating J1 connector. . . . 97
4.7 Front view of the cooling block featuring fastening holes. . . . 98
4.8 Side view of the cooling block featuring the top pocket. . . . 98
4.9 Machined Cooling block with the detachable the top plate [80]. . . . 99
4.10 CAD drawing of the cooling block. . . . 100
4.11 Layout of cooling block prototype, and chilled water feed-through flange (Image credits: [80]). . . . 101
4.12 Silicon wafer chip. . . . 101
4.13 Diced Chips. . . . 102
4.14 Thermal pad with rough texture. . . . 103
4.15 Thermal pad with smooth texture. . . . 103
4.16 All planes with integration of chips over them. . . . 104
4.17 Step-by-step process for assembling the heater using resistors. . . . 105
4.18 Using Nichrome wire as the heating element . . . 106
4.19 Wire secured with clamps and coating of thermal epoxy. . . . 109
4.20 Final heater assemblies. . . . 109
4.21 Diagram showing the silicon diode (sensor) connections to the 6-pin DIN connectors and input connector of the temperature Lakeshore monitor . . . 111
4.22 Placement of Temperature Sensors. . . . 113
4.23 Dual plane assemblies for the Electron Detector. . . . 115
4.24 Complete Electron Detector Assembly . . . 116
4.25 Experimental Setup at the ambient conditions (while data recording, the electron detector asssembly was enclosed in a handmade styrofoam box). . . . 116
4.26 Results of data recorded at the ambient conditions. . . . 117
4.27 Vacuum Chamber used for Testing in the Local Lab at the University of Manitoba. 118
4.28 CAD render of the vacuum chamber with prototype of electron-detector setup placed inside it. . . . 119
4.29 Results of data recorded in the vacuum without cooling. . . . 119
4.30 Computational Results of the Electron Detector with Water at 12 °C and 3 W of Power per Plane: Front View. . . . 120
4.31 Computational results of the electron detector with water at 12 °C and 3 W of power per plane: side view. . . . 121
4.32 Results from the local lab setup, where all the sensors labeled on the side with colors, indicating the temperature recorded. . . . 121

5.1 Wire Bonder [86] . . . 124
.2 Simulated results of the electron detector with water at 4°C and 12 W of power supplied (3 W of power per plane). . . . 125
.3 Measured results of the electron detector with water at 4°C and 12 W of power supplied (3 W of power per plane). . . . 126

.4 Simulated results of the electron detector with water at 8°C and 12 W of power supplied (3 W of power per plane) . . . 126
.5 Measured results of the electron detector with water at 8°C and 12 W of power supplied (3 W of power per plane) . . . 127
.6 Simulated results of the electron detector with water at 16°C and 12 W of power supplied (3 W of power per plane) . . . 127
.7 Measured results of the electron detector with water at 16°C and 12 W of power supplied (3 W of power per plane) . . . 128
.8 Simulated results of the electron detector with water at 4°C and 6 W of power supplied (1.5 W of power per plane) . . . 128
.9 Measured results of the electron detector with water at 4°C and 6 W of power supplied (1.5 W of power per plane) . . . 129
.10 Simulated results of the electron detector with water at 8°C and 6 W of power supplied (1.5 W of power per plane) . . . 129
.11 Measured results of the electron detector with water at 8°C and 6 W of power supplied (1.5 W of power per plane) . . . 130
.12 Simulated results of the electron detector with water at 12°C and 6 W of power supplied (1.5 W of power per plane) . . . 130
.13 Measured results of the electron detector with water at 12°C and 6 W of power supplied (1.5 W of power per plane) . . . 131
.14 Simulated results of the electron detector with water at 16°C and 6 W of power supplied (1.5 W of power per plane) . . . 131
.15 Measured results of the electron detector with water at 16°C and 6 W of power supplied (1.5 W of power per plane) . . . 132
.16 Simulated results of the electron detector with water at 4°C and 15 W of power supplied (3.75 W of power per plane) . . . 132
.17 Measured results of the electron detector with water at 8°C and 15 W of power supplied (3.75 W of power per plane) . . . 133
.18 Simulated results of the electron detector with water at 8°C and 15 W of power supplied (3.75 W of power per plane) . . . 133
.19 Measured results of the electron detector with water at 8°C and 15 W of power supplied (3.75 W of power per plane) . . . 134
.20 Simulated results of the electron detector with water at 12°C and 15 W of power supplied (3.75 W of power per plane) . . . 134
.21 Measured results of the electron detector with water at 16°C and 15 W of power supplied (3.75 W of power per plane) . . . 135
.22 Simulated results of the electron detector with water at 16°C and 15 W of power supplied (3.75 W of power per plane) . . . 135
.23 Measured results of the electron detector with water at 16°C and 15 W of power supplied (3.75 W of power per plane) . . . 136

List of Tables

1.1 Lepton Classification [3] 5
1.2 Quark Classification [3] 6

3.1 Comparison of the temperature at periphery for different models. 86

4.1 Electrical characteristics of the heaters 110
4.2 Description of the input connectors [67] 112
4.3 comparison of temperature results at different sensors locations for both the CFD analysis and experimental setup, for this specific case: coolant temperature: 12 °C, flow Rate: 7.5 L/min, power per plane: 3 W. 122
4.4 Comparison of the experimental (lab) results with the computational (CFD) results. 122

Chapter 1

Introduction

Physics aims to provide a precise description of the physical system, appropriate to the energy scale being considered. Researchers attempt to comprehend the mysteries of the smallest constituents of matter, seeking insight into the fundamental building blocks that compose the world around us [1]. Depending on the energy scale, this field is known as Nuclear physics, Subatomic physics or High-Energy physics [2]. Atoms, the fundamental constituents of matter, manifest as bound states with negatively charged electrons (e^-) orbiting around a central nucleus comprising positively charged protons (p) and electrically neutral neutrons (n). The electrons are bound to the nucleus through electrostatic attraction, a low-energy manifestation governed by the fundamental theory of electromagnetism, Quantum Electrodynamics (QED). The structure of the elements of the periodic table emerges from quantum mechanics, which dictates the precise electronic structure of the different atoms. In the atomic nucleus, the protons and the neutrons are bound together by a strong nuclear force, which is a manifestation of the fundamental theory of strong interactions, Quantum Chromodynamics (QCD) [1].

Dramatic progress has been made in particle physics over the last few decades. A succession of experimental findings has solidified our understanding of the subatomic world of quarks and leptons. The theoretical framework of Quantum Electrodynamics, the Glashow-Weinberg-Salam theory explaining electroweak process, and Quantum Chromodynamics collectively forms what we refer to as the Standard Model of Particle Physics. No one predicts that Standard Model is the final answer to everything, but it provides us, for the first time, a foundational framework to further explore the universe. Our knowledge of the subatomic world relies on the key theories within the Standard Model [3]. However, the development and the validity of the Standard Model would have been impossible without a close interplay between theory and experiment [1].

1.1 Overview of the thesis

The present study demonstrates the thermal studies and in-vacuum performance analysis supporting the capability of the HV-MAPS technology to be used as an electron detector for the MOLLER experiment at Hall A of the Jefferson Lab. This thesis is divided into following 5 chapters:

Chapter 1 introduces the general physics phenomenon relevant to the MOLLER experiment and outlines the motivation driving the experiment. It also provides a brief description of the experimental setup to achieve the study's objectives.

Chapter 2 offers explanation of the key components of the polarized electron beam source and the Compton polarimeter. It also discusses the use of semiconductor diodes as electron detectors and temperature sensors, along with an explanation of HV-MAPS technology.

Chapter 3 presents the CAD models and components of the detector module. The main focus of this chapter is the basic heat transfer mechanism and the thermal/cooling analysis of the different models of the electron detector.

Chapter 4 focuses upon the experimental techniques adopted in a local laboratory to achieve a working prototype inside the vacuum chamber. The results are discussed in detail at various power levels deposited onto the HV-MAPS chips. Finally, the comparison of these measurements with computational fluid dynamics data is shown.

Chapter 5 concludes the work conducted in this study and discusses the future plans based upon the findings of this thesis.

1.2 Fundamental particles and their interactions: The Standard Model

The core of this introduction to the field is an account of the rise and verification of the Standard Model through numerous experiments. Over time, the Standard Model has become established as a well-tested physics theory. It consists of matter particles (quarks and leptons, also called fermions) and the force carrying particles (bosons), and the Higgs boson. There are 12 fermions, split into six quarks, up (u), charm (c), top (t), down (d), strange (s), bottom (b) and six leptons, electron (e), muon (μ), tau (τ), electron neutrino (ν_e), muon neutrino (ν_μ), tau neutrino (ν_τ). The electron, muon, and tau are matched with the electron neutrino, muon neutrino, and tau neutrino. Neutrinos have very little mass and they interact only weakly with the rest of the matter particles making them extremely difficult to detect. These particles

interact through the exchange of bosons, which carry three of the four fundamental forces of nature: the strong force, the weak force and the electromagnetic force. The bosons are five in number (gluons (g), W, Z, photon (γ), Higgs). The gluon carries the strong force. It holds quarks together to make protons, neutrons and other exotic particles. Protons and neutrons are not part of the Standard Model because they are composite particles and are made out of quarks. All the composite particles and all the matter that we see in the universe are made out of just quarks and leptons. The electromagnetic force is carried by the photon. This force holds the atoms together. The weak force is conveyed by the W and Z bosons. The gravitational force, which is the fourth fundamental force, is notably weak at the atomic scale and there is no experimental evidence available to prove the existence of its carrier. The Higgs boson, unlike the other bosons, does not mediate a force; instead, it is a manifestation of the Higgs field, which spreads all over space and gives mass to elementary particles through their interaction with it [3]. These fermions (the fundamental particles)and bosons (carrying the interactions) are shown in the Fig. 1.1.

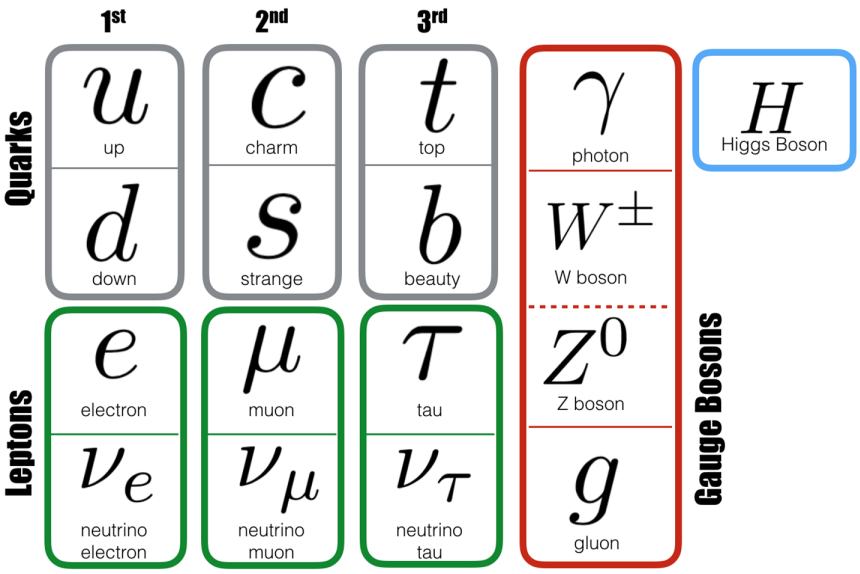

Figure 1.1: The Standard Model of Particle Physics [4]

Elementary particles have an intrinsic angular momentum S. Every elementary particle is characterized by a spin quantum number. Spin is inherently quantized, meaning it can only take on certain specific values. Fermions possess half-integral spin quantum numbers, such as $\frac{1}{2}, \frac{3}{2}, \frac{5}{2}$ and so on, whereas bosons are characterized by integral spin quantum numbers like 0, 1, 2, etc. It is important to note that spin numbers cannot exist between these discrete values. When particles are composed of multiple fermions, their overall spin is determined by the combination of the individual spins of the constituent fermions. For instance, a baryon, which is composed of three quarks, will have an overall spin that is combinations of $\frac{1}{2} \pm \frac{1}{2} \pm \frac{1}{2}$. Consequently, all

baryons, such as protons and neutrons, are classified as fermions. Similarly, a meson, which consists of a quark and an antiquark, will have an overall spin of either 0 or 1 with combinations of $\frac{1}{2} \pm \frac{1}{2}$. Therefore, all mesons are classified as bosons. The force-carrying bosons within the Standard Model, including gluons, photons, and the W and Z bosons, each have a spin of 1 and are association with vector fields. The Higgs boson corresponds to a scalar field, and thus has a spin of 0. If the graviton, a hypothesized particle associated with the gravitational field were to be discovered, it would have a spin of 2, as it corresponds to a tensor field. Fermions and bosons, with their different spin characteristics, form the foundation of our understanding of elementary particles and the fundamental forces that govern the universe [5].

Lepton Classification: In the realm of Particle Physics, leptons are a fundamental class of particles in the Standard Model of particle physics, differentiated by their unique properties such as charge (Q), electron number (L_e), muon number (L_μ), and tau number (L_τ). These properties help categorize the six leptons into three different generations as shown in 1.1. The **first generation** consists of the electron (e) and the electron neutrino (ν_e) (Table 1.1). The electron is perhaps the most familiar lepton, as it is a fundamental component of the structure of atoms. It has a negative electric charge ($Q = -1$) and an electron number ($L_e = 1$). The electron neutrino, on the other hand, is a neutral lepton ($Q = 0$) with an electron number ($L_e = 1$). Neutrinos are very light and interact feebly with matter, and makes them difficult to detect. The **second generation** includes the muon (μ) and the muon neutrino (ν_μ). The muon is similar to the electron but has greater mass. Like the electron, the muon carries a negative electric charge ($Q = -1$) and has a muon number ($L_\mu = 1$). The muon neutrino is electrically neutral ($Q = 0$) and has a muon number ($L_\mu = 1$). Muons are unstable and decay into electrons and neutrinos, still they can be produced and studied in the particle accelerators. Similar to electron neutrinos, the muon neutrino is extremely light and interacts weakly with matter. The **third generation** consists of the tau (τ) and the tau neutrino (ν_τ). The tau is the most massive among all the charged leptons, with a mass approximately 3,477 times that of an electron. It has a negative electric charge ($Q = -1$) and a tau number ($L_\tau = 1$). The tau neutrino, like the other neutrinos, is electrically neutral ($Q = 0$) and has a tau number ($L_\tau = 1$). It has a very short lifetime, making it unstable even as compared to muons and they tend to decay into lighter leptons and neutrinos [3].

Each lepton generation is distinguished by increasing mass and decreasing stability, with the first generation being the lightest and and most stable, and the third generation being the heaviest and the least stable. The lepton number conservation is an important principle. Hence, in all particle interactions in the Standard Model, the total number of leptons of each kind must be constant. This principle helps us to understand the outcomes of particle collisions and decays. There are also six antileptons, with all the signs reversed. The positron, for example, carries a charge of (Q = +1) and an electron number ($L_e = -1$) [3].

Table 1.1: Lepton Classification [3]

Generations	Lepton	Q	L_e	L_μ	L_τ
I	e	-1	1	0	0
I	ν_e	0	1	0	0
II	μ	-1	0	1	0
II	ν_μ	0	0	1	0
III	τ	-1	0	0	1
III	ν_τ	0	0	0	1

Quark Flavour Classification: Similarly, there are six distinct "flavors" of quarks, much like leptons, each classified according to several properties: charge (Q), strangeness (s), charm (c), bottomness (b), and topness (t), upness (u) and downness (d), even though these terms are rarely used in practice. The six quark flavours are further categorized into three generations, each with increasing masses as shown in Table. 1.2. The **first generation** consists of the up quark (u) and the down quark (d). The up quark has a charge of $+\frac{2}{3}$ and the down quark carries a charge of $-\frac{1}{3}$. The up quark is lightest among all the quarks. The mass of down quark is almost double of that of the up quark, but both of them are still the lightest of all the other generations of the quark family. These quarks combine to form protons and neutrons, the building blocks of nucleus of the atom. This generation is the most stable and actually forms most of the matter that we see in the universe. The **second generation** includes the charm quark (c) and the strange quark (s). The charm quark has a charge of $+\frac{2}{3}$ and introduces the property of charm quantum number $C = 1$. It is significantly heavier than the up quark. The strange quark, with a charge of $-\frac{1}{3}$, is characterized by a strangeness quantum number $S = -1$. These quarks are less stable than the first-generation quarks and are much heavier than the first generation quark family. The **third generation** comprises the top quark (t) and the bottom quark (b). The bottom quark has charge of $-\frac{1}{3}$, is heavier than the last generations discussed. It has a beauty quantum number $B = -1$. The top quark, on the other hand, is the heaviest of all quarks, with a charge of $+\frac{2}{3}$, and was the last to be discovered due to its massive nature and short lifespan [3].

Similar to the conservation of lepton numbers, an essential principle in particle physics is the conservation of quark flavor numbers. This principle says that the total number of quarks of any flavour in electromagnetic or strong interaction must remain constant and only weak interactions can change quark flavour. Again, all signs would be reversed on the table of anti-quarks. Meanwhile, each quark and antiquark also exists in three colors [3].

Table 1.2: Quark Classification [3]

Generations	quark	Q	D	U	S	C	B	T
I	u	$+\frac{2}{3}$	0	1	0	0	0	0
I	d	$-\frac{1}{3}$	-1	0	0	0	0	0
II	s	$-\frac{1}{3}$	0	0	-1	0	0	0
II	c	$+\frac{2}{3}$	0	0	0	1	0	0
III	b	$-\frac{1}{3}$	0	0	0	0	-1	0
III	t	$+\frac{2}{3}$	0	0	0	0	0	1

In the current understanding of particle physics, as best as we can comprehend, the studies rely on four type of interactions as below [6]:

1. Strong interaction
2. Electromagnetic interaction
3. Weak interaction
4. Gravitational interaction

The range of the **strong interaction** is very short, typically limited to the scale of the atomic nucleus (10^{-15} m). The charge carriers in strong interactions are massless particles called gluons. Particles which are bound by the strong force are referred to as hadrons. Baryons, characterized by the half-integral spin quantum number, are one of the class. The baryons at the lowest energy levels, and having the least mass include proton and neutron. The strong nuclear force plays a significant role in binding the quarks together to form protons and neutrons within the atomic nuclei. These are collectively termed nucleons. Mesons, with integral values of the spin quantum number, are the other class. Hyperons, another category of baryons with atleast one unit of strangeness (S), charmness (C) or bottomness (B), are unstable, and prefer to undergo decay through the weak interaction. These possess a non-zero value for the internal quantum number [6] [1].

Early theories of strong interaction helped us predicting the existence of Λ hyperon and the Ω hyperon. Resonant particles decay through strong interactions with lifetimes of the order of 10^{-23} s. Travelling at the speed of light, their brief lifespan is too short for the particles to cover a measurable distance at laboratory scale. So, the properties of the resonances are understood on the basis of their stable decay products. Further, in the subatomic domain, it was observed that free quarks have never been observed. According to the Bag Model of quark confinement, if one of the constituent quark of the hadron is given enough energy, it tries to leave the hadron. It causes a new quark-antiquark pair to form as shown in Fig. 1.2. These pairs then come together to form other hadrons. When the initial energy provided to a quark is large, the process of it separating from the hadron can produce a narrow spray of hadrons called a jet [6].

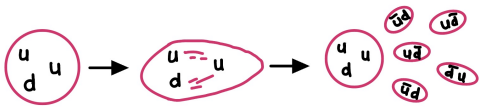

Figure 1.2: Bag of quarks releasing a jet of mesons upon imparting enough energy [7].

Electromagnetic interaction enters the framework when we talk about the interaction of particles carrying electric charge. Both leptons and quarks undergo electromagnetic interaction. The charge carrier in this case is the photon (γ). Their electromagnetic properties depend on their electric charges and magnetic moments. The interactions via which the electrostatic force keeps the atom stable by holding them together is called electromagnetic interaction. The electrostatic force affects all the particles that carry an electric charge. Many detectors rely on these interactions of particles within matter, which are well described by one of the most successful theories in physics, Quantum Electrodynamics (QED). These interactions yield long-range forces, but the strength of the electromagnetic force diminishes with the distance, becoming insignificant at large distances. The photon is the mediator of the electromagnetic interaction [6]. We can categorize the electromagnetic phenomena crucial in understanding of the interactions of matter with high-energy radiation quanta. Consider first the phenomena that occour when a charged particle passes near an atom. This results in ionisation or excitation of the atom. We can analyze this phenomena using the conventional methods of quantum mechanics without considering radiation. However, if the distance of closest approach is at the scale of atomic dimensions, interaction no longer involves the passing particle and the atom, but rather the passing particle and one of the atomic electrons. As a consequence of such interaction, the electron is ejected from the atom with considerable energy. The phenomenon is often described as Auger process. While radiation phenomenon can still be neglected, the magnetic moment and spin of the interacting particles must be accounted for. When the distance of closest approach decreases below the atomic radius, the deflection of the trajectory of the passing particle in the electric field of nucleus becomes the predominant effect. This problem would be treated as scattering of particles. Now, turning our attention to the interaction of photons with matter, primarily used in the particle detectors, we may classify few cases. The interaction of a photon with atom as a whole induces the photoelecttric effect. The interaction of photon with free electron triggers compton scattering, with detailed information provided in the Sec. 1.4 of this chapter. Lastly, when a photon interacts with the coulomb field of the nucleus, the phenomenon is termed as pair [8].

The **weak interaction**, the third fundamental force of nature, is mediated by the $W^{\pm}$ and Z^{o} bosons particularly important for neutrino interactions and the decay of most metastable particles. This force is responsible for processes such as certain forms of radioactivity and the decay of the hyperon particles. The extremely short range of the weak interaction, confined

to a distance of approximately 10^{-17} m exists. Enrico Fermi proposed the first theory of the weak interaction in 1933, known as Fermi's interaction, which suggested a process in which a neutron decays into a proton, an electron, and an antineutrino. His theory introduced the concept of a new type of force existing between particles, which is now known as a weak force, responsible for this decay. The $W^{\pm}$ and Z^o bosons were predicted in the 1960s by Nobel laureates Weinberg, Glashow, and Salam, and were experimentally discovered in 1983 at CERN [9]. These bosons are significantly heavier than protons or neutrons. The weak interaction breaks parity symmetry (or mirror image symmetry), also sometimes breaks charge-parity symmetry. Two significant examples of this are the asymmetry measured in the scattering of a polarized electrons off the nuclei at SLAC (Stanford Linear Accelerator Center) [10] and the asymmetry in muon pair production in electron-positron collision at PETRA (Positron-Electron Tandem Ring Accelerator) [11]. This breaking of symmetry is a unique property of the weak force that plays a crucial role in analyzing the behaviour of the elementary particles. The field strength of the weak force is several orders of magnitude less than that of the electromagnetic force over any given distance, which itself is further orders of magnitude weaker than the strong nuclear force. The W bosons are electrically charged and are designated by their symbols: W^+ and W^-. The Z boson, being neutrally charged, mediates only the weak neutral current, making its interactions with particles more challenging to detect.The elementary particles, fermions, with half-integer values of intrinsic angular momentum, and right-handed antifermions interact through the weak interaction by exchanging W^+, W^-, and Z^o bosons [3].

The **gravitational force** is a fundamental interaction that governs the interaction between massive bodies separated by vast distances. When considering interactions between everyday massive objects, gravitational interaction dominates. However, when it comes to elementary particles, this force becomes inconsequential. This force is the weakest of all the above mentioned forces. It is approximately 10^{38} times weaker than the strong nuclear force, which binds protons and neutrons within the atomic nucleus, 10^{36} times weaker than the electromagnetic force, which dominates the interactions between charged particles, and 10^{29} times weaker than the weak nuclear force, which is accountable for certain types of radioactive decays. However, the impact of gravitational force changes significantly when we shift our focus to larger scales.

Shortly after the Big Bang, an event occoured that conferred mass upon the particles. In 1960s, some physicists proposed a theory to elucidate how particles get their mass. They proposed the existence of a force field that came into action shortly after the big bang. Particles that interact with this field get mass. This force field is now known as the Higgs field. The theoretical prediction of the Higgs Boson and its associated field was made in 1964 with different approaches explaining how mass could arise in local gauge theories, as shown in 1964 PRL symmetry breaking papers which were written by three teams (Peter Higgs [12] and Robert Brout and François Englert [13] [14]). Since every particle can be represented as a wave in the quantum field, introducing a new field into the theory means that a particle associated with this

field should also exist. It was extremely difficult to manipulate the omnipresence of the Higgs field in the past. To observe it, scientists should generate its quantum particle, the Higgs boson, by colliding particles at high energies using large particle accelerators. Like most other particles in nature, the Higgs boson is unstable. It decays into lighter particles immediately after its production. In July 2012, after analyzing the vast numbers of proton proton collisions over two years, ATLAS [15] and CMS [16] observed a new particle whose properties were consistent with the Higgs boson's. It confirmed the Brout-Englert-Higgs (BEH) mechanism and the Higgs field. As a result, the 2013 Nobel Prize in Physics was awarded to Peter Higgs and Francois Englert for their foundational contributions to the work. The Higgs field is the first scalar quantum field ever observed. Hence, the Higgs boson is the first elementary scalar particle ever observed with spin quantum number of zero. Physicists are still exploring its properties by measuring its mass and studying its various modes of production and transformations.

1.3 Electroweak Unification theory and weak mixing angle

Shortly after the Big Bang, the electroweak force split into the electromagnetic and weak forces as the universe cooled down. Just before this event, the universe's temperature was approximately 10^{15} K, a temperature that is currently unattainable in experimental facilities to replicate the effects of these two forces. Thus, the electroweak interaction or electroweak force represents the unified description of two of the four fundamental interactions in nature: electromagnetism and the weak interaction. Sheldon Glashow, Abdus Salam, and Steven Weinberg were awarded the 1979 Nobel Prize in Physics for their contributions to the unification of these forces, known as the Weinberg-Salam theory. The photon, associated with electromagnetic interaction, and the W and Z bosons, associated with the weak interaction, are key components in this unification. The W and Z bosons, with masses around 81 GeV and 92 GeV respectively, were the heaviest particles discovered at the time, while the photon remains massless. The disparity in their masses is due to spontaneous symmetry breaking that occurred as the universe cooled down [17].

The fundamental concept of electroweak unification is to represent the two neutral vector bosons, the photon and the Z^0, as orthogonal linear combinations of the W^0 and B^0 bosons. This relationship is described through a rotation characterized by the electroweak mixing angle, θ_W (also known as the Weinberg angle), which also defines the coefficients of the linear combination as follows:

$$|\gamma\rangle = cos\theta_W \left|B^0\right\rangle + \sin\theta_W \left|W^0\right\rangle \tag{1.1}$$

$$\left|Z^0\right\rangle = -\sin\theta_W \left|B^0\right\rangle + \cos\theta_W \left|W^0\right\rangle . \tag{1.2}$$

The electromagnetic charge is then determined in terms of the angle θ_W ,

$$e = g \sin \theta_W. \tag{1.3}$$

The weak mixing angle, θ_W, also establishes the relationship between the masses of the W and Z bosons (denoted as m_W and m_Z),

$$\cos \theta_W = \frac{m_W}{m_Z}. \tag{1.4}$$

Thus, the electroweak unification theory could be used for the prediction of absolute masses of the W and Z bosons even before their actual discovery. From electron-positron scattering, the weak-mixing angle determined with the help of the weak charge of the electron is given by,

$$Q_W^e = 1 - 4 \sin^2 \theta_W. \tag{1.5}$$

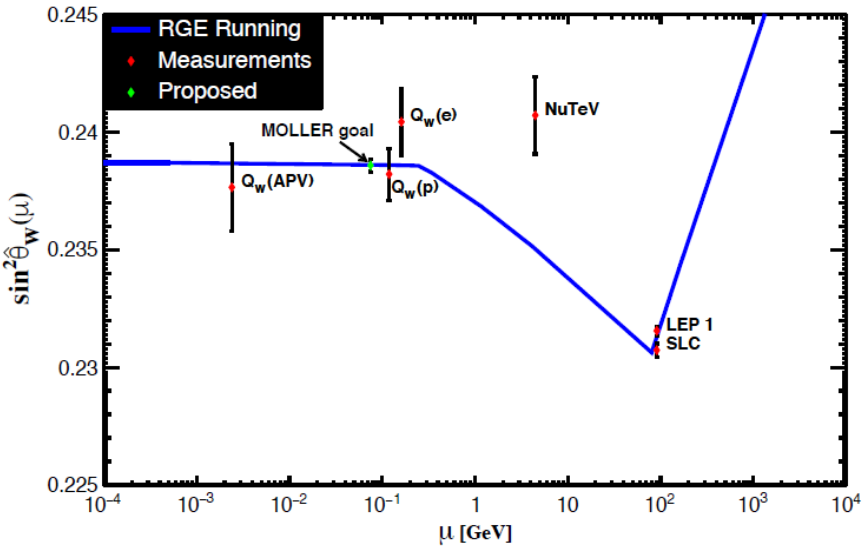

Figure 1.3: Most precise measurements of the weak mixing angle shown as red diamonds in error bars vs. energy scale μ. The proposed MOLLER goal is shown as green diamond in the error bar. [18]

The weak mixing angle, $\sin^2 \theta_W$, has especially crucial in testing the theory at the quantum loop level, which is a primary focus of precision electroweak physics. In Fig. 1.3, the blue curve represents the theoretical prediction of the weak mixing angle, and the theoretical error in the low energy extrapolation range is equal to the width of the line. The two most precise measurements of the weak mixing angle at lower energies come from the SLAC E158 experimental measurement, and the measurement of weak charge of ^{133}Cs through the table-top atomic parity violation studies. As it is clearly noticeable, at lower energies, there has been no measurement of this quantity with a precision comparable to the theoretical curve. If a new measurement sig-

nificantly diverges from the theoretical prediction, it could suggest the presence of new physics. The MOLLER (Measurement Of a Lepton-Lepton Electro-Weak Reaction) experiment aims to achieve this by measuring the parity-violating asymmetry in Møller scattering [19] [18].

1.4 The Standard Model vertices

The essence of the strong, electromagnetic, and weak forces is described by the properties of the bosons in the associated quantum field theory. There are a few possible ways in which the gauge bosons can couple to the fermions, and the understanding of these coupling strengths and their respective interaction vertices gives us profound insights into working of the Standard Model. This framework offers predictive insights for a wide array of particle interactions observed in nature. These coupling processes are illustrated in Fig. 1.4. Each interaction between gauge bosons and fermions happens via a three-point vertex. This vertex involves the gauge boson and an incoming and outgoing fermion. Each type of force—strong, electromagnetic, and weak has an associated coupling strength denoted by g. For Quantum Electrodynamics (QED), which governs the electromagnetic force, the coupling strength is represented by the electron charge, symbolized by $g_{QED} = e \equiv +|e|$. This coupling constant plays a critical role in the interactions between charged particles and their associated fields [1].

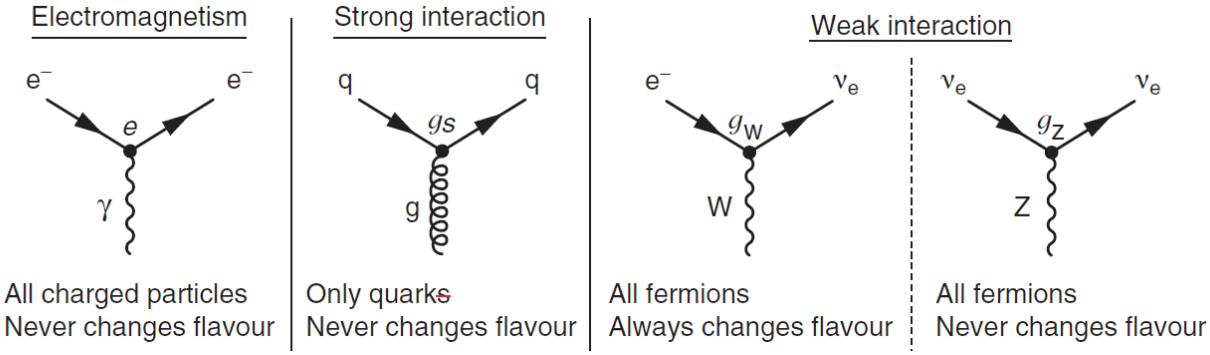

Figure 1.4: Subset of interaction vertices of the Standard Model. [1]

A particle interacts with a force-carrying boson only if it carries the charge for that interaction. For example, only the quarks carrying the color charge of Quantum Chromodynamics (QCD) participate in the strong interaction and couples with gluon, and only the charged particles carrying the electric charge participate in electromagnetic interaction and couple to photon. Only the quarks carry the color charge of QCD, and hence only quarks participate in the strong interaction. All left-handed fermions (both quarks and leptons) carry the charge

associated with the weak interaction, known as weak isospin. Thus, they all participate in weak interactions. The weak charged-current interaction couples different flavor fermions, enabling one type of fermion to transform into another. The W^+ and W^- bosons, which mediate the weak charged-current interaction, possess electric charges of + e and − e, respectively. To maintain the conservation of electric charge in the weak charged-current interaction, only coupling of pairs of fermions that differ by one unit of electric charge is allowed. Hence, for a lepton such as a neutrino, which is electrically neutral, interactions occur only through the weak force by converting into its corresponding charged lepton (such as an e, μ, or τ), and vice versa [1].

For quarks, the weak interaction pairs up all the possible combinations which differ by one unit of charge. The weak charged-current coupling interaction is most significant between the u, c, t quarks with a charge of $+\frac{2}{3}$ and the d, s, b quarks with a charge of $-\frac{1}{3}$. This coupling interaction is the greatest for the quarks of the same generation. Since the weak interaction is the only interaction known so far for which the incoming and outgoing fermions are different, and hence introduces a change of flavour, this interaction becomes more important while considering particle decays. As can be seen in the scattering process shown in Fig 1.5, the strength of the fundamental interaction at the vertices is denoted by coupling constant g, which can be served as a measure of the probability that a spin-half fermion will absorb or emit the boson associated with the interaction. The quantum mechanical transition matrix element for an interaction process including a factor of the coupling constant g at each vertex is therefore [1],

$$M = g^2. \tag{1.6}$$

And the interaction probability, which is proportional to the square of the matrix element is [1],

$$|M|^2 = M^* M \quad = g^4. \tag{1.7}$$

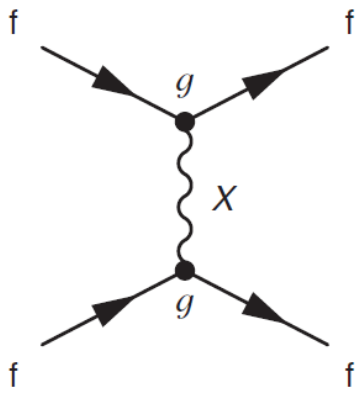

Figure 1.5: Scattering process [1]

1.5 Production of elementary particles

Electrons and protons are the stable components of ordinary matter. Generating electrons is a straightforward process which is heating a piece of metal, causing the electrons to be emitted. To have a directed electron beam, one then sets up a positively charged plate neraby, to attract them there, and incorporate a small aperture. All the electrons that make through this aperture constitute an electron beam. Such an electron gun serves as a component in devices like oscilloscope, televisions and the biggest electron accelerator experiments. To have a proton beam, ionization of hydrogen is done. Infact, when we are using the protons as the target, the electrons become negligible due to their lightweight nature, as an incoming energetic particle knock all the electrons off the hydrogen atoms. So we can say that a reservoir of hydrogen is essentially a containment of protons. For more exotic particles, three primary sources are available: nuclear reactors, cosmic rays, and particle accelerators [3].

Among theses sources of particle production, only particle accelerators are relevant to the experiment discussed in this thesis. Particle Accelerators have the ability to produce and study various particles through the acceleration and collision of elementary particles. While the study of cosmic rays and their cascades continues to be an interesting subject on its own, nearly all the experiments now use man-made beams produced by particle accelerators. Initiating with a source of low-energy particles, accelerators elevate their energy by applying electric forces. Accelerators are only directly capable of producing beams of stable, electrically charged particles, such as protons, anti-protons or electrons but there are indirect methods for producing beams of unstable particles and even for producing some neutral particles, including neutrinos. Particle production in accelerators involves several stages, each contributing to our understanding of the properties and behaviour of the particles. Particle accelerators use electric field to accelerate the the charged particles to high speed, and magnetic field to steer the particle's direction. There are two main types of accelerators, the linear accelerator (linacs), and the circular accelerators (like cyclotrons and synchrotrons) [3]. They accelerate the particles to speeds as higher as velocity of light. Starting with electrons and protons, elevating the energy levels, and finally colliding them with the designated target, one can separate out the resulting debris the particle species you wish to study. Nowadays this approach enables the production of intense secondary beams of positrons, pions, muons, kaons, and antiprotons. Subsequently, these beams can be directed towards a different target. The stable particles can also be directly introduced into the storage rings and are guided by the powerful magnets, these particles circulate at high velocities for a longer time , allowing extraction and usage at the required moment. In general, the heavier the particle you are looking for, the higher must be the energy of collision. Therefore, historically, lightweight particles were discovered first, and with the progression of time, accelerators became more powerful, and much more heavier particle have been found till the date. It appears that particle experiences a significant increase in energy when two high-speed particles collide head-on, in contrast to firing one particle at a stationary target. Thus, the experiments often involve colliding beams from intersecting storage rings.

If these particles fail to collide on the first attempt, they can make another attempt on the next revolution. Notably, the same ring can be used for electrons and positrons, with positive charges going around in one direction and negative charges in the other. Generally, higher the energy of the collision, the closer particles approach one another. Study of interaction at extremely small rate necessitates highly energetic particles. In terms of quantum mechanics, a particle of momentum p has an associated wavelength λ given by the de-broglie formula $\lambda = \frac{h}{p}$, where h is the planck's constant. Study of the small scale structures, requires dealing with the smaller wavelength (larger momentum) [3].

1.6 Detection of Elementary particles

High- energy particle physics experiments are structurally planned to detect the particles produced in collisions. Among the particles that can be produced, only the electron (e^-), proton (p), photon (γ), and neutrinos (ν) (which are effectively undetectable) are stable. Unstable particles travel a distance of $\gamma v \tau$ before decaying. High-energy collisions can produce relativistic particles with lifetimes exceeding approximately 10^{-10} s, which can go several meters, and are directly detectable. Conversely, particles with lifetimes less than 10^{-10} s are typically known to decay before traveling a significant distance from their point of origin, making their direct detection impossible. In such cases, the decay products are available to detect. For a particle to be detected, it must interact with the material of the detector. The nature of these interactions varies depending on the type of particle and its energy. Detecting a particle involves more than merely locating it, precise localization (or resolution) is needed to separate particles in both space and time and to determine their interaction type. Physicists desire to do particle identification and measure its energy and momentum accurately. Given all the particles and their associated different types of interactions, it is difficult for a single detector to be able to meet all these requirements. Modern particle physics experiments often use large, multi-component detectors that integrate various sub-detectors into a single device. These sophisticated setups allow detailed measurements of complex interactions, including those involving very short-lived particles. Such large-scale experiments involve extensive collaboration, years of effort, and millions of dollars to measure the properties of new particles [2]. In particle physics collider experiments, the observable particles are the ones that are stable and relatively long-lived. The methods used to detect and identify these particles vary based on how they interact with matter.

For the charged particles which are heavier than electrons, the interactions within a medium are non-destructive. These particles experience only a minor energy loss and a slight momentum transfer, leaving themselves largely undisturbed. The primary mechanism of energy loss for these particles within the detector medium is the ionization of atomic electrons. As a relativistic charged particle moves through a medium, it engages in electromagnetic interactions with the atomic electrons, resulting in energy loss through ionization. The ionization energy loss per unit length for a singly charged particle with velocity v = βc in a medium having

atomic number Z and number density n is quantified by the Bethe–Bloch equation,

$$\frac{dE}{dx} \approx -4\pi\hbar^2 c^2 \alpha^2 \frac{nZ}{m_e v^2} \{\ln[\frac{2\beta^2\gamma^2 c^2 m_e}{I_e}] - \beta^2\}. \tag{1.8}$$

The effective ionization potential, I_e, represents the average ionization potential of the material for all the atomic electrons. For any given medium, the rate at which a charged particle loses energy through ionization is expressed via its velocity. Due to the $\frac{1}{v^2}$ term in the Bethe–Bloch equation, the energy loss per unit distance, $\frac{dE}{dx}$ is highest for low velocity particles. In modern particle physics, the focus is primarily on highly relativistic particles, where $v \approx c$. For such particles, in a given medium, dE/dx shows a logarithmic dependence on $(\beta\gamma)^2$ resulting in a slowly rising rate of ionization energy, where

$$\beta\gamma = \frac{\frac{v}{c}}{\sqrt{1-(\frac{v}{c})^2}} \quad = \frac{p}{mc}. \tag{1.9}$$

resulting in a slow "relativistic rise" of the rate of ionization energy loss. The rate of ionization energy loss is largely independent of the specific material, except in terms of its density ρ. This can be understood by expressing the atomic number density as $n = \frac{\rho}{A\mu}$, where A is the atomic mass number and $m_u = 1.6610^{-27}$ kg is the unified atomic mass unit. Consequently, the bethe-bloch equation can be reformulated as follows:

$$\frac{1}{\rho}\frac{dE}{dx} = -\frac{4\pi\hbar^2 c^2 \alpha^2}{m_e v^2 m_u}\frac{Z}{A}\{\ln[\frac{2\beta^2\gamma^2 c^2 m_e}{I_e}] - \beta^2\}. \tag{1.10}$$

It is observed that $\frac{dE}{dx}$ is proportional to the ratio $\frac{Z}{A}$. Since atomic nuclei contain roughly equal numbers of protons and neutrons, $\frac{Z}{A}$ remains nearly constant across different elements. Therefore, the rate of energy loss due to ionization is primarily dependent on the material's density and does not significantly vary with different materials. However, other energy-loss mechanisms may come into play depending on the type of particle [1, 6].

These charged particles can be detected by using different sets of detectors. Detecting and measuring the momenta of charged particles is an important component of any major particle physics experiment. Charged particles, irrespective of the medium they traverse, leave behind a path of free electrons and ionized atoms. By detecting this ionization, one can reconstruct the trajectory of the charged particle. In a large gaseous tracking volume, the freed electrons drift toward sense wires under the influence of a strong electric field, allowing the recording of signals [1]. Computer software then combines the spatial locations of these detector interactions to determine the particles' trajectories, a process known as tracking, and are detected by **tracking detectors**. When a charged particle passes through a silicon wafer that is properly doped, it generates electron-hole pairs through the ionization process, as shown in Fig. 1.6 . By applying a potential difference across the silicon, the holes drift towards the electric field and

are collected by the p–n junctions. These sensors can be configured into silicon strips or silicon pixels, providing precise two-dimensional spatial points. After being collected, the signals are amplified by dedicated electronics, resulting in a clear signal corresponding to the specific strip or pixel where the charge was collected [1].

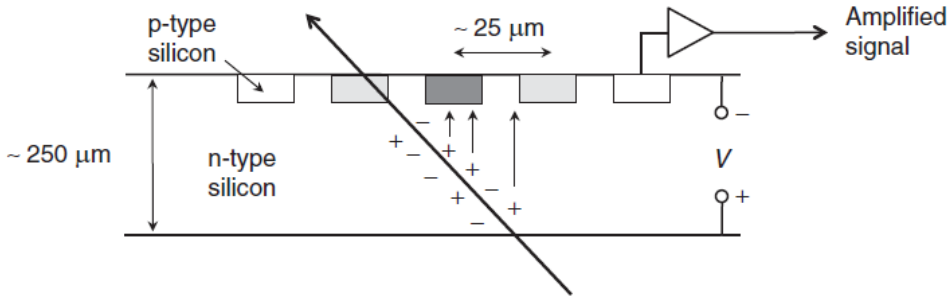

Figure 1.6: Silicon tracking detector mechanism [1]

The spatial resolution is the most critical characteristic of a tracking chamber, determining the precision with which the particle's trajectory can be localized. Other vital characteristics include the detector's response time and dead-time. Response time is the duration required to generate a signal following a particle's trajectory, encompassing both the intrinsic interaction time between the particle and the detector medium and the time required to collect the resultant photons or charges. If a second particle enters the detector during this response time, its signal may overlap with the first, potentially limiting the maximum input event rate. The required spatial and temporal resolutions of tracking detectors are influenced by the event rate and average particle multiplicity [6].

Organic scintillators are widely used in modern particle physics to detect charged particles without needing precise spatial data. When a charged particle traverses an organic scintillator, it excites molecules. The excited atoms then can deexcite by emitting light. This phenomenon, fundamental to scintillation counters , relies on efficiently collecting emitted light, directing it onto a photomultiplier tube, which converts it into electric signals and amplifies the signals for analysis.

Charged particles could also potentially be detected via **Cherenkov detectors**. The particles traveling through a dielectric medium with a velocity greater than the speed of light in that medium emit Cherenkov radiation. This occurs as the particles induce polarization in the medium's molecules, which emit photons as they return to their original state. The resulting Cherenkov radiation forms a coherent wavefront at a specific angle to the particle's path. This light can be collected and converted into an electrical signal using a photomultiplier tube. These detectors are suitable for particle identification [1, 6].

For electrons, predominant energy loss is through ionization at low energy scale. However, above a critical energy (E_c), bremsstrahlung energy loss becomes the primary energy loss mechanism. When defected by the electrostatic field of a nucleus, the electrons emit photons. The critical energy is approximately related to the nuclear charge (Z) by $E_c \approx \frac{800}{Z}\,\text{MeV}$. In most particle physics experiments, electrons typically possess energies in the multi-GeV range, well above the critical energy, leading them to lose energy mainly through bremsstrahlung as shown in Fig 1.7. While bremsstrahlung can occur for all charged particles, its rate is inversely proportional to the square of the particle's mass.

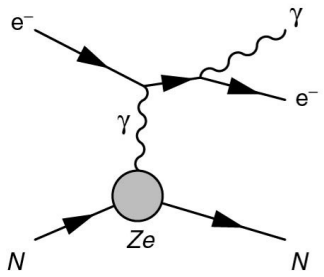

Figure 1.7: The bremsstrahlung process [1]

For photons, at lower energies, the interactions with matter are primarily through the photoelectric effect, where photons are absorbed by atomic electrons, causing their ejection from atoms. At intermediate energy around 1MeV, an interesting phenomenon, Compton scattering ($\gamma + e \rightarrow \gamma + e$) takes place . At even higher energies above 10 MeV, photon interactions are dominated by pair production in the field of a nucleus, as depicted in Fig 1.9.

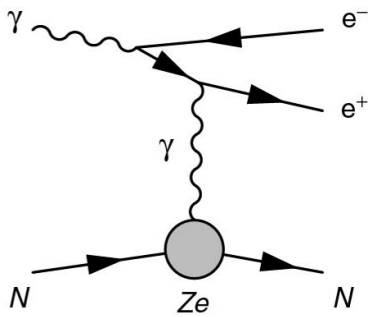

Figure 1.8: The pair production process [1]

The high energy electrons and photons undergo electromagnetic interactions in matter. These interactions are determined by the radiation length X_0. This is the mean distance over which the electron's energy is reduced by bremsstrahlung radiation by a factor of 1/e. This characteristic length depends upon the atomic number Z of the material, and can be calculated as below:

$$X_0 = \frac{1}{4\alpha n Z^2 (r_e)^2 \ln\left(\frac{287}{Z^{\frac{1}{2}}}\right)}, \tag{1.11}$$

where n is the number density, α is the fine-structure constant, and r_e is the classical radius of the electron. As the atomic number of the material increases, the radiation length becomes shorter [1].

As discussed earlier, photons and electrons can initiate an electromagnetic shower, the characteristics of which can be measured using an electromagnetic calorimeter (ECAL). The typical calorimeter comprises alternating layers of absorbers and detectors, effectively capturing the shower's development. Similarly, high-energy hadrons produce showers that can be measured with a hadron calorimeter (HCAL). Beyond these, several specialized detectors serve specific purposes like bubble chambers, emulsions and streamer chambers, and transition radiation detectors [6]. The explanation of these calorimeters falls out of the scope of this thesis.

1.7 Spin, Helicity and Parity of fundamental particles

Spin refers to the intrinsic angular momentum inherent in elementary particles, as well as composite particles like hadrons, atomic nuclei, and atoms. This phenomenon is exclusively quantum mechanical and has no counterpart in classical physics. The existence of spin was experimentally confirmed by Stern and Gerlach in 1922 through their work with silver (Ag) atoms. All elementary particles possess particular magnitudes of spin angular momentum, which are described using a spin quantum number. The intrinsic spin angular momentum is represented by the S quantum number, from which the magnitude of spin angular momentum can be calculated [20]. The allowed values for S are

$$S = \hbar\sqrt{s(s+1)}, \tag{1.12}$$

where $\hbar = \frac{h}{2\pi}$ is the reduced planck constant.

Spin is a quantized property, meaning it can only have discrete values. The spin angular momentum of an electron, measured along any specific direction is represented by the spin quantum number S and its component along the z-axis is denoted as S_z. The eigenvalues of the

square of the spin operator are given by $S^2 = s(s+1)\hbar^2$. The eigenvalues of the S_z operator are $m_s\hbar$, where m_s ranges from $-s$ to $+s$ in integer steps. For electrons, as considered in the context of the MOLLER experiment, the spin quantum number s is $\frac{1}{2}$, resulting in $S^2 = (\frac{3}{4})\hbar^2$.

All particles with spin exhibit a magnetic moment. This can be experimentally detected by passing the particles through an inhomogeneous magnetic field, as in a Stern-Gerlach experiment. The intrinsic magnetic moment (μ) for a spin-$\frac{1}{2}$ particle with charge q, mass m, and spin angular momentum S, is given by:

$$\mu = -g_s \frac{e}{2m_e c}\vec{S}, \tag{1.13}$$

where g_s is called the Lande$^{'}$ factor or the gyromagnetic ratio. Its experimental value is 2.

Particles with half-integer spins, such as $\frac{1}{2}$, $\frac{3}{2}$, and $\frac{5}{2}$, are classified as fermions, while particles with integer spins, such as 0, 1, and 2, are known as bosons. These two categories of particles follow different principles and play distinct roles in the physical world [**spin˙utk.edu**].

Helicity refers to the projection of a particle's spin onto its direction of motion and can either be positive (+1; for right-handed particle) or negative (−1; for left-handed particle) as shown in Fig. 1.9. The two distinct electron beam polarizations correspond to different helicity states of the electron [21].

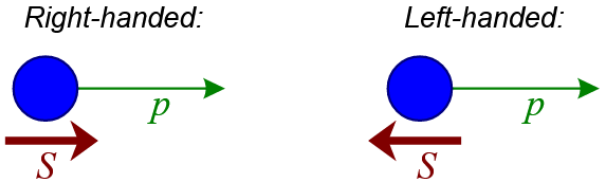

Figure 1.9: Spin and momentum vector orientation for left-handed and right-handed particles. [21]

Mathematically, it is given as:

$$H = \frac{\vec{s}.\vec{p}}{|\vec{s}||\vec{p}|}. \tag{1.14}$$

Parity functions as an operation within three-dimensional physical space, which can be shown in a coordinate system by a matrix:

$$P : I = \begin{bmatrix} -1 & 0 & 0 \\ 0 & -1 & 0 \\ 0 & 0 & -1 \end{bmatrix} = -I, \tag{1.15}$$

Application of parity operator twice restores the coordinate system to its original state, $P^2 = I$. It is an operation that switches between the left-handed particles into right-handed particles and vice versa. According to Dirac theory, particles have positive parity, while antiparticles have negative parity. Therefore, particle currents can also be classified as right- or left-handed. The weak interaction prefers left-handed particle currents over right-handed ones. In the MOLLER experiment, electrons will be left-handed when they are in the negative helicity state and right-handed when they are in the positive helicity state. This distinction leads to an asymmetry when polarized electrons scatter off an unpolarized target [3].

Electromagnetic and strong interactions are symmetric under parity transformation. However, in 1956, T. D. Lee and C. N. Yang proposed that parity is not conserved in weak interactions. This hypothesis was soon tested and confirmed by C. S. Wu and her colleagues in 1957 through their study of the beta decay of Cobalt-60.

1.8 MOLLER Experiment Overview

There are several projects around the world aimed at performing ultra-precise measurements of electroweak observables at scales significantly below that of electroweak symmetry breaking, where these measurements can be theoretically calculated with high accuracy. Among these experiments, the MOLLER (Measurement of the Lepton Lepton Electroweak Reaction) experiment pursues such a strategy. This experiment is specifically designed to extend the sensitivity for detecting new dynamics beyond the Standard Model of electroweak interactions, involving both low energy scales (approximately 100 MeV) and high energy scales (multi-TeV). The MOLLER experiment measures the parity-violating asymmetry A_{PV} in the Møller scattering of longitudinally polarized electrons off unpolarized electrons, utilizing the upgraded 11 GeV beam in Hall A at Jefferson Laboratory (JLab). The experiment uses the highly polarized electron beam from Jefferson Lab's Continuous Electron Beam Accelerator Facility (CEBAF), creating optimal conditions for high-precision measurements [22].

Møller scattering ($e^- + e^- \rightarrow e^- + e^-$) refers to the interaction between two electrons within the framework of quantum field theory, named after Danish physicist Christian Møller. This process is significant in both experimental and theoretical physics. This process is described by four tree-level diagrams in the electroweak theory, two from QED and two analogous diagrams where a Z boson is exchanged instead of a photon [23]. These Feynman diagrams, which visually represent the interaction between particles are shown in Fig. 1.10. The differential cross-section for Møller scattering, which describes the probability of scattering at a specific angle, can be calculated using QED principles. This calculation involves integrating over the possible scattering angles and considering the polarization states of the electrons.The weak force is inherently left-handed, while the weak and electromagnetic forces mix to produce the

particles we observe. Parity violation comes into the picture due to weak interaction, unlike the electromagnetic interaction, is not symmetric under the spatial inversion. The Z boson prefers left-handed particles over right-handed ones. This leads to different cross-sections for left-handed and right-handed electrons. This serves foundation for the asymmetry in measurement of the scattering cross-sections for electrons with opposite helicities. The cross-section is a crucial parameter in experiments as it helps in predicting the scattering rates and designing the detectors accordingly [24].

The fractional accuracy of the measurement is anticipated to be 2.4% [22]. This measurement

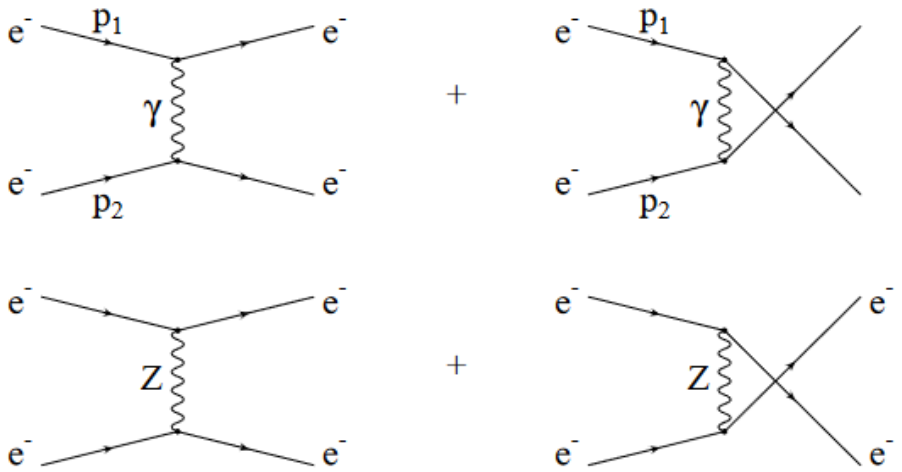

Figure 1.10: The Feynmann diagras for s-channel and u-channel of the Møller scattering with photon and Z bosons as exchange particles. [24]

is capable of achieving more than a factor of five improvement in fractional precision compared to the previous measurement of the same quantity conducted by the E158 experiment at SLAC. Therefore, the upgraded 11 GeV beam at JLab offers an exceptional opportunity to reach new heights in the sensitivity of this measurement. The experimental setup for measuring Møller scattering involves a high-intensity polarized electron beam incident on a target composed of electrons, typically in a liquid hydrogen form. The scattered electrons are detected using an array of detectors positioned to capture a wide range of scattering angles. By analyzing the angular distribution and polarization of the scattered electrons, researchers can extract the parity-violating asymmetry and, consequently, the weak charge of the electron.

This asymmetry arises from the interference between photon exchange and Z^0 boson's direct and exchange diagrams 1.11 of the scattering of longitudinally polarized electrons on unpolarized target electronsgiven as:

$$A_{PV} = \frac{\sigma_R - \sigma_L}{\sigma_R + \sigma_L}. \tag{1.16}$$

The scattering cross section, denoted as σ_L for the incident left-handed electrons and σ_R for inci-

dent right-handed electrons, gives insight into parity non-conservation. A non-zero asymmetry value of between σ_L and σ_R provides information regarding the violation of parity symmetry. The mathematical relation demonstrating the calculation of A_{PV} related to the weak mixing angle is,

$$A_{PV} = mE\frac{G_F}{\sqrt{2}\pi\alpha}\frac{4\sin^2\theta}{(3+\cos^2\theta)^2}Q_W^e. \tag{1.17}$$

G_F is the fermi weak coupling constant, Q_W^e is the weak charge of the electron, α is the fine structure constant, m is the mass of the electron, θ is the scattering angle, and E is the incident beam energy. However, the beam of electrons can never be fully polarized, and thus can significantly impact the measured parity-violating asymmetry (A_{PV}) [22]. Therefore, it is important to accurately measure the polarization of the electron. Compton polarimetry 2.2.3 is among the most effective methods for achieving continuous and precise polarization measurements. The detailed explanation o electron beam polarization and its measurement is given in chapter 2

The MOLLER experiment aims to measure a unique aspect of particle physics and is expected to be one of the most sensitive experiments in the coming decade for detecting specific types of particle interactions that conserve flavor and CP symmetry. This experiment will complement both precise low-energy research and high-energy experiments conducted at the Large Hadron Collider (LHC). If the LHC continues to confirm the Standard Model at its full 14 TeV energy, MOLLER will play a crucial role in discovering new physics that could escape detections at LHC. This includes scenarios like lepton number-violating interactions, compressed supersymmetry, and light dark matter mediators known as dark Z particles. If the LHC finds anomalies, MOLLER will provide data to help figure out possible explanations beyond the Standard Model (BSM). Potential examples of BSM scenarios that MOLLER could explore include new particles from the Minimal Supersymmetric Standard Model and TeV-scale $Z^{'}$ bosons [22].

1.9 Experimental apparatus for the MOLLER

The primary objective of the MOLLER experiment is to achieve highly precise measurements at low energy. As discussed in the previous section, enhancing sensitivity across the entire multi-dimensional space of new operators is critical, especially if higher sensitivity searches at the LHC do not yield new discoveries. This necessity shapes the experimental design of MOLLER. The schematic diagram of the MOLLER is illustrated in the figure 1.11

The design is informed by the large experience accumulated by the collaboration through other high flux integrating parity-violation measurements, including MIT-Bates ^{12}C [25], SAMPLE [26], HAPPEX [27], SLAC E158 [28], PREX [29], and Qweak [30].

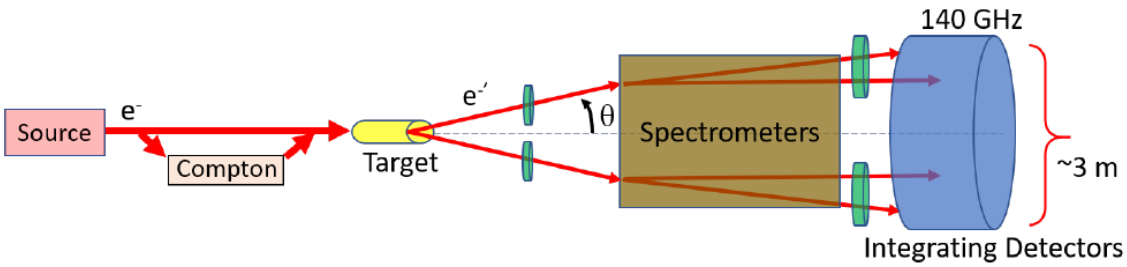

Figure 1.11: The schematic diagram of the key components of the MOLLER experiment. The arrows shown in red are the paths followed by the electrons. Image Link: Schematic Diagram

Key factors in the experimental design include a stable beam optimized for high-intensity, highly polarized beam for asymmetry measurements. This beam is directed at a long, highly-stable liquid hydrogen (LH_2) cryogenic target to ensure high luminosity. The spectrometer is optimized for high acceptance, capable of focusing Møller scattered events away from background signals, directing them onto an integrating detector system. Calibration is conducted at reduced beam current to track individual scattered electrons, allowing for characterization of the spectrometer acceptance and detector response. Additionally, auxiliary detectors operating in both integrating and calibration modes are essential for measuring background sources [22]. A CAD model of the experimental apparatus of MOLLER to be placed in Hall A at JLab is shown in the Fig. 1.12 consisits of:

CEBAF: Over the past fifteen years, the development of experimental techniques at JLab has significantly improved the production of stable polarized electron beam, allowing for systematic control at the part-per-billion (ppb) level. These advancements include calibration methods that control normalization errors, to be able to have electron beam polarization to within 1%. JLab's CEBAF (Continuous Electron Beam Accelerator Facility) (further explanation provided in Sec. 2.1) generates a 90% longitudinally polarized electron beam by directing a circularly polarized laser onto a gallium arsenide (GaAs) photocathode. The conservation of angular momentum in this process causes the electrons emitted through photoemission to possess either positive or negative helicity states, depending on the polarization of the incident light. The electrons are subsequently accelerated through two linear accelerators, ultimately reaching an energy of 11 GeV with a maximum current of 70μA. Based on extensive experience acquired from previous experiments (as mentioned above), achieving the desired electron beam polarization is feasible. The helicity of the electron beam is planned to be reversed rapidly at a rate of 1.92 kHz to mitigate the effects of slow drifts. It is also essential to correct for any correlations between position, angle, energy, and the electron beam helicity. Well-established procedures from prior experiments are available for this purpose. Throughout the data collection period, the beam trajectory must remain consistent with respect to the electron beam polarization at a sub-nanometer level to maintain beam-related false asymmetry corrections at the 1 ppb level [18, 19].

Halls of JLab: At the Thomas Jefferson National Accelerator Facility (TJNAF), the three experimental halls are situated underground and protected by substantial shielding with thick concrete walls. Hall A, the largest of these halls, measures 174 feet in diameter and 55 feet in height. As illustrated in Fig. 1.12, the apparatus for the MOLLER experiment is designed to enable simultaneous operations with other experiments utilizing the 11 GeV electron beam in Hall A at JLab.

Polarimetery: A significant fraction of the physics experiments conducted at Jefferson Lab [31] relies on highly-polarized electron beam with currents reaching up to 100μA. These experiments necessitate continuous and precise measurements of the polarization of electrons of the incoming beam before it reaches the target. To achieve this, two independent polarimeters are employed to provide robust and cross-checked measurements of beam polarization with a precision of 0.4%. Compton polarimetry, detailed further in Sec. 2.2.3, is a highly effective technique for achieving high precision in polarimetry with high-energy electron beams. This non-invasive method involves detecting electrons produced via Compton scattering, as elaborated in Sec. 2.2.1, where the electron beam interacts with an intense circularly polarized photon beam. By independently analyzing scattered electrons and photons, this technique offers continuous measurements with minimal systematic errors. Momentum-analyzation technique is utilized to separate the scattered electrons from the main beam line, directing them to an electron detector where their polarization is measured(as shown in Fig. 2.9). Currently, in Hall A, a silicon strip detector is used for this purpose. However, plans are underway to replace this detector with High Voltaic Monolithic Active Pixel Sensors (HV-MAPS) technology (described in Section 2.3.1) for polarization measurement. This technology is adopted to achieve a higher signal-to-noise ratio and greater spatial resolution. To ensure the accuracy and reliability of these measurements, the Compton polarimeter will be periodically cross-checked against measurements obtained from a Møller polarimeter. This additional verification step helps maintaining the precision of electron beam polarimetry at the desired 0.4% level.

Liquid Hydrogen Target (LH_2): To achieve the necessary rate of Møller scattered electrons, the electron beam exiting the polarimeter will be directed onto a liquid hydrogen target. (LH_2) is the optimal choice due to its high electron density and low radiation length. The planned LH_2 target will be 125 cm in length and will require a cryogenic system capable of handling approximately 4.0 kW of power. This target will represent the highest power LH_2 target ever constructed, building on the experience gained from the Qweak target, which successfully operated with a total power consumption of 2.9 kW [18, 19].

Toroidal Spectrometer: After the electron beam interacts with the liquid hydrogen target, it undergoes Møller scattering, Mott scattering, and other background processes. The MOLLER spectrometer, features two toroidal magnets and 7-fold symmetric collimators. Water-cooled

copper coils steer and focus scattered electrons 26.5 m downstream of the target, while tungsten and copper collimators set the scattering angle, azimuthal acceptance, and provide radiation shielding. The spectrometer is desired to achieve two goals: 100% azimuthal acceptance and directing Møller-scattered electrons to areas with minimal background interference and separates them kinematically from Mott electrons and other unwanted backgrounds [18, 19].

Main Detectors: The MOLLER experiment's primary measurement, the parity-violating asymmetry, is determined by using high-precision integrating detectors. High event rates are necessary to achieve the required precision for these small asymmetries. The electron detector system is designed to integrate the incident signal rather than counting individual electrons. Each detector element consists of a quartz Cherenkov radiator in a gas-filled light guide, which directs the Cherenkov light to a photomultiplier tube (PMT) for collection. The quartz thickness is optimized for resolution, and the PMTs are designed for a linear response to photon rates, read out by using specialized low-noise integrating electronics [18, 19].

Tracking Detectors: The tracking system calibrates primary detectors, spectrometer optics, and background processes across polar and azimuthal ranges. Operating at lower beam currents, it uses Gas Electron Multiplier (GEM) detectors and trigger scintillators. Objectives include verifying the optical properties and acceptance of the spectrometer and quartz detectors, measuring light output, and analyzing electron distributions to confirm background levels from scattering events [18, 19].

Auxiliary Detectors: Auxiliary detectors, such as quartz/tungsten sandwich "shower-max" detectors, offers a cross-check for measuring the Møller flux. Additional detector systems are specifically designed to measure pion backgrounds and monitor beam asymmetries or other background variations [18, 19].

Data Aquisition and Trigger: The data acquisition (DAQ) system collects signals from all experimental components, synchronizing within the helicity window and with detector elements. It supports both high beam current integrating mode and low beam current counting mode. MOLLER experiment will utilize, a dedicated analysis cluster ensuring efficient data analysis, crucial for monitoring apparatus performance [18, 19].

A key component of the current studies, which form the core of this thesis, involves a specific subsystem within the broader experimental framework: performing the cooling analysis of the electron detector designs to be positioned behind the dipole field D3 of the Compton polarimeter in Hall A of JLab. As previously mentioned, there are plans to replace the older version of the detector with HV-MAPS technology. It is essential to ensure that the new version does not introduce any issues into the system. One major concern is that, due to ohmic heating, electrical energy is converted into heat. Since the detector is placed in a vacuum, there

is no medium to carry the heat away from it. As a result, the temperature can rise significantly, and HV-MAPS stops responding to data acquisition once it reaches around 70°C. Therefore, it is necessary to find a way for proper heat dissipation and verify that its thermal performance remains within the required temperature ranges. The cooling analysis aims to optimize the detector's functionality under various operational conditions. Chapter 2 provides a comprehensive explanation of the Compton Polarimeter, detailing its key components and their roles within the experimental setup, thereby laying the groundwork for the subsequent analysis.

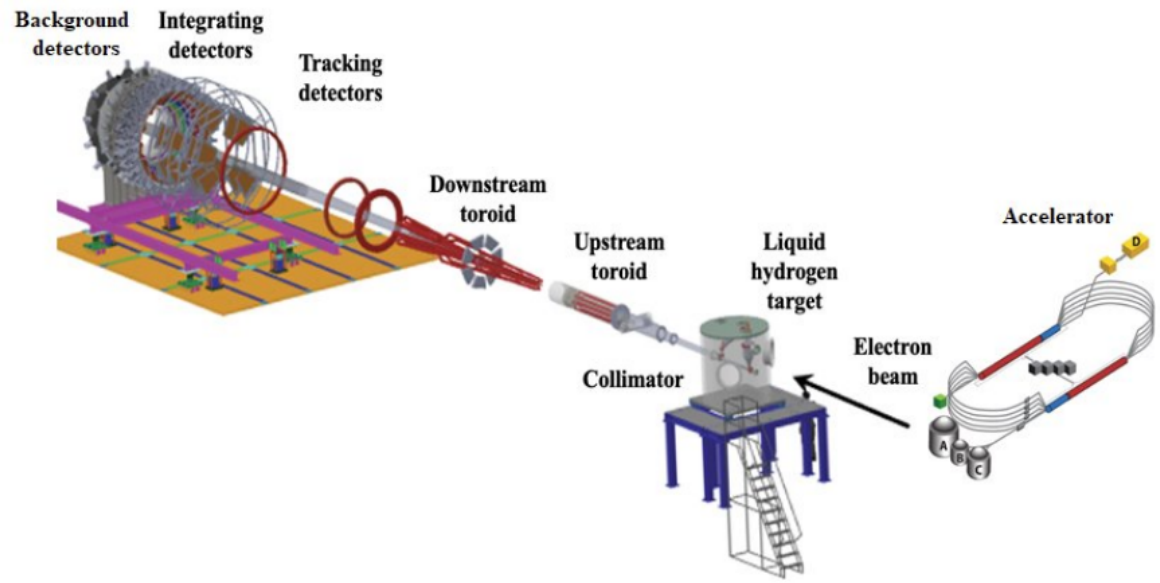

Figure 1.12: CAD model of the Experimental Apparatus of the MOLLER experiment at Hall A, Thomas Jefferson National Accelerator Facility (TJNAF). [19]

Chapter 2

The CEBAF Facility and Compton polarimetry

In this chapter, I discuss the advanced accelerator technology at the Thomas Jefferson National Accelerator Facility (TJNAF) and the Compton polarimeter's setup and physics of the Compton scattering. Additionally, I cover the semiconductor diodes and their two applications in our local experimental setup.

2.1 The Continuous Electron Beam Accelerator Facility

The Thomas Jefferson National Accelerator Facility (TJNAF) in Newport News, Virginia, USA, is one of the national laboratories under the U.S. Department of Energy (DOE). The primary facility which is a test bed for various technologies at Jefferson Lab is the Continuous Electron Beam Accelerator Facility (CEBAF) shown in Fig. 2.1. CEBAF generates beams of electrons with high-intensity and well-controlled polarization [32]. Established in 1984 as CEBAF and beginning operations for physics in 1994, the accelerator comprises an polarized source injector, two anti-parallel linacs linked by 10 recirculating beam lines, enabling up to five passes [33]. The CEBAF facility is utilized by an international community of physicists, supports a broad program of nuclear and hadronic matter exploration, strong interaction studies, and investigations into fundamental symmetries, complementing both atomic and high-energy particle physics [32]. Initially delivering its first electron beam in 1994 and achieving a 4 GeV electron beam by 1998, CEBAF's efficiency and operational improvements allowed it to deliver a 6 GeV electron beam by 2000. A 12 GeV upgrade, completed in 2017 [34], further enhanced its scientific capabilities. The facility at JLab includes four experimental halls (Halls A, B, C, and D) dedicated to a variety of particle and nuclear physics experiments [35]. The MOLLER experiment will run in Hall A as shown in Fig. 2.1, which is biggest of all the halls in JLab.

The CEBAF underwent substantial developments and changes from its initial conceptual design through its construction stages, commissioning, and eventual operation. It transitioned from conventional copper-based accelerating technology to Superconducting Radio-Frequency

(SRF) technology, enabling more efficient acceleration. It also incorporated multipass beam recirculation and the capability for Continuous Wave (CW) beam delivery to multiple experiments simultaneously. The project implemented the polarized source technology and addressed various accelerator physics and design challenges that arose due to these advancements. The components of the CEBAF are detailed in the following sections.

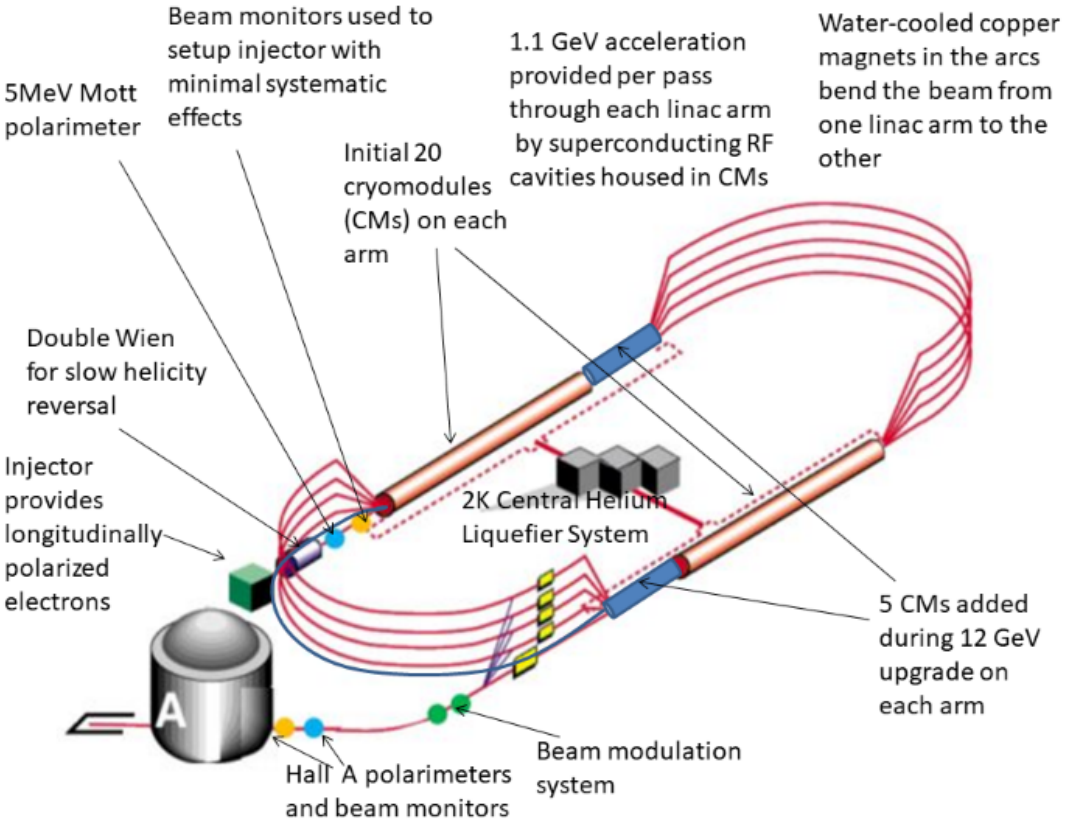

Figure 2.1: Continuous Electron Beam Accelerator Facility (CEBAF) at the Thomas Jefferson National Accelerator Facility, Newport News, Virginia, USA [35].

Polarized electron beam source/injector's development went through multiple advancements from its inception in early 1997 to early 2000. Initially constructed at the University of Illinois, the original electron source featured a 100 keV electron gun, closely modeled after the SLAC PEGGY II polarized source [36]with only minimal modifications. In 1994, after the commissioning of CEBAF with a hot-filament thermionic electron gun, a spin-polarized electron source was introduced into the injector. This source utilized spin-polarized electron photo-emission from gallium-arsenide (GaAs) semiconductor material, which was illuminated by polarized laser light—a technique first demonstrated by D.T. Pierce *etal.* [37] in 1975 [38].

The injector at CEBAF serves as the source of the polarized electron beam. As depicted

in Fig. 2.2, the injector setup comprises several key components: a laser with a wavelength range of 780-850 nm, a linear polarizer, a Rubidium Titanyl Phosphate (RTP) Pockels cell, an insertable half-wave plate (IHWP), a rotating half-wave plate (RHWP), a Gallium Arsenide (GaAs) photocathode, and a double Wien filter configuration [39], [40]. The process begins with light from the 780-850 nm laser being linearly polarized before passing through the RTP Pockels cell. This cell, which receives a random helicity signal, transforms the linearly polarized light into circularly polarized light with alternating helicities, depending on the input signal state. The IHWP is used for slow helicity reversals, flipping the laser polarization intermittently to reduce helicity-correlated beam asymmetries. The RHWP, positioned after the Pockels cell is employed to perform scans for aligning the Pockels cell and for analyzing systematic effects such as vacuum window birefringence, position differences, and laser beam steering. Finally, the laser beam is directed onto the GaAs photocathode, which emits longitudinally polarized electrons with the same helicity as the incoming photons [32, 33, 35].

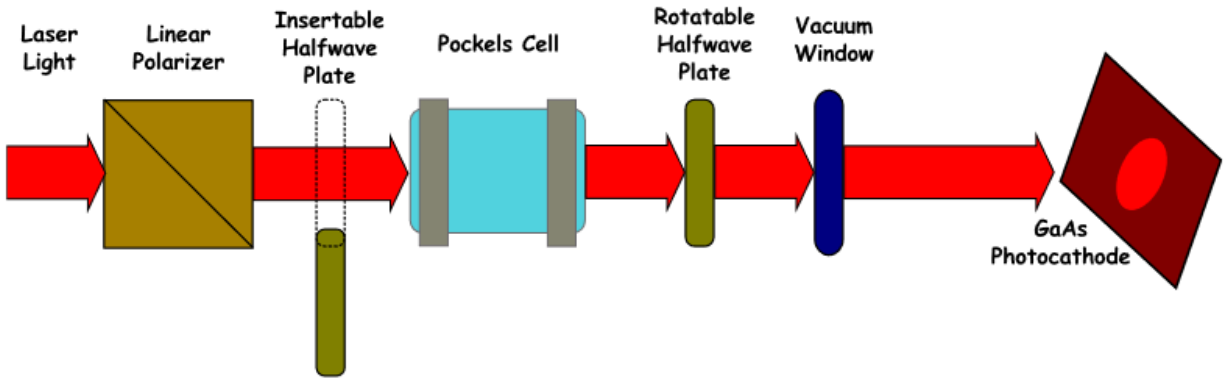

Figure 2.2: Schematic diagram of the beam transport line [38].

A semiconducting photocathode made of GaAs is thus illuminated with the incoming photon beam. The surface of the GaAs photocathode has been chemically treated to create a negative work function, known as a negative electron affinity surface. The wavelength of the laser light is carefully chosen to excite electrons from a specific valence band to the conduction band of the semiconductor. The photocathode is maintained at a negative potential, causing the electrons in the conduction band to be accelerated as they leave the cathode and enter the injector beamline. Through doping the photocathode, the degeneracy in the spin-orbit states of the valence band are split, as illustrated in fig. 2.3. When illuminated with circularly polarized light, these photons selectively excite electrons to a specific spin state, yielding an electron beam with nearly 100% polarization. However, some depolarization occurs during the diffusion of these electrons to the photoconductor surface. So we cannot ensure a proper 100 % polarized beam [38].

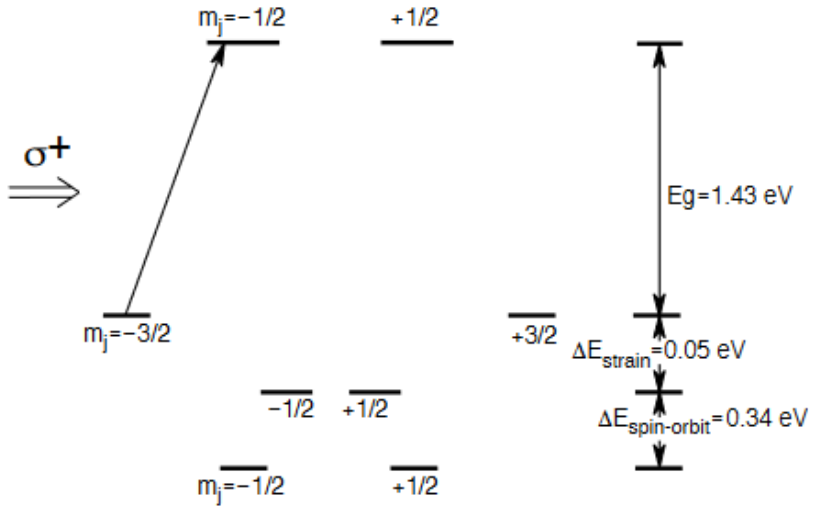

Figure 2.3: Production of polarized electrons from circularly polarized laser light shown via band structure of GaAs [38].

The polarization of the electron is fully controlled by the polarization of incoming laser light that hits the photocathode. By quickly changing the laser polarization, the helicity of the electron beam can be altered. This is done using an electro-optic Pockels cell, which functions like a quarter-wave plate to convert linearly polarized light to circularly polarized light. Reversing the voltage applied to the Pockels cell changes the circular polarization of the laser light and, consequently, the helicity of the electron beam. Fig. 2.2 shows a schematic diagram of the experimental setup [38].

Spin-polarized electrons are emitted within a high-voltage DC electron gun, accelerate from rest, and focus into a beam with an energy of 100 keV. A specialized laser utilized with this polarized source is developed in-house. The system comprises of a diode-laser-based oscillator and an amplifier, where the diode-laser oscillator is RF gain–switched to generate an optical pulse train [41]. Later, a unique laser system is developed, comprising three 499 MHz diode lasers, enabling the simultaneous delivery of three independent continuous-wave (CW) electron beams to three experimental areas. Steady technological advancements have led to substantial improvements in electron gun performance [42], achieving exceptionally low vacuum levels (10^{-12} Torr) to protect the photocathode. Currently, the operational lifetime of the photocathode is primarily limited by ion back-bombardment, making the most suitable measure of cathode life the total charge delivered per illuminated area rather than the number of operational hours. The operational lifetimes of thin, strained gallium arsenide cathodes now routinely exceed 10^5 C/cm^2, with the non-illuminated areas remaining unaffected while operating. Also, novel GaAs-based semiconductors (as explained above), having the capacity to produce high spin-polarization (85%) with high quantum efficiency (1%), high-frequency

gain-switched fiber amplified lasers, along with high-power have enabled the production of high-current electron beams with relatively modest gun voltages. A double Wien filter complemented by two solenoidal magnets positioned in between is available after this setup, enabling independent slow helicity reversals of the electron beam. The purpose of this approach was to further reduce systematic effects.

Jefferson Lab has gained substantial experience in using the polarized electron source for parity-violation experiments [43]. A significant challenge in these experiments is that variations in beam properties directly affect the detected scattered flux. If these beam changes correlate with the electron helicity, they can replicate the small parity-violating asymmetries being measured. While these changes are usually measured and corrected, the corrections are only accurate to about 10%. This means that helicity-correlated beam asymmetries (HCBAs) could be a potential source of systematic error, requiring extremely precise control for accurate measurements. There is deep understanding of the HCBAs with HAPPEX-II [27], PREX [29] and Qweak [30] experiments.

Superconducting radio-frequency technology is adopted by the CEBAF to accelerate the particle beam to be used for different experiments. CEBAF upgrade 7-cell cavity has the Low-Loss shape to reduce dynamic heat load and stiffeners for operational stability 2.4 The polarized electron beam generated in the injector region is accelerated by superconducting radiofrequency (SRF) cavities within cryomodules (CMs) along the two arms of the linear accelerator. CEBAF's key innovations include the use of SRF technology and multipass beam recirculation. The accelerator consists of two 1400-meter-long SRF linear accelerators in an underground tunnel containing in each "straightaway" a microwave superconducting linac operating at 2K. These linacs are connected by arc sections containing steering magnets. With an extensive global assessment, SRF cavities developed at Cornell University are chosen for CEBAF's linacs. This technology applies superconducting materials to RF devices, where superconductors exhibit zero DC electrical resistance below their critical temperature (Tc). While the RF surface resistivity is zero only at absolute zero (0 K), it remains minimal above 0 K but below Tc. This ultra-low resistivity allows RF resonators to achieve high quality factors (Q). These high-Q resonators, with their narrow bandwidth, are advantageous for various applications [44].

Superconducting radiofrequency (SRF) technology enables the acceleration of subatomic or atomic particles, such as electrons, protons, or ions. In SRF systems, electromagnetic fields are generated within a metallic resonant cavity that operates at microwave frequencies. These fields are synchronized with the arrival of charged particle bunches, allowing the particles to gain acceleration via interaction with the fields. These accelerators employ a sequence of drift tubes or cavities arranged in a linear configuration which are subjected to an alternating high-energy field. As particles move towards a cavity, they are accelerated by an opposite polarity charge.

When passing through an aperture in the cavity, the polarity reverses, causing the tube to repel the particles and further accelerate them towards the next cavity. This process is repeated for a series of particle bunches with controlled voltage applied to each plate. As particles near the speed of light, the switching rate of the electric fields reaches to radio frequencies. This progression to microwave cavities is essential for maintaining the efficiency and effectiveness of particle acceleration at these elevated speeds. Unlike conventional radiofrequency (RF) accelerators, SRF technology uses a metallic structure that is almost entirely lossless, which allows for the maintenance of very high field levels without dissipating power that could otherwise damage the structure.



Figure 2.4: Superconducting radiofrequency (SRF) cavities [45]

Niobium is the preferred material for superconducting characteristics at the temperature achievable with liquid helium temperatures (1.8-4.2 K). The cryomodules housing these niobium superconducting resonators are specifically engineered to maintain the necessary cryogenic environment and ensure precise alignment of the cavities with the beam passing through them. Jefferson Lab's Central Helium Liquefier is operational since 1994. This facility maintains 70,000 liters of liquid helium at a vacuum pressure of 0.031 atmospheres within the superconducting cryomodules used to accelerate the CEBAF accelerator electron beam. By opting for (SRF) technology, Jefferson Lab offers the advantage of immense power savings, significantly lowering the costs related to a multi-hundred-megawatt SRF system.

Recirculation of beam was required to reduce the cost of straightforward linac. CEBAF was distinguished as the first major application of beam recirculation on this large scale. In this system, the electron beam traverses both linear accelerators (linacs) multiple times, accumulating energy with each passage. A key feature of this recirculation process is that the electron velocities remain nearly constant at the speed of light, enabling the simultaneous acceleration of multiple beam energies. The magnetic recirculation system's primary functions include bending the electron beam using dipole magnets and focusing it using quadrupole magnets between each linac As shown in Fig. 2.1. This system ensures that the electron distribution remains both achromatic and isochronous, meaning there is no dependence on energy or time respectively. Thus, recirculating linacs provides high beam energies, and at the same time preserves the beam quality. CEBAF's design incorporates recirculation arcs. These arcs play a vital role in managing the path length of the electron beam. They allow for precise control

over path length adjustments to accommodate the seasonal contraction and expansion of the accelerator. This flexibility is essential for maintaining consistent beam quality throughout the year. Additionally, these independent arcs enable the management of emittance effects due to synchrotron radiation during higher-energy passes. Synchrotron radiation can cause the electron beam to spread out, which affects the quality of the beam. By allowing independent control of the recirculation arcs, CEBAF can minimize these effects, ensuring a more focused and high-quality beam [33].

Beam delivery is achieved using properly phased RF separators operating at 499 MHz. The maximum beam energy can be achieved through five recirculations. However, some beams may be extracted from the accelerator at a lower energy. The RF deflecting cavities that direct one bunch train toward the beam switchyard while the others continue for additional recirculation. Once extracted, each beam is further directed into the appropriate position of a septum Lambertson magnet [46]. The installation of these RF separators in the various recirculation paths enables the simultaneous delivery of beams with different but correlated energies to different halls: A, B, C or D. This system allows experimental halls to receive a lower pass or maximum pass energy with choice.

A 12 GeV upgrade to the beam energy has been completed for the next phase of improvements for the CEBAF. A schematic view of these improvements is shown in Fig. 2.5 diagramatically.

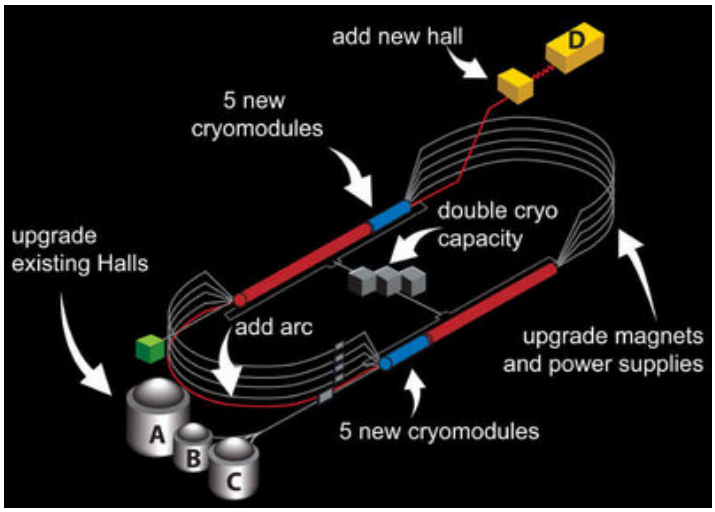

Figure 2.5: Intended improvements in CEBAF facility for upgrade to 12 GeV beam energy. [47]

This introduced advanced class of SRF cavities that were four times more powerful than the previous design. The upgrade also involved adding five new cryomodules, which housed a total of 40 high-performance 7-cell cavities for each linac. Doubling the capacity of the helium refrigerator enabled the accelerator to achieve 2.2 GeV per pass through two linacs. Modifications to the existing recirculation magnets and beam extraction system allowed each of the

experimental stations to receive an 11 GeV beam. Additionally, a new tenth arc was added to reach the top energy of a 12 GeV beam in the new Hall D.

2.2 Compton Polarimetry

The concept of Compton polarimetry is based on the elastic scattering of polarized electrons by polarized photons. The reaction cross-section is influenced by the relative orientation of the electron's spin to the photon's spin. This section covers the physics of Compton scattering, including cross-section and asymmetry. Also, it details the apparatus of the Compton polarimeter used to measure the polarization of incoming electrons.

2.2.1 Mechanics of Compton Scattering

The Compton effect was observed by Arthur Holly Compton for which he received Nobel prize in Physics in 1927. The Compton effect emerges from the interaction between a photon and an electron. When a photon collides with an electron, it scatters, transferring some of its energy to the recoiling electron. Both the photon and the electron possess spin angular momentum, and the alignment or anti-alignment of these spins plays a crucial role in the kinematics of Compton scattering. The electron beam consists of individual electrons traveling along a specific direction or axis, as illustrated in Fig. 2.6. In the laboratory frame of reference, the z-axis is defined as the direction of both the incident electrons and incoming photons. The polar angles of the scattered photon and electron are denoted by θ_γ and θ_e, respectively. The azimuthal angle ϕ determines the orientation of the scattering plane with respect to the incident plane [48].
The incident electron has energy E and momentum oriented along the z-axis, is described as

$$\vec{p} = (0, 0, p). \tag{2.1}$$

The incident photon has energy k and momentum vector given by

$$\vec{k} = (0, -k\sin\alpha, -k\cos\alpha). \tag{2.2}$$

α is the crossing angle. After the scattering takes place, the electron possesses an energy E', scattering angle θ_e, and a momentum as

$$\vec{p'} = (p'\sin\theta_e\sin\phi,\ p'\sin\theta_e\cos\phi,\ p'\cos\theta_e) \tag{2.3}$$

The scattered photon has energy k', scattering angle θ_γ, and momentum as

$$\vec{k'} = (k'\sin\theta_\gamma\sin\phi,\ k'\sin\theta_\gamma\cos\phi,\ k'\cos\theta_\gamma). \tag{2.4}$$

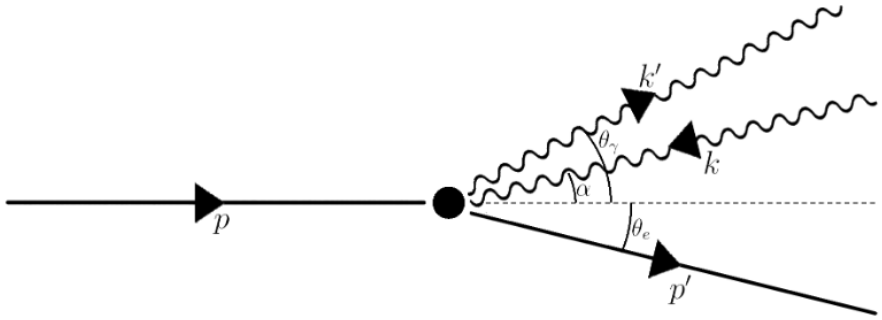

Figure 2.6: Compton scattering [48]

In this two-body kinematics, by applying the conservation of four-momentum, we can describe the relationship between the incident and scattered photons with the relevant scattering angle as follows:

$$k\,' = \frac{k(E + p\cos\alpha)}{E + k - p\cos\theta_\gamma + k\cos\left(\theta_\gamma - \alpha\right)}\,, \tag{2.5}$$

and the energy of recoiled electron is,

$$E\,' = E + k - k\,'. \tag{2.6}$$

In two-body kinematics, the conservation of four-momentum allows us to express the relationship between the incident and scattered photons with the relevant scattering angle. To maximize the interaction between the incident electron and photon, thereby increasing the likelihood of Compton scattering, we assume $\alpha = 0$ i.e. head-on collision. Additionally, by considering $\gamma = \frac{E}{m_e}$ for small photon scattering angles, the eq. 2.5 becomes,

$$k\,' = k\frac{4\,\gamma^2}{1 + \frac{4k\gamma}{m_e} + \theta_\gamma^2\,\gamma^2}. \tag{2.7}$$

Using a kinematical parameter as follows:

$$a = \frac{1}{1 + \frac{4k\gamma}{m_e}} \tag{2.8}$$

$$k' = k\frac{4a\,\gamma^2}{1 + a\,\theta_\gamma^2\,\gamma^2}\,. \tag{2.9}$$

The maximum scattered photon energy ($k' = k'_{max}$), which is called Compton edge, is obtained for $\theta_\gamma = 0$. In this scanerio, the outgoing electron has to compensate and scatters off with minimum energy (E_{min}). Both of these energies at Compton edge are given below;

$$k' = k'_{max} = k\frac{4aE^2}{(m_e)^2} \tag{2.10}$$

Using it in eq. 2.6, the minimum energy of the scattered electron is;

$$E_{min} = E + k - k\frac{4aE^2}{(m_e)^2} \tag{2.11}$$

2.2.2 Cross Section and Asymmetry of Compton Scattering

The differential cross section quantifies the probability of an interaction between an electron and a photon. This probability is determined by the effective area presented by the target particle to the incident particle. In polarized Compton scattering, the interaction occurs between a circularly polarized photon beam and a polarized electron beam. Compton scattering is a fundamental phenomenon in quantum electrodynamics, the theory of electromagnetic interactions. During 1950s and 1960s, the advancements in QED allowed physicists like Klein and Nishina to precisely calculate the Compton interaction cross section through the application of Feynman diagrams as shown in Fig.2.7

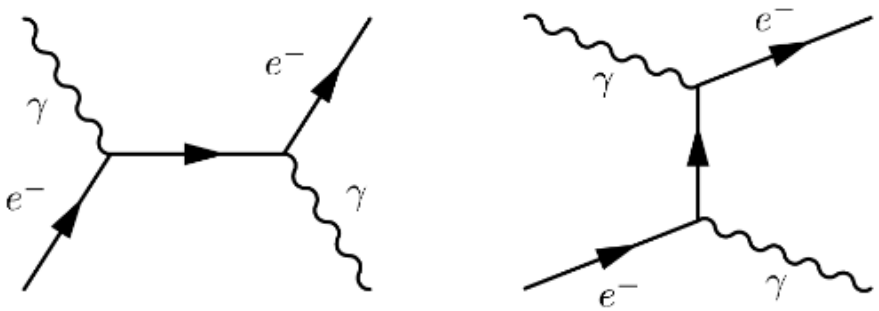

Figure 2.7: Feynman diagrams for Compton Scattering [48]

In the laboratory frame, for a laser beam with zero crossing angle and circularly polarized photons, the unpolarized differential cross section is expressed as [49]:

$$\frac{d\sigma}{d\rho} = 2\pi {r_0}^2 a[\frac{\rho^2(1-a)^2}{1-\rho(1-a)} + 1 + (\frac{1-\rho(1+a)}{1-\rho(1-a)})^2], \tag{2.12}$$

where r_0 is the classical electron radius given by $r_0 = \frac{\alpha_c \hbar c}{mc^2}$, ρ is the energy of the scattered photon normalized to the maximal energy represented as $\rho = \frac{k'}{k'_{max}}$, and a is the kinematic parameter described in eq. 2.12. The plot for unpolarized differential cross section ($\frac{d\sigma}{d\rho}$) as a function of ρ can be seen in Fig. 2.8.

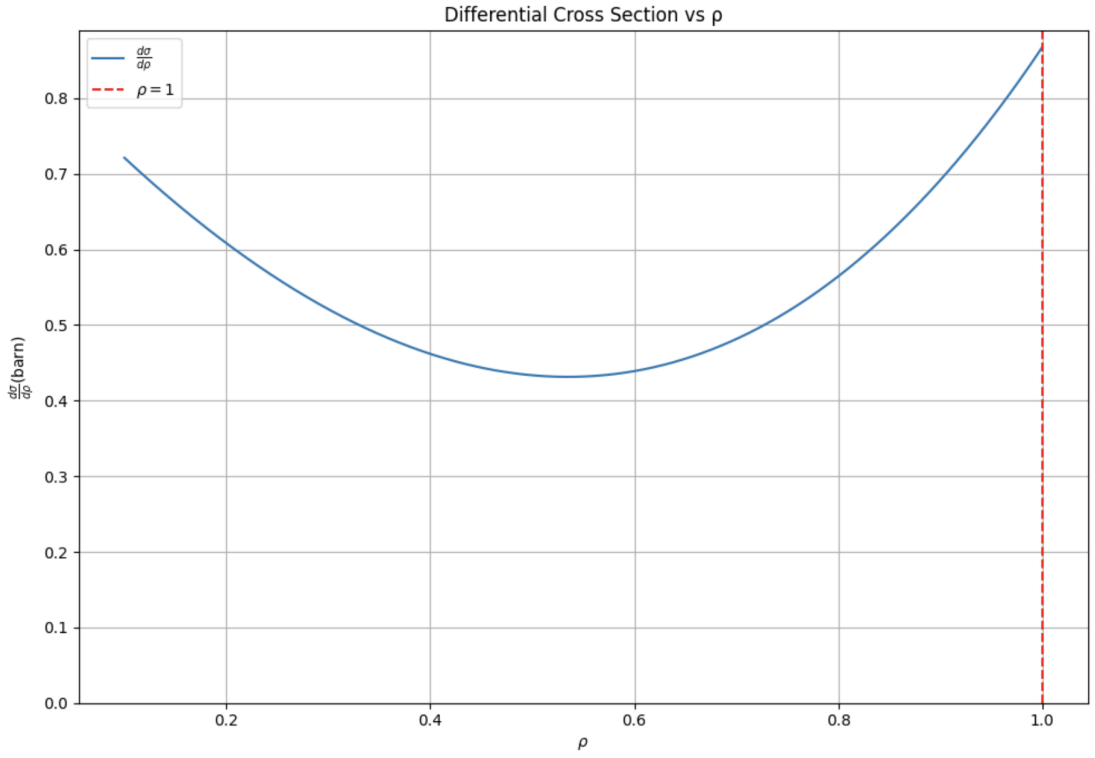

Figure 2.8: Variation of the unpolarised differential cross-section ($\frac{d\sigma}{d\rho}$) as a function of ρ (gernerated using Python).

The differential Compton scattering cross section, $\frac{d\sigma}{d\rho}^{\pm}$, is a combination of both the unpolarized $\frac{d\sigma}{d\rho}$ and polarized $\frac{d\sigma}{d\rho}_p$ components as shown below:

$$\frac{d\sigma}{d\rho}^{\pm} = \frac{d\sigma}{d\rho} \pm \frac{d\sigma}{d\rho}_p, \tag{2.13}$$

where $\frac{d\sigma}{d\rho}^{+}$ is the cross section for the electron and photon polarized parallel with respect to each other, and $\frac{d\sigma}{d\rho}^{-}$ is the cross section for electrons and photons polarized anti-parallel to each

other. The total cross-section after integrating eq. 2.12 is

$$\sigma = \pi {r_0}^2 a \frac{-1 - 14a + 16a^2 - 2a^3 + a^4 + 2\ln a - 12a\ln a - 6a^2 \ln a}{(1-a)^3}. \tag{2.14}$$

To determine the theoretical longitudinal asymmetry A_l in Compton scattering, it is essential to first understand the longitudinal polarization P_e of the electron beam relative to the z-axis (refer to Fig. 2.9). This polarization plays a key role in the analysis, as it directly influences the asymmetry in the scattering process, and is given as

$$P_e = \frac{{N_e}^+ - {N_e}^-}{{N_e}^+ + {N_e}^-}. \tag{2.15}$$

Here, ${N_e}^\pm$ represents the number of electrons with electron spin either $+\frac{1}{2}$ or $-\frac{1}{2}$. The total electron count of ${N_e}^\pm$ is given as

$${N_e}^\pm = \frac{N_e(1 \pm P_e)}{2}. \tag{2.16}$$

As the electron beam and laser are never 100% polarized, the longitudinal polarization in Compton polarimeter of the electron beam is determined by measuring the experimental asymmetry (A_{exp}) that arises from the scattering of an polarized electron beam (P_e) off the circularly polarized photon beam (P_γ) as depicted in Fig.2.7. The experimental asymmetry (A_{exp}) can be defined as

$$A_{exp} = \frac{n^+ - n^-}{n^+ + n^-} \tag{2.17}$$

Here, n^+ denotes the number of detected scattering events or counts when the beam helicity is positive and n^- is the number of detected scattering events (or counts) when the beam helicity is negative. The experimental asymmetry A_{exp} derived from these measurements is linked to the theoretical longitudinal asymmetry A_l for the Compton scattering, which describes the interaction between an electron and a photon with their spins either parallel or antiparallel,

$$A_l = \frac{\sigma^+ - \sigma^-}{\sigma^+ + \sigma^-} = \frac{\sigma^{\rightarrow}_{\Rightarrow} - \sigma^{\leftarrow}_{\Rightarrow}}{\sigma^{\rightarrow}_{\Rightarrow} + \sigma^{\leftarrow}_{\Rightarrow}} \tag{2.18}$$

via the relation,

$$A_{exp} = P_e P_\gamma A_l, \tag{2.19}$$

where

$$A_l = \frac{2\pi {r_0}^2 a}{(\frac{d_\sigma}{d_\rho})}(1 - \rho(1+a))[1 - \frac{1}{1 - \rho(1-a)^2}] \tag{2.20}$$

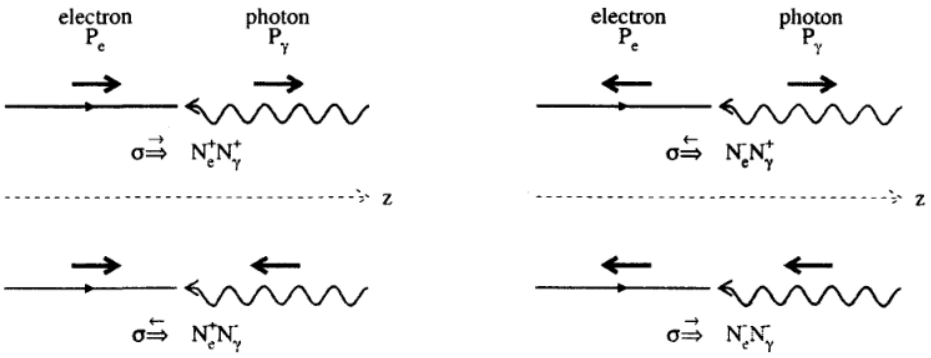

Figure 2.9: Helicity configuration of electron and photon. [49]

The variation of the theoretical longitudinal asymmetry (A_l) as function of (ρ) is shown in Fig. 2.10.

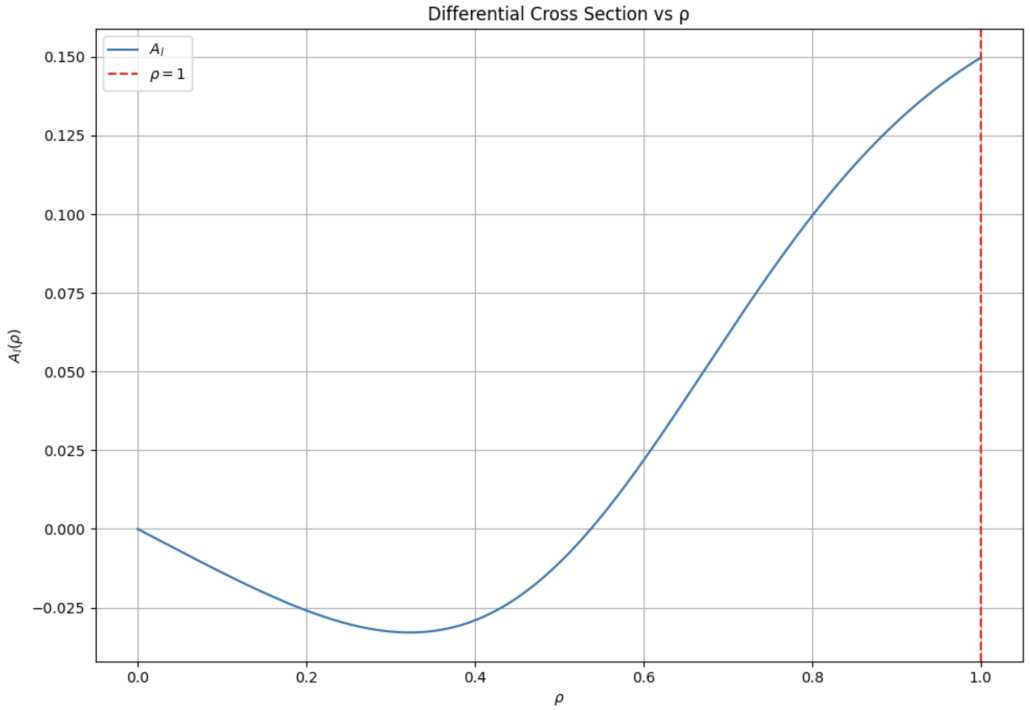

Figure 2.10: Plot of theoretical longitudinal asymmetry (A_l) as function of (ρ) (generated using Python).

The quantities A_{exp} and P_γ are meased quantities, while A_l is computed within the framework of the Standard Model [50] [51]. Consequently, the only remaining variable is the longitudinal polarization of the electron beam, P_e. This approach is a well-established technique and is currently employed at JLab [52]. Jefferson Lab's (CEBAF) is among the pioneering

low-energy accelerators to implement a Compton polarimeter for measurement of the electron beam polarization, and it was the first to achieve a measurement precision of the electron beam polarization better than 1%.

2.2.3 Compton Polarimeter

The Compton polarimeter is designed to continuously and non-intrusively measure the electron beam's polarization through Compton scattering, as explained in Sec. 2.2.2. A magnetic chicane is employed to direct the beam precisely. The polarization is aligned to be nearly longitudinal, minimizing azimuthal scattering asymmetry that could arise from transverse polarization components. Given that the observed parity-violating asymmetry is directly proportional to the longitudinal polarization of the electron beam, achieving a highly precise polarization measurement is essential [19].

The objective of the Compton polarimeter is to determine the absolute polarization with a control over systematic uncertainties, aiming for an accuracy of approximately 0.4% and to continuously monitor the polarization for any significant fluctuations. The delivered electron beamis expected to be around 90% polarized. The MOLLER collaboration members bring substantial expertise [53] from their work in achieving these objectives. For most of the Hall A experiments at JLab, it is essential to measure the polarization of the polarized electron beam both quickly and accurately. Traditional polarimeters, such as the Møller or Mott [54], necessitate the installation of a target within the beam path. This requirement means that polarization measurements cannot be conducted simultaneously with data collection, as the interaction with the target disrupts the beam's polarization, momentum, and position. Consequently, an alternative method must be developed to allow for non-invasive polarization measurements. This necessity is the primary driving force behind the development of Compton polarimetry. To accurately measure the polarization of the electron beam, it is essential to detect the recoil electrons without disturbing the primary unscattered electrons traveling along the main beamline. In the Compton scattering, high-energy electrons are deflected at a very small angle, making it challenging to separate them from the primary beam path. Given the proposed laser and beam energies, achieving even a minimal deflection of 5 mm from the beamline would require over 500 meters of space, which is an impractical distance in most experimental setups. A magnetic chicane provides a compact and efficient method to deflect electrons away from the main beam line, requiring significantly less space than by Compton scattering alone [48].

Fig. 2.11 illustrates the schematic schematic layout of the Compton polarimeter used in Hall A. The polarimeter's design is centered around several key components:

Magnetic Chicane: A vertical magnetic chicane, consisting of four dipole magnets, guides the CEBAF electron beam to the Compton Interaction Point (CIP) and then towards the liquid hydrogen target of the MOLLER experiment, ensuring precise beam alignment.

Photon Target: A high-finesse Fabry-Perot (FP) cavity serves as the photon target. Positioned in the lower straight section of the chicane relative to the electron beam, this cavity enhances the interaction between the beam and the photons.

Photon Detector: A specialized photon detector is employed to capture back-scattered photons, providing critical data on the beam's polarization.

Electron Detector: The electron detector is strategically placed to detect recoil electrons that are deflected from the primary beam by the third dipole of the chicane, offering further insights into the beam's properties like measuring the polarizations of these Compton scattered electrons.

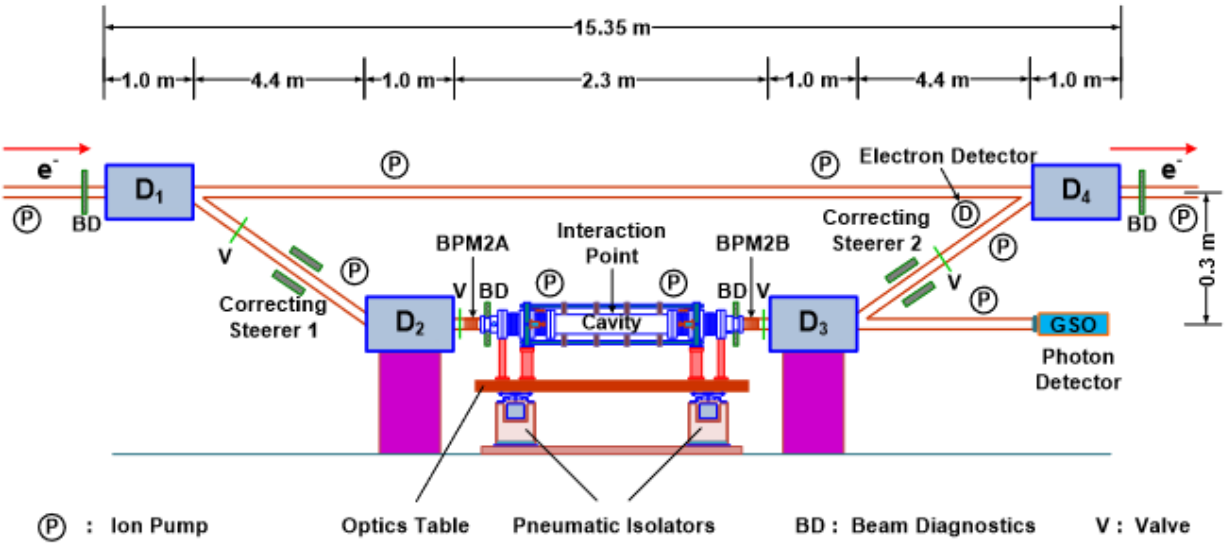

Figure 2.11: Hall A Compton polarimeter setup [55]

This magnetic chicane is an important part in the Compton polarimeter setup. It ensures that the electron beam is transmitted achromatically, meaning that the beam's size and shape remain unchanged as it exits the chicane. The electron beam is vertically deflected inside the chicane by a series of four identical dipole magnets, labeled D1, D2, D3, and D4, each measuring 1 meter in length (L_d). These dipoles produce a maximum magnetic field of 1.5 T. The direction of the magnetic field alternates between each consecutive dipole, guiding the electrons back to their original trajectory by the time they exit the chicane. As symmetry is critical in this setup, necessitating that the magnetic fields of all four dipoles be identical. Consequently, the distances between D1 and D2, as well as D3 and D4, are equal. However, the gap between D2 and D3 (D_{23}) is minimized to enhance the transverse deviation of the beam, which is a key factor in the polarimeter's functionality. The total length allocated for the magnetic chicane

is 15.1 meters, accounting for 15.5 meters of the Compton polarimeter's region, minus 0.4 meters for the external coils of dipoles D1 and D4 (D_{14}). The spacing D_{23} is set at 2.3 meters to accommodate the optical cavity, leaving the drift lengths D_{12} and D_{34} at 4.4 meters each. The optical cavity is positioned between dipoles D2 and D3 (refer to Fig. 2.11). It is housed within a vacuum chamber that connects to the beam pipe both upstream and downstream. This cavity, along with the laser and associated optical components, is mounted on an optics table. The cavity input point is located centrally between D2 and D3. To monitor the electron beam's position during experiments, two beam position monitors (BPMs) are installed on either side of the cavity. Additionally, the 'beam diagnostics (BD)' systems, designed to detect the beam halo, are positioned at four points along the chicane (Fig. 2.11). Each BD unit consists of four scintillator bars, which are connected to photomultiplier tubes and surround the beam pipes at those points. Pneumatic gate valves manage the chicane's vacuum environment, allowing isolation of the chicane beam pipe from the main beamline when required. Two ion pumps situated between D2 and D3 ensure a vacuum level of 10^{-9} Torr inside the cavity. Upon entering the region between D2 and D3, the electron beam interacts with the circularly polarized photons in resonance in a Fabrey-Perot cavity fed by a laser of 1064 nm wavelength, which is aligned to overlap with the electron beam in this area. As a result of this interaction, the electrons scatter at a small angle relative to the trajectory of the primary beam. The recoil electrons, having lost energy due to the Compton scattering, continue to follow a path close to the main beam line, with their momenta ranging from that of the primary beam down to the Compton edge momentum. Although electrons lose energy during Compton scattering, they continue along the main beamline until they encounter the next dipole, D3 [49].

Given a uniform magnetic field along the magnetic length (L_d) of a dipole (depicted in Fig. 2.12), the bending radius (R_d) of the trajectory of incident electrons can be determined by [49]

$$R_d = \frac{p[GeV]}{0.3B[T]}\,, \tag{2.21}$$

where p is the incident electron's momentum. The bending angle from D1 to D2, θ_e, shown in Fig. 2.12 is given by:

$$\sin\theta_e = \frac{L_d}{R_d}. \tag{2.22}$$

Let us consider, H_{12} = Vertical deflection of a beam over a horizontal distance D_{12} (again shown in Fig. 2.12), then

$$\tan\theta_e = \frac{H_{12}}{D_{12}}. \tag{2.23}$$

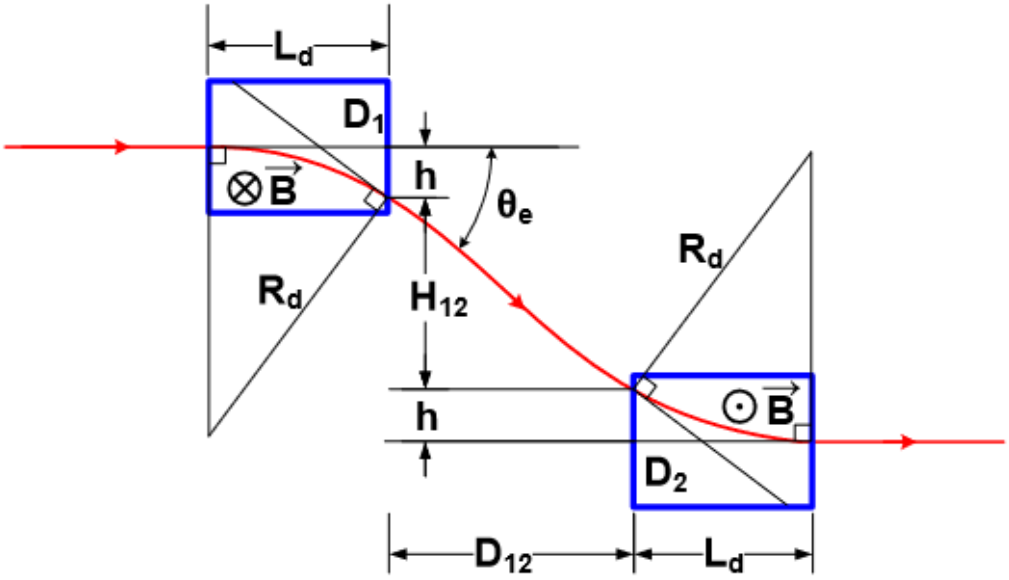

Figure 2.12: Transverse motion of electron beam trajectory [55]

The total transverse deviation (d) of the beam between entrance and exit of the electron beam is

$$d = 2h + H_{12} = 2R_d(1 - \cos\theta_e) + D_{12}\tan\theta_e. \tag{2.24}$$

The deflection of the electron beam by dipole is given by

$$\tan\theta_e = 0.3\frac{\int \vec{B}.dl}{p[GeV]}\,, \tag{2.25}$$

where $\int \vec{B}.dl$ represents the line integral of the magnetic field. For the energy range at JLab and considering the parameters provided, with each dipole capable of producing a maximum magnetic field of 1.5 Tesla, calculations indicate that the resulting angle is quite small [49]. Thus, considering θ_e is very small, and using eq. 3.15 and 3.16, we get

$$d = R_d\theta_e^2 + D_{12}\theta_e \quad = 0.3\frac{B}{p}L_d(L_d + D_{12}). \tag{2.26}$$

Based on Equation (3.20), it is evident that the angular deviation of the electron beam is influenced by the integral of the magnetic field along its path, given a constant energy E (or momentum) of the beam. Consequently, altering the magnetic field in all four dipoles will affect the vertical position of the electron beam between dipoles D2 and D3. If the magnetic field changes by an amount $\Delta B = B' - B$, the resulting vertical displacement Δd is shown in Fig. 2.13is given by:

$$\Delta d = 0.3\frac{\Delta B}{p}L_d(L_d + D_{12}). \tag{2.27}$$

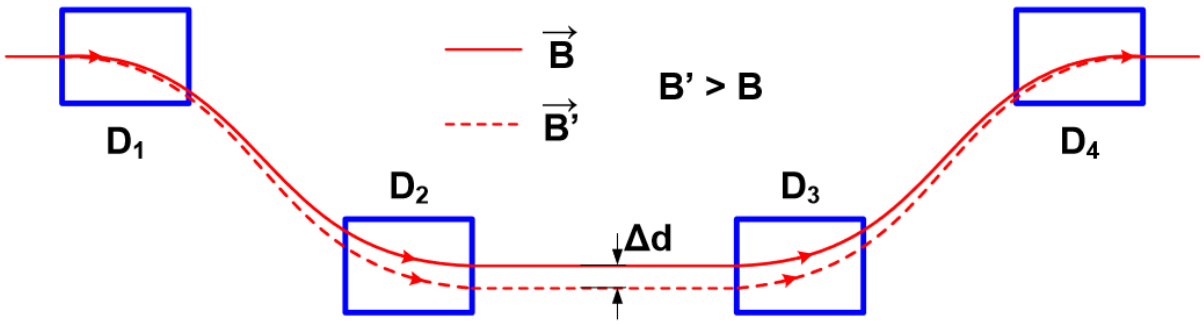

Figure 2.13: Transverse deviation of electron beam trajectory between D2 and D3. [55]

Upon reaching the third dipole magnet, electrons are deflected based on their momentum, with lower-momentum electrons experiencing greater deflection compared to those with higher momentum. This process is known as momentum analysis, as the deflection of electron is a function of electron's momentum. Finally, the primary beam passes through fourth dipole magnet and leaves the polarimeter. Also, we know that a magnetic field can induce precession of the electron spin. To meet these constraints, the magnetic chicane dipoles must be carefully selected so that they possess identical magnetic lengths and fields of equal magnitude but opposite signs.

As discussed above, the third dipole separates the unscattered and scattered electrons, the unscattered electrons are bent further by the fourth dipole D4, and guides them back into the original beam trajectory. On the other hand, the scattered electrons reaches the electron detector. One possible place for an electron detector is after the fourth dipole. It offers the greatest recoil electron deflection at the Compton edge. However, this location exposes the detector to significant synchrotron radiation emitted by electrons as they accelerate through the bend in the fourth dipole. A potentially more advantageous location for the detector would be situated 20 cm before the fourth dipole. Although the maximum electron deflection at this position is slightly reduced, the exposure to synchrotron radiation is significantly lower, reducing potential interference with the detector. Thus, the electron detector is mounted in between dipole D3 and dipole D4. It consists of four silicon microstrip planes, each containing 192 pixels. These planes are mounted on a motorized vertical stage that can be remotely controlled during measurements. However, High Voltaic Monolithic Active Pixel Sensor (HV-MAPS) (described in detail in Sec. 2.3.1) is a planned detector to replace the current electron detector technology.

The Compton backscattered photons are deflected at a minimal angle, θ_γ, relative to the beam axis. When the main beam is redirected by the third dipole, these photons, which remain unaffected by the magnetic field, continue in a straight trajectory. Once they exit the third

dipole, they can be captured by a photon detector. This setup allows for the measurement of polarization through the detection of Compton backscattered photons. The detection is achieved using an electromagnetic calorimeter featuring a single GSO crystal paired with a photomultiplier tube. For measurements involving higher energy levels, alternative crystals are being considered, with recent tests conducted using lead tungstate crystals, also coupled to photomultiplier tubes. This photon detector is positioned beneath the fourth dipole, D4.

The remainder of this thesis will concentrate on the design and characteristics of the recoil electron detector.

2.3 Semiconducting detectors in MOLLER experiment

Detecting particles, as discussed in Sec. 1.6, is a fundamental aspect of experimental particle physics. It enables physicists to probe the basic building blocks of matter and understand their interactions. In this context, the precise measurement of Compton asymmetry, caused by the variation in scattering intensities based on the polarization of the incoming photon and electron beam, is essential. Mapping this asymmetry as a function of momentum is important because it provides detailed insights into the physics underlying these interactions, ultimately facilitating a more accurate determination of the electron beam's polarization. The precision of this extraction depends heavily on the ability to measure the displacement and momentum of recoil electrons; electrons that are deflected from their original path during the interaction. The detector used for this purpose is a semiconductor-based device specifically designed for high-precision applications in particle physics experiments. This semiconductor detector, essential for tracking the recoil electrons, consists of individual readout strips embedded in a semiconductor material, arranged across the detector's surface. When an electron passes through the detector, it strikes one of the pixels, indicating its vertical displacement relative to the main beam. The detector's spatial and momentum resolution is closely tied to the pitch of these strips, with finer pitch leading to better resolution. Moreover, the detector must have a high rate capability and strong resistance to radiation damage, as it will be situated in close proximity to the primary beam line. To meet these demanding requirements in the context of MOLLER experiment, the detector for the measurement of polarization of electron in the compton polarimeter setup will be constructed using High Voltage Monolithic Active Pixel Sensors (HV-MAPS) technology.

HV-MAPS represent an advanced approach in particle detection, merging high-voltage operation with monolithic pixel sensor technology to achieve superior performance. The term "HV" refers to the application of a high reverse-bias voltage across a deep n-well and p-substrate junction. This high voltage creates a depletion zone that enables fast charge collection. The "monolithic" nature of HV-MAPS means that the sensor and readout electronics are built into the same silicon die, as opposed to traditional hybrid pixel detectors that require bump bond-

ing between separate sensor and readout chips. This integration results in a thinner (can be thinned down to 50 μm) [56], hence lighter detector. They are also radiation hard. The "active pixel" concept means that each pixel has its own amplification and processing circuitry, enabling faster readout and higher spatial resolution. Their deployment in the electron detector is expected to significantly improve the precision of polarization measurements. Together, these features define the HV-MAPS as a compact, radiation-hard, fast, and precise tracking detector, making it ideal for applications like the Compton polarimeter in the MOLLER experiment.

Before discussing the specifics of HV-MAPS, it is important to understand the underlying principles of semiconductor materials, doping, and diodes, which form the foundation of this technology. Semiconductors are materials with electrical conductivity that falls between that of conductors and insulators. They can be pure elements, like silicon or germanium, or the compounds such as gallium arsenide. The behavior of semiconductors is largely governed by the concept of energy bands. In a crystalline structure, the energy levels of closely packed atoms merge into continuous bands, with gaps where no electron states exist. At absolute zero, electrons occupy the lower energy bands, leaving the higher bands empty. In semiconductors, the valence band and conduction band are two significant bands as shown in Fig. 2.14. The energy difference between the top of the valence band (E_v) and the bottom of the conduction band (E_c) is called the bandgap (E_g). For silicon, this bandgap is about 1.1 electron volts (eV). In semiconductors, electrical conductivity arises when electrons gain sufficient energy to move from the valence band to the conduction band, leaving behind positive"holes" in the valence band. Both electrons in the conduction band and holes in the valence band contribute to electrical current flow. Bandgap size is a crucial factor in determining a material's conductivity. Metals, with no bandgap, allow free electron flow, making them excellent conductors. In contrast, due to the large bandgap of insulators, the electron movement is prevented under normal conditions. Semiconductors, with a moderate bandgap, exhibit conductivity that increases with temperature, as sufficient energy is acquired by more electrons to move into the conduction band. This property makes semiconductors distinguishable in electronic devices, where they are crucial in modulating and controlling electrical signals.

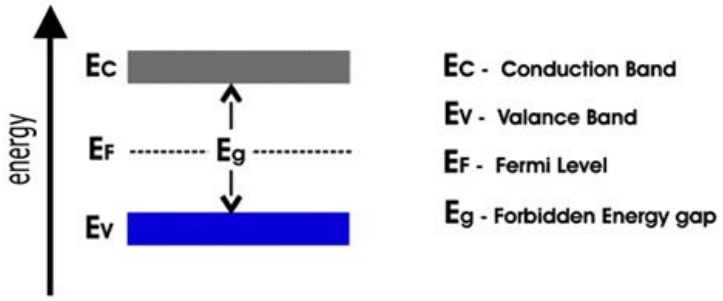

Figure 2.14: Energy band representation of semiconductors [57]

The electrical properties of semiconductors can be further tailored through doping, a process that introduces specific impurities into the material. In their pure form, semiconductors have limited conductivity because their valence bands are completely occupied, restricting electron movement. However, doping allows for the intentional alteration of a semiconductor's electrical, optical, and structural characteristics, resulting in what is known as an extrinsic semiconductor. When pentavalent impurities, such as antimony, arsenic, or phosphorus, are introduced, they provide additional free electrons, increasing the material's conductivity—this is referred to as n-type doping. Conversely, trivalent impurities, like boron, aluminum, or gallium, create "holes" or positive charge carriers, leading to p-type doping. When n-type and p-type semiconductors are brought together, they form a p-n junction, which is critical in the functioning of semiconductor devices. This junction creates a charge distribution and an electric potential due to the movement of electrons from the n-type region to fill holes in the p-type region, resulting in the contact potential. This fundamental principle underlies the operation of diodes and is integral to the design of the HV-MAPS detectors used in this research explained more in Sec. 2.3.1. Silicon is a popular choice for particle detection because of its excellent energy resolution and its ability to function effectively at room temperature, which is possible due to its relatively high band gap energy of 1.11 eV. By utilizing these semiconductor properties, HV-MAPS technology allows precise detection and measurement abilities, which are crucial for improving our understanding of particle interactions and electron polarization.

2.3.1 Silicon diodes as Electron Detector HV-MAPS Technology

High Voltage Monolithic Active Pixel Sensors (HV-MAPS), an array of silicon diodes, designed by Ivan Perić at the Karlsruhe Institute of Technology (formerly ZITI, Heidelberg University), leverage a commercial CMOS process. This enables efficient drift-based charge collection while integrating the readout electronics directly on the same chip. Due to their thin active regions, these sensors can be reduced to thicknesses below $50\mu m$, having a low material consumption, making them particularly effective for tracking low-momentum particles at extremely high rates. In the MOLLER experiment, and in the context of this thesis, HV-MAPS will be deployed in the Compton polarimeter, where they will play a crucial role in accurately tracking and mapping the points of electron interaction within the detector. HV-MAPS integrate the strengths of both fast hybrid pixel detectors and thin monolithic active pixel sensors (MAPS). Fabricated using HV-CMOS technology, it integrate both analog and digital readout electronics directly onto the same silicon die as the sensor, making them a promising technology for future pixel tracking detectors. Monolithic active pixel sensors (MAPS) offers a strong alternative to conventional hybrid designs, where sensors and readout chips are housed on separate dies. The need for interconnects, such as wires or bump bonds, in hybrid designs can limit spatial resolution and obstruct scalability, especially when covering large areas. MAPS, conversely, offer a more efficient and scalable approach to building large-area semiconductor trackers. Since their initial development in 2006, HV-MAPS have been the focus of ongoing research. Their perfor-

mance, including strong radiation tolerance, has been demonstrated by physicists worldwide, as evidenced by several studies [58, 59, 60, 61, 62, 63]. Hence, these sensors are proving to be prime candidates for use in tracking detectors. Over the past decade, segmented radiation sensors integrated into standard Complementary Metal-Oxide-Semiconductor (CMOS) technologies have seen a expanding trend in both research and practical applications. CMOS sensors have become the preferred choice in many commercial fields, gradually overtaking the older Charge-Coupled Device (CCD) technology that was once prevalent. This is because CMOS allows fast readout from each pixel, while CCDs read out sequentially and are slower. CMOS also consumes less power, producing less heat than CCDs [64].

The functionality of CMOS pixel sensors is concentrated on the collection of signal charge, which is directed to a positively biased n-type doped region known as the n-well. Each pixel in HV-MAPS is a well of n-doped semiconductor fixed in a p-doped substrate as shown in Fig. 2.15. The amplifier electronics is embedded inside the n-well. Within each pixel, this charge is then converted into a voltage and subsequently amplified, thus making every pixel an individually acting electron detector. Because initial signal processing occurs within the pixel itself, these sensors are often referred to as active pixel sensors (APS) [64]. The inherent design of Active Pixel Sensors (APS) does not offer complete sensitivity across the entire pixel area. However, in high-energy physics applications, techniques are utilized to minimize such charge losses. The electronics within these pixels are built around n-channel MOS transistors.

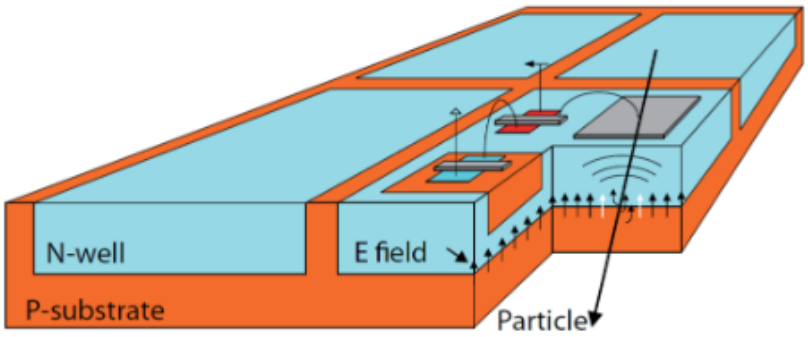

Figure 2.15: HV-MAPS design [65]

The purpose of exploring HV-MAPS in our project is to upgrade the conventional diode-based strip sensors used in detectors by replacing them with HV-MAPS technology to enhance the electron detection capabilities of the Compton polarimeter in Hall A at Jefferson Lab. The key benefit is that HV-MAPS use commercial CMOS (Complementary Metal-Oxide-Semiconductor) technology, making them cheaper to produce over a large area. They also come with active circuits that allow for new features, like better spatial information and flexible grouping of channels. The idea is to replace the large strip sensors (wire bonded to multi-channel ASICs) with a large CMOS sensor that can cover a bigger area by stitching together multiple

wafer reticles. For the Compton Polarimeter, the electron detector has four planes, and each plane uses three HV-MAPS chips. These chips are wire-bonded to each other and to a printed circuit board (PCB) to create a larger detection area for scattered electrons.

The MOLLER experiment will use MuPix Version 11 with minor changes to the internal components. Each chip is 2 cm $\times$ 2 cm, and when arranged together, they provide a total detection area of 6 cm $\times$ 2 cm per plane. Each sensor chip contains $80\mu m \times 80\mu m$ sized pixels, and each chip has 64,000 silicon pixel diodes. Every pixel has a tiny, low-power amplifier and comparator to process signals. The individual pixel outputs a timestamp and its corresponding address where a particle is detected. The chips's high response rate reduces dead time and ensures high event rates. The chip generates 1 Watt of power while operation. Most of the heat in MuPix Version 11 HV-MAPS chips is generated by the state machine and readout electronics, which are concentrated at the periphery of the chip as shown in Fig. 4.1. These component dissipates power, and as a result, efficient thermal management at the chip's edges is crucial to prevent overheating and ensure steady operation.

High-Voltage Monolithic Active Pixel Sensors (HV-MAPS) are acknowledged as alternatives to traditional detector technologies at CERN, and is promising technology for the MOLLER experiment as well. These sensors offer compactness, high resolution, and radiation tolerance, making them suitable for challenging environments. In the MOLLER experiment, in general, HV-MAPS are intended for two key roles. First, they will be utilized in the Compton polarimeter to precisely measure the electron beam's polarization, ensuring the experiment's high accuracy by minimizing uncertainties. Second, these chips will be integrated into Ring 5 of the main detector, positioned next to the quartz crystal, where they will track the profile of scattered electrons from the main beam (refer to [66]). Their ability to provide detailed spatial information about these electrons will enhance the overall precision of the experiment, allowing for better data interpretation and analysis of the Compton scattering process.

Each chip in the electron detector prototype contains 64,000 silicon pixel diodes, and with 12 chips in the current design, a significant amount of power is dissipated. This power loss results in thermal energy being released through ohmic heating, affecting both the detector chip and the carrier board. Given that the detector operates under vacuum conditions, managing this heat becomes critical to ensure the device maintains optimal performance. Without adequate cooling, the rising temperature could impair functionality, potentially affecting the accuracy and reliability of the measurements. To address this, effective cooling solutions are essential to regulate the temperature of the detector. The vacuum environment presents additional challenges, as conventional cooling methods are less effective in such conditions. Therefore, careful thermal monitoring is necessary to evaluate the detector's performance. This is the next application where silicon diodes are utilized to analyze the thermal behavior of our detector system, as explained in Sec. 2.3.2 Various cooling strategies are explored and implemented, as detailed

in the Chapter 3. These methods aim to improve the heat dissipation capabilities of the detector as we advance to more refined models. By adopting these enhanced cooling techniques, we ensure that the electron detector remains stable and operates within safe temperature limits throughout the experiment.

2.3.2 Silicon diodes as Temperature Sensors

Another application of silicon diodes in our experimental setup is to measure the temperatures, and subsequently reduce the risk of overheating of the HV-MAPS chips inside the vacuum. The maximum allowable temperature for the detector to operate inside the magnetic chicane is around 70°C (158°F), beyond which the HV-MAPS stop responding. Overheating may cause outgassing in the vacuum and lead to thermal expansion of components, which could disrupt the system. Also, HV-MAPS detectors are sensitive to heat, higher temperatures introduce thermal noise, reducing signal quality and measurement precision. These are the things we want to avoid. Silicon diodes are commonly utilized because of their anticipated voltage response to temperature changes. The forward voltage of a diode varies as a function of temperature, making them highly effective for accurately measuring temperature when placed on heated surfaces. These temperature sensors in our setup were instrumental in testing and recording the maximum temperatures during HV-MAPS operation (further detailed in Chapter 4).

Selecting the proper sensor is vital to monitoring temperature. It is important to consider the sensor's operational temperature range, as exposure to temperatures beyond its limits can damage the sensor. For our purpose, the temperature sensor we selected is DT-670 silicon diode for which the temperature range is 1.4K to 500 K [67]. The DT-670 silicon diode from Lakeshore is pre-calibrated to offer accurate temperature readings across the given temperature range. The calibration curve provided by the manufacturer relates the diode voltage to temperature, and in this experiment, a constant current was applied to the diode to ensure stable operation. These calibration process involves taking different set of temperature measurements at diffferent known temperatures and fitting the curve to describe the Voltage-temperature relation. At absolute zero (T=0), semiconductors act as insulators, but as the temperature increases, they exhibit a band gap, E_g, up to their melting point. The resistivity, $\sigma(T)$, follows an exponential relationship,

$$\sigma(T) \propto \exp \frac{-E_g}{2k_B T}\,, \tag{2.28}$$

meaning the resistivity decreases as temperature rises. This increase in temperature boosts the likelihood of thermally excited electrons, which in turn lowers the contact potential, as illustrated by the curve given in the Fig. 2.16.

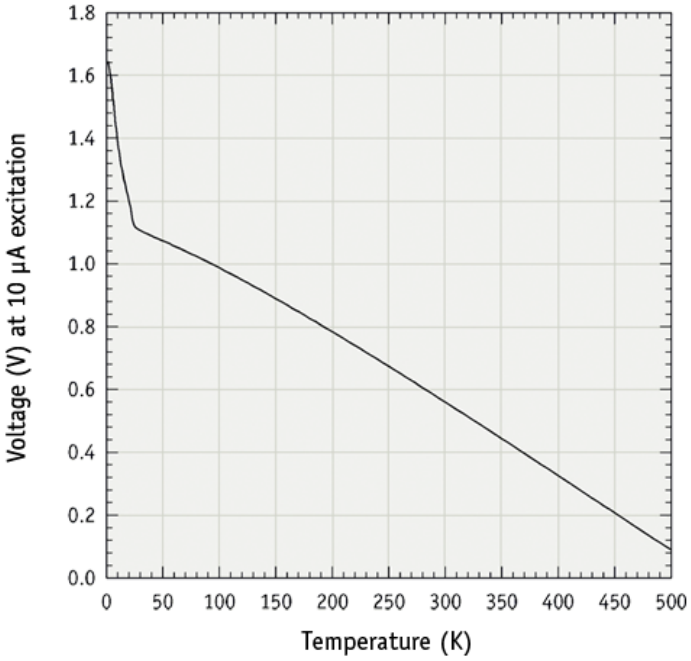

Figure 2.16: DT-670 diode Voltage Curve [68]

By placing DT-670 silicon diodes directly on the HV-MAPS chips and other heated components of the electron detector, we are able to constantly track the temperature. This real-time data made it possible to control the cooling system effectively, ensuring the temperature stayed below the 70°C limit required for safe operation (refer to Chapter 4)

Environmental conditions, such as high vacuum, magnetic fields, corrosive substances, or radiation, also play a significant role in sensor selection. Some sensors are unsuitable for these harsh conditions. Lake Shore has developed sensors designed to endure the extreme temperatures, vacuum pressures, and materials common in cryogenic systems. Experiments done in magnetic fields are very common. In experiments involving magnetic fields, the sensor's response to field variations becomes a crucial criterion in the selection process [67].

Lake Shore sensors come with detailed instructions that specify the connections for each sensor lead, including the correct polarity for the positive and negative leads, as well as the appropriate voltage and current settings where applicable. Adhering to these guidelines is crucial, as diode sensors are highly sensitive to polarity. If connected incorrectly, they can appear as an open circuit to the measurement instrument [67]. A diagram showing the correct polarity for the diode is included in Fig. 2.17.

To address the issue of resistance of the electrical leads within our vacuum system, we implemented a 4-lead configuration for sensor connections. In this setup, the positive voltage lead is connected to the positive current lead, while the negative voltage lead is linked to the negative current lead. The circuit diagram for this 4-lead measurement system is illustrated in Fig. 2.18.

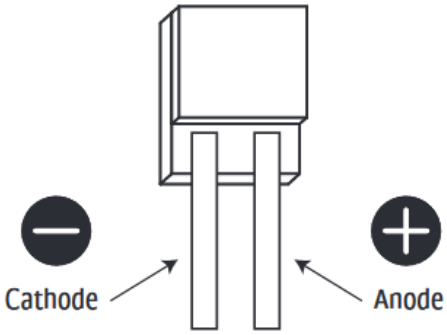

Figure 2.17: Lead arrangement of the DT-670 silicon diode [67]

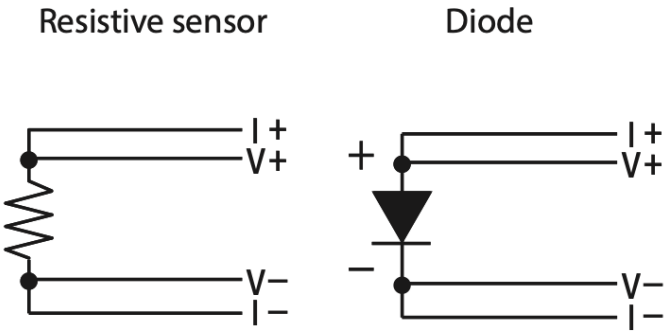

Figure 2.18: 4-Lead arrangement for DT-670 diode [67]

Chapter 3

Optimization of HV-MAPS Electron Detector models based on Thermal Simulations

In the previous chapter, we addressed the challenge of operating HV-MAPS detectors in vacuum environments, where heat dissipation is significantly constrained. This makes efficient thermal management essential to maintaining their performance and reliability. In this chapter, we focus on the thermal behavior of these electron detectors through Computational Fluid Dynamics (CFD) simulations. These simulations investigate the operating temperature of the detectors and help us refine the model to improve its efficiency in mitigating heat by exploring and testing different cooling strategies on CFD. Maintaining stable thermal conditions is critical, especially within the magnetic chicane, where the vacuum environment requires active cooling due to the lack of a medium for heat dissipation. While the previous chapter highlighted the importance of dissipating heat away from detectors in a vacuum environment, this chapter explores how the proper regulation of heat generated by the electronics is performed. Heat management is essential to avoid overheating and potential damage to the detectors.

To understand the concept of heat regulation, we begin with the concept of heat transfer: Heat is a form of thermal energy, and temperature measures the energy level of a system. Heat transfer occurs whenever there is a temperature difference, either within a material or between two materials, through interactions with the surroundings. The process which underlie the heat transfer are: Conduction, Convection and Radiation.

Conduction: Heat transfer through stationary materials occurs via conduction, which involves the movement of heat due to direct physical contact between particles. This process is driven by differences in temperature between regions, with heat flowing from areas of higher temperature to areas of lower temperature. The mechanism at play is the transfer of kinetic energy as atoms and molecules, which are vibrating, pass their energy to adjacent particles. This transfer persists until thermal equilibrium is achieved across the substance. When discussing

conduction, it is important to consider the atomic and molecular activity that forms the basis of this form of heat transfer as conduction involves the transfer of energy from more energetic particles to less energetic ones through their interactions. At higher temperatures, particles have more energy, and as they collide with neighboring particles, energy is transferred to those with less energy. This energy transfer continues in the direction of the temperature gradient. To quantify the rate of heat conduction, we use mathematical models such as Fourier's law, which calculates the rate of heat transfer over time. In a one-dimensional system with a temperature distribution T(x), Fourier's law which gives the rate at which heat energy is conducted through the material is expressed as following:

$$Q_{cond.} = -k\frac{dT}{dx}. \tag{3.1}$$

The heat flux Q (W/m^2) is the heat transfer rate in the x-direction per unit area perpendicular to the direction of transfer, and it is proportional to the temperature gradient, $\frac{dT}{dx}$, in this direction. The parameter k is a transport property known as the thermal conductivity (W/m.K) and is a characteristic of the wall material. T_1 and T_2 are the temperatures at the two end of the material, T_2 being the temperature of the source and T_1 being the temperature of the sink. The minus sign is a consequence of the fact that heat is transferred in the direction of decreasing temperature.

For the system under steady-state conditions (linear temperature distribution), the heat flux is given as

$$Q_{cond} = -k\frac{T_2 - T_1}{L}\,, \tag{3.2}$$

and the heat rate via conduction through surface area A is given as

$$q_{cond} = Q.A, \tag{3.3}$$

or

$$q_{cond} = -k\frac{T_2 - T_1}{L}A\,. \tag{3.4}$$

In our model, one of the primary mechanisms of heat transfer is conduction. This process has a critical role in maintaining the thermal stability of the detector components. As we learn design intent in section 3.1, we will see how the conductive process is utilized extensively in various components of the system for effective removal of excess heat [69].

Convection: Convection, or convective heat transfer, represents the movement of heat through a fluid as the fluid itself moves from one area to another. While convection is often treated

as a separate mode of heat transfer, it actually incorporates both conduction (the diffusion of heat) and advection (the mass transport of heat through fluid motion). Our focus is on the heat transfer that occurs between a moving fluid and a surface, especially when there is a temperature difference between them. Heat transfer through convection occurs in two means: random molecular movement and the overall fluid flow. Close to the surface, where the fluid moves slowly, heat is mainly transferred by the random motion of molecules, known as diffusion. At the point where the fluid meets the surface, the fluid is not moving, so only diffusion transfers heat. Convective heat transfer can be classified on the basis of how the fluid flow is generated. Forced convection arises when external devices, such as fans or pumps, drive the movement of the fluid. On the other hand, natural convection takes place when fluid movement is caused by buoyancy effects. These buoyancy forces result from variations in fluid density due to temperature differences. For example, when fluid heats up nearby the hot surfaces, its density decreases. This lighter, warmer fluid rises, creating a natural upward flow, while cooler fluid from the surroundings moves in to replace it, ensuring a continuous circulation. The rate equation for convection can be expressed as following:

$$Q_{conv} = h(T_s - T_f),$$

where Q_{conv} is the convective heat flux W/m^2, T_s is the surface temperature and T_f is the fluid temperature. The convective heat flux is proportional to the variation between the surface and fluid temperature, and the h (W/m^2.K) is convective heat transfer coefficient. The convective heat transfer then is described by the following equation:

$$q_{conv} = h(T_s - T_f)A,$$

A is the surface area. We can see from the above equation (Newtons law of cooling) that the heat flux is positive if heat is transferred from surface to the fluid, and is negative when transferred from fluid to the surface [69].

In our local lab setup, detailed in chapter 4, we have used convective heat transfer within a certain volume of the cooling block called water pocket (see Fig. 4.8). Additionally, a cooling pipeline was installed for the inlet and outlet of the coolant (see Fig. 4.11). We are using a forced convection method using the Industrial Chiller, model CW- 5000TG from S&A [70].

Radiation: Thermal radiation is the mechanism by which energy is emitted by matter with a temperature above absolute zero. This energy is propagated through electromagnetic waves, or photons. Unlike conduction and convection, which depend on the existence of a material medium, radiation can transfer energy in a vacuum. The radiation transmitted from a surface to its surroundings is a result of the thermal energy within the material, and the rate of energy

emission per unit area (W/m^2) is known as emissive power of the surface, denoted by E. The maximum possible emissive power for a surface is governed by the Stefan–Boltzmann law as following:

$$E = \epsilon\sigma T^4, \tag{3.5}$$

where ϵ is the emissivity of the surface, σ is the Stefan Boltzmann constant (its value is $\sigma = 5.67 \times 10^{-8}\mathrm{W/m^2.K^4}$) and T is the absolute temperature (K) of the surface. ϵ indicates how efficiently a surface radiates heat/ energy compared to a blackbody, and its value ranges from $0 \leq \epsilon \leq 1$.

A surface can receive radiation from its surrounding environment as well. Regardless of its origin, the rate at which radiation falls on a unit area of the surface is referred to as irradiation, andis given as follows:

$$G_{abs} = \alpha G, \tag{3.6}$$

where α is the absorption coefficient varies from $0 \leq \alpha \leq 1$. The absorption of the radiation mainly depends upon how strong is the absorption coefficient for that surface of the material. Thus, the net radiative heat flux between the surface and surrounding can be calculated by following difference:

$$Q_{rad} = E - G_{abs}, \tag{3.7}$$

and subsequently, the radiative heat transfer is given by:

$$q_{rad} = (E - G_{abs})A, \tag{3.8}$$

A is the area of the surface of the material. In our case, we can ignore the radiative effects as per the Stefan–Boltzmann law [69],

$$Q_{flux} = \epsilon\sigma({T_1}^4 - {T_2}^4)$$

T_1 is the temperature of the heat load (for our case, these are HV-MAPS chips) and T_2 is the temperature of the surrounding (for our purpose, it would be the vacuum chamber). ϵ is the emissivity of the material, and σ is the Stefan–Boltzmann constant.

The maximum temperature the heat load/ HV-MAPS chips are allowed to go in our case would be 70° C, and assuming the vacuum chamber is at the room temperature. We know that value for Stefan–Boltzmann constant is $\sigma = 5.670374419 \times 10^8 Wm^{-2}K^{-4}$ and we assume

emissivity to be 1. Using these values in the Stefan–Boltzmann law mentioned above, we get

$$Q_{flux} = (1)(5.670374419 \times 10^{8}\mathrm{Wm^{-2}K^{-4}})((343.15)^4 - (298.15)^4)K^4, \tag{3.9}$$

$$Q_{flux} = 340.38\,\mathrm{Wm^{-2}} \tag{3.10}$$

or,

$$Q_{flux} = 0.034 W cm^{-2} \tag{3.11}$$

This is the radiative heat transfer per unit area. The area of the heat load/periphery of the HV-MAPS chips per plane is (width of the periphery($0.3cm$)$\times$ length of the periphery of all the chips in a plane($6cm$)) $1.8cm^2$. So, the radiative heat transfer per plane is given by:

$$Q_{rad.} = Q_{flux}.A_{periphery}, \tag{3.12}$$

$$Q_{rad.} = 0.034\,\mathrm{Wcm^{-2}} \times 1.8\,\mathrm{cm^2}, \tag{3.13}$$

$$Q_{rad.} = 0.0612\,\mathrm{W}. \tag{3.14}$$

This is the radiative heat transfer per plane. As we have 4 planes in the detector system, the total radiative heat transfer would be

$$Q_{total_rad.} = 0.24\,\mathrm{W}. \tag{3.15}$$

This total radiative heat transfer has very small contribution. Hence, we can safely ignore the radiative effects in our case.

3.1 Electron detector design in Compton Polarimeter

In Section 2.3.1, we discussed that the currently existing strip detectors in Hall A will be substituted by HV-MAPS technology. This section considers the design purpose and considerations for using HV-MAPS as electron detectors within the Compton polarimeter. The current setup for the strip detectors, which are part of the microstrip detector system used as electron detectors, is illustrated in Fig. 3.1. The electron detector is positioned between dipoles D3 and D4, located 4.102 meters from the center of dipole D3. It comprises four parallel planes spaced 1 cm apart horizontally, with a 200-micron vertical offset between the planes. Each plane incorporates 192 silicon strips, each having a width of 240 microns. The detector assembly is mounted on a translator, allowing for vertical motion up to 120 mm away from the primary beam path. The present technology, although functional, suffers from a low signal-to-noise ratio, limiting measurement precision, which does not align with the accuracy standards of

the MOLLER experiment. Therefore, replacing the current detector with HV-MAPS technology offers significant improvements, including reduced noise and enhanced spatial resolution, supporting more accurate measurements of the electron beam polarization. The design of the HV-MAPS detector will maintain certain key elements from the previous setup, such as the use of four planes. However, the technological advancements introduced by the HV-MAPS will strengthen the system's overall performance. For comparison, Fig. 3.2 demonstrates the side-by-side layouts of both the previous microstrip silicon technology and the upcoming HV-MAPS technology. The primary mechanical setup, including the vertical translator and the remote-controlled stepper motor that enables the detector's movement into and out of the beam path, will largely remain the same.

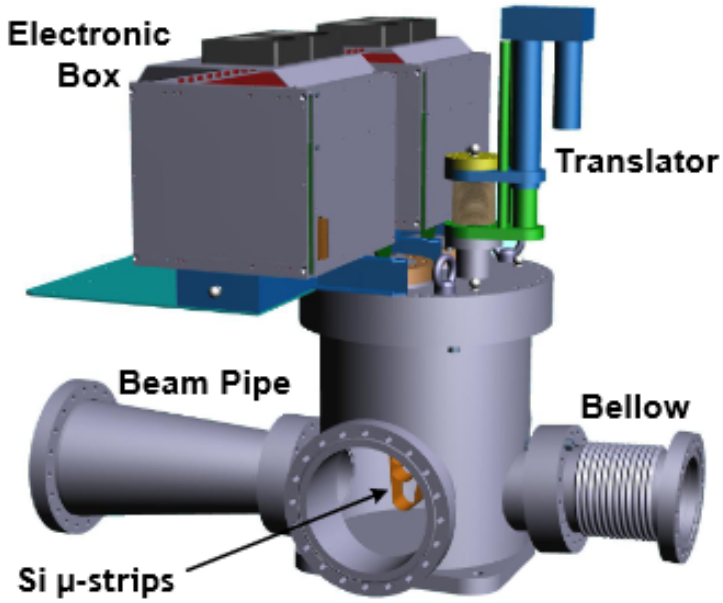

Figure 3.1: Vertical translator for strip detectors in Hall A [55]

The planned detector design includes multiple planes to effectively trace the trajectories of electrons that went through Compton scattering. Each plane of the new detector is equipped with three HV-MAPS chips, with each chip measuring $2 \times 2\, cm^2$. This configuration offers a total active detection area of $2 \times 6\text{cm}^2$ for each plane, considerably enhancing the detector's capability to capture scattering events. During functioning, each chip generates 1 Watt of power. Since the design includes four planes, each housing three chips, the total power output within the vacuum environment will reach 12 Watts. To regulate the heat generated during operation, we plan to employ conduction and convection approaches. Multiple modeling strategies will be explored and discussed in Section 3.2 of this thesis, focusing on effective thermal management. Preliminary studies examining the thermal behavior of these chips (with Mupix8) were conducted at the Department of Physics and Astronomy at the University of Manitoba, as detailed in previous

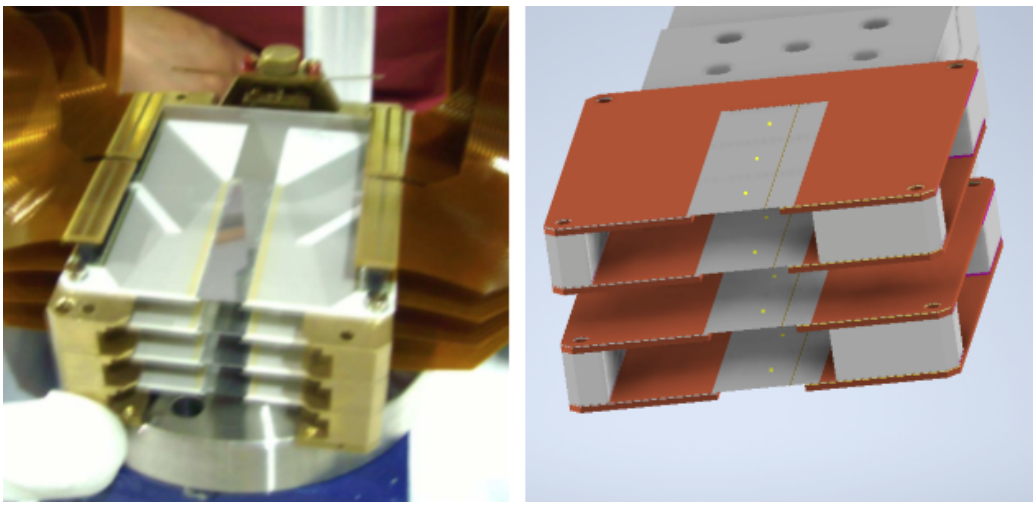

Figure 3.2: Comparison of new and old version of the detector, Credits for left image: [55]

theses, including *Thermal Measurements of a Silicon Diode Pixel Detector and Carrier Board* by Garrett Leverick, and *Detector Development for the MOLLER Experiment* [66]. The HV-MAPS chips will be secured to a Printed Circuit Board (PCB), with direct bonding of the connections to facilitate data acquisition from the chips when they are incidental to the electron beam. This bonding process will utilize a wire bonder located in the Department of Physics and Astronomy at the University of Manitoba. The entire detector assembly will be housed within the vertical translator, as previously described.

3.2 Iterative design of the electron detector driven by cooling simulations

This research focuses on the thermal simulations of several electron detector models designed for the Compton polarimeter, which measures the polarization of the electron beam required for the MOLLER experiment. Ongoing efforts for the development process involves continuous design improvements, with a strong emphasis on fluid dynamics and heat dissipation. The primary contribution of this thesis towards this project is analyzing the fluid and heat flow of each model by performing thermal simulations using Autodesk CFD [71], and suggesting the changes in the detector design depending upon the foreseen cooling necessities and predicted cooling solutions. CFD is a branch of fluid mechanics that uses numerical methods to solve fluid flowing (liquids or gases) problems. These simulations are not only aimed at ensuring that the detectors remain within acceptable temperature ranges but also at identifying how various design parameters influence thermal behavior. This is crucial for detectors operating in vacuum conditions, where cooling solutions are inherently challenging. The work extends beyond simple thermal management by addressing the fluid flow within the detector's cooling channels, which is critical for effective heat transfer. We have used Autodesk Inventor [72] to prepare the CAD (Computer-Aided Design) models. CAD softwares helps us in designing, modifying, alalyzing

the designs. This software produces accurate drawings of the models which helps in easier communication of the designs to be machined. To evaluate the thermal properties of our CAD designs of the electron detector, we used CFD. We import CAD files into the CFD softwares and assign material, initial and boundary conditions. We try creating the environment onto and in the surroundings of the design as much as we can replicate the real-world conditions, providing insights into how the design would perform in practical, real-time scenarios.

Six detector models have been developed, with each version addressing the limitations of its predecessor and progressively solving cooling challenges. For instance, early models were found to have limitations in terms of heat dissipation, particularly at critical junctions where thermal hotspots were detected. Subsequent models addressed these issues by incorporating more efficient cooling channels, modifying the geometry of key components, and optimizing the positioning of heat sinks. These iterative design improvements have significantly enhanced the overall thermal stability of the detector models. One key focus of these simulations is ensuring that the detectors can operate inside the vacuum chamber without exceeding the temperature thresholds required for reliable operation. In particular, the models were tested to ensure that the temperature remains below 70°C, a critical limit to prevent damage to sensitive electronics. Achieving this requires balancing the detector's cooling needs with the practicalities of manufacturing and integration into the overall system. For example, while some cooling configurations may perform exceptionally well in simulation, they must also be feasible to manufacture and install within the limited space available in the polarimeter.

This thesis focuses solely on the modification and evolution of these detector designs based on thermal simulations. A significant portion of the work, containing detailed strategies and techniques used to modify these models [73] are available in thesis [66]. This thesis provides an in-depth study and thermal analysis of these six models, explaining why modifications were necessary from one model to the next. Each model's thermal performance is analyzed based on both simulation results and practical manufacturing constraints, with the goal of determining the optimal design for efficient operation within a vacuum environment. The CAD models of the detectors, along with their corresponding cooling analysis results, are discussed in the following sections.

3.2.1 Model 1

The initial model of the first detector design is shown in the Fig. 3.3. It features three chips placed adjacent to each other in a 3 by 1 grid, and mounted on a PCB. There is a cold plate placed onto the chips. Since the chips cannot be directly attached to either the PCB or the cold plate, doing so could lead to physical damage due to their delicate nature and the uneven surfaces creating air gaps between the components. These gaps would reduce the efficiency of heat transfer and risk damaging the chips from overheating. To prevent this and ensure proper thermal management, we will use a layer of thermal pad. The thermal pad is TG-A4500 [74],

and is an ultra-soft thermal pad, which is high-performance silicone gap pads (shown in Fig. 4.14 and 4.15) with a thermal conductivity of 4.5 W/mK. This low thermal impedance pad is soft and flexible, and it can be supplied either in sheets or as custom-cut pieces depending on the design requirements. The main job of this pad is to fill any gaps between the chips and the PCB, and between PCB and the cold plate. These gaps exist because surfaces are not always perfectly flat or smooth. The pad becomes soft at higher temperatures, which helps it fill those gaps and maintain good thermal contact. It also provides a cushion between two adjoining surfaces, which is important because the chips are very thin and fragile, breakage could compromise the functionality of the state machine located on their periphery. If the chip breaks, the data generated when the electron beam interacts with them for polarization measurement would be lost. The Fig. 3.3 shows the front view of the detector plane without cold plate.

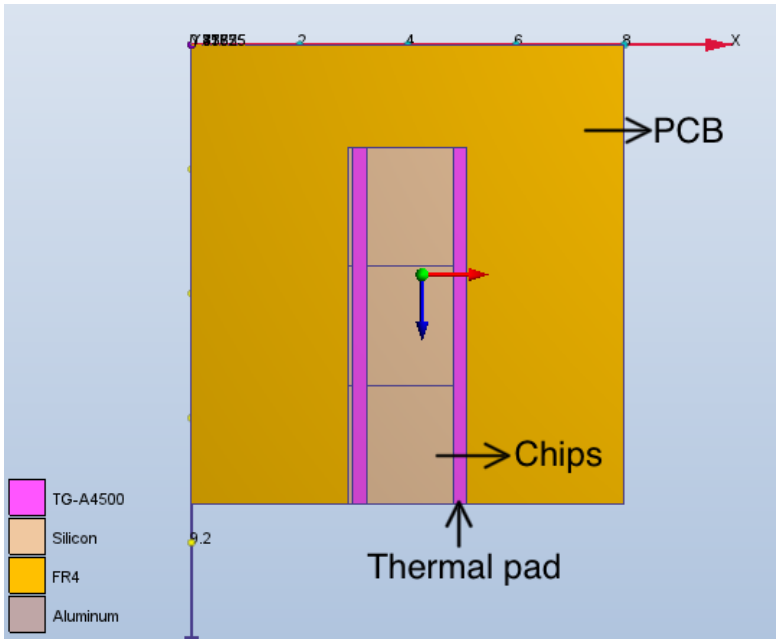

Figure 3.3: Computational Aided Design (CAD) of the Model 1 for the electron detetor(Front View featuring therml pad, chips and PCB)

The TG-A4500 [74] thermal pad also has some natural stickiness, which means it can adhere to the surfaces on its own, which eliminates the need for additional epoxy to bond the chips to the PCB and then PCB to the cold plate. These pads are helpful because they are an alternative to the thermal paste to be used as a thermal interface material. The cold plate is added to distribute the temperature/heat away from the chips, because HV-MAPS see data loss around 70°C. For initial thermal analysis purposes, it is configured with only one plane as can be seen in the fig. 3.4. Material for the system involves: silicon for the chips, TG A-4500 for the thermal pad, copper for the cold plate. Fig. 3.4 refers to the front view and fig. 3.5 shows the angled view of the detector plane with cold plate.

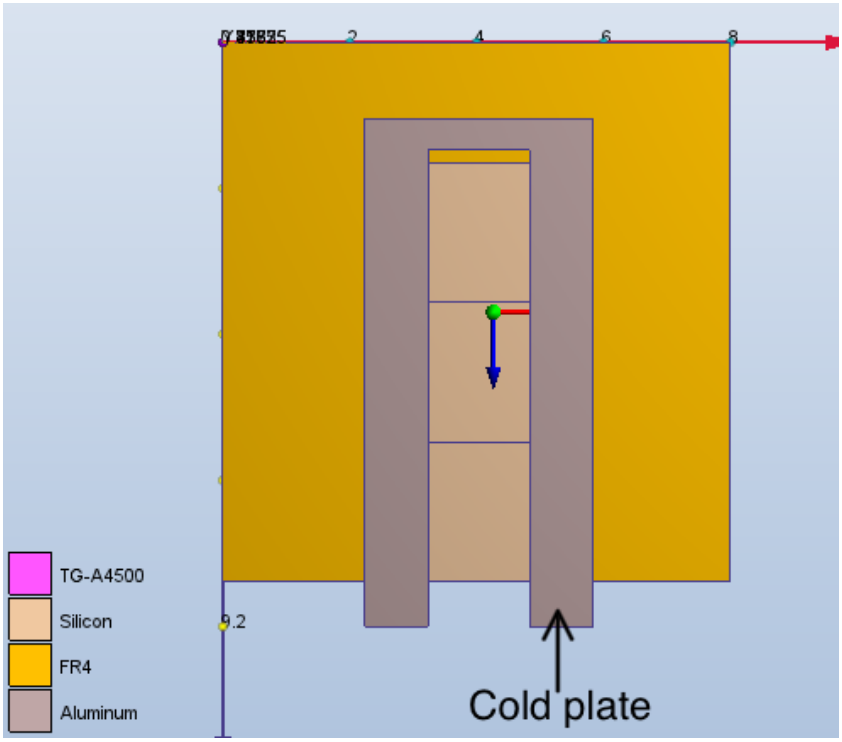

Figure 3.4: CAD of the Model 1 for the electron detector (front View featuring cold plate)

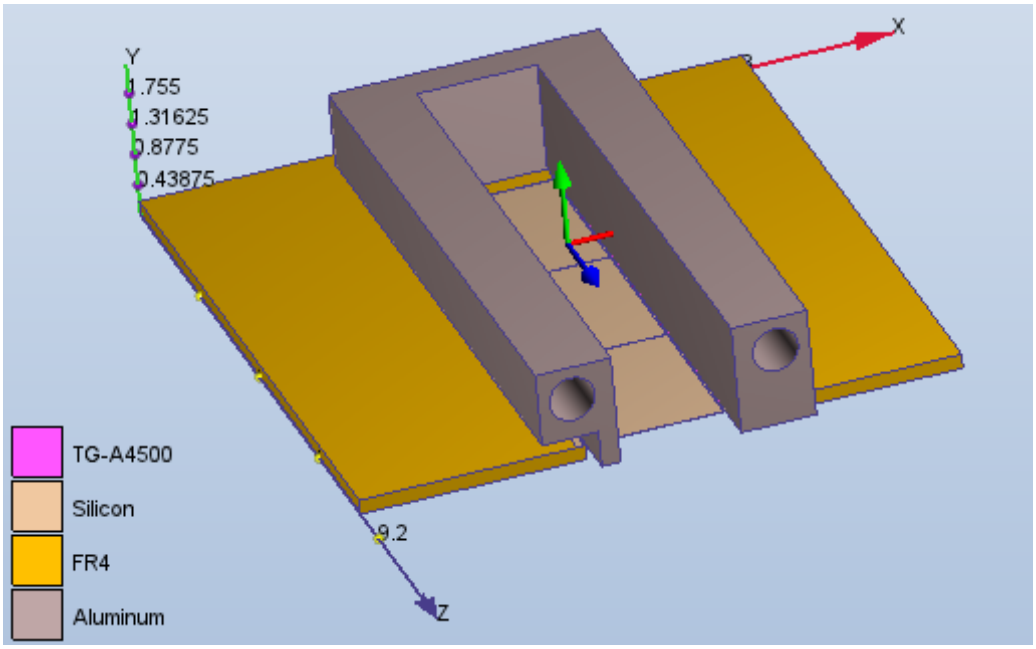

Figure 3.5: CAD of the Model 1 for the electron detector (angled view)

The CAD drawing for the model 1 is shown in Fig. 3.6. All the dimensions are measured in mm.

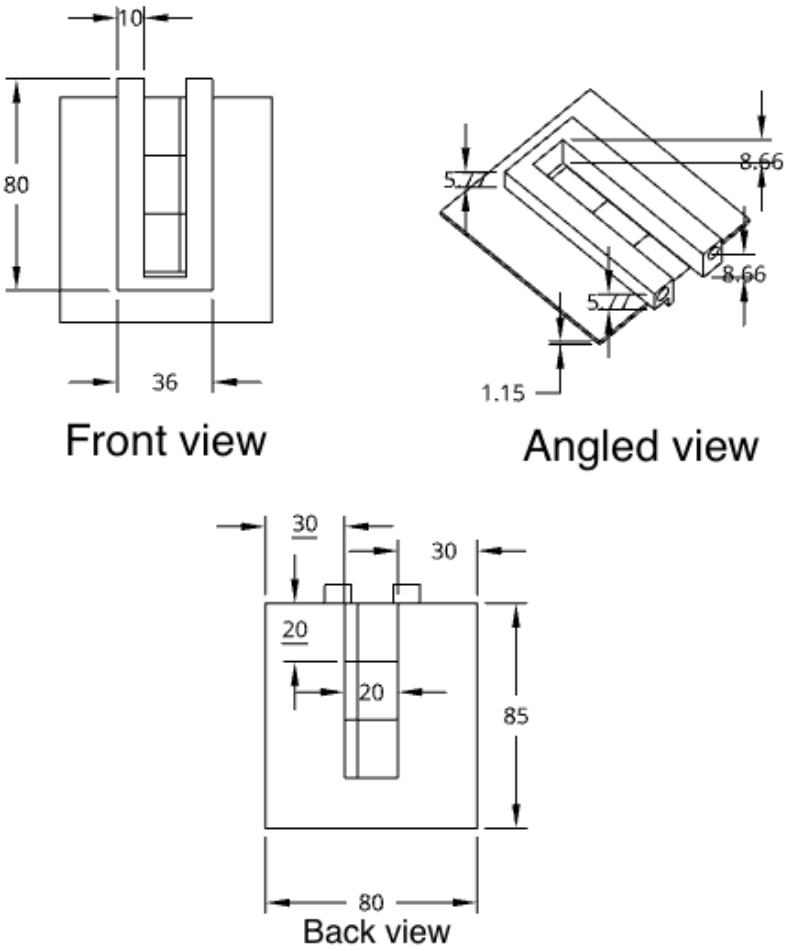

Figure 3.6: CAD drawing of Model 1 (units: mm)

We used the computational fluid dynamics to analyze the model thermally (shown in Fig. 3.7). As Mupix 11 is rated to generate about 1 Watt of heat during operation, we put 0.25 W/cm^2 heat flux over each chips in CFD. As we can see from the simulation results, the temperature at the center of the chip is recorded to be 58.3^{o}C. There is quite a lot to be placed inside the vacuum, also considering that these are the simulation results, and when we do it practically the temperature might increase, we need to find a solution to take this much heat away from the system. We have placed the thermal pad in between the pcb and the chips on both the long edges keeping those at 10°C, but we do not have any thermal pad attached onto the short upper edge, and we can see in the simulation results that the two long edges where we have placed the thermal pads, the temperature is relatively low as compared to the top/ shorter side of the PCB, where temperature reaches nearly 41°C. This is because we have applied boundary condition on the thermal pads, setting the temperature to be 10°C.

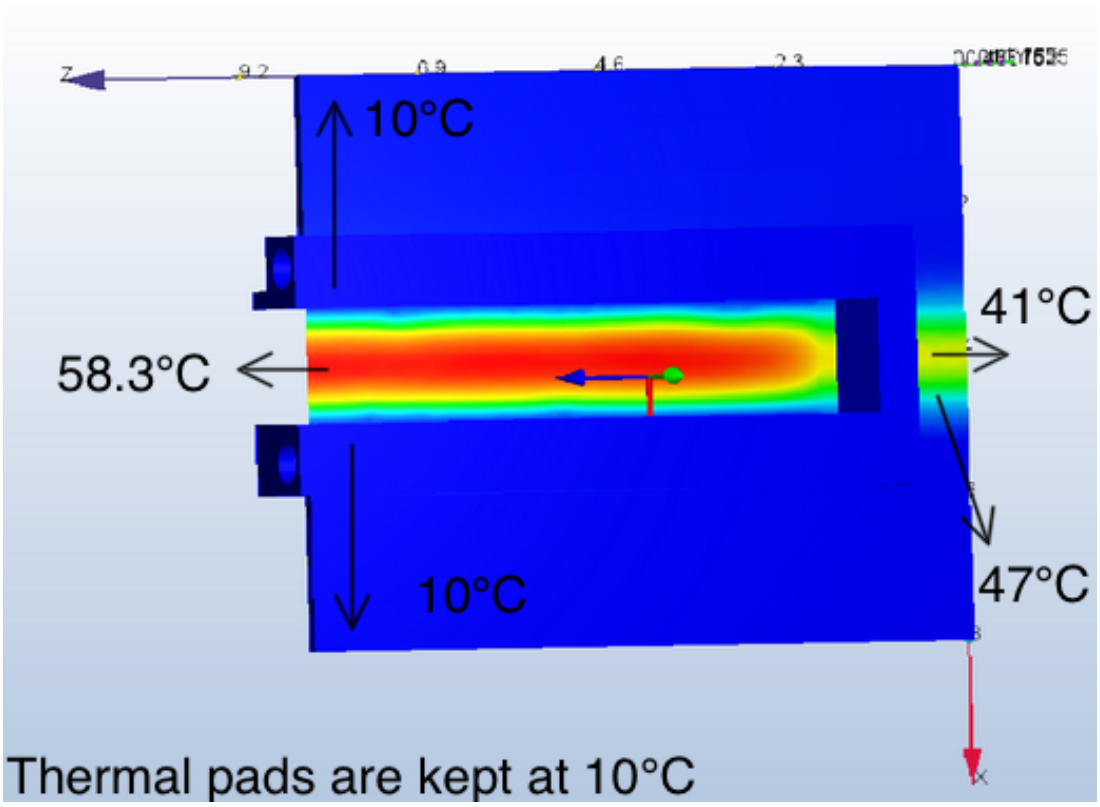

Figure 3.7: Thermal simulation results from Computational Fluid Dynamics (CFD)

3.2.2 Model 2

After analyzing the results from the Model 1, it was clear that modifications were needed for effective heat removal from the chips. Model 2 was designed with this goal in mind, featuring a key addition:

- A cooling strip attached on one side to help dissipate heat from the HV-MAPS. In the Fig. 3.8 only one plane is shown for the reference, but the full design for model 2 would include four such planes. This figure features the newly designed cooling strip, constructed primarily from copper for its excellent thermal conductivity, a PCB that supports the chips, and a cold plate to enhance proper heat regulation. The function of the big cooling copper strip attached on one side of the detector is to channel the heat away from the chips.

- Another significant design improvement in Model 2 is the inclusion of a cold plate placed beneath one side of the PCB. This block is positioned directly above the cooling strip to enhance the overall heat transfer process. The block can be manufactured from either copper or aluminum, both materials known for their thermal conductivity.

- A layer of thermal pad is sandwiched strategically between the cold plate and the PCB to fill in any microscopic gaps and imperfections between the two surfaces. It also creates an efficient heat transfer pathway from the PCB to the cold plate. Bridging these gaps, these pads help in preventing thermal buildup in critical areas of the detector. By positioning

the cold plate in this manner, we aim to better channel heat away from the chips through both the cooling strip and the cold plate, improving the overall thermal management of the detector.

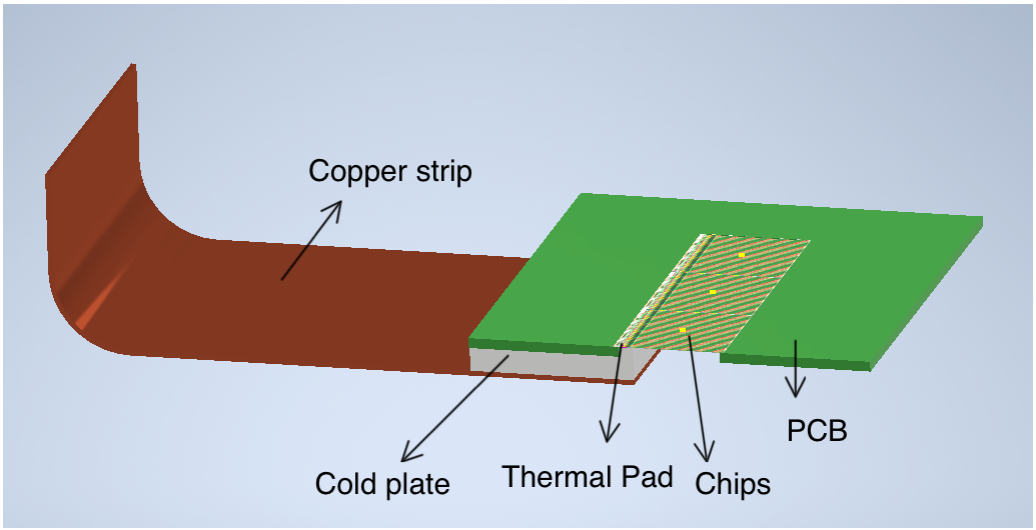

Figure 3.8: CAD of the Model 2 for the electron detetor

Fig. 3.9 shows the CAD drawing of model 2.

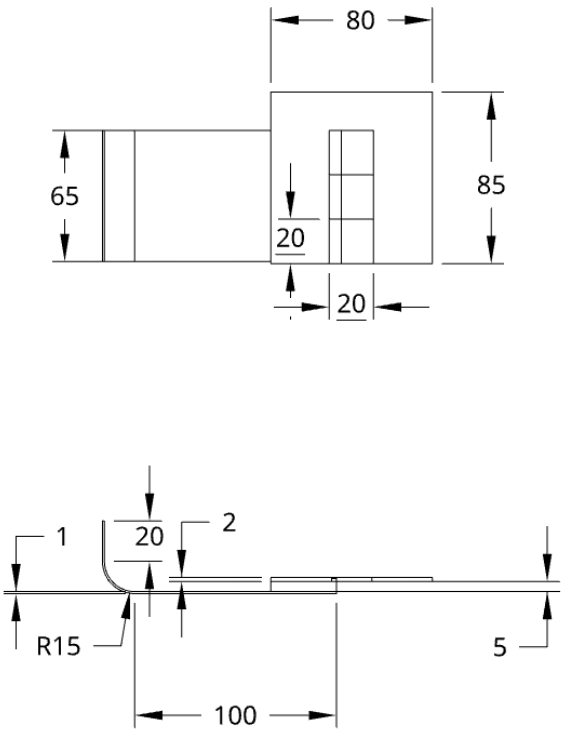

Figure 3.9: CAD drawing of Model 2 (units: mm)

To evaluate the effectiveness of this design, thermal simulations with CFD were run for two scenarios: Case 1, where the cold plate is aluminum, and Case 2, where it is copper. The end of the copper strip is kept at room temperature via external means. The boundary condition on the ends of the copper strip is applied, setting the temperature to be 30°C. The results showed that Model 2 recorded the hottest temperature at the periphery as 47.5°C (shown in Fig. 3.10) with the aluminum block, and by 45.9°C (shown in Fig. 3.13) with the copper block. The total heat generation targeted at the periphery of every chip using boundary condition is 1 W, and the end of the copper strip is kept at the room temperature. While this temperature reduction is notable, the maximum temperature in both cases remained below safe operational limits for a vacuum environment, this emphasizes the need for additional design improvements. The results of the CFD analysis, which display the temperature distribution along the heat removal path, are presented in Figs. 3.11 and 3.14 for cold plates made of aluminum and copper respectively, respectively. Figs. 3.12 and 3.15 illustrate the temperature generated at the periphery and its varying along the depth of the cold plates, providing further insight into the thermal gradients that necessitate refinement of the cooling design. Therefore, further modifications are needed in the detector design. From this analysis, copper proved to be the better option, so further modifications will focus on using copper cold plates in future models.

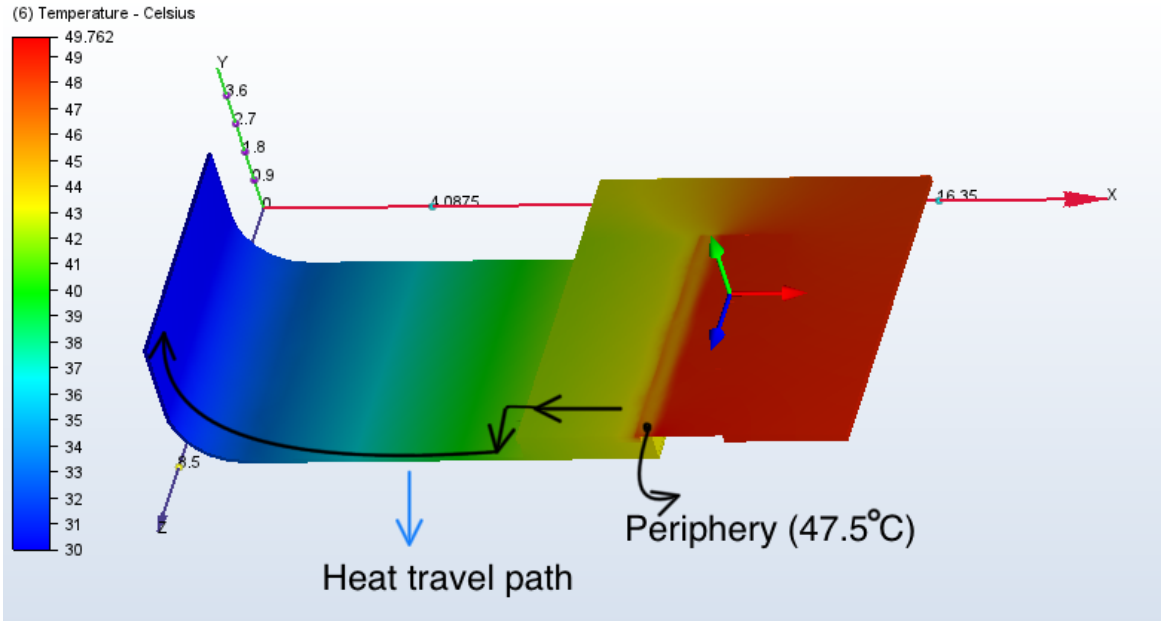

Figure 3.10: Thermal simulation results from CFD for cold plate as aluminum featuring the heat flow path and the periphery temperature.

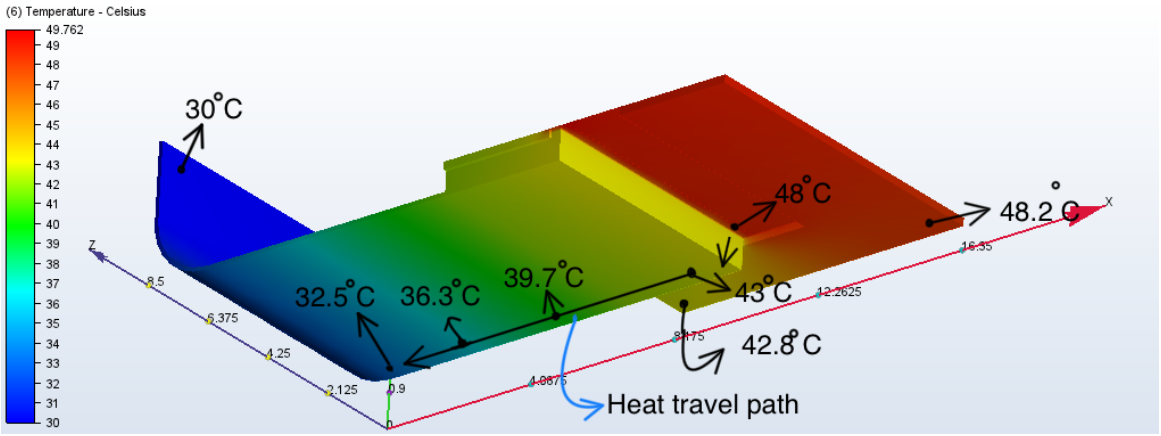

Figure 3.11: CFD thermal simulation results for the aluminum cold plate, showing temperature values along various points in the heat flow path.

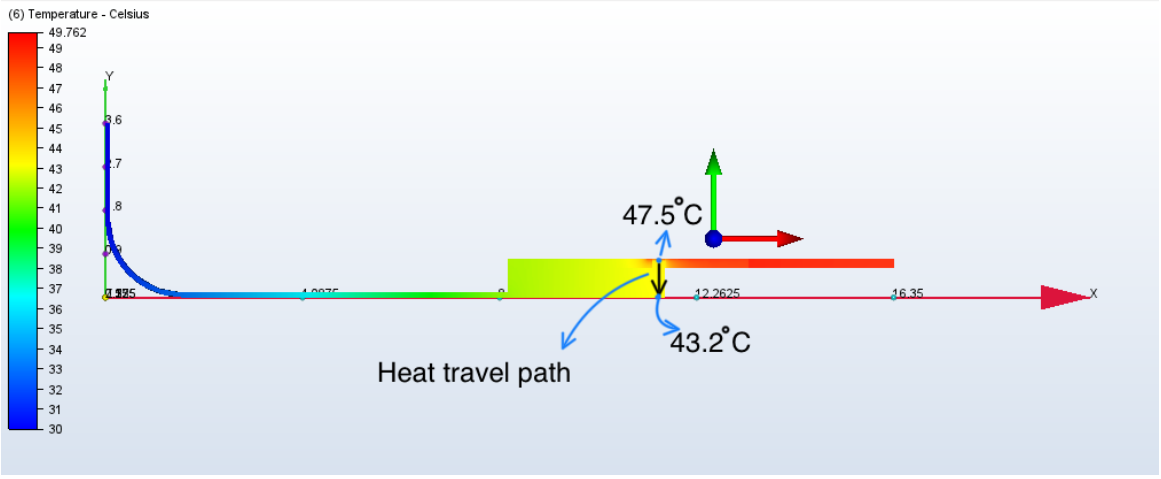

Figure 3.12: Thermal simulation results from CFD results for an aluminum cold plate, illustrating temperature generated at at the periphery and its variation along the depth of the aluminum block.

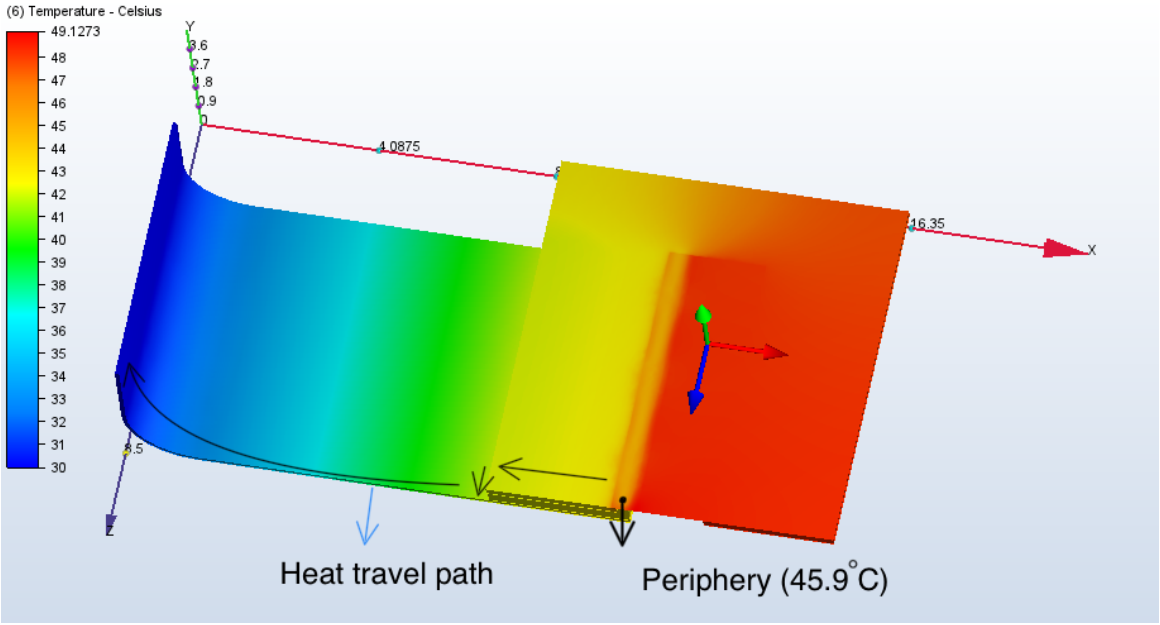

Figure 3.13: Thermal simulation results from CFD for Copper cold plate.

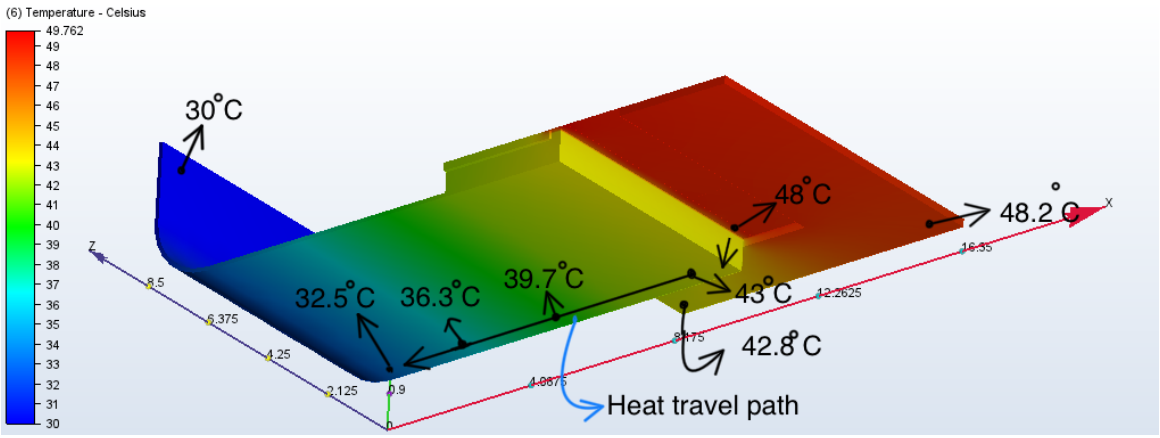

Figure 3.14: CFD's thermal simulation results for the copper cold plate, showing temperature values along various points in the heat flow path.

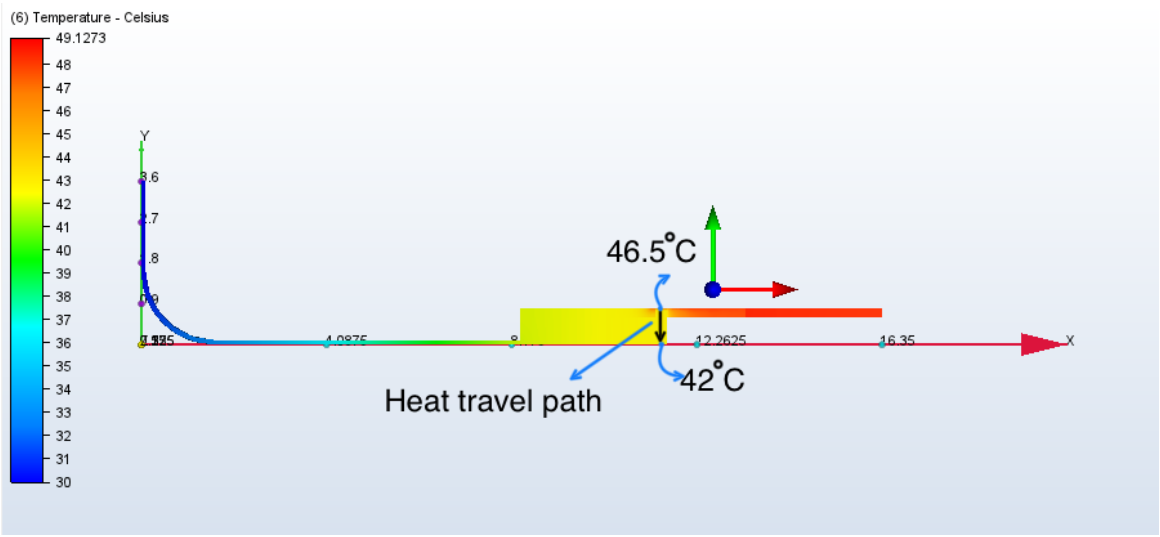

Figure 3.15: Thermal simulation results from CFD results for a copper cold plate, illustrating temperature generated at the periphery and its variation along the copper block.

3.2.3 Model 3

Model 3 is shown in Fig. 3.16 offers another solution by adding few solutions as follows:

- A metal core PCB is incorporated into the design. This PCB has a copper core, creating a two-layered structure where FR4 makes up the first layer and copper forms the second. The PCB itself has a thickness of 1.6 mm, with 0.3 mm being the top FR4 layer, and 1.3 mm being the base copper layer. This copper core plays a key role in enhancing thermal handling, as copper's high conductivity ensures more efficient heat dissipation compared to standard FR4.

- We also widened the cold plate to cover the entire underside of the PCB, not just the area with the copper strip as we saw in previous models. This broad coverage allows for better heat transfer across the entire board.

- A wider thermal pad is placed between the cold plate and the PCB. As discussed previously as well, the thermal pad serves two purposes: it fills any gaps that could obstruct proper contact, and it creates a conductive thermal pathway between the PCB and the copper strip. This way, we were able to allow for more uniform heat transfer and mitigate localized overheating.

The PCB contains traces for carrying signal and power to and from the J1 connector on the board, which are essential for the system's functionality. The chips will be wire bonded to one side of the PCB, where the readout side exists. The proper positioning and fastening of the chips is required, as even slight misalignments could compromise the system's ability to record the path of an incoming electron with precision.

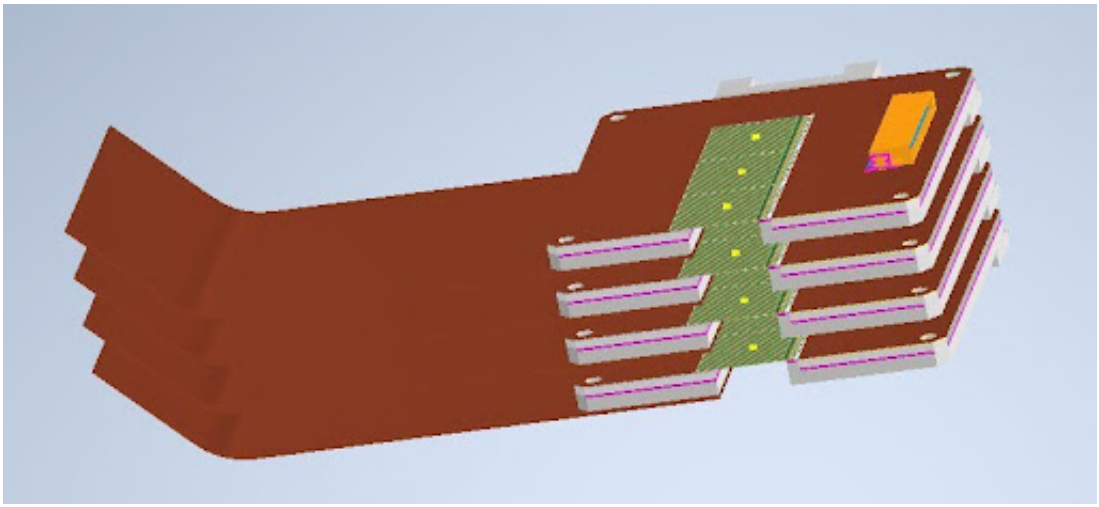

Figure 3.16: CAD of the Model 3 for the electron detetor

Based on the computational analysis shown through Figs. 3.17, 3.18, 3.19, we can observe a meaningful improvement in thermal performance compared to previous cases. The temperature has been reduced to 26.4°C, a notable achievement considering the previous model's thermal results. This reduction clearly indicates that the new heat conduction methods added to the system are working efficiently in properly channelizing the heat away from the detector components. In addition to adding a metal-core PCB, there is a boundary condition added to the end of the copper strip, which is setting the temperature there to be 10°C to make the thermal sink more efficient.

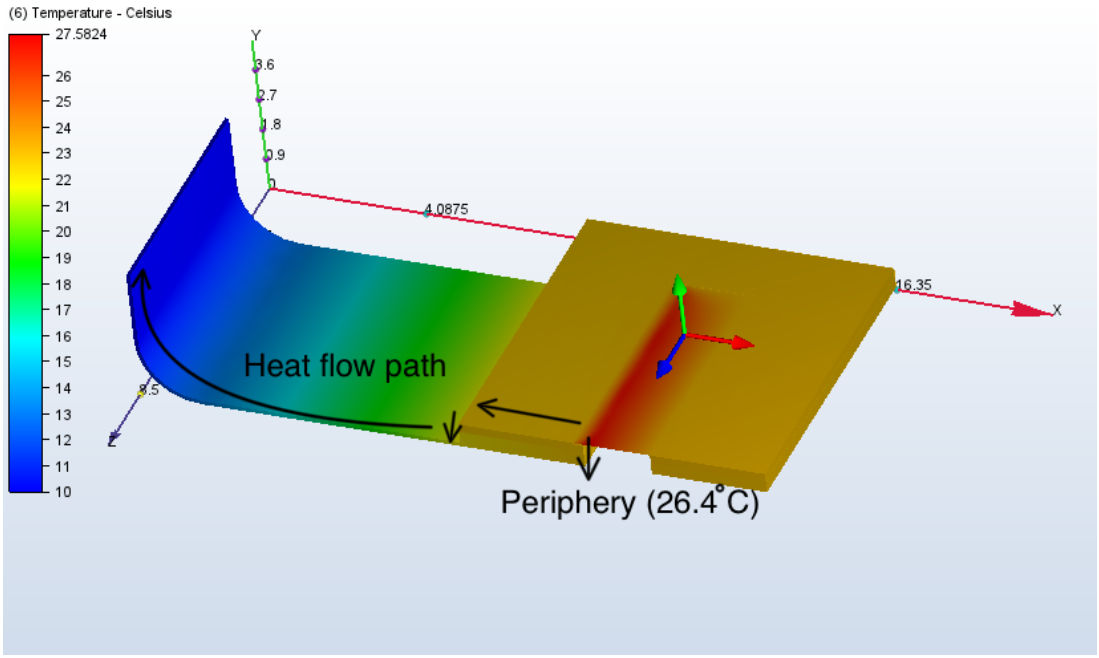

Figure 3.17: Thermal simulation results from CFD for a metal core PCB featuring the heat flow path and the periphery temperature.

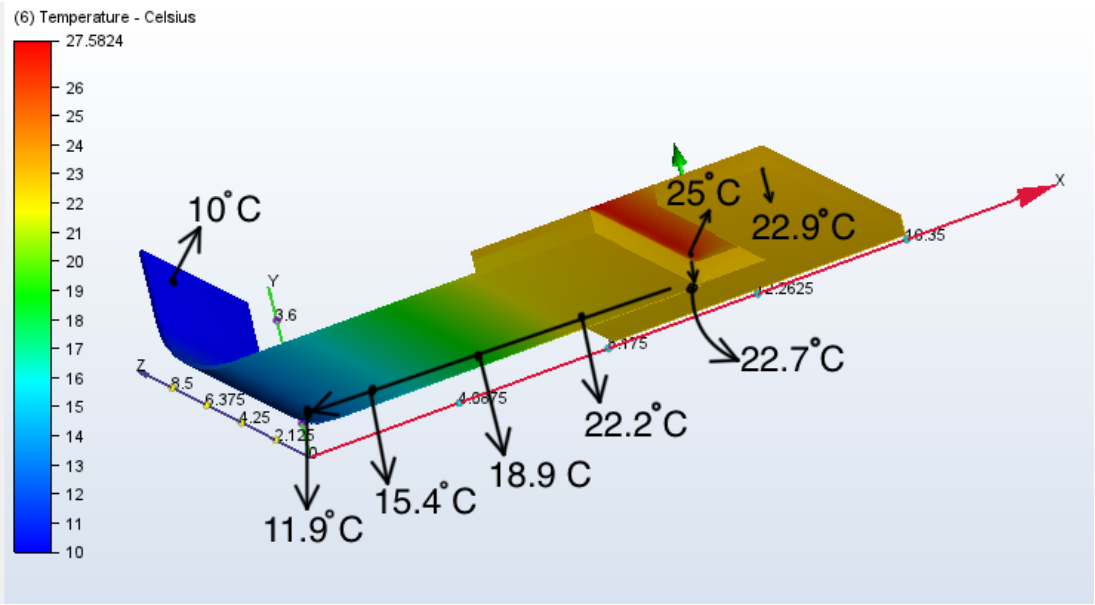

Figure 3.18: CFD's thermal simulation results for the metal core PCB, showing temperature values along various points in the heat flow path.

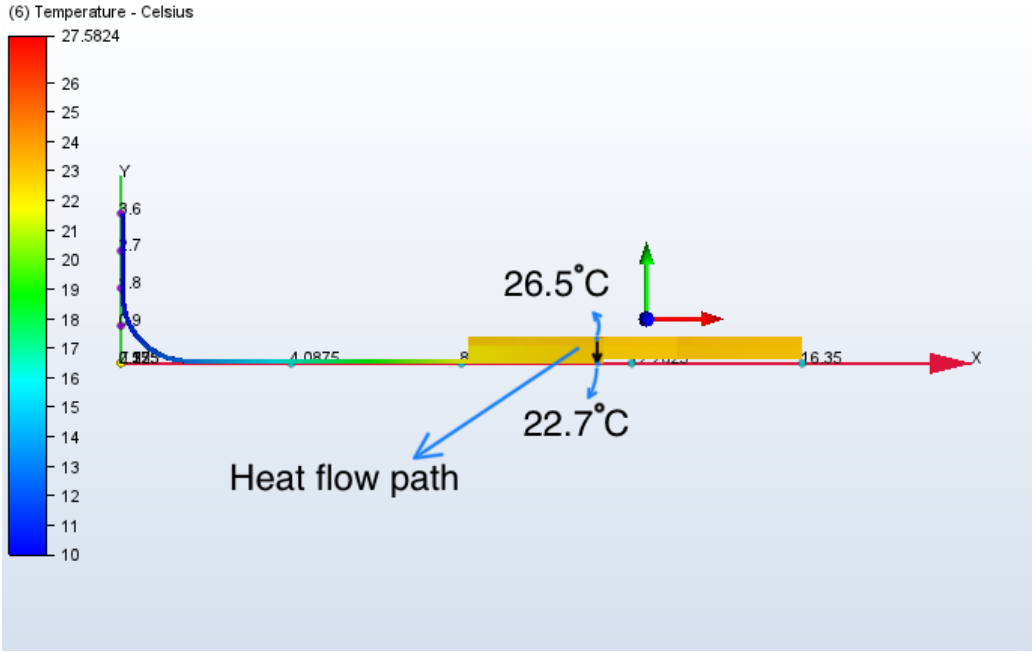

Figure 3.19: Thermal simulation results from CFD results for a metal core PCB, illustrating temperature generated at the periphery and its variation along the copper block.

This model has similar dimensions as model 2 has except the feature that cold plate and thermal pad are extended under the whole PCB. Hence, no new CAD diagram were generated for this model. However, Model 3 is not without its limitations. One of the most significant issues lies in the placement of the copper strips. The plane in which copper strips lie is perpendicular to the motion of the electron detector. As a result, while Model 3 offers some improvements,

it still faces practical challenges and provides a space for further refinements for effectively managing the heat generated at the chip periphery.

3.2.4 Model 4

Model 4 was designed to address and eliminate the limitations of Model 3.

- The copper strips, which you see in Fig. 3.16 have been strategically relocated to the top of the model, directly over the chip periphery where the most heat is generated (shown in Fig. 3.22). The copper strips that are proposed to be used are shown in Figs. 3.20 and 3.21.

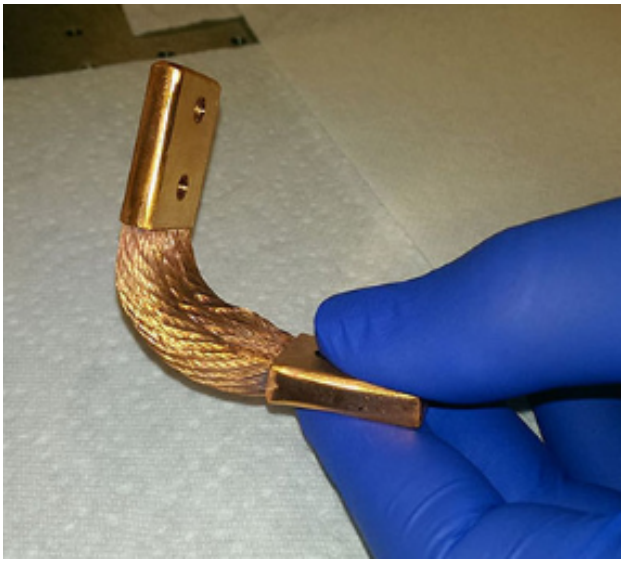

Figure 3.20: Flexible thermal copper strap [75]

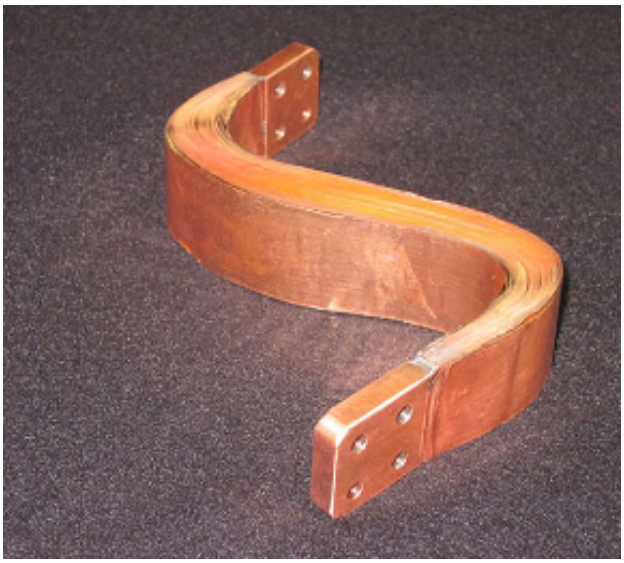

Figure 3.21: Flexible thermal copper strap [75]

- Model 4 also incorporates a cooling block at the top, significantly improving the conduction area.

The combination of the copper strips and the thermal block creates a more efficient thermal management system compared to the previous design. This modification ensures that the chips remain within an optimal temperature range, even under high-load conditions. The PCB plane features four corner holes as shown in Fig. 3.22 as a,b,c and d, which will be used to fasten the PCB with the cold plate.

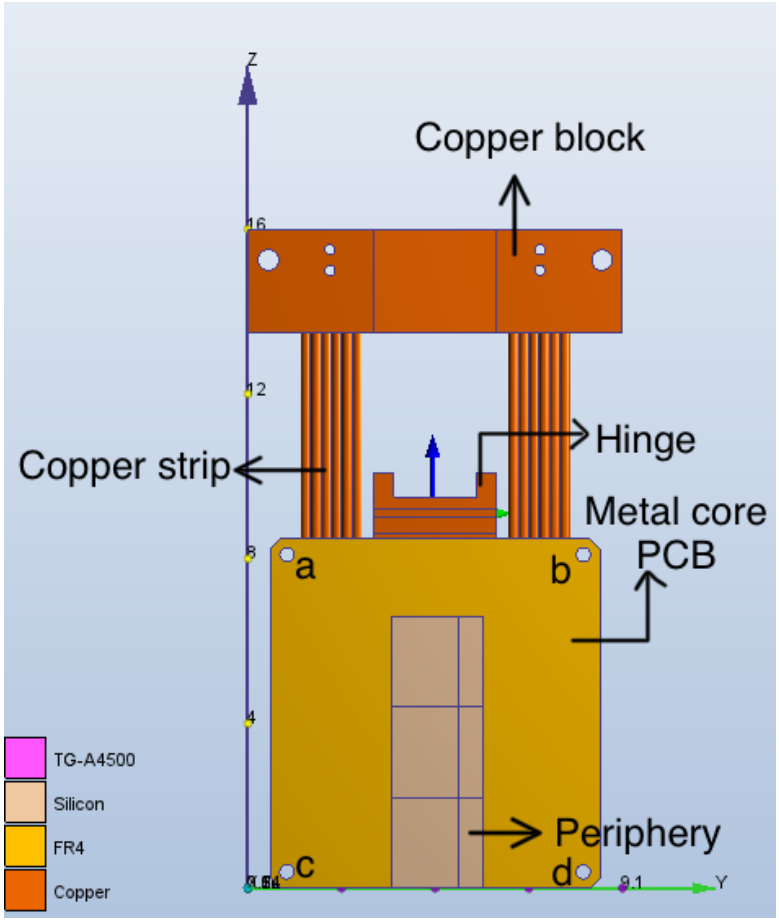

Figure 3.22: Front view of the Computational Aided Design (CAD) of the Model 4 for the electron detetor.

In terms of structural improvements, Model 4 includes a precise alignment mechanism for the detector planes. As shown in Fig. 3.23, the detector planes are secured in place with brackets attached to a hinge at the top of the assembly. This hinge is pivoted at one end, allowing the entire plane assembly to be tilted separately. This design enables the planes to be aligned perpendicular to the incoming beam inside the chamber, which is important for accurate data measurement. Maintaining this perpendicular alignment ensures the chips collect reliable data with less error. A side view and an angled view of the detector illustrated in Figs. 3.23 and 3.24 respectively shows the alignment mechanism of the four planes of the detector denoted as p1, p2, p3 and p4. All the planes should be equidistant from each other, in this case the distance between each plane is 12 mm. The enhanced conduction area provided by the cold

plate works alongside with the copper strips to maximize heat transfer, thereby improving the overall thermal performance of the system.

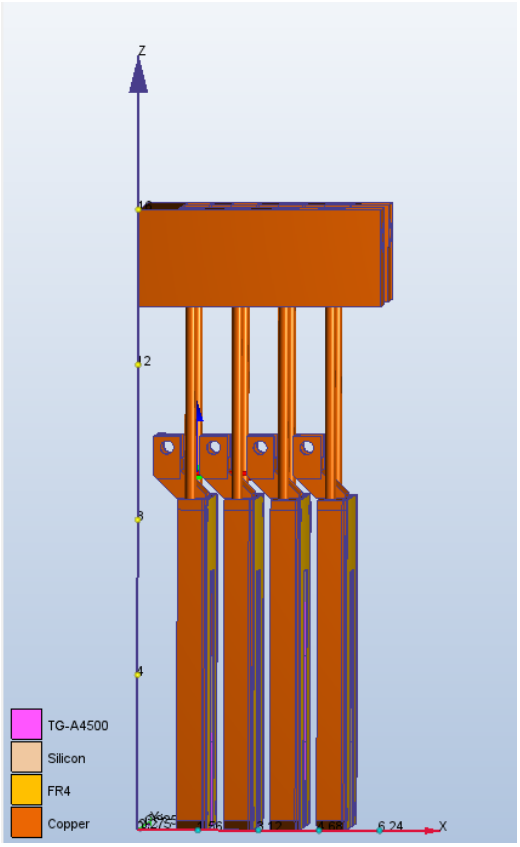

Figure 3.23: Side view of the CAD of the Model 4 for the electron detetor

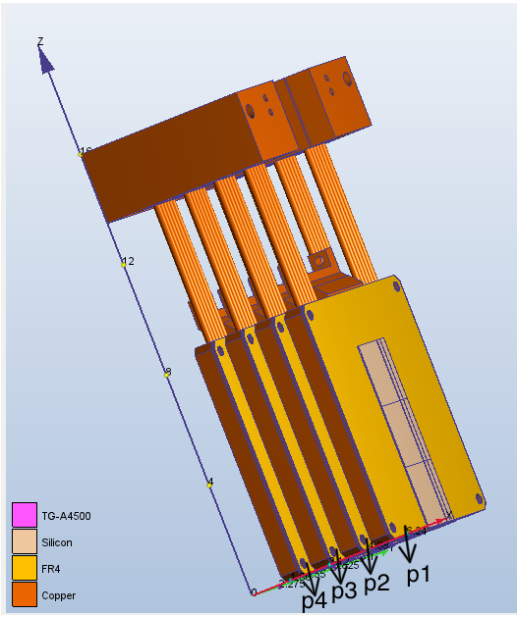

Figure 3.24: Angled view of the CAD of the Model 4 for the electron detetor

The CAD drawing model the model 4 is shown in Fig. 3.25

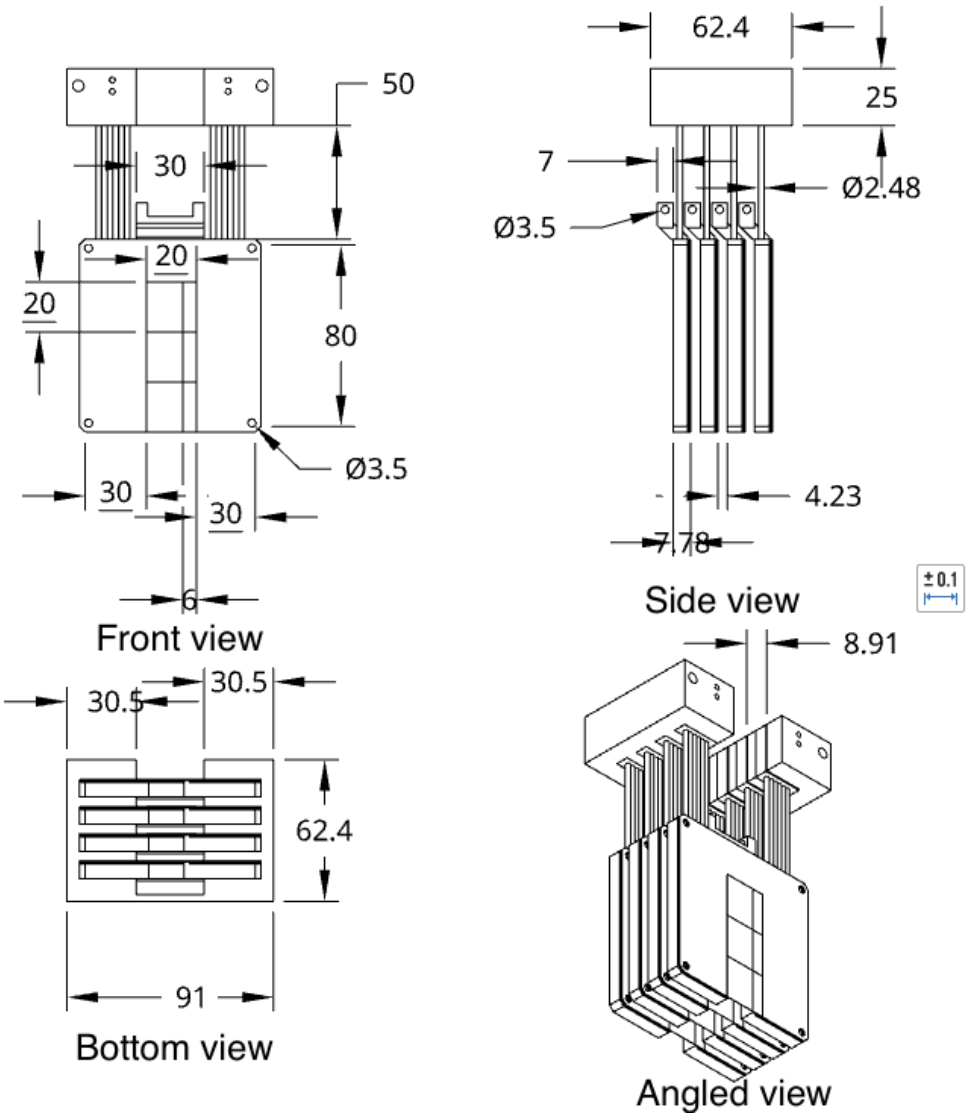

Figure 3.25: CAD drawing of Model 4 (units: mm)

The simulation results are shown in Fig. 3.26, which is acceptable for our requirements. The boundary conditions provided to the system are such as to provide total heat generation of 1 Watt at the periphery of each chip and the thermal block at the top is kept at 10^oC. The highest temperature at the periphery according to the computational simulations is recorded to be 24^oC. The temperature at various potential points in the simulation were recorded and are shown in Fig. 3.26. An angled view of the simulation with temperature variation along the depth of the cold plates on both the sides of the chips (periphery side and the side opposite to periphery) are shown in the Fig. 3.27.

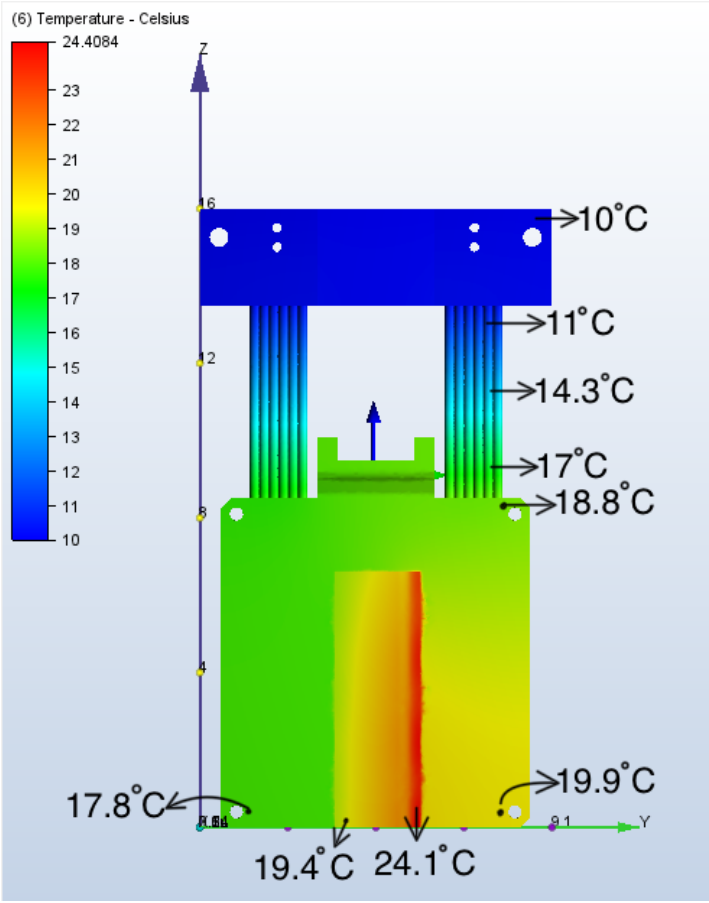

Figure 3.26: CFD results for model 4

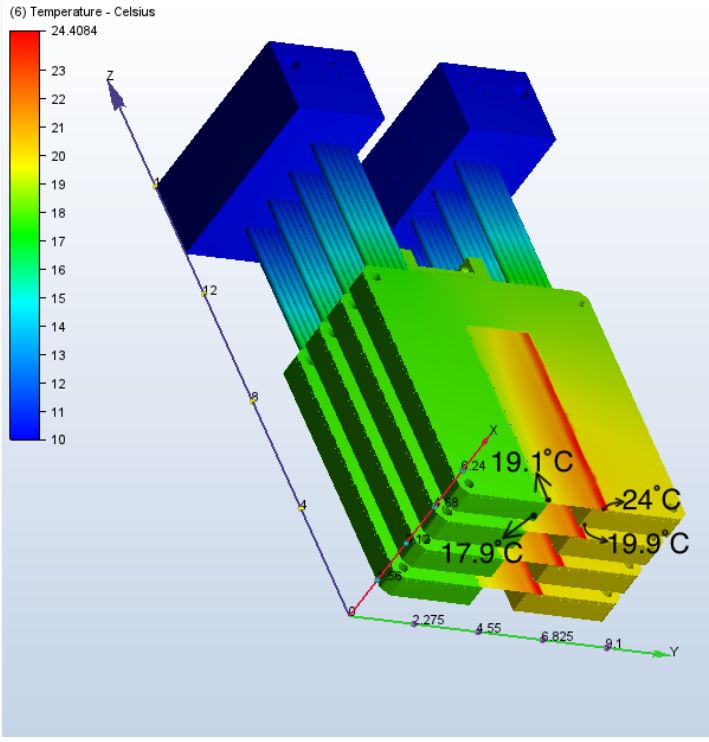

Figure 3.27: Angled view of CFD results for model 4

Model 4 requires updates from a manufacturing perspective. It is important to carefully assess whether this design is feasible for prototyping, considering both the practical and technical challenges that may arise during production. Resolving these practical concerns during prototyping is essential before moving forward with the final design. So, the design intent of the model 5 and model 6 will largely be built on the foundation set by model 4. By focusing on the challenges and strengths faced in model 4, we can ensure that the next models will improve the performance and streamline the manufacturing and installation process, making them more easy to integrate into the Compton polarimeter.
Given this assurance, we shifted our focus to Model 5. In Model 5, we planned to introduce a coolant system to improve heat dissipation. This combination of materials and cooling strategies is expected to provide superior thermal performance, ensuring that the chips remain well within the optimal temperature range.

3.2.5 Model 5

In Model 5, we further focused on enhancing the thermal management by introducing a dedicated coolant system to improve heat dissipation.

- This involved the addition of a coolant pipeline and a shaft at the top of the detector for the inward and outward flow of the chilled water. We chose stainless steel for the coolant pipeline shaft and included chilled water as the coolant. This combination was expected to effectively manage the heat generated by the system, making model 5 a strong candidate for meeting our thermal requirements. Chilled water was chosen as the coolant due to its easy availability. By integrating a coolant pipeline directly into the system, we anticipated considerable progress in heat dissipation compared to earlier models.

The stainless steel construction of the pipeline further supported this by offering durability and excellent heat conduction properties. The CAD model of Model 5 (shown in Figs. 3.28 and 3.29) detailed the design elements, including the coolant pipeline shaft and other key components.

However, despite these cooling benefits, Model 5 will face significant challenges from manufacturing and simulation point of view. The detailed nature of the design resulted in computational difficulties, which obstructed the ability to fully validate the model's thermal performance through simulation. The complexity of the design, particularly with its numerous small components like swagelok fittings and multiple connections within the detector, made it difficult to simulate accurately using Computational Fluid Dynamics (CFD) software. From a manufacturing standpoint, Model 5 also proved to be complex. The cooling block was designed to be vertically attached to the copper strips, and the cooling pipelines had to bend through the cooling block, adding more complexity to the assembly of the detector design. These components were constructed from different materials and small pieces, which required many fittings to ensure secure connection and proper alignment.

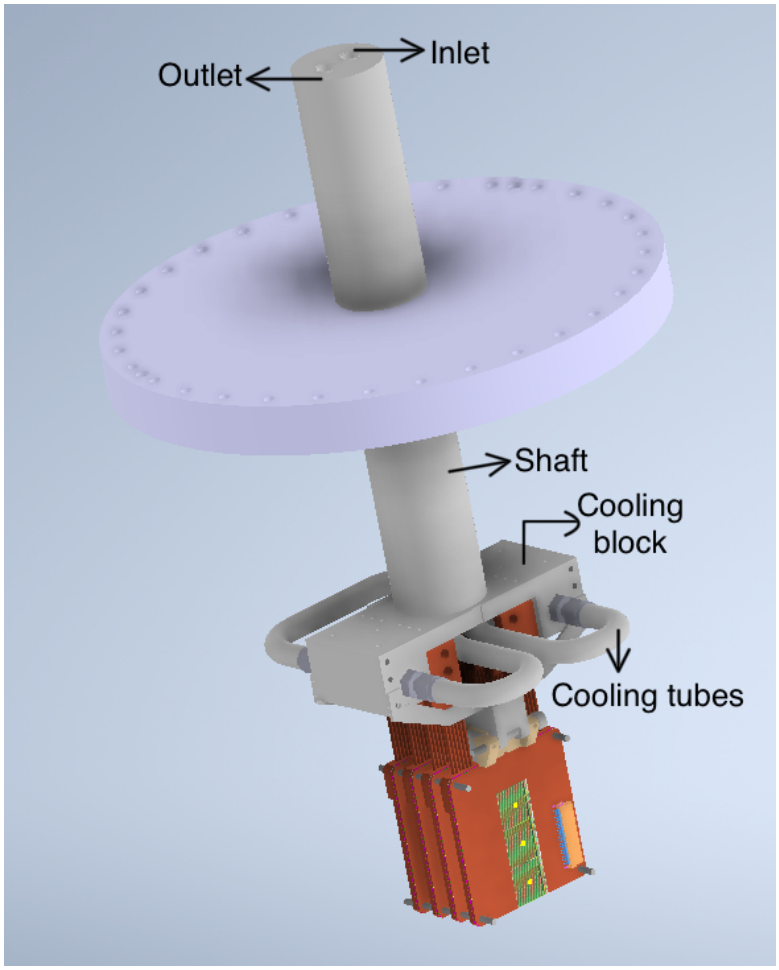

Figure 3.28: CAD model of Model 5.

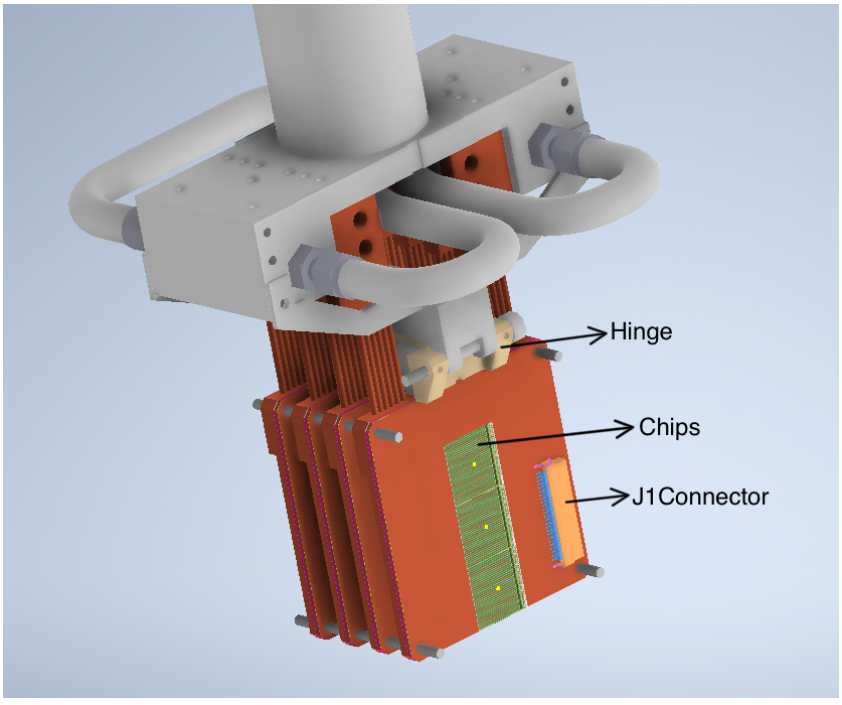

Figure 3.29: CAD model for Model 5 featuring detector planes.

The CAD drawing of model 5 is shown in Fig. 3.30. Ensuring the system was leak-free became a critical concern, as even a minor leak within the vacuum environment could compromise the functionality of the beamline. These were the concerns about the overall reliability of the system in real-world applications.

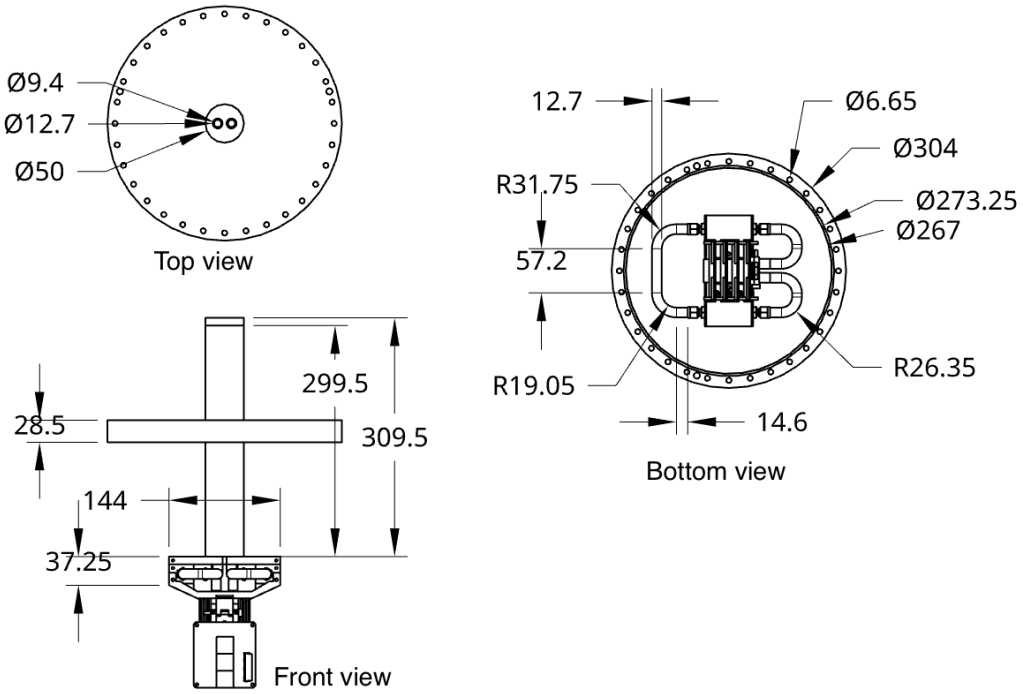

Figure 3.30: CAD drawing of Model 5 (units: mm)

This required rethinking to minimize the number of fittings, and to reduce the overall number of connections. These required the re-arrangement of the cooling block and coolant pipelines to create a more straightforward and efficient design. By reducing the number of individual components and opting for more uniform materials, we aimed to improve the reliability of the system. Our ultimate goal was to create a model that could be easily produced and maintained, ensuring that it would perform effectively in the vacuum environment without compromising the integrity of the beamline. These requirements led to the development of Model 6, which addressed the complexities of model 5. The CAD model of Model 6 reflects these changes, showing a more simpler and efficient system that meets the thermal management requirements without compromising the integrity of Compton polarimeter and the beamline.

3.2.6 Model 6

Model 6 underwent a comprehensive redesign, focusing primarily on the copper cold plates. As the copper strips were slightly flimsy (the one that we were planning to use are shown in Figs. 3.20, 3.21), we had concerns about their ability to support the four vertical detector planes upside down, so we transitioned from using separate, threaded copper strips to a more

robust continuous copper design. This change led us in redesigning the whole cold plate. We eliminated the threaded copper strips and integrated them into a solid copper material, merging them with the cold plates. This change in the design not only simplified the construction but also improved the overall integrity of the cooling system. Model 6 can be seen in Fig. 3.31.

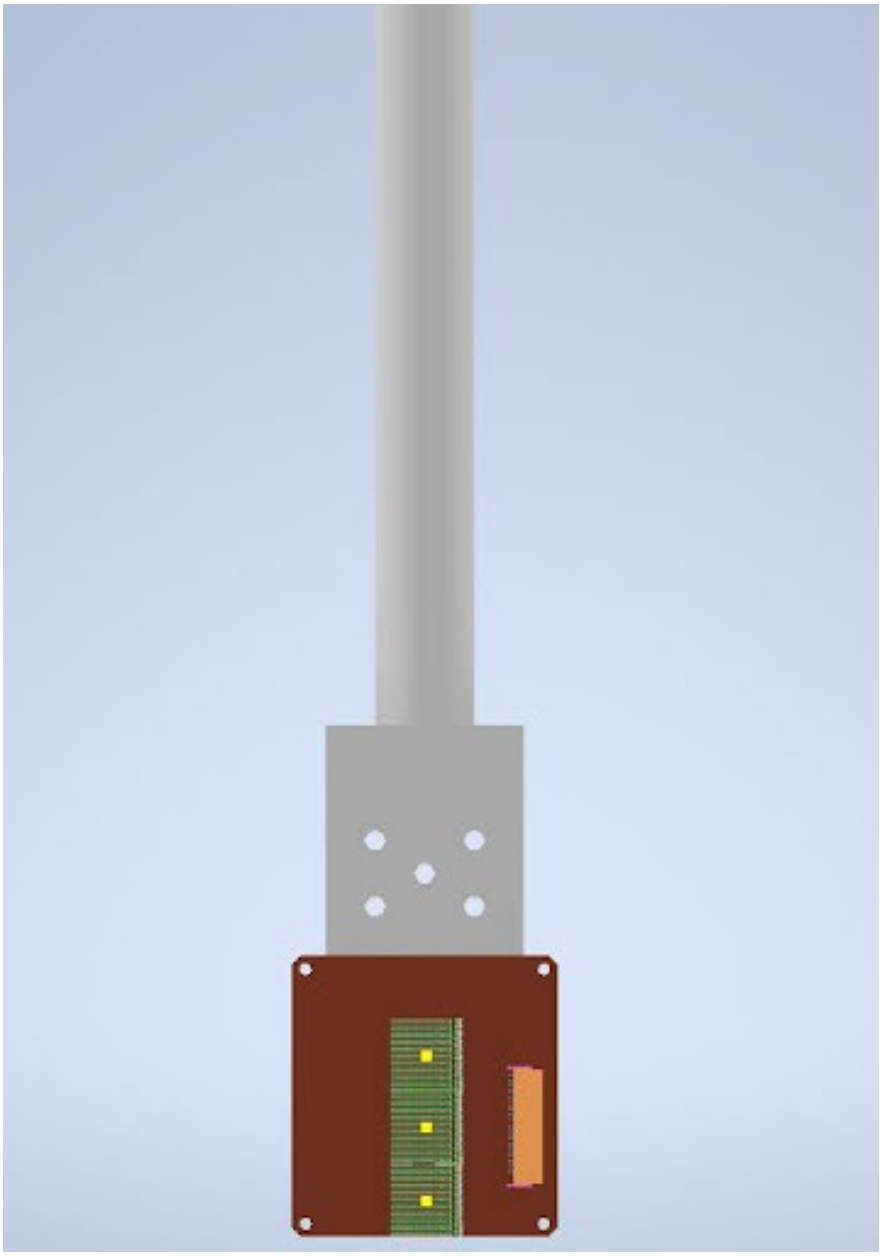

Figure 3.31: Front view of the CAD model for Model 6

This new design includes two cold plates within the detector system, which are strategically sandwiched between two planes of the detector, as illustrated in Fig. 3.32. This reconfiguration not only enhances stability but also allows us to reposition the J1 connectors, making the system more practical. Additionally, the cooling block was redesigned to sandwich between the two cold plates, as shown in Fig. 3.32. A shaft was directly introduced for facilitate the inlet and outlet flow of chilled water, facilitating efficient heat transfer. To further enhance

heat dissipation, a pocket was incorporated into the cooling block to increase the contact area between the coolant and the cooling blocks. The larger contact area allows for better heat dissipation, ensuring that the chips remain at a stable temperature during operation.

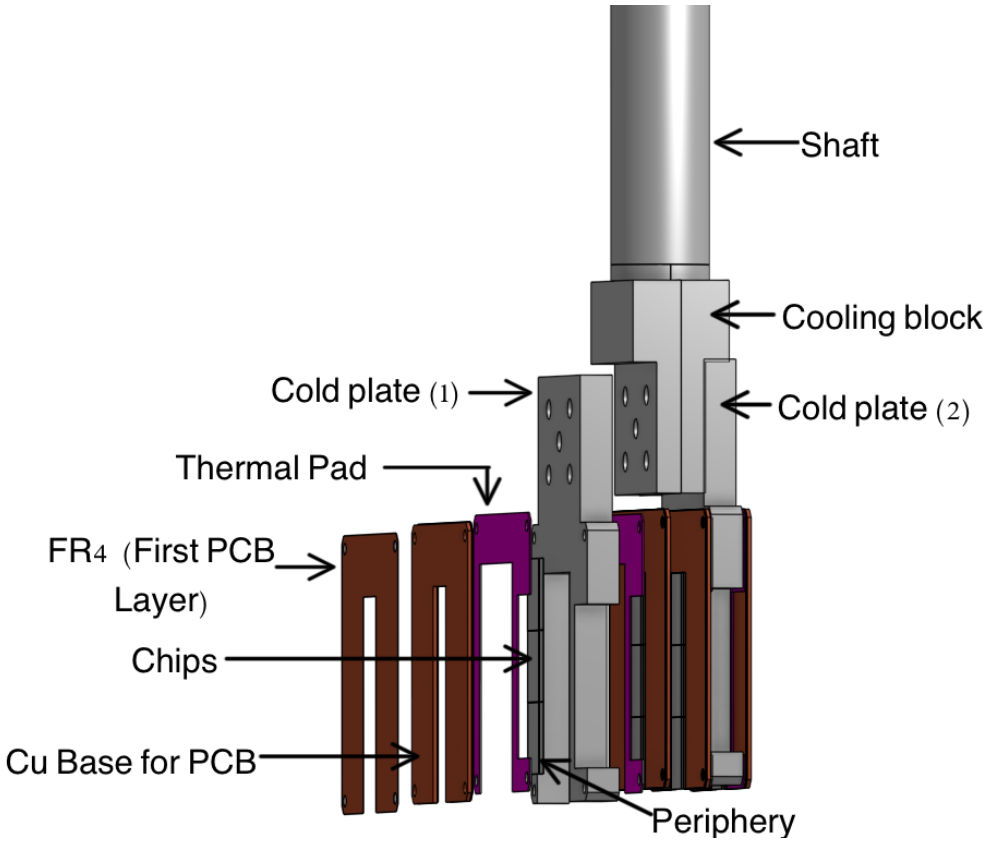

Figure 3.32: Side view of CAD model for Model 6

The image shown in fig. 3.33 illustrates the water flow within the shaft in the CFD software. In the previous version of the test of cooling of the HV-MAPS as the electron detector (detailed in this [66]), liquid nitrogen was used as the coolant. Whereas, due to some operational challenges, we reconsidered using it. Liquid nitrogen boils at very less temperatures, it rapidly evaporates, releasing large volumes of nitrogen gas. In a vacuum system, this rapid evaporation can lead to dangerous pressure build-ups if not properly vented. Such pressure can damage system components or, in extreme cases, cause the system to rupture, leading to hazardous situations. This alone made liquid nitrogen less ideal for our setup. Furthermore, the evaporation process can displace oxygen in enclosed spaces as it is heavier than oxygen, increasing the risk of asphyxiation for personnel where individuals may lose consciousness or suffocate without warning. These safety concerns made liquid nitrogen hazardous for regular use. Moreover, since nitrogen gas is colorless, odorless, its accumulation can go unnoticed in enclosed or poorly ventilated spaces. Also, the infrastructure for storing and transporting liquid nitrogen is expensive and requires trained personnel for safe operation. Considering these risks, we propose replacing liquid nitrogen with chilled water as a coolant for various reasons— Chilled water offers a safer and cheaper option, ensuring compatibility with the vacuum environment and

maintaining system integrity during operation. Water does not evaporate as rapidly, so it does not cause dangerous pressure build-ups like liquid nitrogen. Unlike nitrogen gas, water does not displace oxygen, ensuring safe working conditions. So, in the present study and testing, chilled water serves as a coolant, efficiently drawing heat away from the cooling block. This continuous flow of chilled water ensures that hot water is constantly replaced, facilitating heat transfer from the chips to the coolant. The heat flows naturally from areas of higher temperature to lower temperature gradients, allowing for effective heat exchange from the cooling block to the chilled water. This process optimizes thermal management, maintaining the chips at a stable temperature for optimal performance.

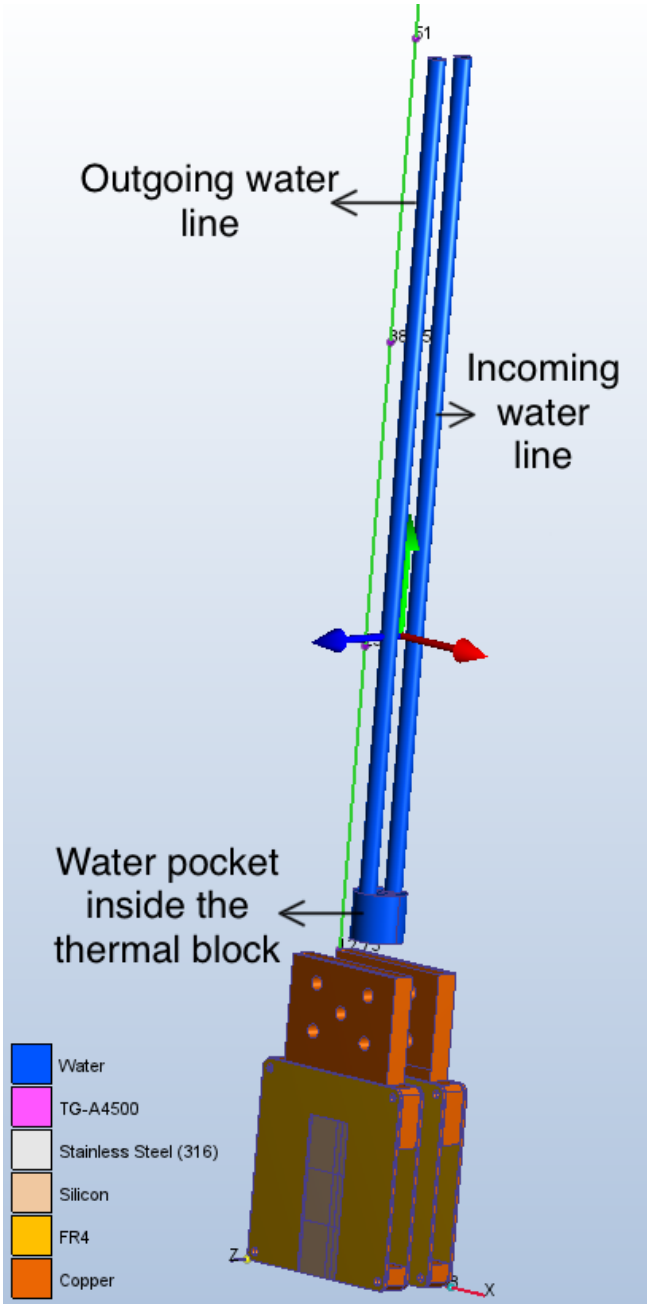

Figure 3.33: Illustration of water flowing through the shaft, depicted in blue, highlights the internal cooling mechanism

The CAD drawing showing the dimensions for Model 6 is shown in fig. 3.34

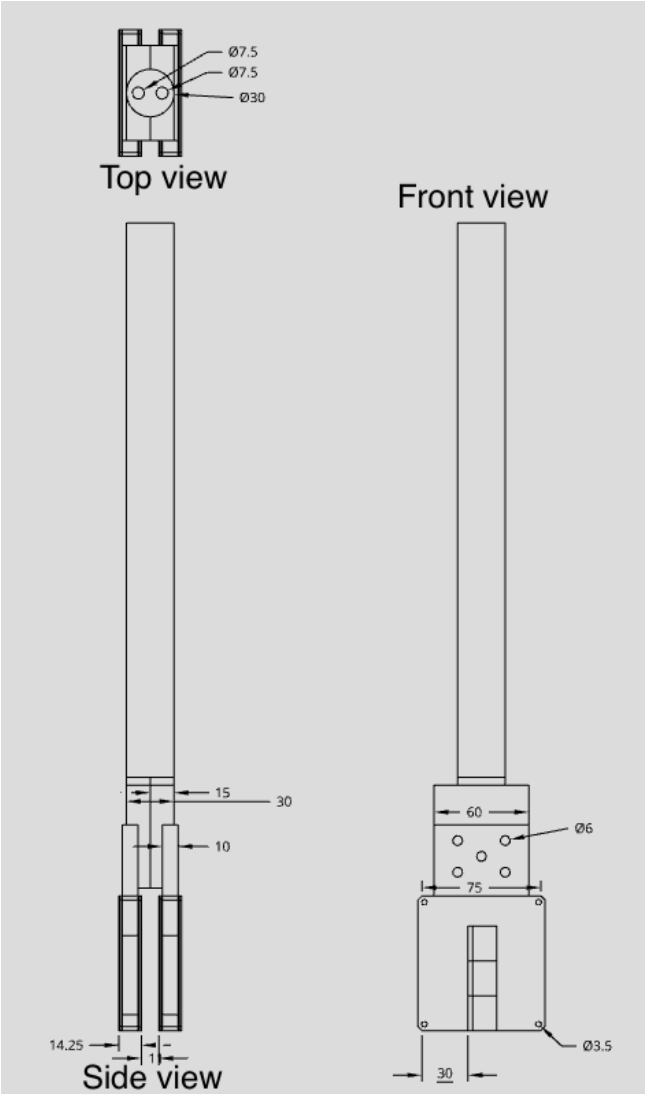

Figure 3.34: CAD drawing of Model 6 (units: mm)

The results of the CFD analysis are depicted in Fig. 3.35 with its front face, and the temperature variation is shown along the depth of the cooling block in Fig. 3.36, where the maximum recorded temperature was 28.3^{o}C. This result is favorable for the detector's operation within a vacuum environment, as the HV-MAPS detectors can perform as designed at these temperatures. The water at the inlet is introduced at 4°C with an initial volumetric flow of 12 l/min. The outlet pressure is maintained at zero, while each chip periphery generates a thermal output of 1 W. Maintaining the detector within this temperature range ensures reliable electron detection and contributes to accurate measurements of electron polarization. In summary, the redesign of Model 6 significantly improved both the thermal and structural features of the system. The new continuous copper cooling block, combined with the efficient coolant flow, provide a stable, effective solution for managing the heat generated within the detector.

These changes make Model 6 a strong candidate for successful integration into the Compton Polarimeter.

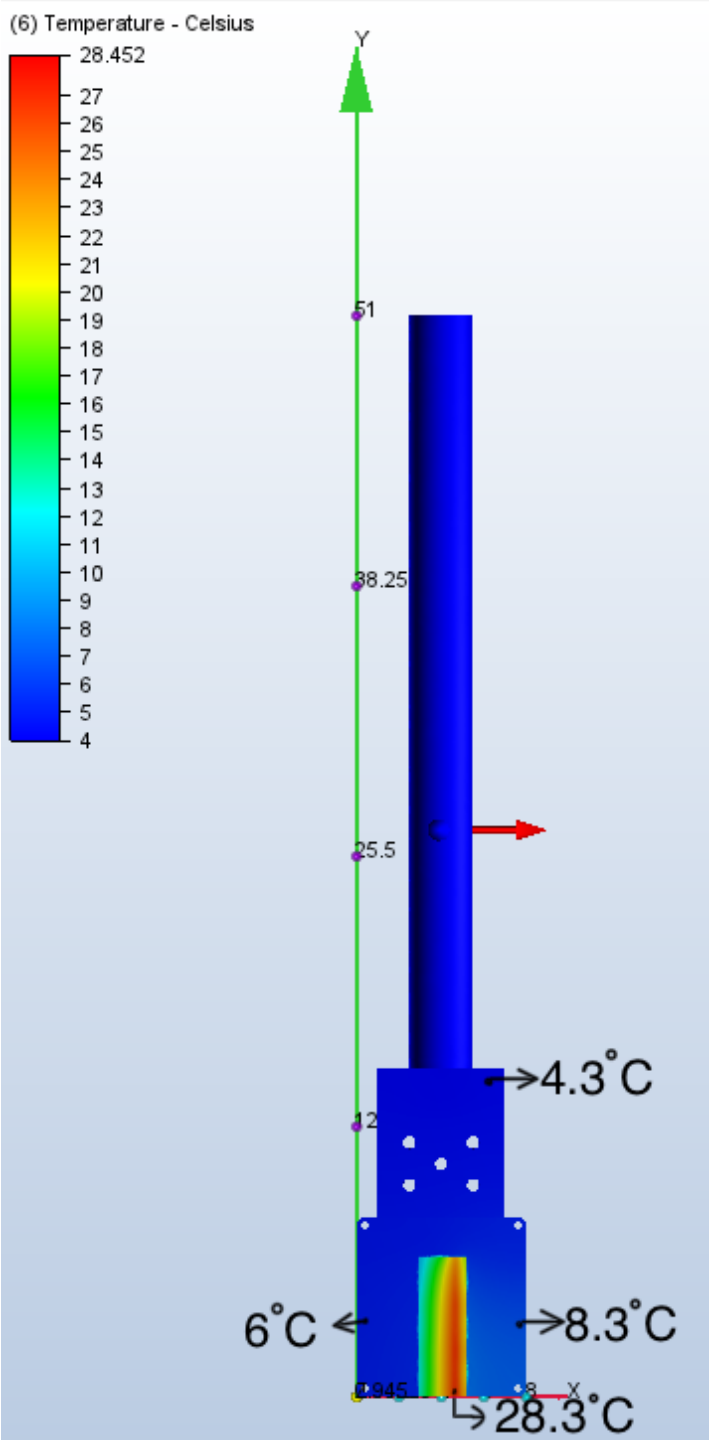

Figure 3.35: CFD simulation for Model 6 featuring front view showing various potential temperature regions.

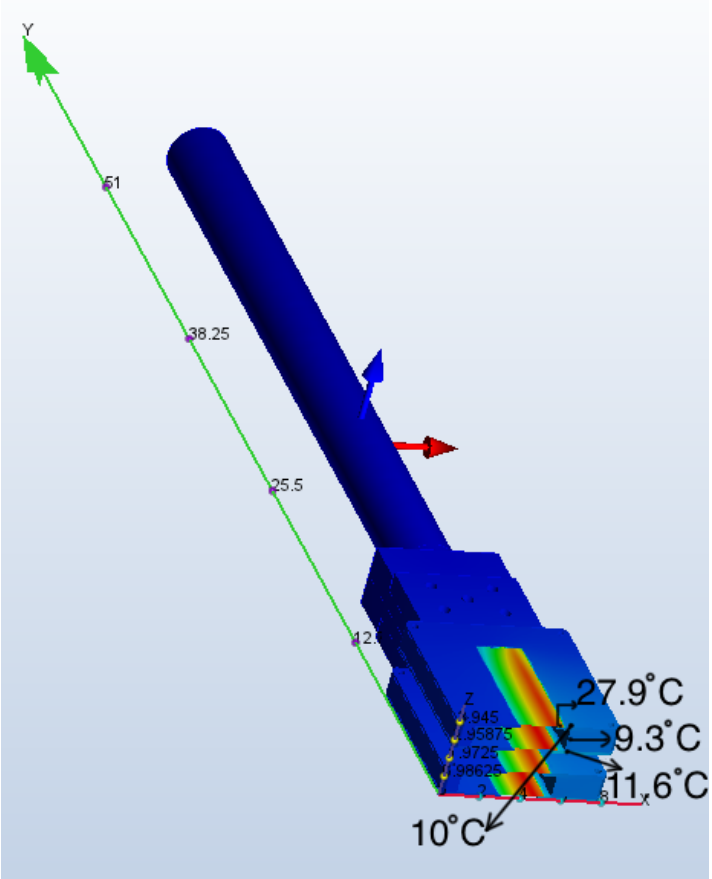

Figure 3.36: Temperature variation for Model 6 along the depth of the cold plates.

3.3 Adapting Model 6 for final prototyping

All the models discussed above played an important role in deciding the most effective design for our application. After assessing each model's performance in detail, we were able to highlight the strengths and weaknesses of each approach. The summary of temperatures at the periphery of each model is shown in Table 3.1

CFD modeling provides thorough understanding of heat transfer across the entire setup. By carefully specifying materials and setting up boundary conditions at each point of contact between surfaces, the simulation closely replicates the system's real behaviour. All the boundary conditions and the material properties are detailed in the previously outlined results. The heat source originates from the 12 HV-MAPS chips (Mupix 11). The heat reduction technique combines conduction and convection methods, leading to a temperature gradient between the HV-MAPS chips, the thermal block, and the water-cooled shaft. This gradient effectively channels the heat generated at each chip away from the system. The outcomes of each CFD simulation have been previously reviewed, showing that, the temperature decreases as distance

Table 3.1: Comparison of the temperature at periphery for different models.

Electron detector's models	Temperature at the periphery
Model 1	58.3°C
Model 2 (Aluminum as cold plate)	47.5°C
Model 2 (Copper as cold plate)	45.9°C
Model 3	26.4°C
Model 4	24.1°C
Model 5	N/A – complex model structure
Model 6	28.3°C

from the chips increases. This results in a steady-state condition where temperature variation is minimal across components. In each CFD simulations, the average PCB temperature is presented. Observations indicate a continuous reduction in temperature as the model transitions from Model 1 to Model 6, signaling favorable thermal management and validating Model 6 as the optimal choice. Model 6 incorporates a water line with a coolant introduced at 4°C, achievable through Low-Conductivity Water (LCW) systems. This design helps maintain HV-MAPS chip temperatures well below 70°C, ensuring safe operation. So the simulation outcomes from Model 1 through Model 6 shows that the Model 6 is the most viable option for maintaining the HV-MAPS within the targeted temperature range, even under vacuum conditions required for the compton polarimeter. This satisfactory simulation results with Model 6 gave us the confidence to proceed with the development of a physical prototype based on its design.

Model 6 not only achieves the desired result, but also proves to be the simplest model from the manufacturing point of view. With most of its components being continuous, it significantly reduces the need for multiple connections, which in turn minimizes the risk of leaks and multiple surface impedence issues that can arise from fastening various small multiple components (as we saw in model 5) or joining two surfaces together. From a prototyping point of view, which we will test in a local lab before the final implementation (discussed in Chapter4), a few parts required machining to replicate the model's design. The prototyping is extensively discussed in the next Chapter 4. This prototype would embody the design principles and features tested in the simulation, aiming to replicate the efficient heat dissipation and thermal management observed in the virtual environment. With the simulation results obtained from this model validating our approach.

In the next chapter, we will be presenting the results from the physical prototype tested in a local lab at the department of Physics and Astronomy at the University of Manitoba. Based on the practical outcomes and feedback, we will further refine the design to ensure it performs optimally in real-world conditions.

3.4 Calculation of Energy deposited by Beam Halo on the Electron Detector

In the models discussed above, we have accounted only for the heat generated by the HV-MAPS chips, trying to replicate that heat generation in the CFD analysis. However, an additional heat source can arise from the Halo of the main beam line. So, before moving to the construction and testing, it is essential to investigate whether any heat or power is deposited on any part of the detector via the halo of the main beam line.

A beam halo consists of a collection of particles that surround a particle beam line and deviate from the core of the main particle beam. These particles wander off the path from the tightly focused, high-intensity central beam, creating a less concentrated "halo" around it. The existence of halo is an important characteristic of high-intensity beams. It can also be defined as the beam losses associated with a small fraction of particles encircling a dense beam core. These halo particles can arise as a result of various factors, including imperfect focusing, various scattering, and interactions with the residual gas in the accelerator. In high-energy physics experiments, the beam halo can interact with the surrounding components, leading to undesirable effects like signal noise, heat deposition and radiation damage. Effectively managing the beam halo is important for maintaining the experiment's accuracy and to safeguard the sensitive equipment from damage. In our case, we have an electron beam with 100 μm beam current and 11 GeV beam energy coming straight from the CEBAF facility of the Thomas Jefferson National Accelerator Laboratory as descderibed in the Sec. 2.1. This electron beam has a halo around it. Let us consider for the initial case that energy is deposited by all halo particles. Some part of the incident electrons can interact with the cooling/copper block, potentially causing extra heating of the lower edge of the electron detector.

Assuming the Beam Current to be 100μ A and charge $= 1.6 \times 10^{-19}$,

$$\begin{gathered} \text{Current(I)} = \frac{\text{Charge(q)}}{\text{time(t)}}\,, \\ t = 1.6 \times 10^{-15} s. \end{gathered} \tag{3.16}$$

Next, we calculate the rate of electrons:

$$\text{Rate of electrons} \quad = \frac{1}{1.6 \times 10^{-15} s} = 0.625 \times 10^{10} s^{-1}. \tag{3.17}$$

$$\text{Power} = \frac{\text{Energy(E)}}{\text{time(t)}} = \frac{11GeV}{1.6 \times 10^{-15}s} = \frac{17.622 \times 10^{-10}J}{1.6 \times 10^{-15}s}. \tag{3.18}$$

Power deposited by single electron as it passes through the cold plate assuming all the energy is deposited is 11.014×10^5 watt, and the power deposited by all halo particles (10^{-5}) when passes through the cold plate assuming all the energy is deposited is 11.014 watt. In next case, we consider the energy deposited due to Bremsstrahlung Radiation. The energy loss due to this process can be estimated using the radiation length.

Energy due to bremsstrahlung is [76],

$$-\langle\frac{dE}{dx}\rangle = \frac{E}{X_0}$$

Characteristic Radiation Length = $X_0 = 12.86 g/cm^2$ [77]

$$X = \frac{X_0}{\rho_{(Cu)}} = \frac{12.86 g/cm^2}{8.96 g/cm^3} = 1.43 cm$$

Let a = 2 cm (consider two planes) is the thickness of the copper block and E is the final energy ([76]) of electron after interacting with the copper block.

$$E = E_0.e^{\frac{-a}{X}}$$

$$E = (17.622 * 10^{-10}).e^{-1.39}$$

$$E = 4.2293 * 10^{-10} J$$

Energy deposited by all the Halo electrons (10^{-5}) = $E = 4.2293 * 10^{-5}J$

Percentage of energy taken away by the electrons = $(\frac{E}{E_0}) \times 100 = 24\%$

Percentage of energy left behind/deposited by electrons = 76%

The first approximation was 100% energy is deposited on the copper block with power of 11.014 W. The next approximation is, 76% of energy is deposited with power = 76% of 8.37 = 3.85 W. Now, assuming that 46% of the energy is deposited on the first plane, such thta the power associated with that would be = 46% of 8.37 = 3.304 watt. And, if we assume that 30%

of the energy is deposited on the second plane, power associated with that would be = 30% of 11.014 = 3.304 watt. These energy values are relevant and can deposit a significant amount of energy.

Now, our next task is to find the energy deposited upon the cooling/copper block via Bremsstrahlung Radiation. We need to figure out whether all of this energy is lost via Bremsstrahlung gets deposited on the Copper block or not. Assuming all of the halo is in band, but our detector is located at only one position of the band. So, we are not going to see a 100% energy of all the band around the beam but just the energy of the part of halo which overlaps with our detector, so we have to calculate what fraction or amount of that energy is. The Fig. 3.37 shows one plane of the electron detector, let us say this is the front plane. We can see in the figure that this electron detector is placed between two dipole magnets D_3 and D_4 (also explained in Sec. 2.2.3). The pink line shows the scattered electron beam and red line shows the main electron beam. There is a circular halo description around the main electron beam, which might interact with some part of this detector.

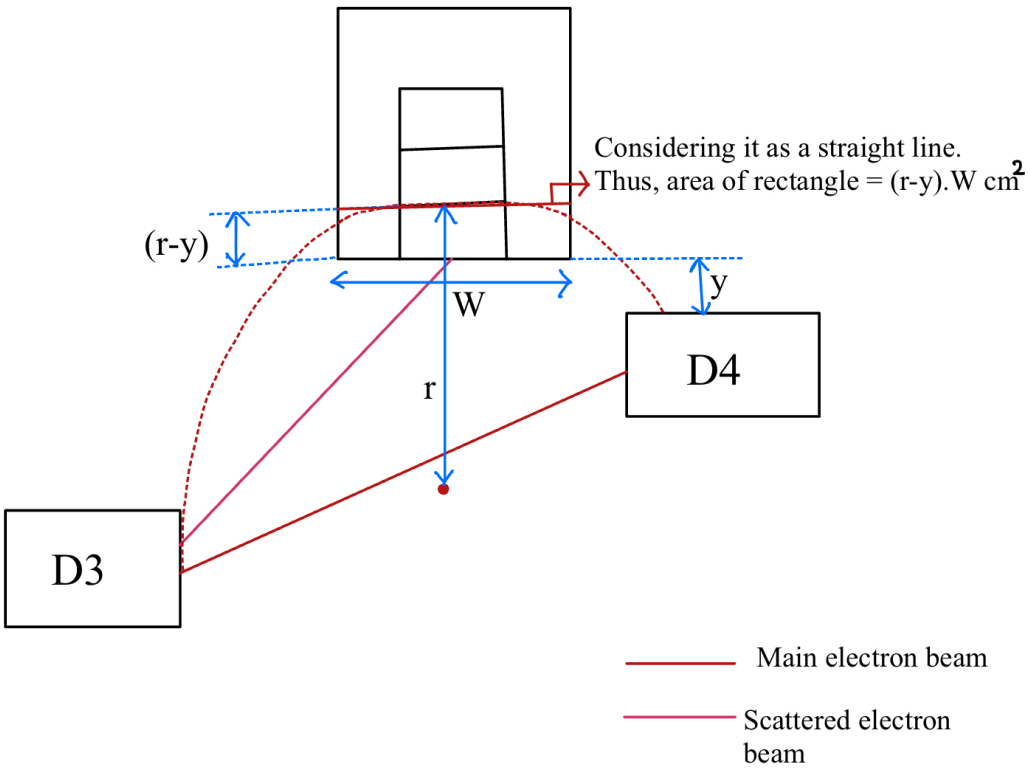

Figure 3.37: Electron beam halo interacting with the detector

The Dimensions of the cold plate are: l (length), w (width), t (thickness). Also, let us consider the vertical distance between the D4 and the electron detector = y cm.(shown in fig. 3.37). The area of the beam halo = p $cm^2 = \pi r^2 - \pi {r_0}^2$, where r is the radius of the beam halo from

the centre of the core of the beam and r_0 is the radius of the core of the beam. The transverse length of the beam halo interacting with the cold plate = (r-y) cm.

Assuming the beam halo is uniform, it would have same particle distribution per unit area. Consider the halo incident on the copper block forms a rectangular shape. Such that,
The area of the halo incident on the copper block = Transverse length of beam halo interacting with the copper block*width of the electron detector = ((r-y)$\times w$)cm^2 = z cm^2

Now, the number of halo particles interacting with the copper block = $10^{-5} * \frac{z}{p}$

So that, the final energy of the beam halo = $E' = E_0'.e^{\frac{a}{X}} = (10^{-5} * \frac{z}{p}).E_0.e^{-1.39}$

There are some unknowns in the above equation, like r (radius of halo), r_0 (radius of the core of the beam), y (vertical distance from the upper edge of the dipole magnet D_4 till the lower edge of the detector) and w (width of the detector).By putting exact values of these, we can find the energy deposited by the part of the halo which is overlapping with our detector.

Upon, further investigation we found that the radius of the halo = 0.75 in = 1.9 cm, and the distance between main beamline and the lower edge of the electron detector 3.75 cm, which is larger than the radius of the halo, so we concluded that the beam halo would not even interact with the cold plate, meaning there would not be any energy deposited on the cold plate of our detector via halo. However, this calculation remains valid should there be any changes in any of the aforementioned parameters or for similar purposes.

Chapter 4

Assembly and Testing of HV-MAPS Electron Detector in a local laboratory

In the preceding chapter, we investigated the iterative design process and the cooling of the electron detector model for the Compton polarimeter, focusing on the computational analysis (CFD) and its role in optimizing the thermal performance of the detector. Now, in this chapter, we shift from the theoretical and computational domain to the practical aspects, presenting the results from a local lab-based testing of the prototype and cooling of the electron detector. These results are important as it serves as a bridge between computational predictions and real-world outcomes.

The key aim of this chapter is to compare the experimental data with the results obtained from our CFD simulations, examining how closely the two agree. This comparison is crucial, as if our experimental results match the CFD predictions, it would validate the use of CFD as a predictive tool for testing the thermal behavior of this and the future electron detector models. Such validation would not only enhance the efficiency of future detector design but also reduce the need for extensive and potentially costly physical testing, as CFD simulations could serve as a reliable predictor.

Equally important is the necessity to accurately replicate the experimental setup and surrounding conditions within the CFD environment to achieve results that closely match the expected outcomes. By providing all the experimental settings—such as vacuum chamber conditions or ambient temperature, heat loads and cooling mechanism as close as possible to the real parameters, we can correctly predict the thermal behavior of the electron detector. This analysis will be significant for improving the design of future electron detectors and to practice the actual tests under the safety considerations (for example, avoiding high temperature inside the vacuum in our case). Moreover, having a dependable reference point between the simulation and experimental results will allow us to fine-tune future models, creating more efficient designs.

To achieve these goals, the prototyping process in the lab demands machining and assembling the prototype, which involves working with multiple components. This chapter focuses into step-by-step explanation of the test, with each section showing developments as the chapter progresses— like prototyping process, planning and executing the processes involved in assembling, initial and final testing. The initial tests were carried out at room temperature to set an initial measure and to see if each electrical connection and detector setup is working properly before moving on to more complex tests within the vacuum chamber. Testing the detector in a vacuum environment (nearly 10^{-6} Torr) is essential, as it closely resembles the actual operational conditions of the Compton polarimeter during the MOLLER experiment. These tests are performed under the supervision of Dr. Mohammad Laheji (a postdoctoral fellow, University of Manitoba) [78]. These results are significant for determining whether the detector can function safely under the likely situations.

4.1 Components required for prototyping and testing

Several key components were required to Create a prototype of the electron detector. Each component of the detector is essential, and their details are outlined below:

4.1.1 PCB

Printed circuit board is a key part within the detector system, serving as the main support structure for HV-MAPS and a platform for connecting and interfacing multiple components essential for data collection. It features multiple electrically conductive traces that provide routes for signals to flow across different components. Shown in the Fig. 4.1, the PCB design illustrates the strategic placement of three HV-MAPS chips, which are securely placed over specific locations to optimize signal transmission. The Fig. 4.1 features a J1 connector, which acts as the primary interface for data readout, streamline data acquisition and signal output, which are important for the accurate functioning of the detector. As previously mentioned, this PCB is designed as a two-layered structure: the top layer, consisting of 0.3 mm of FR4, chosen for its insulating and durable properties, while the base layer, made of 1.3 mm of copper, improves thermal conductivity shown in the CAD drawing 4.3. Fig. 4.2 highlights the design of electrical traces.

The surface on which the chips are supposed to be attached must be flat to ensure stability. If the surface is not flat, a generous amount of adhesive is necessary to secure the chips. Ideally, there should be a consistent layer of adhesive under the bond pads on each chip that minimizes the risk of vibrations or potential breakage during bonding. A viable alternative to glue is the use of thermal pads. As discussed in the previous chapter, thermal pads offer significant advantages: they are flexible and can fill any small gaps that may exist between the PCB and the chips, providing a secure and reliable connection. Thermal pads not only improve

bonding but also help with heat dissipation, which is important for heat-sensitive parts. More details regarding the selection and advantages of thermal pads can be found later in this section.

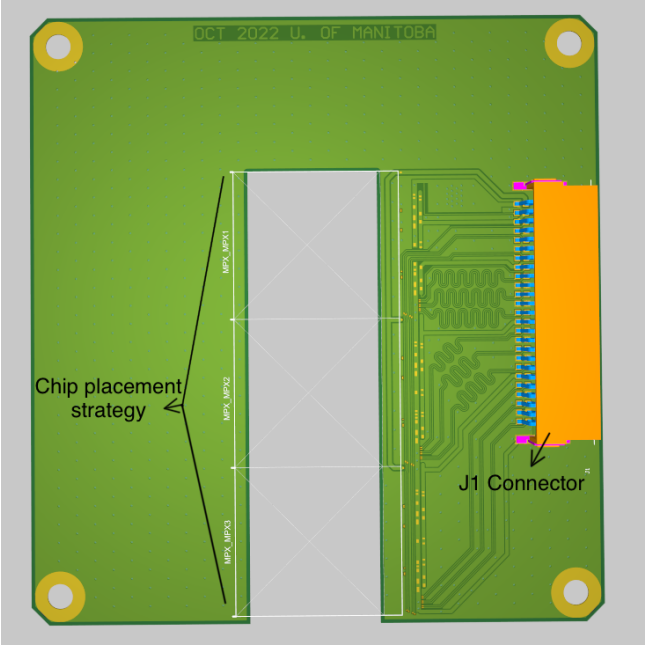

Figure 4.1: Printed Circuit Board with J1 connector and chip placement strategy.

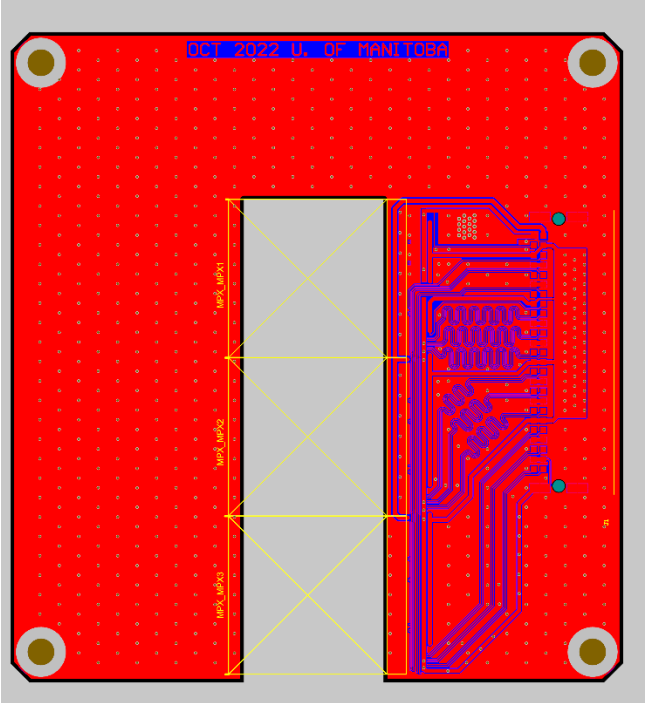

Figure 4.2: Printed Circuit Board [79], with highlighted path of the electrical traces over it.

For accurate temperature monitoring over the surface of the PCB, temperature sensors must be placed in various places over/under the PCB. Therefore, these areas of the PCB should also have smooth and level surfaces to facilitate easy sensor attachment. The strong structure for

PCB is essential, as it prevents the two arms of the PCB from twisting relative to each other. Any twisting could potentially bend the sensors away from the surface or, in a worst-case scenario, can cause the chips to crack.

Visual representations of this design are provided in the Fig. 4.3. The dimensions of the original protype were a bit different than the one we have in simulation (refer to Fig. 3.9).The PCB design includes the inclusion of carefully placed mounting holes located at each corner. These holes are not arbitrary but are thoughtfully positioned to fasten the PCB securely to the cold plates and the other plane of the PCB. This allows for effective cooling and alignment, ensuring that the entire PCB is in contact with the cold plate for proper transmission of the heat. The design of Model 6, including this PCB, has been discussed in detail in Sec. 3.2.6 [79].

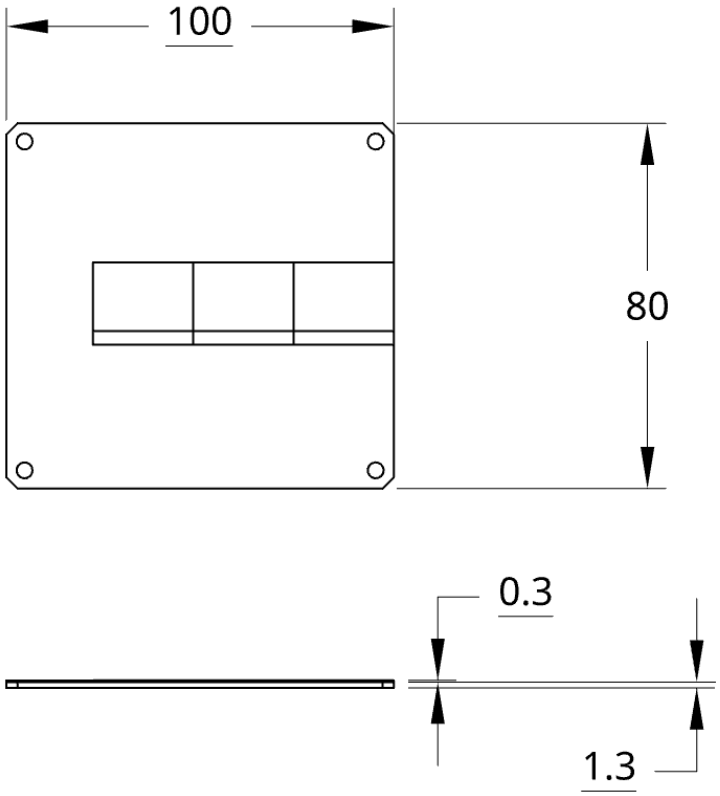

Figure 4.3: CAD drawing of the Printed Circuit Board, Units: mm.

4.1.2 Cold plate

Cold plates are one of the most important part of the assembly, maintaining the desired temperature of the chips by adequately dissipating heat acting as the heat sink. The design and material composition play a crucial role in ensuring efficient thermal management. The material chosen for the cold plates is Cu-110, a grade of copper known for its high thermal

conductivity. This material is highly effective in conducting heat, making it ideal for applications that require rapid and efficient heat dissipation. By using Cu-110, we ensure that the heat generated by the HV-MAPS chips is quickly taken away from the sensitive electronics. In addition to its thermal properties, Cu-110 is also a strong material, which ensures that the cold plates can withstand the mechanical stresses of installation and operation without deforming or losing efficiency. The machined cold plate can be seen in Fig. 4.4.



Figure 4.4: Machined cold plate [73, 80]

For prototyping, the cold plates were machined with precision [73, 80]. The manufacturing process for these cold plates showcased the importance of precision engineering in experimental physics. The cold plates met the required details to integrate seamlessly into the overall detector design. The CAD drawing of the cold plate can be seen in Fig. 4.5. The precise sizing ensures that the blocks not only fit well within the system but also allow for the necessary

connections, such as the J1 connectors, to be securely mounted, which are positioned on the sides shown in Fig. 4.6.

At the top of the cold plates, several holes are strategically made. These holes are designed to secure the cooling block in place. The cold plate is an important part of the cooling system, as it contributes to transferring heat away from the detector's sensitive components. During operation, it is sandwiched between two cold plate as can be seen in Fig. 3.32, a configuration designed to maximize surface contact. This arrangement maximizes the area available for conduction and improves the rate of heat dissipation from the HV-MAPS chips.

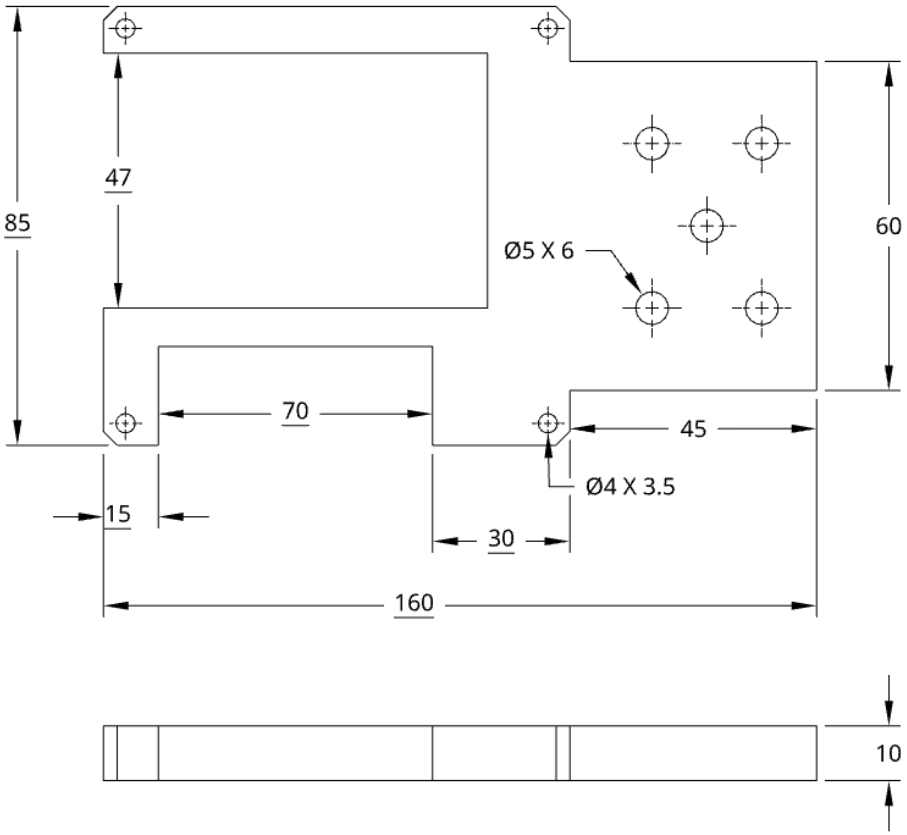

Figure 4.5: CAD drawing of the cold plate.

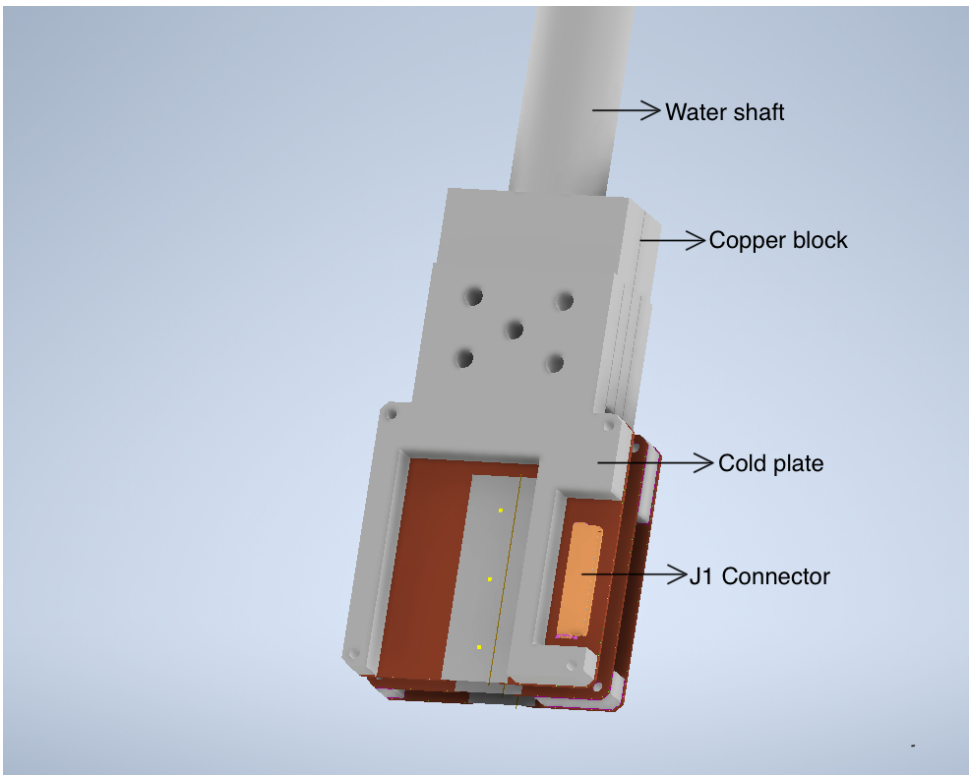

Figure 4.6: Design of the cold plate acommodating J1 connector.

4.1.3 Cooling block and Top plate

The cooling block is also one of the important components of the cooling system. It is integrated into the shaft for the continuous flow of cold water for cooling as discussed in Model 6, Sec. 3.2.6. Top plate is a simple plate that bolts onto the cooling block via the four threaded holes in the top of the cold plate. Both the cooling block and the top plate are shown in Fig. 4.9. As outlined in Model 6, this configuration supports a dual-method cooling strategy by incorporating both conductive and convective heat dissipation techniques. The cooling block, shown in the Figs. 4.7 and 4.8, serves two primary functions: First, it adds to the heat conductive cooling method. Secondly, it introduces convective cooling by employing a top pocket that interfaces with the shaft. This pocket has a broad internal surface area, allowing incoming water to circulate and absorb heat before exiting, removing a significant portion of the accumulated heat, creating a dynamic cooling loop that maintains the temperature within safe operating limits. The holes labeled as e, f, g, h and i must align precisely while fastening with the corresponding holes marked with same letters in Fig. 4.4. Fig. 4.8 shows the water pocket.

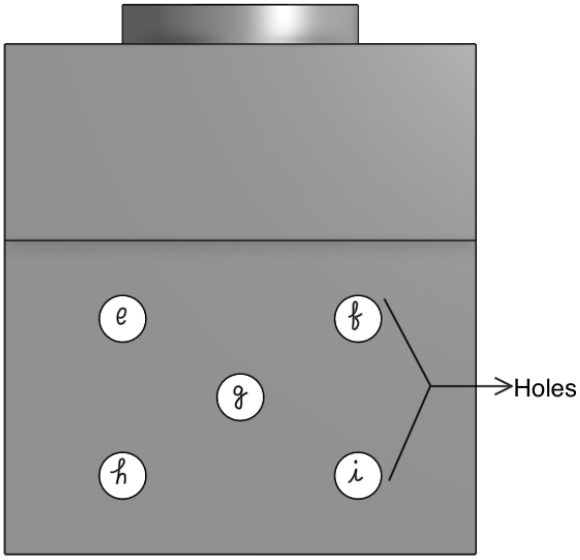

Figure 4.7: Front view of the cooling block featuring fastening holes.

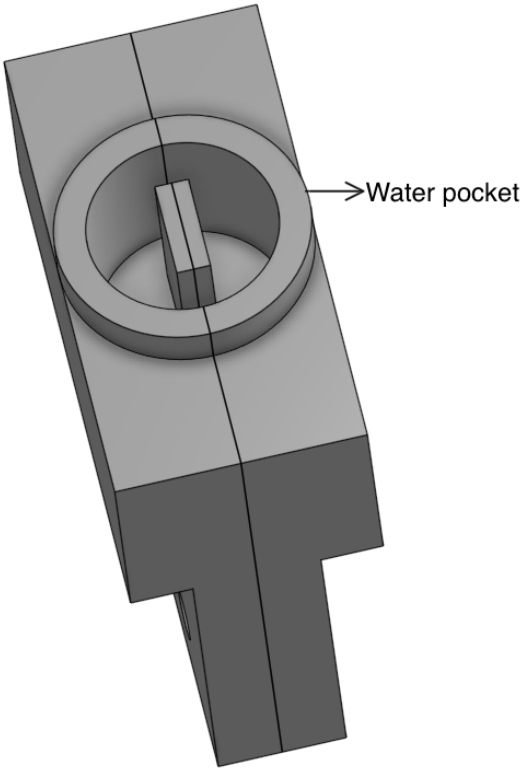

Figure 4.8: Side view of the cooling block featuring the top pocket.

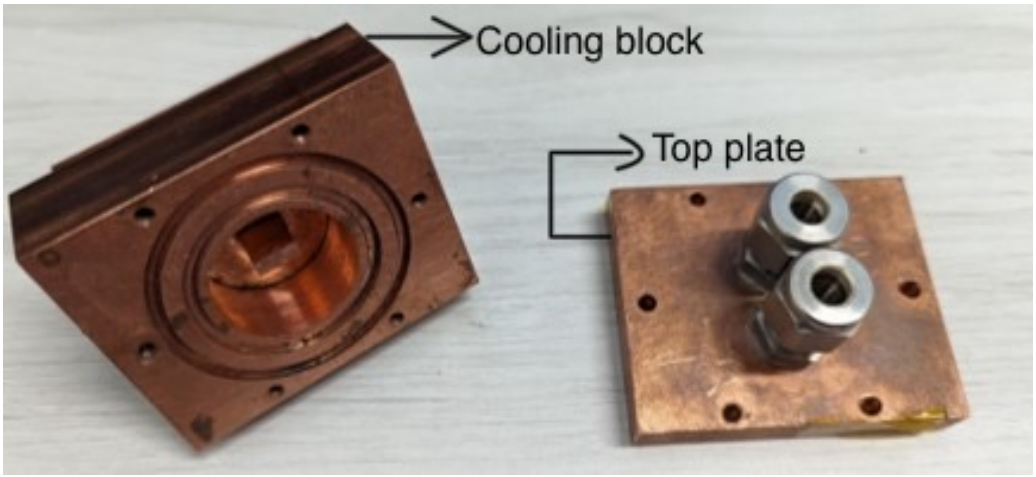

Figure 4.9: Machined Cooling block with the detachable the top plate [80].

The Compton cooling block prototype design was built keeping in mind some performance goals. As can be seen in Fig. 4.9, cooling block has been split into two pieces, the main cooling block and a detachable top plate. For effective sealing under vacuum conditions, the cooling block will feature two O-ring glands. These O-rings, made from a specialized fluoroelastomer material, are chosen for their low outgassing properties and minimal porosity, ensuring they perform reliably within a vacuum environment. Long term, fluoroelastomer O-rings may need to be changed more regularly as this material can take on the shape of the gland more easily than something like a Nitrile or Silicon O-ring.

The pocket in the cooling block will feature a tab to invoke turbulence as the inlet and outlet water streams mix, improving heat transfer. The cooling block has 5 fastening holes at the lower end, to fasten it to the cold plates as shown in the Fig. 4.11. These holes are intended to increase the area of contact of the cooling block with the cold plates, ensuring proper connection. Through careful attention to materials, structural design, and thermal dynamics, the Compton cooling block prototype meets high standards for operational reliability and cooling performance.

The Top Plate (Fig. 4.9) will have two holes tapped with NPT tapered thread to accomodate two Nickle-Copper Alloy Swagelok fittings that will act as the water inlet and outlet, respectively. Nickel Copper fittings are selected as this material is galvanically similar enough to copper to not cause galvanic corrosion. To further enhance the durability of the system, the design incorporates ceramic (Alumina) tubing to connect the Nickel-Copper fittings with the Stainless Steel fittings on the feedthrough flange, electrically insulating the two metals to prevent galvanic corrosion as water passes through the system. The NPT thread in the Top Plate will be sealed with a vacuum-curing Loctite. This Loctite acts as a powerful sealant, curing in vacuum conditions to create a robust barrier that prevents any potential leaks along the spiral leak path commonly associated with tapered threads. This attention to detail in sealing is particularly important for applications where even minor leaks can compromise vacuum con-

ditions. The CAD model illustrating the dimensions of the cooling block's half body, splitting it through middle, is shown in Fig. 4.10. In the CAD model, as can be seen in Fig. 4.8, the cooling block was initially designed in two separate mirrored parts. However, the prototype was manufactured as a single part, which can be seen in Fig. 4.9.

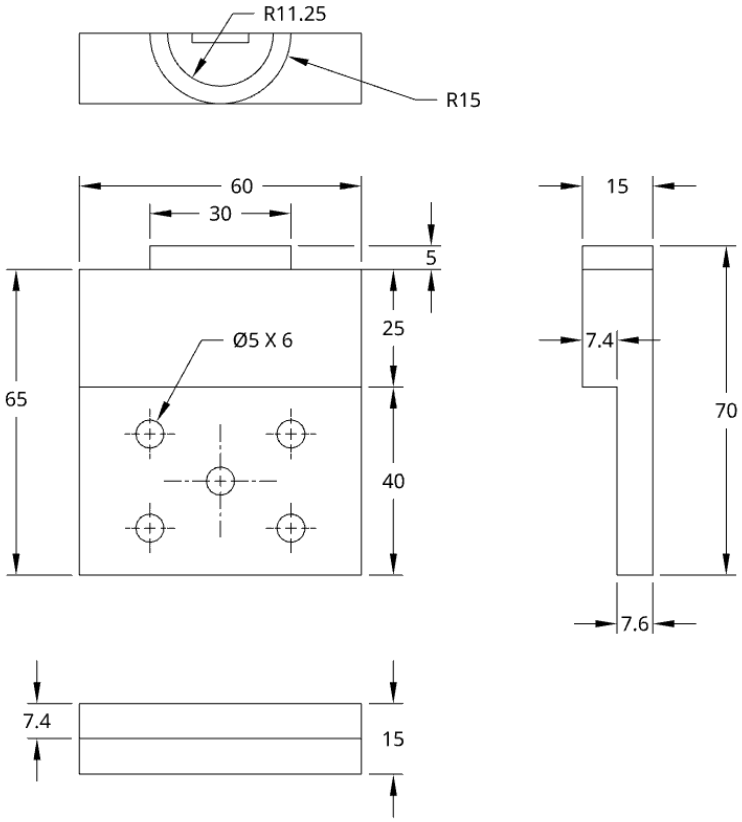

Figure 4.10: CAD drawing of the cooling block.

4.1.4 Coolant Feed through system

The coolant feed-through system is also connected to the cooling block which feeds in the chilled water into and out of the cooling block. The coolant pipelines were made from stainless steel, they act as the shaft that we have in Model 6 (refer to Fig. 3.32). During the prototype development, instead of fabricating a custom copper feed-through cylindrical shaft, which is planned for the final design, separate chilled water lines were used. This is a more economical approach taken to reduce prototyping expenses. These chilled water lines, equipped with high-quality compression fittings, were attached directly to the cooling block. This alternative enables for quick adjustments and ease of assembly, while also taking advantage of existing vacuum-compatible infrastructure. The rough layout of cooling block prototype, including chilled water feed-through flange is shown in the fig. 4.11.

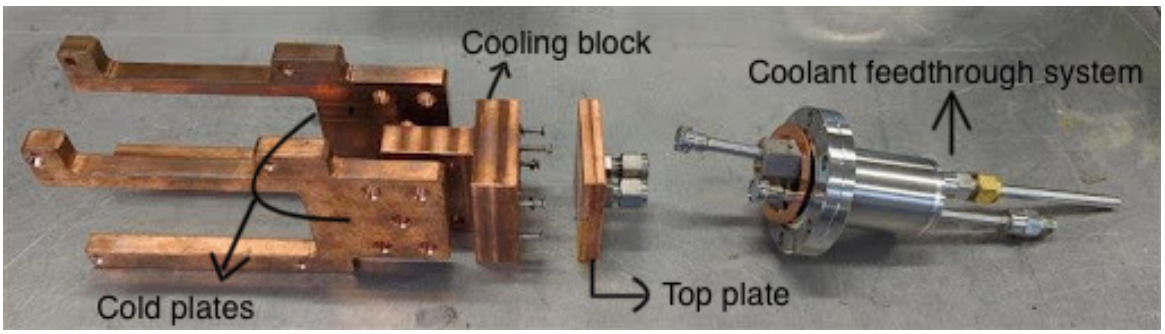

Figure 4.11: Layout of cooling block prototype, and chilled water feed-through flange (Image credits: [80]).

4.1.5 Silicon wafer chips

For the final prototyping, Mupix 11 chips have been chosen due to their suitability for high-efficiency applications. These chips are beneficial because of their high signal to noise ratio. Mupix 11 chip is integration of HV-CMOS (High-Voltage CMOS) technology, operating within a voltage range of 60V to 120 V. Compared to conventional sensors, this technology supports faster charge collection, making the Mupix 11 particularly suitable for applications that require high-speed data acquisition. The use of HV-CMOS enables the production of large-area sensors at a relatively low cost. The Mupix 11 chip also facilitates quick data transfer continuous, via a serial link, making it compatible for high-rate applications that require real-time data processing. This feature is beneficial for use in particle detection systems and high-energy physics experiments, where rapid data transfer and the ability to handle high-frequency signals are required. Mupix 10 version experienced several constraints, including issues related to readout speed, chip configuration, and the functioning of its state machine. There were also issues with weak signal output and power management, impacting the chip's performance. These challenges have been addressed and fixed in the Mupix 11. We used plain silicon wafer chips ($2 \times 2\,\mathrm{cm}^2$) and made heaters on the top of that explained in Sec. (4.2). The thickness of the silicon wafer chip was 80 μm. The picture of the silicon wafer (ordered from University Wafer) and diced chips are shown in Figs. 4.12 and 4.13.

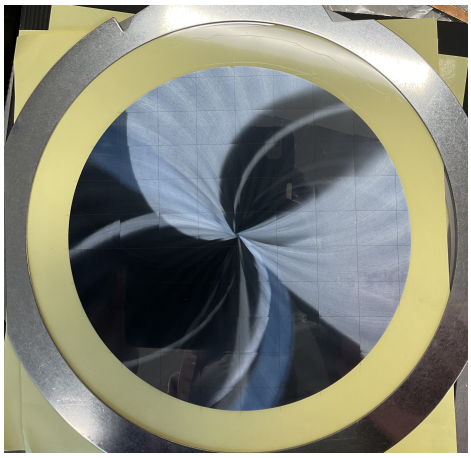

Figure 4.12: Silicon wafer chip.

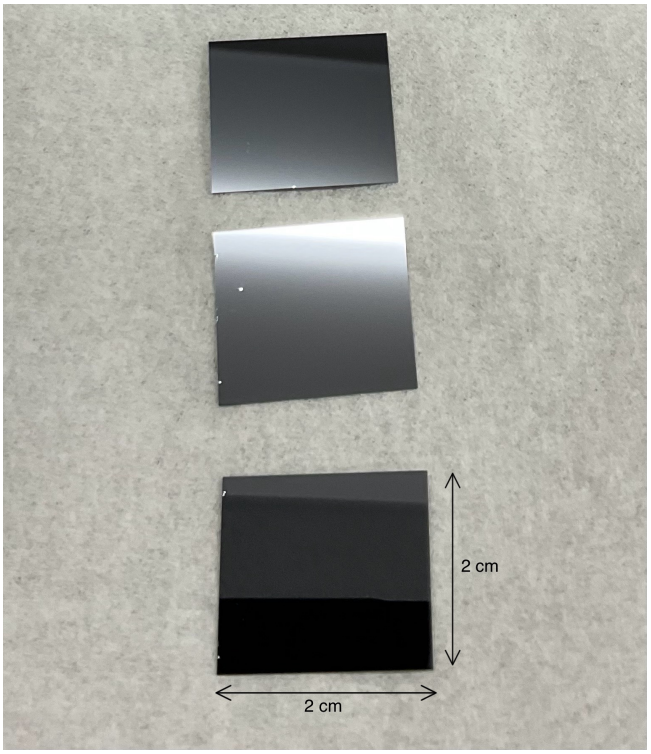

Figure 4.13: Diced Chips.

4.1.6 Thermal pads

The thermal pad used for our experiment is the TG A-4500 [**TGA4500**] and is shown in Figs. 4.14 and 4.15. This particular thermal pad stands out due to its high adaptability and ease of use. Its flexibility makes it adjustable for various applications. These can be cut into the preferred shapes for someone's own use. It presents high compressibility, enabling it to fit smoothly to uneven surfaces, ensuring maximum contact and heat transfer efficiency. With a thermal conductivity of 4.5 W/mK, it excels in heat transfer, making it a suitable thermal interface layer. Also, its natural adhesive properties ensures that it stays in place, simplifying the assembly. The pad has a density of 3.1 g/cm^3, making it reliable yet light, and it is available in thicknesses ranging from 0.5 mm to 8 mm, catering to a wide array of design requirements. This thermal pad also offers excellent electrical insulation properties, with a dielectric breakdown voltage of 6 kV/mm. This make it suitable for high-performance electronic systems. These thermal pads have rough texture on one side (refer to Fig. 4.14), and plain texture on the other side (refer to Fig. 4.15). The rough texture helps the pad grip the surfaces better, while mounting on components prone to movement. The plain texture on the other side makes smooth placement against the secondary surface, such as PCB. The TG-A4500 thermal pad is vacuum-compatible due to its low outgassing properties and silicone-based composition, making it suitable for use in high-vacuum environments without compromising thermal performance.

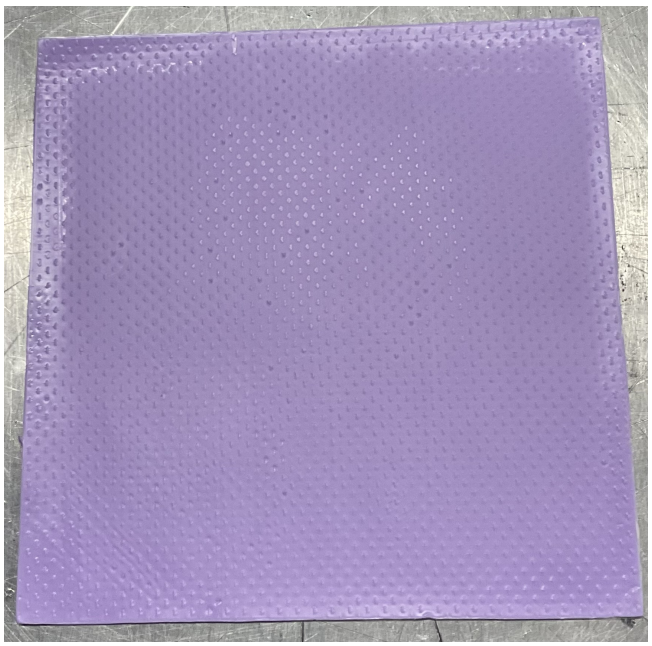

Figure 4.14: Thermal pad with rough texture.

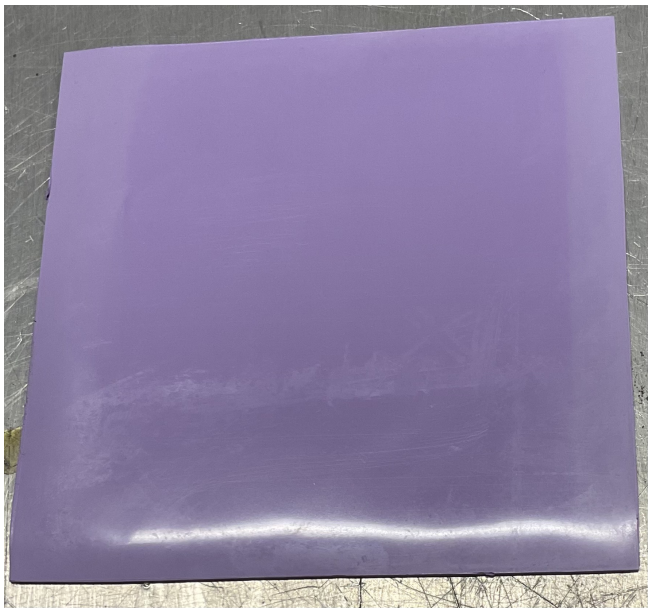

Figure 4.15: Thermal pad with smooth texture.

4.1.7 Integration of chips over PCB

After procuring all the components, the first step involved arranging the chips onto the PCB to make a plane of the electron detector prototype. Fig. 4.16 shows the integration/arrangement of the chips onto the PCB, a layer of thermal pad is sandwiched between the chips and the PCB. Four of such planes were made. The next steps are to make a heater assembly one side of the chip. This heater will be capable of generating 1 W of power per chip, simulating the thermal conditions expected during operation. This heater assembly will act as the peripheral region of the chips, or the "state machine", where most of the power is concentrated.

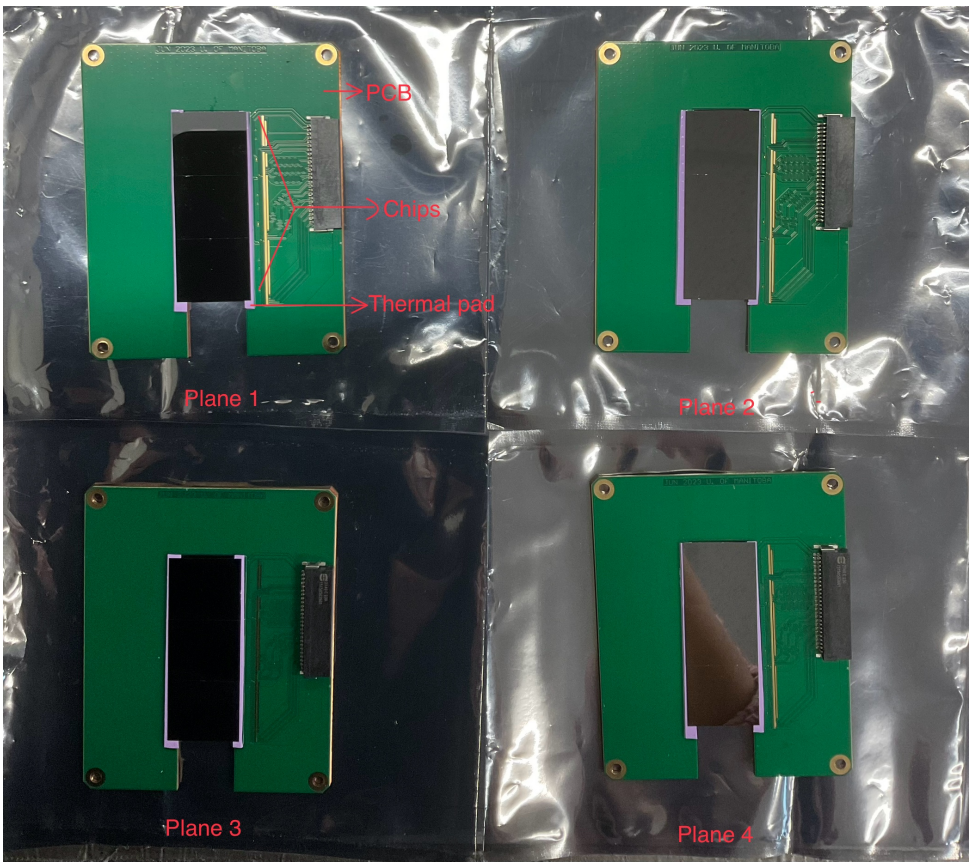

Figure 4.16: All planes with integration of chips over them.

4.2 Dummy HV-MAPS chip assembly with heaters

With the planes now ready, the next steps involve making heaters on one side of the chips which would be capable of depositing 1 W of power per chip. Two possible methods for developing these heater assemblies were explored. The first option involves using commercially available resistors, chosen for their cost-effectiveness, reliability. The second method implemented nichrome wire, a well-known material for its high resistivity and thermal stability. Both techniques were carefully evaluated for their performance, ease of implementation, providing valuable insights into the design and optimization of heater assemblies for precise power deposition.

4.2.1 Use of resistors as a heating element

To proceed with making the heater assembly onto the planes we have in Fig. 4.16, copper tape was used over the chips that has adhesive which allows it to adhere securely to the intended surfaces without the need of any additional bonding agents. Moreover, copper tape was specifically chosen due to its excellent thermal and electrical conductivity, which is essential for our heater design. One of its critical roles is to provide a conductive surface that facilitates the soldering of resistors directly onto it. This application is depicted in Fig. 4.17.
After the copper tape was affixed to the chips, we applied a thin and uniform layer of soldering paste onto the surface of the copper tape. The soldering paste serves as an intermediary mate-

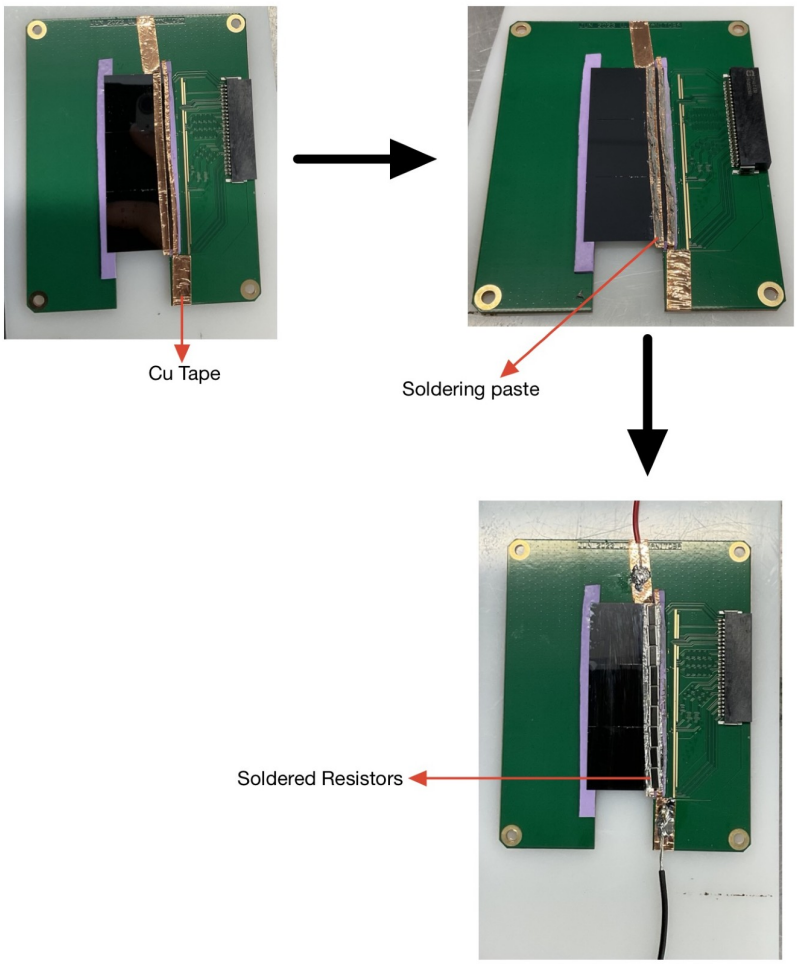

Figure 4.17: Step-by-step process for assembling the heater using resistors.

rial that enhances the bonding between the copper tape and the resistors during the soldering process. This paste ensures strong electrical connections while minimizing resistance at the joints, which is crucial for maintaining the efficiency and durability of the heater assembly. Next, we soldered the resistors over the Cu tape in parallel combination. Each resistor has resistance = 56 Ω. Each chip utilizes 3 resistors to produce 1 W of power per chip. The placement of these total 9 resistors over the 3 chip assembly is shown as the final step in Fig. 4.17.

4.2.2 Use of Nichrome wire as a heating element

The second method to build heaters utilizes Nichrome wire, a material known for its exceptional resistance properties and thermal efficiency. The Nichrome wire that we used has a diameter of 0.15 mm, chosen for its convenient properties, including significant resistance in a short length.

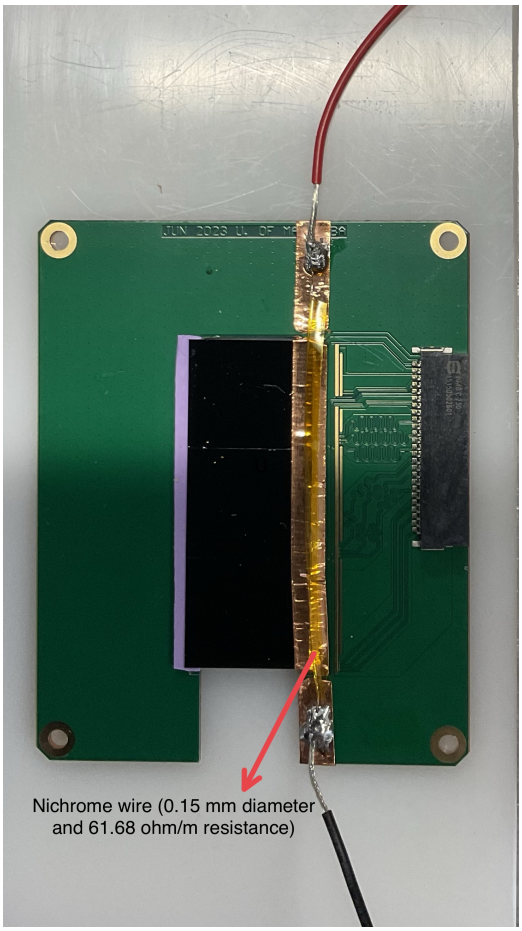

Figure 4.18: Using Nichrome wire as the heating element

This wire is particularly advantageous because it offers significant resistance over short lengths, making it ideal for applications that requires localized heating. In our setup, the Nichrome wire has a resistance of approximately 61.68 Ω/m. For this specific HV-MAPS configuration, we used a segment of nichrome wire measuring around 10 cm in length. This wire serves as the primary heating element in this specific HV-MAPS configuration, replacing a conventional heater element made with resistors. We put Nichrome wire over the Cu tape. After placing it securely onto the Cu tape, we soldered it at both the ends to complete the heater assembly. It can be seen in Fig. 4.18. The Cu tape acts as both a stable mounting base and a conductive layer to ensure efficient thermal distribution and electrical connection. Once the nichrome wire was positioned over the Cu tape, it was secured firmly in place to prevent movement during operation.

4.2.3 Comparison of above two heating elements

The comparison of above two heater assemblies is done below by weighing their advantage and disadvantages/challenges during their use.

Advantages of using combination of resistors as a heating element:

(a) Resistors can be soldered properly as can be seen in Fig. 4.17, with less or no risk of loosening of connections during operation that could compromise performance.

(b) They generally offer a longer operational liferspan as compared to the nichrome wire. However, this advantage is less significant in our short-term setup.

Disadvantages of using combination of resistors as a heating element:

(a) The soldering process was quite challenging due to the delicate nature of the chips. Minimal heat should be applied during soldering, as prolonged exposure to heat could damage or break the chips.

(b) Given the silicon chips used in our case were very thin, measuring just 80 microns, the pressure should be applied with caution during soldering, particularly while applying pressure to keep them securely in place, as a bit of more pressure can easily result in chips cracking.

(c) Another drawback of Cu tape is its adhesion properties, which can change under varying thermal conditions. Thus, the adhesion of the tape to the chip may not be always reliable. This poor adhesion can lead to misalignment or detachment of the chips during operation.

Advantages of using Nichrome wire as a heating element:

(a) Nichrome wire is easy to use due to its flexibility. This characteristic makes it easier to integrate it into the setup. Moreover, it is easy to solder. Thus, offering a secure electrical connection and less complexity of assembly.

(b) The high electrical resistance of the nichrome wire allows it to efficiently convert electrical energy into heat enegy, enabling it to dissipate a substantial amount of power as heat.

(c) Nichrome wire has fast response time, reducing waiting times and allowing it to heat up rapidly when the current is applied.

Disadvantages of using Nichrome wire as a heating element:

(a) Maintaining a secure connection between the wire and the chips is essential during operation. It is important to develop a secure connection at the initial stage because, once the assembly is placed into vacuum environment, addressing such issues are almost impossible without dismantling the system.

The advantages and disadvantages outlined above highlights the comparison between the two approaches for the required heater assembly. After evaluating both the options and gaining hands-on experience with both the setups, we moved forward with the Nichrome wire as it was simple and easier to use than resistors. However, as above mentioned, there was some concern regarding maintaining the proper contact between the chips and the wire. To address this, the use of thermal epoxy became essential. This adhesive played a dual role: providing robust mechanical support to secure the wire in place and enhancing the thermal conductivity between the wire and the chip. The preparation of the final heater assemblies with the Nichrome wire is presented in the Sec. 4.2.4.

4.2.4 Preparation and testing of Nichrome wire final heater assemblies

After making the comparison and determining the most suitable option for our final heater assembly, we proceeded with the Nichrome wire-based heater assemblies. The Nichrome wire was stretched evenly over the silicon chips to be properly aligned and secured in place using two trigger clamps. To establish a reliable thermal connection, we used the thermal paste [81] over the wire, so that there is proper contact between the chip and the nichrome wire (Fig. 4.19). This paste played a crucial role in enhancing thermal conductivity by bridging any microscopic gaps and improving the contact between the components.

The extra nichrome wire on both the ends was trimmed off, and the remaining segments of the wire were soldered to copper tape that had been pre-applied to the ends of the PCB. This ensured a secure electrical connection. As shown in Fig. 4.20, the final configuration of the four planes for the electron detector assembly, with the Nichrome wire as the heating element, was successfully prepared. While the application of thermal epoxy required precision and added an additional step to the assembly process, it proved to be a highly effective solution. By addressing the key concern of maintaining proper contact, it allowed the Nichrome wire assembly to deliver consistent and reliable heating performance. Electrical characteristics of the heaters for 3 Watt of power deposited onto the chip assembly for each plane are given in the Table 4.1. Here, R_h is the resistance over the heater, V_h is the voltage developed over the heaters, V_s is the voltage applied from the power supply, I_s is the current applied from the power supply, and P_n represents the power generated at the nth plane.

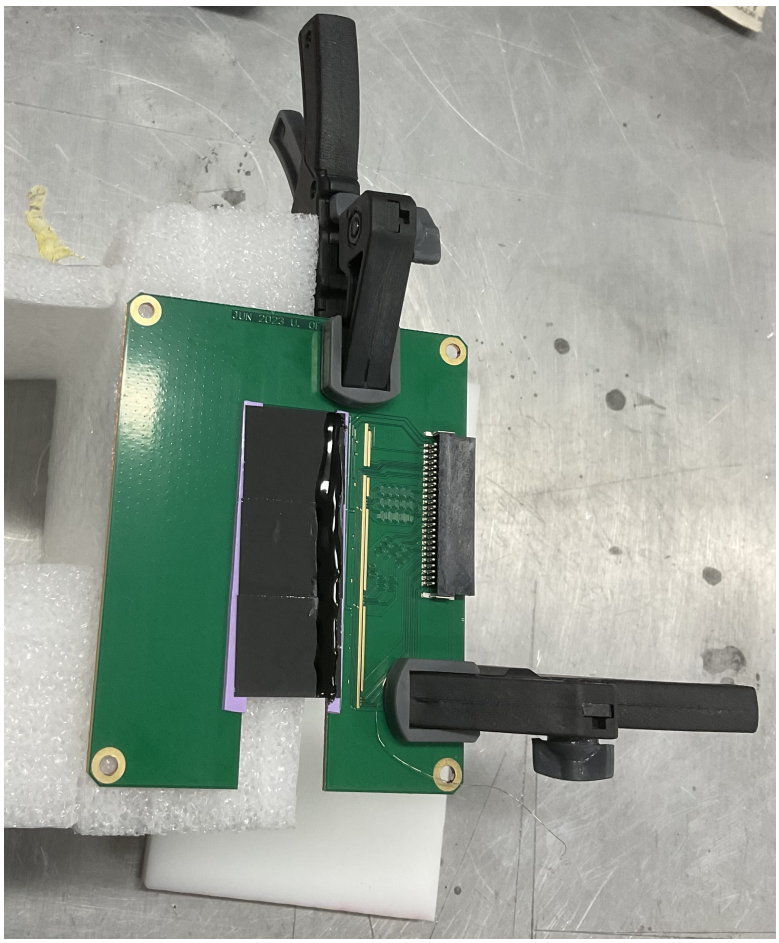

Figure 4.19: Wire secured with clamps and coating of thermal epoxy.

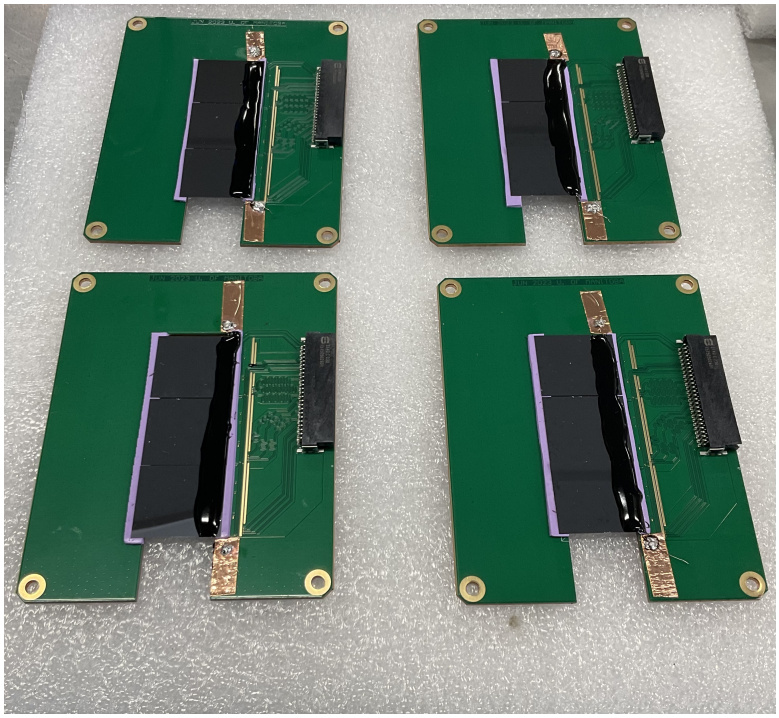

Figure 4.20: Final heater assemblies.

Table 4.1: Electrical characteristics of the heaters

Plane	$R_h[\Omega]$	$V_H[V]$	$V_s[V]$	$I_s[A]$	Power [W]
P_1	4.57	3.61	3.79	0.80	3.02
P_2	4.52	3.60	3.79	0.80	3.02
P_3	4.52	3.59	3.75	0.81	3.02
P_4	4.86	3.75	3.89	0.78	3.03

4.3 Placement of temperature sensors over the critical points of PCB for final testing

With all the planes finalized and prepared, the next steps involve the construction of the electron detector assembly and monitor the temperature dissipation at multiple points throughout the system. In Chapter 3, we carried out the thermal simulations on CFD, which recorded the temperature distributions at various points in the detector assembly during operation. Now, it is essential to validate these simulations by reproducing the conditions in a controlled lab setup. This involves placing temperature sensors at the critical locations identified during the CFD analysis and then testing the measured temperatures against the simulated predictions.

The temperature sensors used are the DT-670-SD diode sensors [82] from Lakeshore, previously introduced in Sec. 2.3.2 and shown in figure. These sensors measure the temperature precisely due to their highly sensitive nature. However, their functionality depends upon the correct polarity of the inputs, as reversing the inputs leaves the diode non-operational making it appear as an open circuit. The cathode and anode arrangement of these DT-670-SD Diode sensor leads is shown previously in Fig. 2.17. These temperature sensors can be connected with either a 2-lead arrangement or a 4-lead arrangement. The purpose of the 4-lead technique is to eliminate the effect of lead resistance on the measurement. The 4-lead arrangement is preferred as it minimizes the impact of lead resistance on measurement accuracy. In this setup, the current and voltage leads are run separately to the sensor. When 2-lead sensors are used in 4-lead measurement, the short leads that are directly from the sensor have an insignificant resistance. However, the practical constraints in cryogenic systems forces the users to read sensors in a 2-lead arrangement because there are not enough feedthroughs or room for lead wires. All of these temperature sensors are attached to the rear panel of the Lakeshore temperature monitor [67] inputs via sensor input mating connector, 6-pin DIN 45322 sockets. We used pins 1, 2, 4 and 5 to connect our arrangement. The diagram illustrating these connections can be found in the Fig. 4.21. The description about the detailed setup of the Model 224 Lakeshore temperature monitor is provided in the lab manual [67]. The pin configurations for the 6-pin DIN plugs are summarized in Table 4.2, specifying the purpose of each pin.

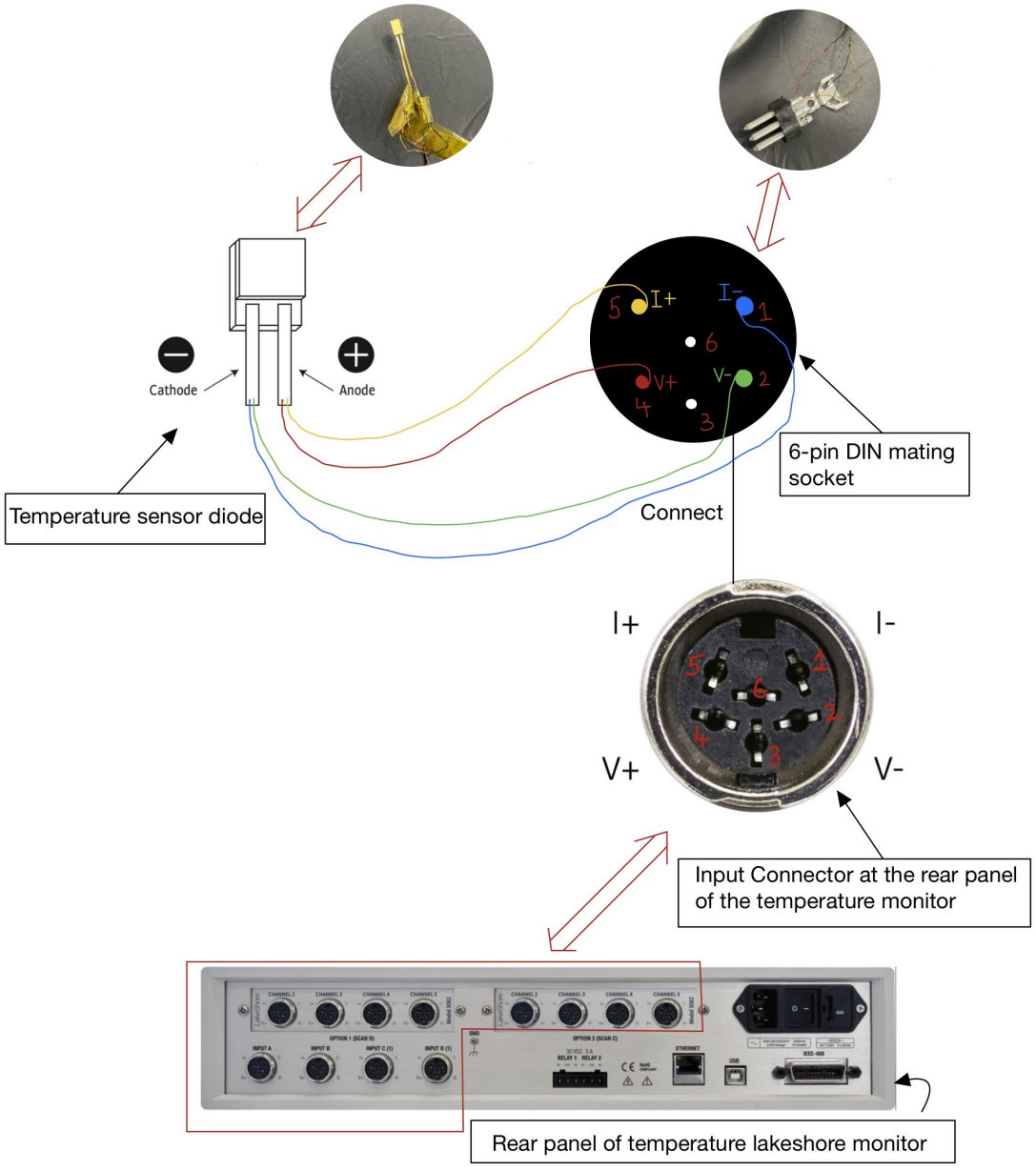

Figure 4.21: Diagram showing the silicon diode (sensor) connections to the 6-pin DIN connectors and input connector of the temperature Lakeshore monitor

To affix the temperature sensors to the detector components, we used a very thin layer of the thermally conductive epoxy suitable for operations inside the vacuum. According to the Safety Data Sheet (SDS) of the epoxy [83] and the respiratory guide [84], it is required to use the F(OV) + F(Form) type respirator [85]. The fitting test was done and approved (certificate reference: FitTest) by University of Manitoba's Environmental Health and Safety office.

Table 4.2: Description of the input connectors [67]

Pin number	Description
1	Current(I-)
2	Voltage (V-)
3	Shield
4	Voltage (V+)
5	Current (I+)
6	Shield

The placement of these temperature sensors was guided by the results of the CFD simulations, ensuring coverage of areas with significant temperature gradients. We divided the PCB into two parts, dividing it through the centre of the chips as can be seen in Fig. 4.22. The right arm of PCB, Part 1, is the peripheral side of the PCB, where most of the heat is concentrated as it has an active heat load, and the left arm of PCB, the Part 2, is the opposite side of the periphery, which is expected to experience lower temperatures due to its distance from the heat source. The motive behind dividing this hypothetical area is to strategically divide the area depending upon their temperatures, which will help in placing the sensors depending on the potential temperature points recorded in the CFD simulations. Out of the 8 sensors in total, we decided to place: four in Part 1, two in Part 2, and two on the cold plate. This can be seen in Fig. 4.22. We have labeled sensors based on their respective input channels at the Lakeshore temperature monitor. This labeling makes it easy to compare the readings of individual sensors and the corresponding temperature curves displayed at the monitor's output.

The sensors are placed in a sequence that reflects the expected temperature distribution, from the hottest to the coolest regions, as detailed below:

Sensor B: The most heated area of the part 1 of the PCB would be the heater itself, so we have to place a sensor to directly measure the heat source's temperature.

Sensor A: The second most heated part of the PCB would be actually in part 1 of the division, which is the area over the chip just horizontally opposite to the heater.

Sensor C2, C3, C5, D1: These sensors are distributed across the periphery of Part 1, in areas of intermediate heat dissipation. Sensor C2 is placed on the PCB near J1 connector. Just below sensor C2, sensor D1 is placed. Sensor C3 is place at the back side of the PCB on the part i.e. the peripheral side. This area is important to measure the difference between the temperature at the heater and at the bottom of the PCB as we want to see how much heat is

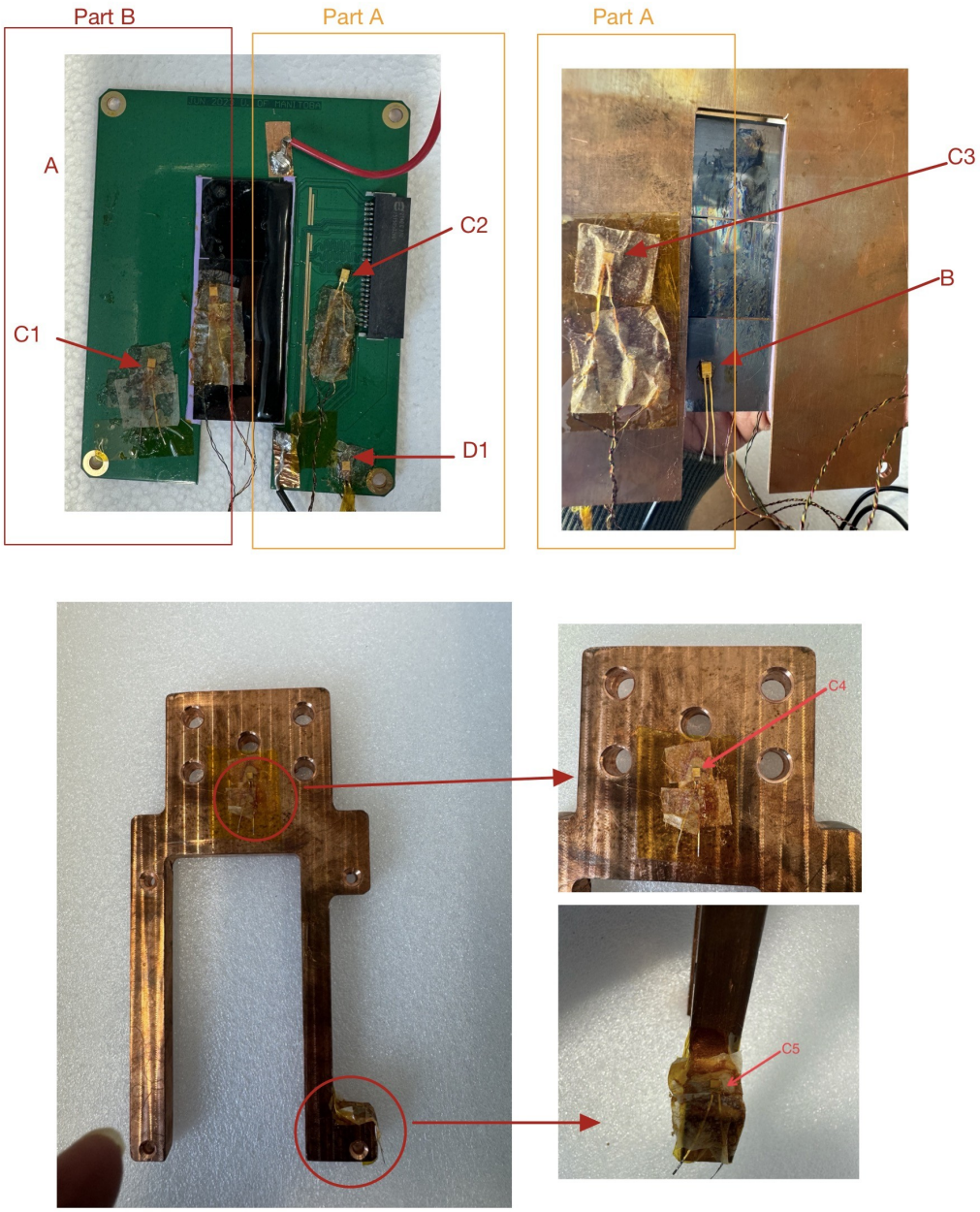

Figure 4.22: Placement of Temperature Sensors.

efficiently sinking through the PCB. The cold copper plate is acting as a major heat sink in this case, so it is interesting to record the temperatures there. Sensor C5 is placed on the lower end of the cold plate.

Sensor C1: The sensor C1 is placed on the Part 2 of the PCB shown in Fig. 4.22. This part is expected to be at a slightly lesser temperature as compared to the previously mentioned sensors because of the obvious reason that it is placed on the arm which is opposite to the heat load, but since PCB has a continuous conductive layer, the temperature will scatter all over

which makes the temperature at this point almost closer to the other arm.

Sensor C4: This sensor is placed at the top of the cold plate. We placed this sensor strategically here as this part is very close to the water pocket of the cooling block. This sensor is expected to record the lowest temperature within the assembly or we can also say that it is expected to be the coolest area of the electron detector while operating inside the vacuum with coolant running through the pocket of the cooling block.

By distributing these sensors across regions with varying thermal characteristics, this setup ensures an understanding of the detector's thermal behavior, a critical requirement for its successful operation within the Compton polarimeter of the MOLLER experiment.

4.4 Temperature measurement with 4-plane assembly under ambient conditions

Testing the final detector assembly at the ambient conditions before putting it into the vacuum chamber is an important step to test that all the connections are working properly and in the expected way. This setup serves as a vital checkpoint, bridging the gap between development and implementation. The process ensures that all the mechanical and electrical connections are functioning properly. The measurements from this setup will suggest any possible challenges early in the process, thereby minimizing the risks during operation inside the vacuum. To carry out such measurements, we need to assemble all the previously introduced and discussed detector parts together into a final assembly of the electron detector, demonstrated in Fig. 3.32, which is planned to be placed inside the Compton polarimeter in Hall A of the Lab. This assembly includes all essential elements, from the HV-MAPS chips to the supporting structures and cooling interfaces, arranged to meet the operational requirements of the experimental setup. During ambient testing, the detector assembly is housed in a hand-made closed enclosure to replicate some aspects of the vacuum environment, albeit with significant differences. Despite complete enclosure, there would have been some cooling effects occurring at the detector surfaces from the natural air convection in the room. At room temperature, no chilled water was introduced through the water pipelines. Although this cooling is not as efficient or controlled as the cooling system (introduction of chilled water) in vacuum, it provides valuable insights into the thermal behavior of the detector under non-ideal conditions. The room in which these tests were performed was approximately 20°C.

The preparation started with mounting of PCB planes with Nichrome wire as heater assemblies (see Fig. 4.20) onto the cold plates, making a sandwich-like configuration where the cold plates are positioned between the two PCB planes. This arrangement ensures structural integrity and efficient heat dissipation. The complete details on PCB and cold plates are discussed in detail in Sec. 4.1.1 and Sec. 4.1.2. There is a layer of thermal pad placed between the PCB

plane and the cold plates to reduce any contact impedance and to create a more uniform and secure connection, and it also expands under heat, reducing any air pockets that could hinder heat transfer. This pad helps absorb the mechanical vibrations that might propagate from the cooling pipelines to the cooling block, cold plates, and ultimately to the PCB planes and chips. This is important because the chips in assembly are extremely delicate and can break from these vibrations. To further protect against mechanical stress, a combination of fasteners was used to join the assembly together. We got two such dual-plane assemblies ready (refer to Fig. 4.23).

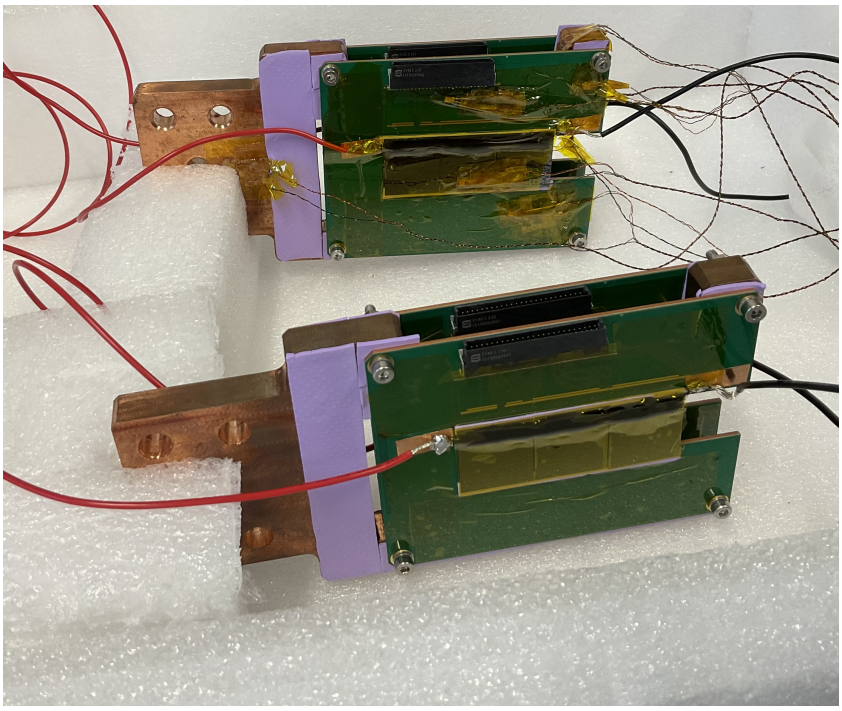

Figure 4.23: Dual plane assemblies for the Electron Detector.

These two dual-plane assemblies, with their cold plates, were then attached to the cooling block in such a way that the cooling block is enclosed between the two cold plates (as shown in Fig. 4.24). This cooling block serves as the primary component for dissipating heat. The coolant feed system is attached to it to introduce a continuous flow of chilled water. The rough schematic layout of the coolant feed-through assembly and its connection to the cooling block can be seen in Fig. 4.11. Additional details and strategies behind the design of the cooling block and the coolant feedthrough system are explained in Sec. 4.1.3 and Sec. 4.1.4.

The layout of the experimental setup of the test conducted at ambient conditions is shown in Fig. 4.25. The side flange (labeled in Fig. 4.25) acts as a central hub for all connections and is further linked to the D-Sub connector. The D-Sub connector facilitates electrical connections for the entire assembly. Through this connector, power is supplied to the planes. Each plane is powered to dissipate 3 W, imitating the expected operating conditions of the actual chips. Also, all of the connections from the sensors are routed through the D-Sub connector to the

rear panel of the Lakeshore temperature monitor, as described in the layout diagram 4.25. By reading the output through the temperature monitor, we measured temperature variations at various heat spots (sensor placement positions) over the detector, which were plotted as temperature vs time (refer to Fig. 4.26). This data provides valuable insights into the thermal behaviour of the system under the conditions applied by us. We can observe results of different temperatures developed over different regions of our detector assembly. This is plotted with time vs. temperature as can be seen in the Fig. 4.26. The data was collected for a certain period of time and compared with our theoretical expectation.

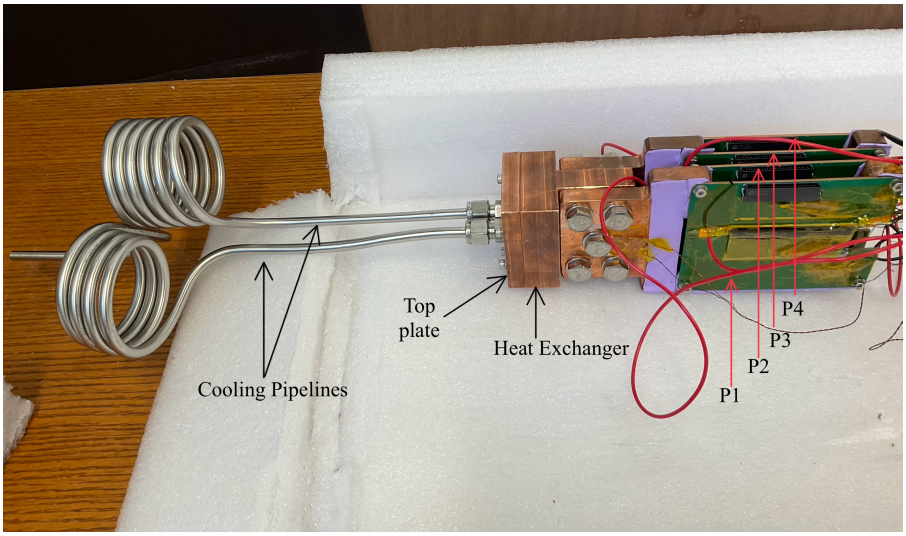

Figure 4.24: Complete Electron Detector Assembly

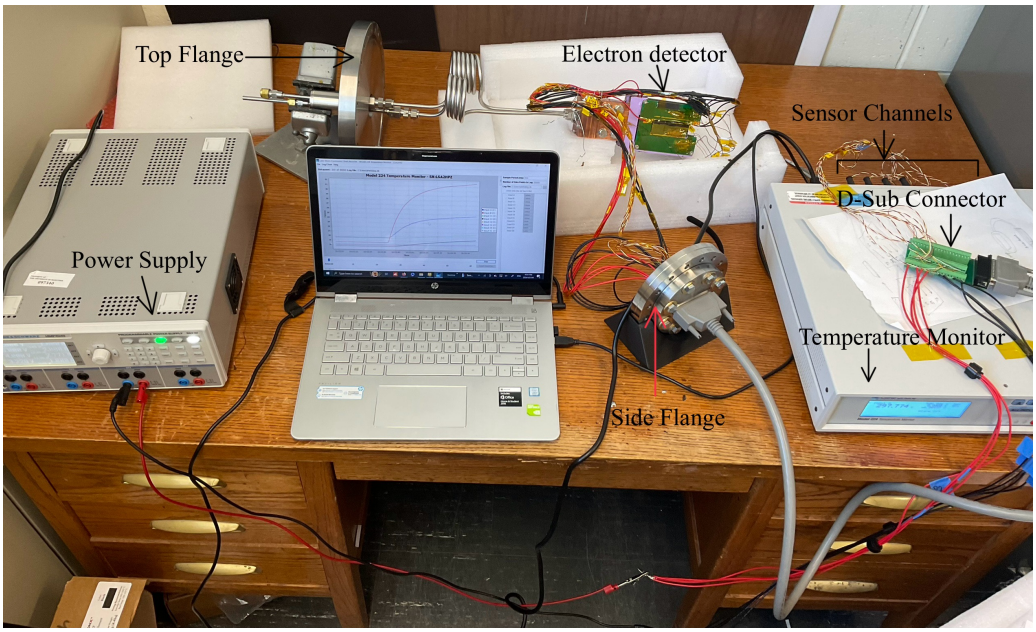

Figure 4.25: Experimental Setup at the ambient conditions (while data recording, the electron detector asssembly was enclosed in a handmade styrofoam box).

As can be seen in the Fig. 4.26, and as discussed in the previous section, the sequence in which the sensors were expected to record heat was B, A, C2, C3, C5, D1,C1,C4. While analyzing the data collected at room temperature, we observed the exact pattern in the heat response as expected (discussed in the previous Sec. 4.3). This consistency between the observed sensor responses and the predicted behavior is an encouraging indication that the system is functioning as we intended, and thus, we can move forward with the final data taking process. For that, we need to record the data with the same setup, but this time placed inside the vacuum chamber.

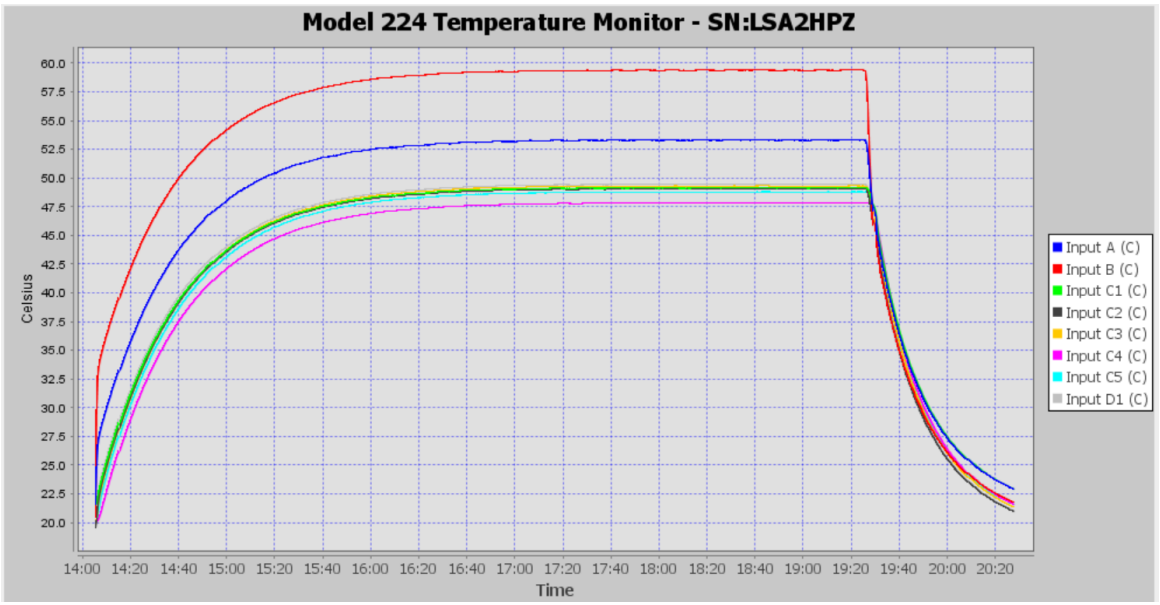

Figure 4.26: Results of data recorded at the ambient conditions.

4.5 Comparison of final measurements inside the vacuum chamber with simulations

In this section, we focus on setting up the experimental setup in the vacuum chamber and run the same tests as described and performed in the previous Sec. 4.4. These tests are the final stage of evaluation and provide an assessment of whether the electron detector we designed and prototyped in the local laboratory meets the performance criteria required for its intended application. Our goal was to design a cooling system that the temperature at any location of the detector should not exceed 70°C. If the results turn out to be within our expectation, the current silicon pixel detector technology in the Compton polarimeter of the Hall A will be replaced with the HV-MAPS technology. The vacuum chamber that had been used for this temporary local setup is shown in the picture 4.27.



Figure 4.27: Vacuum Chamber used for Testing in the Local Lab at the University of Manitoba.

CAD Render of the vacuum chamber with a prototype of the electron-detector setup placed inside it is shown in picture 4.28. To prepare for testing, the vacuum chamber was pumped down to a low pressure of 10^{-4} Torr, simulating the operational environment as closely as possible. Prior to initiating the tests, with neither the coolant system activated nor power supplied to the setup, all sensors were observed to stabilize at room temperature. The initial readings from the sensors ranged between 18°C and 21°C, confirming that the system was starting from an equilibrium state. However, we noticed that sensor C1 (see Fig. 4.22) stopped functioning properly once inside the vacuum chamber. After some troubleshooting, we decided to disable this sensor's channel on the temperature monitor and exclude it from our measurements. To account for its absence, we could extrapolate value at this place with reference to other sensors. This adjustment did not significantly impact our testing goals, as our primary objective was not to record precise temperatures at specific points but to ensure that the overall temperature inside the vacuum remained below the critical threshold of 70°C.

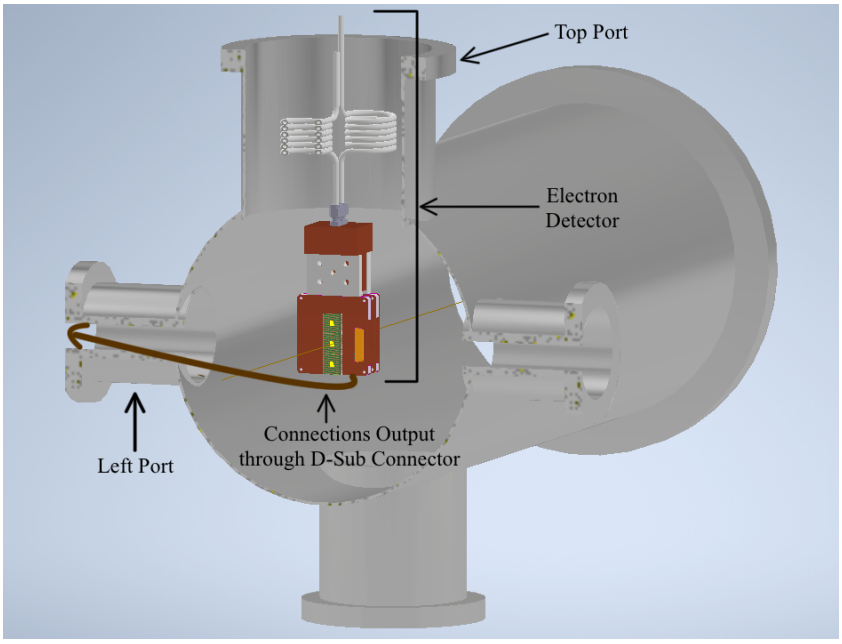

Figure 4.28: CAD render of the vacuum chamber with prototype of electron-detector setup placed inside it.

We began the testing process without activating the coolant system to observe how the setup behaved under these initial conditions. For this test, we supplied 3 W of power per plane to the system. Over the next 4 hours and 45 minutes, we closely monitored the readings from the remaining sensors. As expected, the temperatures across all sensors steadily increased throughout this period. However, what stood out was that the temperatures showed no signs of stabilizing or reaching a saturation point. The maximum temperature recorded just before we decided to shut down the power supply was approximately 93°C (refer to Fig. 4.29). This was significantly higher than our target limit and clearly indicated that without an active cooling system, the heat generated by the detector assembly could not be managed effectively.

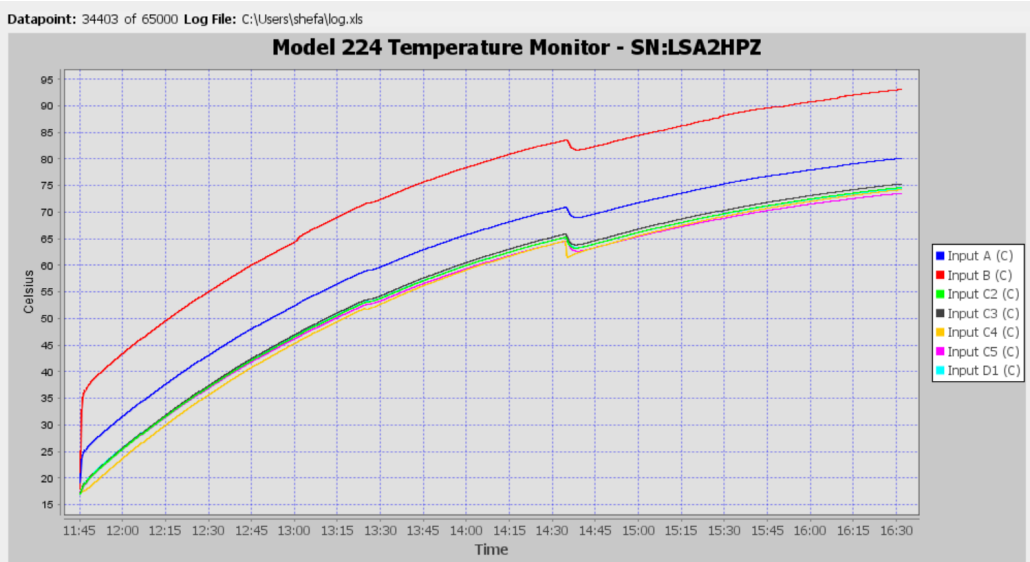

Figure 4.29: Results of data recorded in the vacuum without cooling.

For the next set of observations, we turned on our coolant system which can supply coolant at different temperatures, but with the constant flow rate. The flow rate that we chose for our system is 7.5 L/min. We chose to test our setup in four different temperature ranges, which are 4°C, 8°C, 12°C and 16°C. For these final tests, our aim is to compare the temperature gradient at various positions of the prototype functioning inside the vacuum with the computationally modeled thermal simulations. The results are compared at the specific sensor locations (shown in Fig. 4.22) for both the CFD analysis and local lab setup. For comparison, we selected the results from the setup where we introduced water at 12 ° C, and applied 3 W of power per plane. The results of the computational simulation, run via CFD, are depicted in Figs. 4.30 and 4.31. On the other hand, the experimental results under similar conditions in the lab are shown in Fig. 4.32.

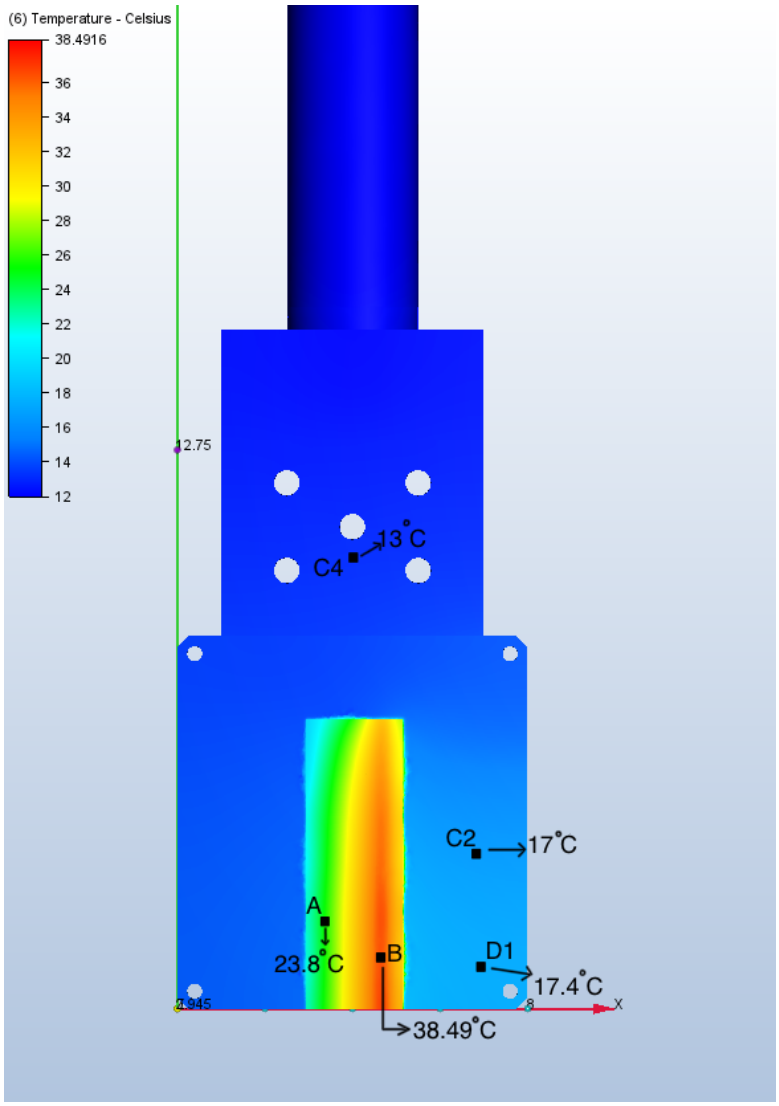

Figure 4.30: Computational Results of the Electron Detector with Water at 12 °C and 3 W of Power per Plane: Front View.

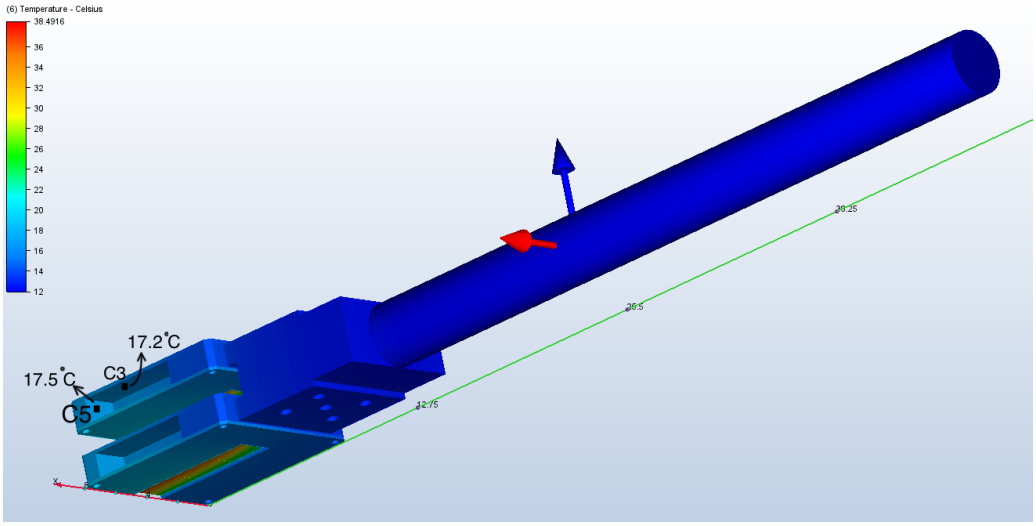

Figure 4.31: Computational results of the electron detector with water at 12 °C and 3 W of power per plane: side view.

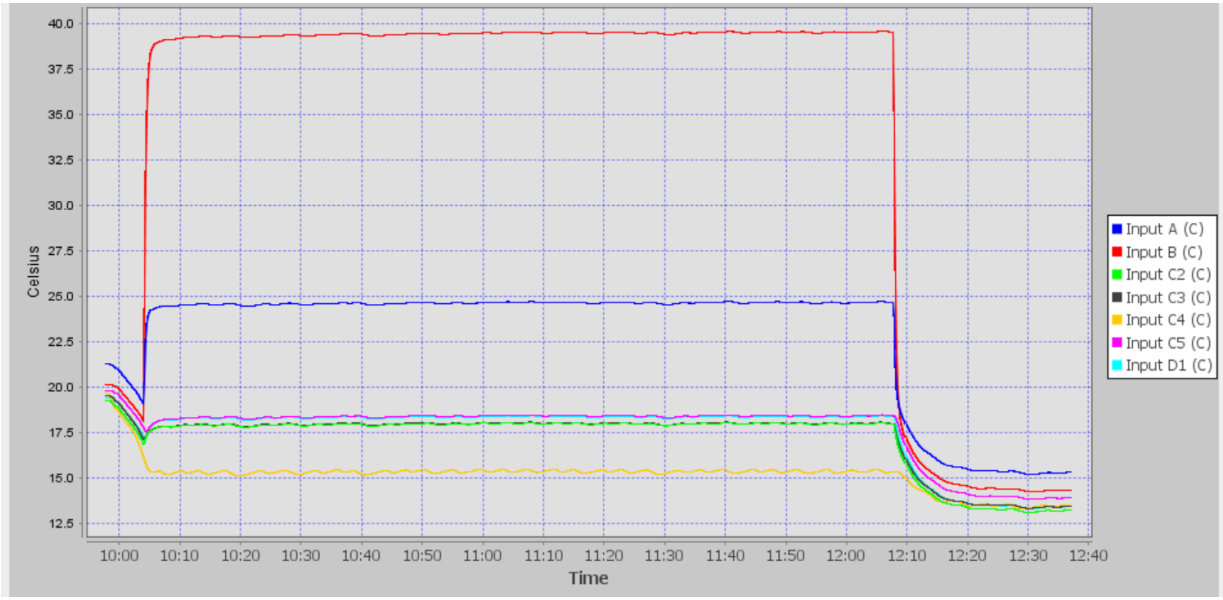

Figure 4.32: Results from the local lab setup, where all the sensors labeled on the side with colors, indicating the temperature recorded.

The coolant was run from the chiller through the cooling pipelines. We compare the experimental data with the CFD simulation results, evaluating the temperature at different sensor locations (shown in Fig. 4.30 or Fig. 4.22), where sensors are directly placed.

The summarized results are presented in Table 4.3. Across both the CFD simulation and the lab experiments, the highest temperature recorded was at the heater load. In the case of the CFD simulation, the maximum temperature reached nearly 38.5 °C, while in the lab setup, the sensor at the heat load recorded approximately the same temperature, which is nearly 39 °C. This measurements are important, as they provides comprehensive insight into the thermal performance of the detector at the intended points in both experimental and simulated models.

Similarly, we performed tests across a range of temperature settings (4 °C, 8 °C, 12 °C, 16 °C) and varying power levels (6 W, 12 W, 15 W) applied to all planes of the detector. The corresponding results are presented in the Table 4.4, and supplementary result figures are provided in Appendix 5 which reflects the consistency of temperature readings across various points in both scenarios.

Table 4.3: comparison of temperature results at different sensors locations for both the CFD analysis and experimental setup, for this specific case: coolant temperature: 12 °C, flow Rate: 7.5 L/min, power per plane: 3 W.

Sensor Location	Experimental Results [°C]	CFD Results [°C]
B	39	38.5
A	24.5	23.8
C2	17.5	17
C3	18	17.2
C5	18.5	17.5
D1	18	17.4
C4	15.3	13

Table 4.4: Comparison of the experimental (lab) results with the computational (CFD) results.

Power [W]	Temp. of the Coolant [°C]	Measured Temperature at the Sensor B [°C]	Simulated Temperature at Sensor the B [°C]	Difference [°C]
6	4	20.8	17.3	2.8
6	8	24.1	21.3	2.8
6	12	27.7	25.2	2.4
6	16	33	29.2	3.7
12	4	33.5	30.5	3
12	8	36	34.4	1.6
12	12	39	38.5	0.5
12	16	47	42.5	5
15	4	43	37.1	5.9
15	8	46	41.1	4.8
15	12	49	45.1	3.8
15	16	55	49.1	5.9

Chapter 5

Summary and Conclusion

The thesis demonstrates the in-vacuum suitability of the HV-MAPS chips as the electron detectors, supported by both computational simulations and experimental data. Present study explores the development and validation of HV-MAPS chips as advanced electron detectors suitable for operation in vacuum environments, intended to be installed at Hall A's Compton polarimeter in JLab for the MOLLER experiment. The measurement of polarization of the incoming electron beam from the CEBAF facility is important before it goes to the main experimental setup. To measure the polarization, the strip detector is currently being used. Recently, there are plans to change that with the HV-MAPS technology. Sincere efforts have been made into the direction of development of these HV-MAPS-based electron detectors to be placed inside the Compton polarimeter. Various designs of the electron detector were tried and tested using CFD simulations (refer to 3), providing motivation to support the development of a physical prototype. Subsequently the prototype was made and tested in the local lab inside a portable vacuum chamber (refer to chapter4). The comparison of these results are shown in Sec. 4.5 and Appendix 5. The thermal management system noticably maintained the detector's temperature well within safe operational limits, confirming its suitability for deployment in vacuum environments. The thermal optimization process was driven by real-time temperature monitoring using silicon diodes (DT-670 from Lakeshore), strategically placed onto the different locations of the detector to observe temperatures below the critical limit of (60-70)°C.

The tests presented in this thesis were conducted using dummy chips with heat load, created with Nichrome wire, as detailed in Section 4.2.4. In future work, these dummy chips will be replaced with fully functional HV-MAPS chips, and similar tests will be carried out at a beamline facility. This advancement will enable cross-verification of actual operational results with the simulated and experimental data obtained in this study. These dummy chips serve as stand-ins for the real HV-MAPS chips to evaluate thermal performance and detector integration in a controlled vacuum environment. The use of Nichrome wire accurately mimics the heat generation expected in operational conditions, allowing us to simulate and analyze the detector's thermal behavior during operation. The placement and integration of the HV-MAPS chips onto the PCB will require precision. The chips must be carefully aligned with the

fiducial markers on the PCB to ensure accurate positioning. This task is challenging due to the alignment required for this small scale setup of the chips assembly. Once positioned, the chips will be securely wire-bonded to the PCB using a wire-bonder. The wire bonder can be seen in Fig. 5.1, which will be uused as a HV-MAPS gluing and assembly station.



Figure 5.1: Wire Bonder [86]

Appendix A

Table 4.4 presents a comparison between the experimental results obtained in lab and the computational results obtained using CFD Autodesk software. The supplementary figures showing these results mentioned in that table are given as below. These results focus on the maximum temperature recorded at sensor location B, as our primary objective is to ensure the overall detector temperature remains below 70°C.

1.) Results for Coolant running at 4°C and Supplied Power of 12 W (3 W per plane).

• Simulated temperature at sensor at B: 30.5°C.

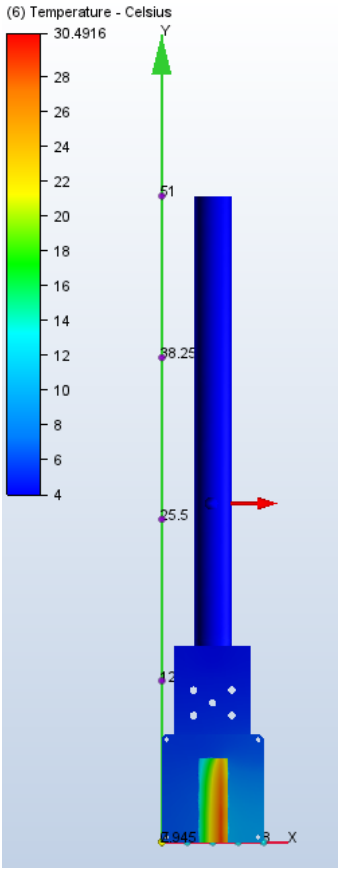

Figure .2: Simulated results of the electron detector with water at 4°C and 12 W of power supplied (3 W of power per plane).

• Measured temperature at sensor at B: 33.5°C.

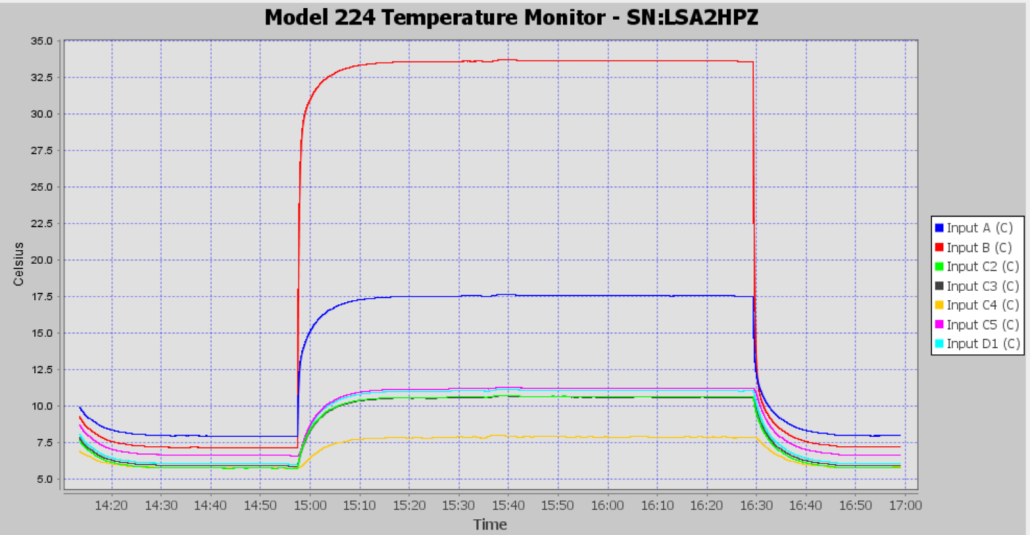

Figure .3: Measured results of the electron detector with water at 4°C and 12 W of power supplied (3 W of power per plane).

2.) Results for Coolant running at 8°C and Supplied Power of 12 W (3 W per plane).

• Simulated temperature at sensor at B: 34.4°C.

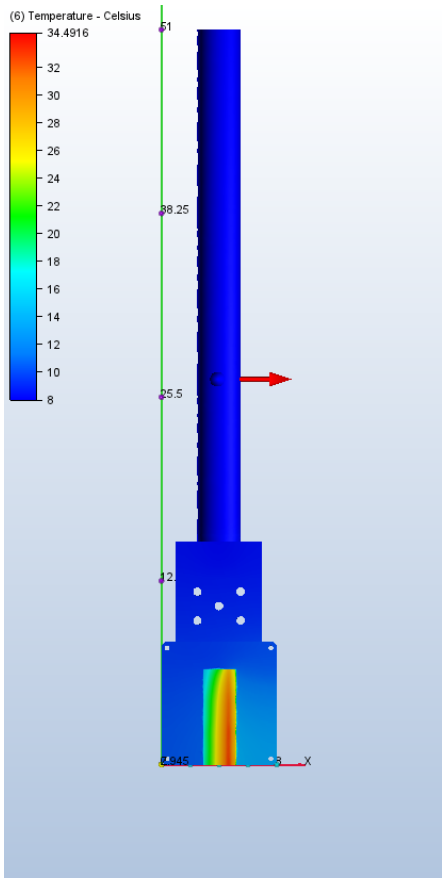

Figure .4: Simulated results of the electron detector with water at 8°C and 12 W of power supplied (3 W of power per plane)

• Measured temperature at sensor at B: 36°C.

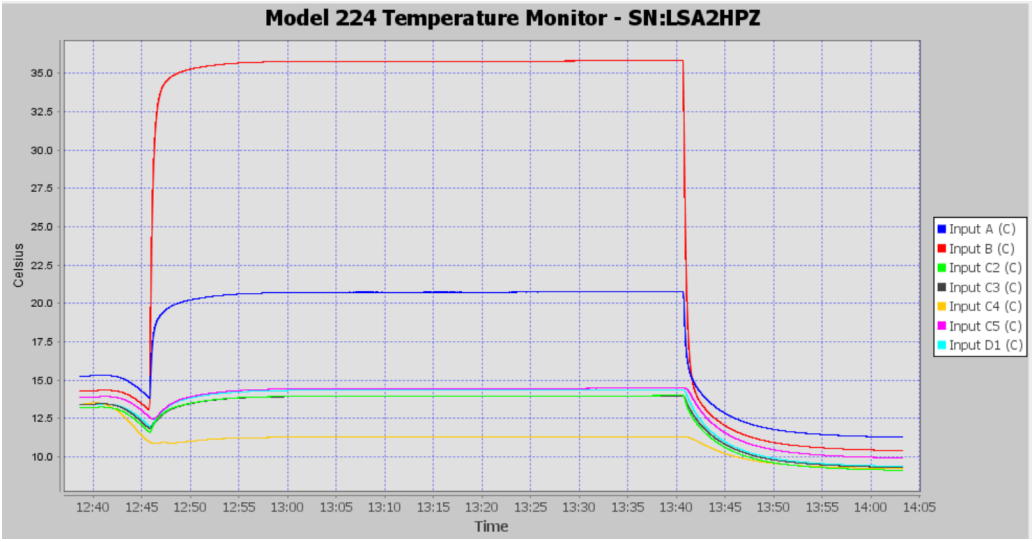

Figure .5: Measured results of the electron detector with water at 8°C and 12 W of power supplied (3 W of power per plane)

3.) Results for Coolant running at 16°C and Supplied Power of 12 W (3 W per plane).

• Simulated temperature at sensor at B: 42.5°C.

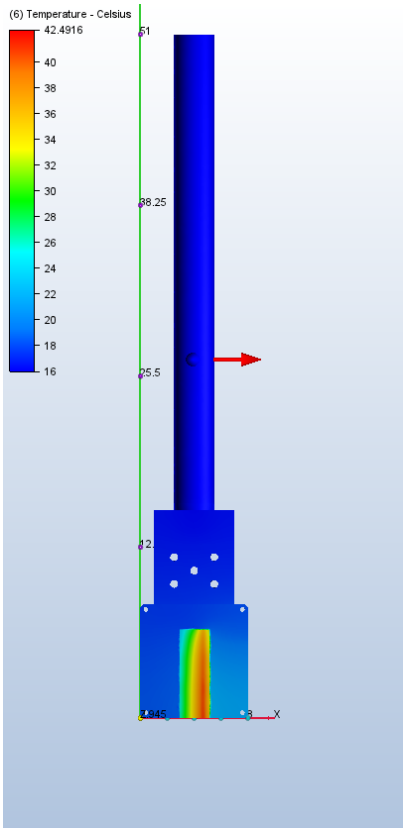

Figure .6: Simulated results of the electron detector with water at 16°C and 12 W of power supplied (3 W of power per plane)

• Measured temperature at sensor at B: 47.6°C.

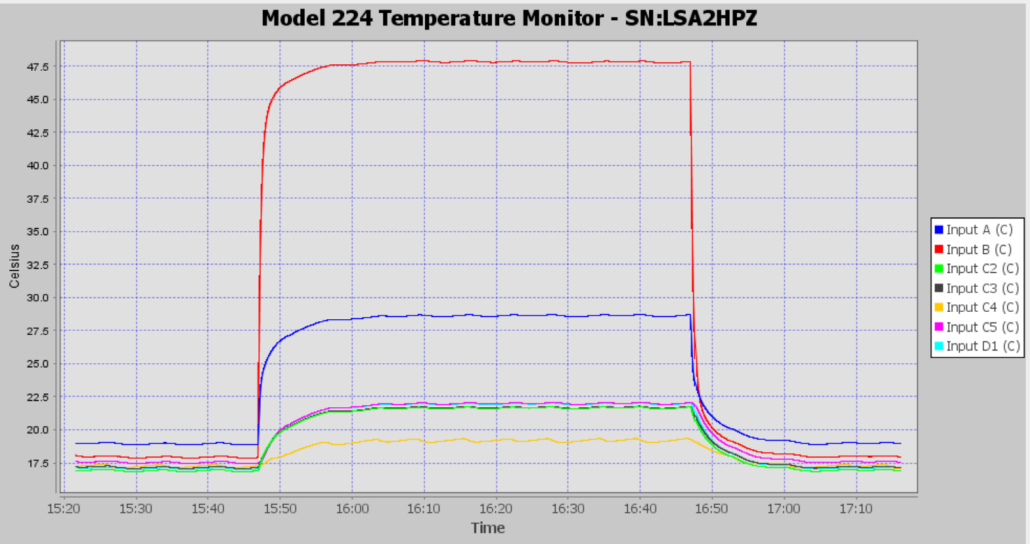

Figure .7: Measured results of the electron detector with water at 16°C and 12 W of power supplied (3 W of power per plane)

4.) Results for Coolant running at 4°C and Supplied Power of 6 W (1.5 W per plane).

• Simulated temperature at sensor at B: 17.3°C.

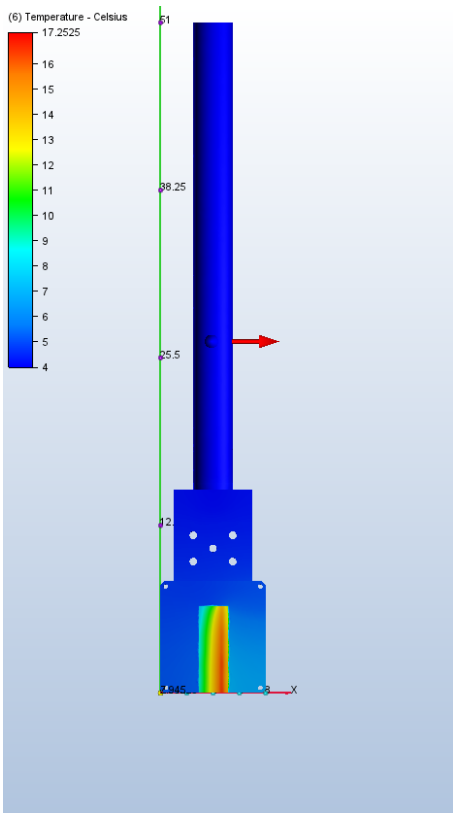

Figure .8: Simulated results of the electron detector with water at 4°C and 6 W of power supplied (1.5 W of power per plane)

• Measured temperature at sensor at B: 20.8°C.

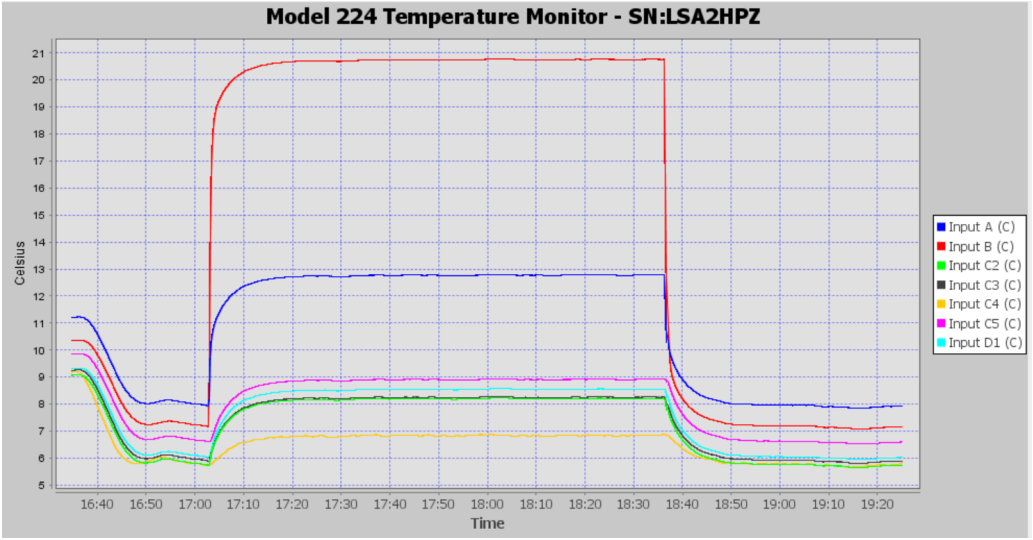

Figure .9: Measured results of the electron detector with water at 4°C and 6 W of power supplied (1.5 W of power per plane)

5.) Results for Coolant running at 8°C and Supplied Power of 6 W (1.5 W per plane).

• Simulated temperature at sensor at B: 21.3°C.

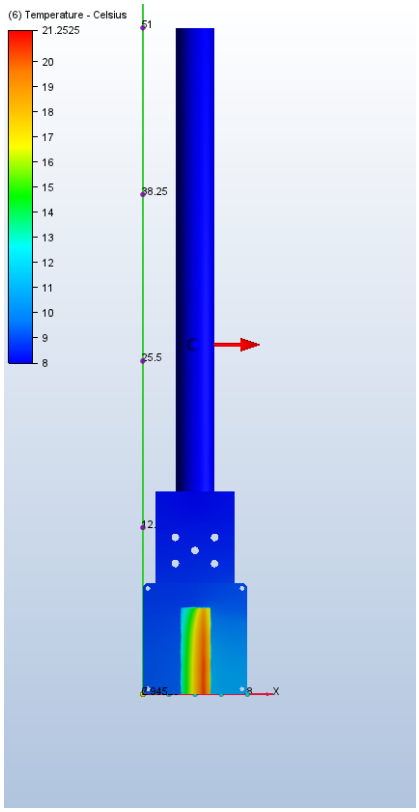

Figure .10: Simulated results of the electron detector with water at 8°C and 6 W of power supplied (1.5 W of power per plane)

• Measured temperature at sensor at B: 24.1°C.

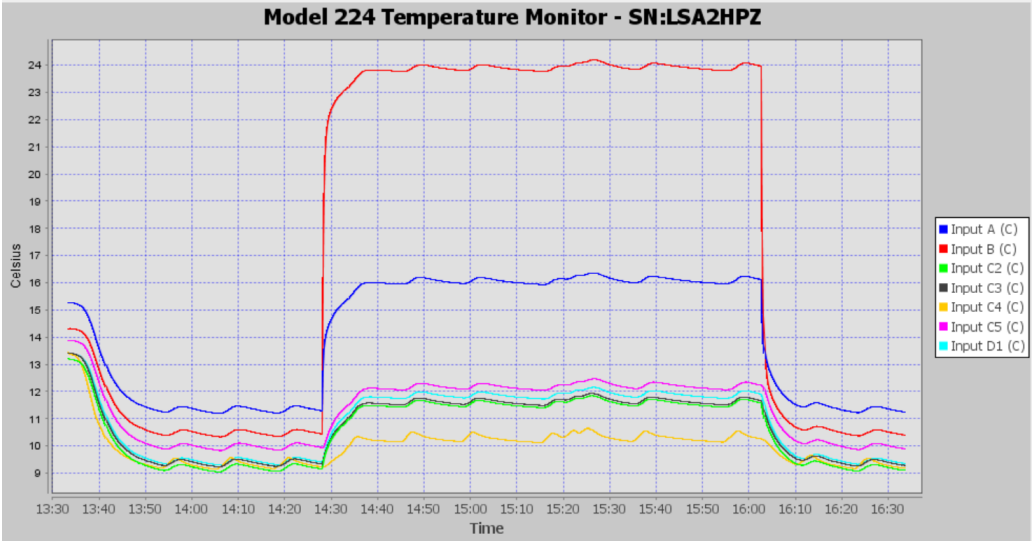

Figure .11: Measured results of the electron detector with water at 8°C and 6 W of power supplied (1.5 W of power per plane)

6.) Results for Coolant running at 12°C and Supplied Power of 6 W (1.5 W per plane).

• Simulated temperature at sensor at B: 25.2°C.

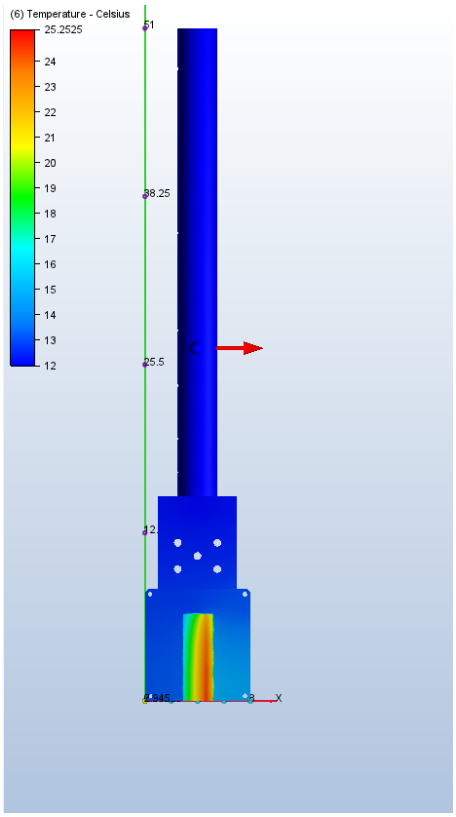

Figure .12: Simulated results of the electron detector with water at 12°C and 6 W of power supplied (1.5 W of power per plane)

• Measured temperature at sensor at B: 27.7°C.

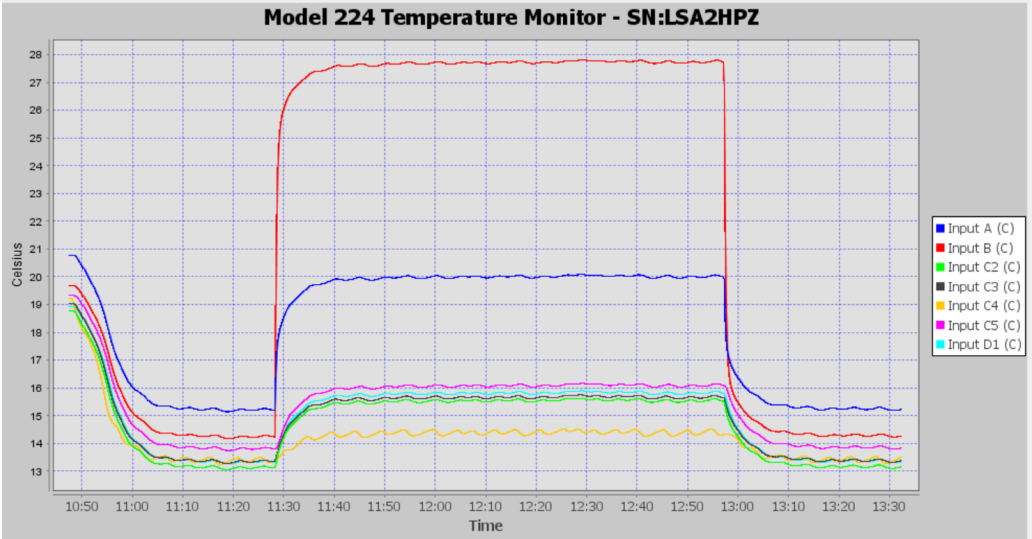

Figure .13: Measured results of the electron detector with water at 12°C and 6 W of power supplied (1.5 W of power per plane)

7.) Results for Coolant running at 16°C and Supplied Power of 6 W (1.5 W per plane).

• Simulated temperature at sensor at B: 29.2°C.

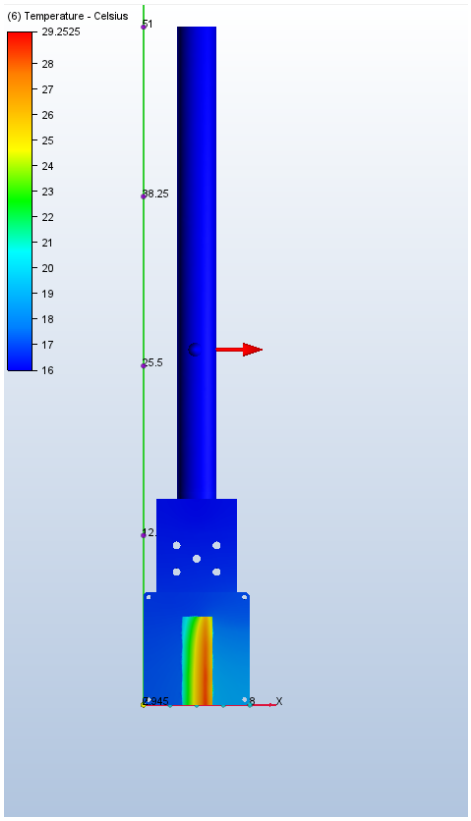

Figure .14: Simulated results of the electron detector with water at 16°C and 6 W of power supplied (1.5 W of power per plane)

• Measured temperature at sensor at B: 33°C.

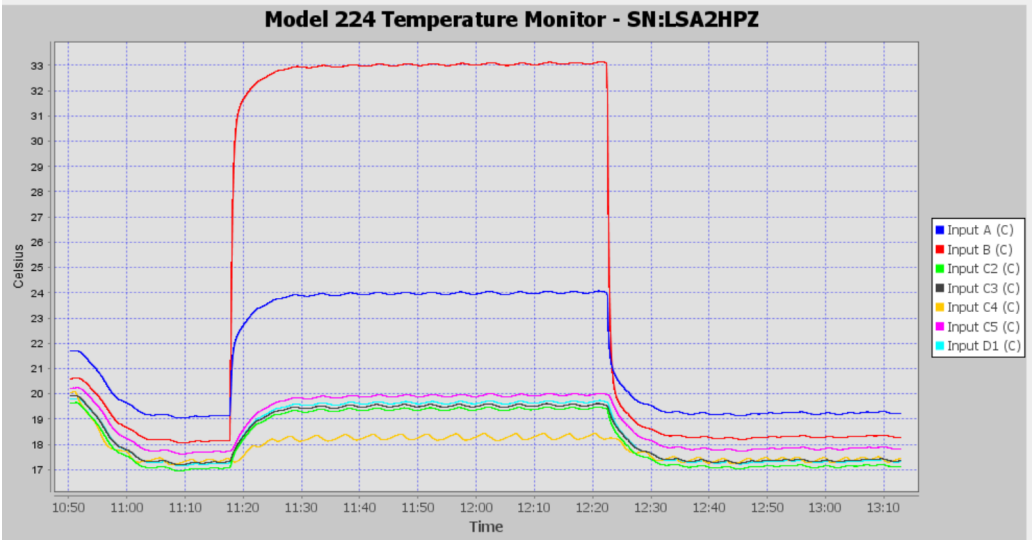

Figure .15: Measured results of the electron detector with water at 16°C and 6 W of power supplied (1.5 W of power per plane)

8.) Results for Coolant running at 4°C and Supplied Power of 15 W (3.75 W per plane).

• Simulated temperature at sensor at B: 37.1°C.

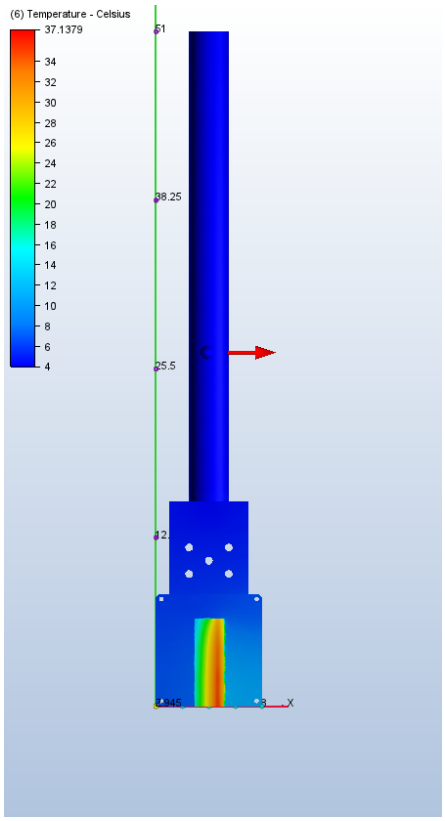

Figure .16: Simulated results of the electron detector with water at 4°C and 15 W of power supplied (3.75 W of power per plane)

• Measured temperature at sensor at B: 43°C.

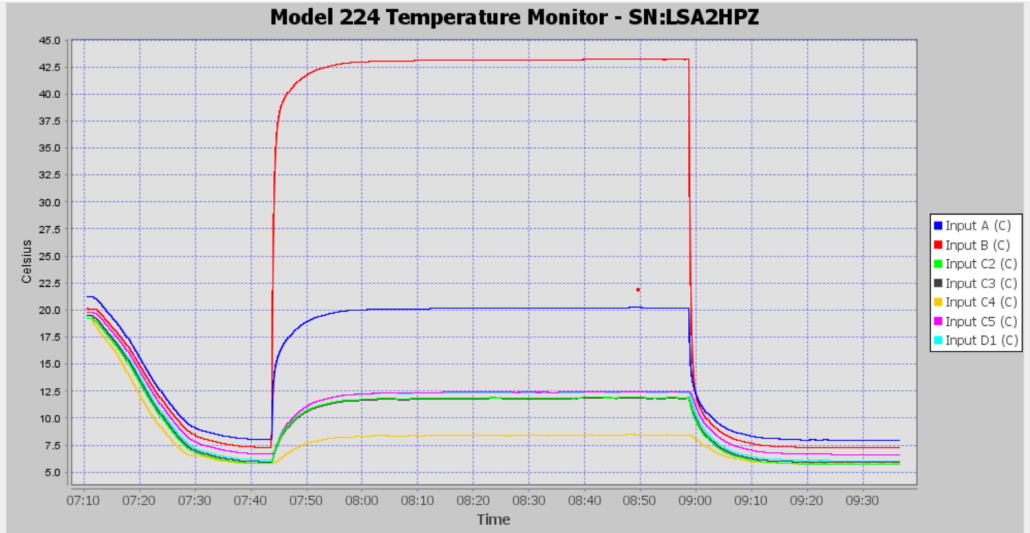

Figure .17: Measured results of the electron detector with water at 8°C and 15 W of power supplied (3.75 W of power per plane)

9.) Results for Coolant running at 8°C and Supplied Power of 15 W (3.75 W per plane).

• Simulated temperature at sensor at B: 41.1°C.

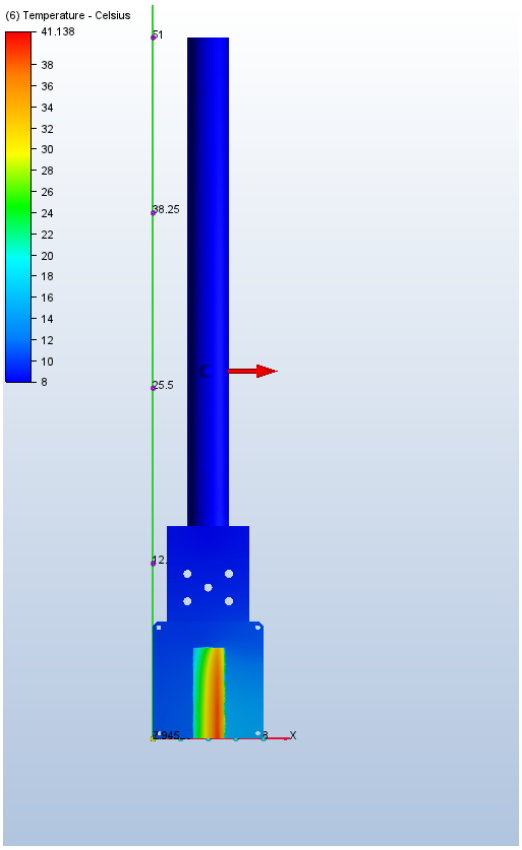

Figure .18: Simulated results of the electron detector with water at 8°C and 15 W of power supplied (3.75 W of power per plane)

• Measured temperature at sensor at B: 46°C.

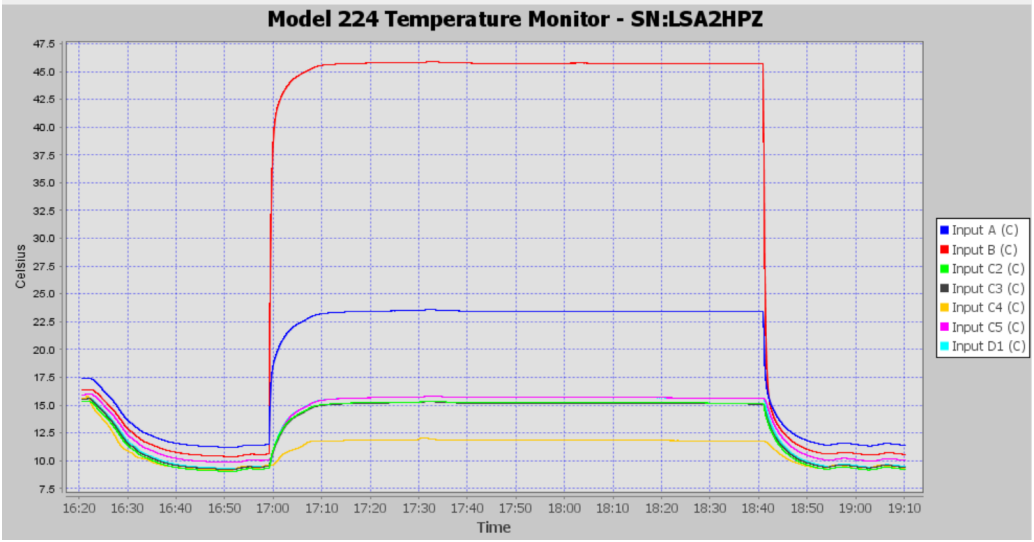

Figure .19: Measured results of the electron detector with water at 8°C and 15 W of power supplied (3.75 W of power per plane)

10.) Results for Coolant running at 12°C and Supplied Power of 15 W (3.75 W per plane).

• Simulated temperature at sensor at B: 45.1°C.

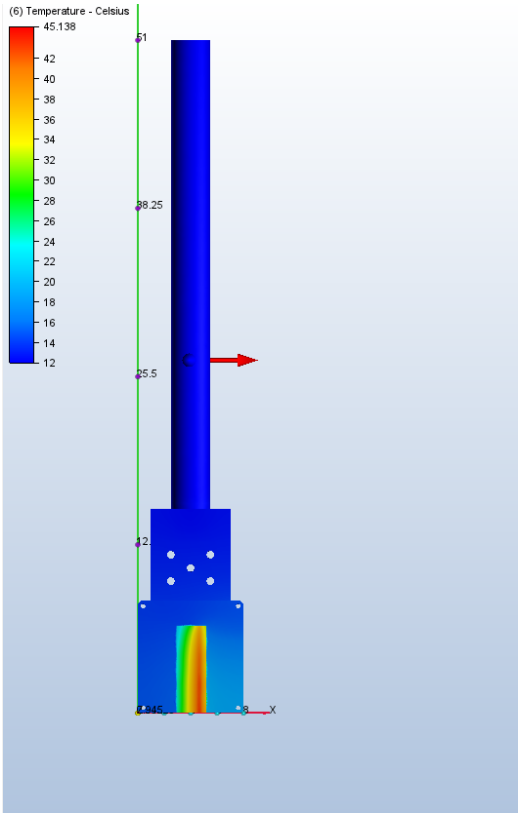

Figure .20: Simulated results of the electron detector with water at 12°C and 15 W of power supplied (3.75 W of power per plane)

• Measured temperature at sensor at B: 49°C.

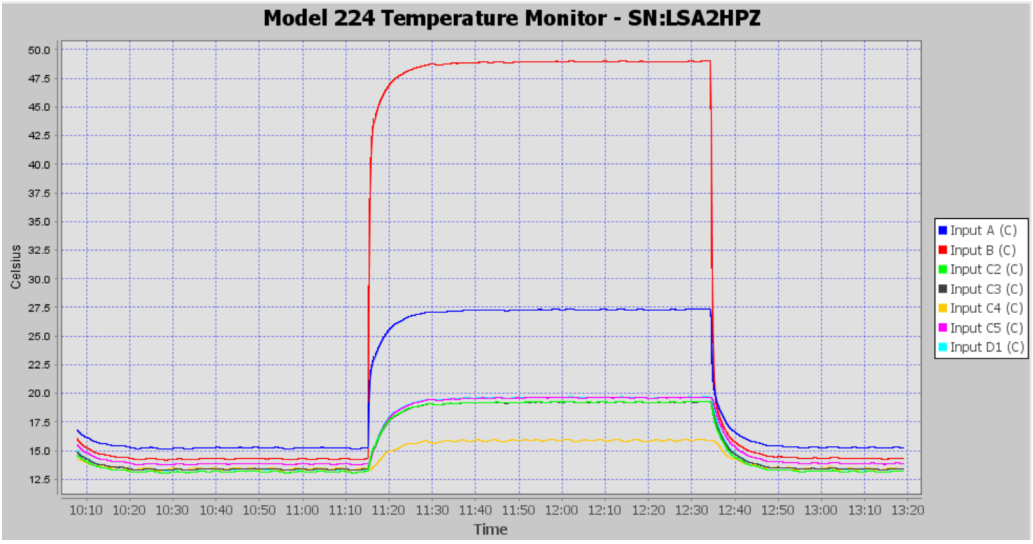

Figure .21: Measured results of the electron detector with water at 16°C and 15 W of power supplied (3.75 W of power per plane)

11.) Results for Coolant running at 16°C and Supplied Power of 15 W (3.75 W per plane).

• Simulated temperature at sensor at B: 49.1°C.

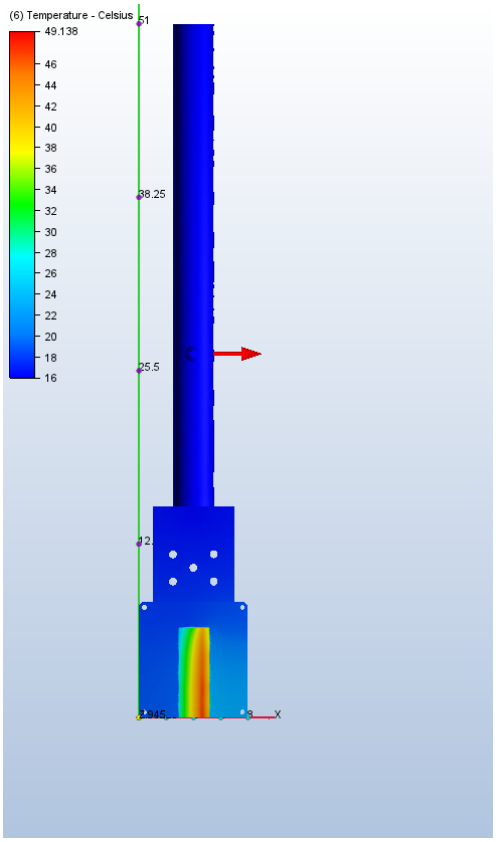

Figure .22: Simulated results of the electron detector with water at 16°C and 15 W of power supplied (3.75 W of power per plane)

• Measured temperature at sensor at B: 55°C.

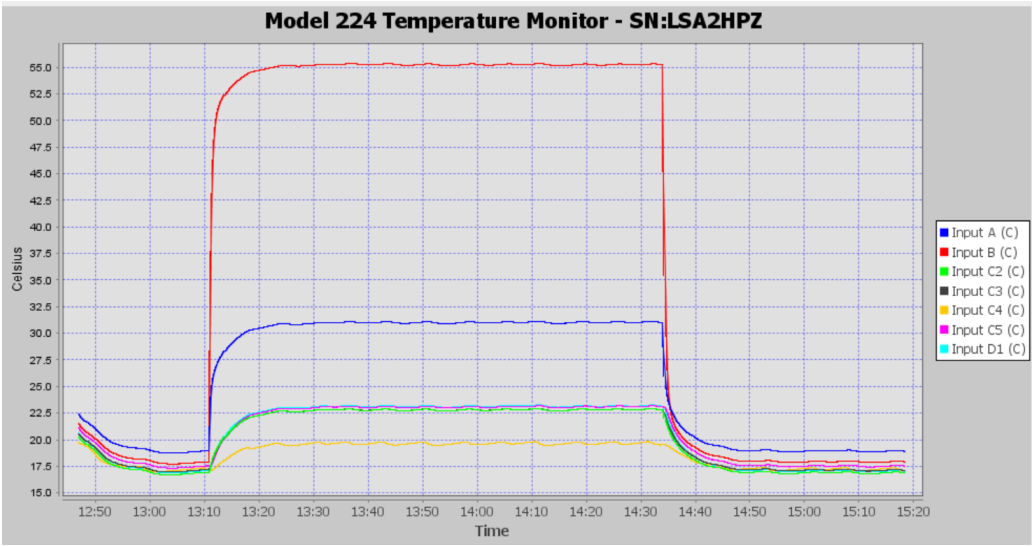

Figure .23: Measured results of the electron detector with water at 16°C and 15 W of power supplied (3.75 W of power per plane)

Bibliography

[1] Mark Thomson. *Modern particle physics*. Cambridge University Press, 2013.

[2] Brian R Martin and Graham Shaw. *Nuclear and particle physics: an introduction*. John Wiley & Sons, 2019.

[3] David Griffiths. *Introduction to elementary particles*. John Wiley & Sons, 2020.

[4] Physik-Institut, Universität Zürich. *Standard Model*. Outreach page by the Serra group, Physik-Institut, Universität Zürich. Accessed on August 26, 2025. 2025. URL: https://www.physik.uzh.ch/en/groups/serra/outreach/StandardModel.html.

[5] Glenn Elert. *The Standard Model — The Physics Hypertextbook*. The Physics Hypertextbook by Glenn Elert; accessed on August 26, 2025. 2025. URL: https://physics.info/standard/.

[6] Richard Clinton Fernow. *Introduction to experimental particle physics*. Cambridge university press, 1986.

[7] R. Nave. *Bag Model of Quark Confinement*. Georgia State University. Accessed on August 26, 2025. 2025. URL: http://www.hyperphysics.phy-astr.gsu.edu/hbase/Particles/qbag.html.

[8] Bruno B. Rossi. "Theory of Electromagnetic Interactions". In: *High-Energy Particles*. Available online via MIT course website. Accessed on August 26, 2025. Englewood Cliffs, NJ: Prentice-Hall, 1952. Chap. 2. URL: https://web.mit.edu/8.13/8.13c/references-fall/muons/rossi-high-energy-particles-1952-ch2-theory-electromagnetic-interaction.pdf.

[9] Luigi Di Lella and Carlo Rubbia. "The Discovery of the W and Z Particles". In: *60 Years of CERN Experiments and Discoveries*. World Scientific, 2015, pp. 137–163.

[10] C Yi Prescott et al. "Parity non-conservation in inelastic electron scattering". In: *Physics Letters B* 77.3 (1978), pp. 347–352.

[11] PLUTO Collaboration et al. "Measurement of the muon pair asymmetry in e^+e^- annihilation at $\sqrt{s} = 34.7$ GeV". In: *Zeitschrift für Physik C: Particles and Fields* 21 (1983), pp. 53–57.

[12] Peter W Higgs. "Broken symmetries and the masses of gauge bosons". In: *Physical review letters* 13.16 (1964), p. 508.

[13] François Englert and Robert Brout. “Broken symmetry and the mass of gauge vector mesons”. In: *Physical review letters* 13.9 (1964), p. 321.

[14] R Brout and François Englert. “Spontaneous symmetry breaking in gauge theories: A Historical survey”. In: *https://arxiv.org/abs/hep-th/9802142v2* (1998).

[15] Georges Aad et al. “Observation of a new particle in the search for the Standard Model Higgs boson with the ATLAS detector at the LHC”. In: *Physics Letters B* 716.1 (2012), pp. 1–29.

[16] Serguei Chatrchyan et al. “Observation of a new boson at a mass of 125 GeV with the CMS experiment at the LHC”. In: *Physics Letters B* 716.1 (2012), pp. 30–61.

[17] Wikipedia contributors. *Electroweak interaction*. Wikipedia. Last edited August 11, 2025; accessed August 26, 2025. 2025. URL: https://en.wikipedia.org/wiki/Electroweak_interaction.

[18] MOLLER Collaboration. *MOLLER Technical Design Report*. Tech. rep. MOLLER-TDR-24-02-15. Final version updated Feb 15, 2024. Jefferson Lab, 2024. URL: https://moller-docdb.physics.sunysb.edu/cgi-bin/DocDB/public/ShowDocument?docid=998.

[19] MOLLER Collaboration. *MOLLER Conceptual Design Report*. Tech. rep. Moller-doc-630-v2. Version v2, contents revised March 17, 2022; initial version submitted August 3, 2020. Jefferson Lab, 2020. URL: https://moller-docdb.physics.sunysb.edu/cgi-bin/DocDB/public/ShowDocument?docid=630.

[20] Department of Physics Astronomy, University of Tennessee, Knoxville. *Spin (Modern Physics Module)*. Physics 250 web module, Department of Physics Astronomy, University of Tennessee, accessed August 26, 2025. 2025. URL: http://electron6.phys.utk.edu/phys250/modules/module%203/spin.htm.

[21] Wikipedia contributors. *Helicity (particle physics)*. Wikipedia. Accessed on August 26, 2025; page last edited approximately 2 months ago. 2025. URL: https://en.wikipedia.org/wiki/Helicity_(particle_physics).

[22] J Benesch et al. “The MOLLER Experiment: An Ultra-Precise Measurement of the Weak Mixing Angle Using Møller Scattering”. In: *arXiv preprint arXiv:1411.4088* (2014).

[23] Wikipedia contributors. *Møller scattering*. Wikipedia. Last edited approximately 2 months ago; accessed August 26, 2025. 2025. URL: https://en.wikipedia.org/wiki/M%C3%B8ller_scattering.

[24] Andrzej Czarnecki and William J Marciano. “Polarized Møller scattering asymmetries”. In: *International Journal of Modern Physics A* 15.16 (2000), pp. 2365–2375.

[25] Paul A Souder et al. “Measurement of parity violation in the elastic scattering of polarized electrons from C 12”. In: *Physical review letters* 65.6 (1990), p. 694.

[26] DT Spayde et al. “The strange quark contribution to the proton’s magnetic moment”. In: *Physics Letters B* 583.1-2 (2004), pp. 79–86.

[27] HAPPEX Collaboration et al. "Precision Measurements of the Nucleon Strange Form Factors at $Q^2 \simeq 0.1\text{GeV}^2$". In: *https://arxiv.org/abs/nucl-ex/0609002v2* (2006).

[28] PL Anthony, RG Arnold, C Arroyo, et al. "SLAC E158 Collaboration". In: *Phys. Rev. Lett* 95 (2005), p. 081601.

[29] Sergey Abrahamyan et al. "Measurement of the neutron radius of Pb 208 through parity violation in electron scattering". In: *Physical review letters* 108.11 (2012), p. 112502.

[30] Qweak Collaboration. "Precision measurement of the weak charge of the proton". In: *Nature* 557.7704 (2018), pp. 207–211.

[31] Lawrence S Cardman. "Jefferson Lab". In: *Nuclear Physics News* 6.4 (1996), pp. 18–25.

[32] Joseph Grames, Douglas W. Higinbotham, and Hugh E. Montgomery. "The Thomas Jefferson National Accelerator Facility". In: *Scholarpedia* 5.7 (2010). Accessed: August 26, 2025, p. 10211. URL: `https://www.scholarpedia.org/article/The_Thomas_Jefferson_National_Accelerator_Facility`.

[33] Christoph W Leemann, David R Douglas, and Geoffrey A Krafft. "The continuous electron beam accelerator facility: CEBAF at the Jefferson Laboratory". In: *Annual Review of Nuclear and Particle Science* 51.1 (2001), pp. 413–450.

[34] CH Rode and JLab 12 GeV Project Team. "Jefferson lab 12 GeV CEBAF upgrade". In: *AIP Conference Proceedings*. Vol. 1218. 1. American Institute of Physics. 2010, pp. 26–33.

[35] Sakib Rahman. *Using parity-violating weak interaction to measure neutron matter density and search for new physics*. Tech. rep. Thomas Jefferson National Accelerator Facility (TJNAF), Newport News, VA 23606, 2021.

[36] C Yi Prescott et al. "Parity non-conservation in inelastic electron scattering". In: *Physics Letters B* 77.3 (1978), pp. 347–352.

[37] Daniel T Pierce, F Meier, and P Zürcher. "Negative electron affinity GaAs: A new source of spin-polarized electrons". In: *Applied Physics Letters* 26.12 (1975), pp. 670–672.

[38] MOLLER Collaboration et al. "The MOLLER Experiment Measurement Of a Lepton Lepton Electroweak Reaction An Ultra-precise Measurement of the Weak Mixing Angle using Mller Scattering". In: *MIE proposal to US DOE* (2014).

[39] Caryn Palatchi. *Laser and Electron Beam Technology for Parity Violating Electron Scattering Measurements*. Tech. rep. Thomas Jefferson National Accelerator Facility (TJNAF), Newport News, VA 23606, 2019.

[40] Ciprian Gal. "New precision measurements of the neutral weak form factor of 208Pb". In: *APS Division of Nuclear Physics Meeting Abstracts*. Vol. 2020. 2020, AA–002.

[41] M Poelker. "High power gain-switched diode laser master oscillator and amplifier". In: *Applied physics letters* 67.19 (1995), pp. 2762–2764.

[42] CK Sinclair et al. “Development of a high average current polarized electron source with long cathode operational lifetime”. In: *Physical Review Special Topics—Accelerators and Beams* 10.2 (2007), p. 023501.

[43] KD Paschke. “Controlling helicity-correlated beam asymmetries in a polarized electron source”. In: *The European Physical Journal A* 32 (2007), pp. 549–553.

[44] Cornell Laboratory for Accelerator-Based Sciences and Education (CLASSE). *Superconducting Radio Frequency (SRF) Research*. Accessed: August 26, 2025. 2025. URL: https://www.classe.cornell.edu/Research/SRF/AboutSrf.html.

[45] Cornell Laboratory for Accelerator-based Sciences and Education (CLASSE). *RF Superconductivity 2010*. Accessed: 2025-08-26. 2010. URL: https://www.classe.cornell.edu/rsrc/Home/Research/SRF/AboutSrf/RF_Superconductivity_2010.pdf.

[46] PA Adderley et al. “The continuous electron beam accelerator facility at 12 GeV”. In: *Physical Review Accelerators and Beams* 27.8 (2024), p. 084802.

[47] Joseph Grames, Douglas W Higinbotham, and Hugh E Montgomery. “Thomas Jefferson National Accelerator Facility”. In: *Nuclear Physics News* 20.3 (2010), pp. 6–13.

[48] Douglas W. Storey. “Compton Polarimetry”. Accessed: 2025-08-26. PhD thesis. University of Winnipeg, 2007. URL: http://nuclear.uwinnipeg.ca/theses/dstorey_thesis.pdf.

[49] Bardin et al. *Conceptual Design Report of a Compton Polarimeter for CEBAF Hall A*. Technical Report. CEA-Saclay / CEBAF, 1996.

[50] A Denner and S Dittmaier. “Electroweak radiative corrections to high-energy Compton scattering”. In: *Nuclear Physics B* 407.1 (1993), pp. 43–56.

[51] G Bardin et al. *A Compton polarimeter for CEBAF Hall A*. Tech. rep. CEA Centre d’Etudes de Saclay, 1994.

[52] G Shapiro et al. “THE COMPTON POLARIMETER AT THE SLC* June 1993 (A/E)”. In: *Proceedings of the International Conference on Particle Accelerators (PAC 1993)* (1993). Date of Conference: 17–20 May 1993, p. 309258. DOI: 10.1109/PAC.1993.309258.

[53] Kurt Aulenbacher et al. “Precision electron beam polarimetry for next generation nuclear physics experiments”. In: *International Journal of Modern Physics E* 27.07 (2018), p. 1830004.

[54] AV Glamazdin et al. “Electron beam Moeller polarimeter at JLAB Hall A”. In: *Fizika B: a journal of experimental and theoretical physics* 8.1 (1999), pp. 91–95.

[55] Abdurahim Rakhman. “The design and construction of a green laser and Fabry-Perot cavity system for Jefferson Lab’s Hall A Compton polarimeter”. PhD thesis. Syracuse University, 2011.

[56] Nafis Niloy et al. “High Voltage Monolithic Active Pixel Sensors for the MOLLER experiment”. In: *Nuclear Instruments and Methods in Physics Research Section A: Accelerators, Spectrometers, Detectors and Associated Equipment* 1069 (2024), p. 169874.

[57] QSStudy. *Band Theory*. Accessed: 2025-08-26. 2017. URL: https://www.qsstudy.com/wp-content/uploads/2017/04/Band-Theory.jpg.

[58] Ivan Perić. “A novel monolithic pixelated particle detector implemented in high-voltage CMOS technology”. In: *Nuclear Instruments and Methods in Physics Research Section A: Accelerators, Spectrometers, Detectors and Associated Equipment* 582.3 (2007), pp. 876–885.

[59] Ivan Perić. “A novel monolithic pixel detector implemented in high-voltage CMOS technology”. In: *2007 IEEE Nuclear Science Symposium Conference Record*. Vol. 2. IEEE. 2007, pp. 1033–1039.

[60] I Perić and Ch Takacs. “Large monolithic particle pixel-detector in high-voltage CMOS technology”. In: *Nuclear Instruments and Methods in Physics Research Section A: Accelerators, Spectrometers, Detectors and Associated Equipment* 624.2 (2010), pp. 504–508.

[61] I Perić et al. “The first beam test of a monolithic particle pixel detector in high-voltage CMOS technology”. In: *Nuclear Instruments and Methods in Physics Research Section A: Accelerators, Spectrometers, Detectors and Associated Equipment* 628.1 (2011), pp. 287–291.

[62] I Perić, Christian Kreidl, and Peter Fischer. “Particle pixel detectors in high-voltage CMOS technology—New achievements”. In: *Nuclear Instruments and Methods in Physics Research Section A: Accelerators, Spectrometers, Detectors and Associated Equipment* 650.1 (2011), pp. 158–162.

[63] I Perić. “Active pixel sensors in high-voltage CMOS technologies for ATLAS”. In: *Journal of Instrumentation* 7.08 (2012), p. C08002.

[64] Ivan Perić et al. “Strip technology and HVMAPS”. In: *21st International Workshop on Vertex Detectors*. 2012, p. 21.

[65] Heiko Augustin et al. “The MuPix high voltage monolithic active pixel sensor for the Mu3e experiment”. In: *Journal of Instrumentation* 10.03 (2015), p. C03044.

[66] Nafis Niloy. “Detector Development for the MOLLER Experiment”. Master’s Thesis. Winnipeg, Canada: University of Manitoba, 2023.

[67] Lake Shore Cryotronics, Inc. *Model 224 Temperature Monitor User’s Manual*. Rev. 1.3. Accessed: August 26, 2025. Westerville, Ohio, USA: Lake Shore Cryotronics, Inc., 2020. URL: https://www.lakeshore.com/docs/default-source/product-downloads/224_manual.pdf?sfvrsn=57de6414_7.

[68] S Courts and C Yeager. "Interchangeability of Diode Temperature Sensors for Various Non-Standard Excitation Currents". In: *Proceedings of the Twentieth International Cryogenic Engineering Conference (ICEC20)*. Elsevier. 2005, pp. 959–962.

[69] Theodore L Bergman. *Fundamentals of heat and mass transfer*. John Wiley & Sons, 2011.

[70] S&A. *S&A CW-5000 User Manual*. Online. Accessed: 2025-08-26. n.d. URL: http://nuclear.uwinnipeg.ca/theses/dstorey_thesis.pdf.

[71] Autodesk Inc. *Autodesk CFD: Simulation Software for Engineering Complex Liquid, Gas, and Air Systems*. Accessed: August 26, 2025. 2025. URL: https://www.autodesk.com/ca-en/products/cfd/overview.

[72] Autodesk Inc. *Autodesk Inventor: 3D CAD Software for Mechanical Design*. Accessed: August 26, 2025. 2025. URL: https://www.autodesk.com/ca-en/products/inventor/overview.

[73] Nafis Rafat Niloy. *Private communication*. Private communication, May 2025. 2025.

[74] T-Global Technology. *TG-A4500 Ultra-Soft Thermal Pad*. Online. Accessed: 2025-08-27. 2025. URL: https://www.tglobaltechnology.com/product/tg-a4500-ultra-soft-thermal-pad/.

[75] Thermal Management Technologies (TMT). *Thermal Strap Catalog*. Online. Accessed: 2025-08-27. URL: https://www.tmt-ipe.com/_files/ugd/4ab2a3_4e2226a5bbb640ae87b6009dcc438019.pdf.

[76] Douglas M. Gingrich. *PHYS 574 Particle Detectors*. Course notes, Department of Physics, University of Alberta. 2011.

[77] Donald E Groom and SR Klein. "Passage of particles through matter". In: *The European Physical Journal C-Particles and Fields* 15.1-4 (2000), pp. 163–173.

[78] Dr. Mohammad Laheji. *Private communication*. Private communication, May 2025. 2025.

[79] Jie Pan. *Private communication*. Private communication, May 2025. 2025.

[80] Kristofer Isaak. *Private communication*. Private communication, May 2025. 2025.

[81] MG Chemicals. *8329TFS-25ML Thermally Conductive Epoxy Adhesive User Manual*. Rev. 1.02. Accessed: August 26, 2025. Burlington, Ontario, Canada: MG Chemicals, 2025. URL: https://www.mgchemicals.com/downloads/tds/tds-8329tfs-2parts.pdf.

[82] Lake Shore Cryotronics, Inc. *DT-670 Series Silicon Diodes Datasheet*. Accessed: August 26, 2025. Westerville, Ohio, USA: Lake Shore Cryotronics, Inc., 2025. URL: https://www.lakeshore.com/docs/default-source/product-downloads/catalog/lstc_dt670_l.pdf?sfvrsn=fc2ebd1f_4.

[83] Von Roll USA, Inc. *GE Varnish 7031 Safety Data Sheet (SDS), Revision 3*. Accessed: August 26, 2025. Apr. 2015. URL: https://estore.oxinst.com/INTERSHOP/static/WFS/Oxinst-EU-Site/-/Oxinst/en_GB/PDFS/VonRoll%207031%20-%20GE%20Varnish%20SDS%20Rev3%2029%2004%202015.pdf.

[84] 3M Company. *3M Respirator Selection Guide*. Accessed: August 26, 2025. St. Paul, MN, USA: 3M Company, 2024. URL: https://multimedia.3m.com/mws/media/6391100/3m-respirator-selection-guide.pdf.

[85] 3M Canada. *3M™ Formaldehyde/Organic Vapour Cartridge 6005, 30 pairs/case*. Accessed: August 26, 2025. 2025. URL: https://www.3mcanada.ca/3M/en_CA/p/d/v000057398/.

[86] F. K. Delvotec Bondtechnik GmbH. *M17S: Fully automatic wire bonder with one bond head*. Online; F & K Delvotec website. Accessed: August 26, 2025. 2025. URL: https://www.fkdelvotec.com/en/machines/ultrasonic-wire-bonder/m17s-fully-automatic-wire-bonder-with-one-bond-head.